Développement d'un modèle de flamme épaissie dynamique pour la simulation aux grandes échelles de flammes turbulentes prémélangées

Itaru Yoshikawa

Itaru Yoshikawa. Développement d'un modèle de flamme épaissie dynamique pour la simulation aux grandes échelles de flammes turbulentes prémélangées. Autre. Ecole Centrale Paris, 2010. Français. NNT : 2010ECAP0017 . tel-00545423

HAL Id: tel-00545423
https://theses.hal.science/tel-00545423
Submitted on 10 Dec 2010

Ecole Centrale Paris

THESE

présentée par

Itaru YOSHIKAWA

pour l'obtention du

GRADE de DOCTEUR

Formation doctorale : Energétique

Laboratoire d'accueil : Laboratoire d'Énergétique Moléculaire
et Macroscopique, Combustion (EM2C)
du CNRS et de l'ECP

Développement d'un modèle de flamme épaissie dynamique pour la simulation aux grandes échelles de flammes turbulentes prémélangées

Soutenue le 23 juin 2010

Jury :	M	Colin	O.	Rapporteur
	MM	Cuenot	B.	Rapporteur
	M	Darabiha	N.	
	M	Vervisch	L.	Président
	M	Veynante	D.	Directeur de thèse
	M	Tanahashi	M.	Professeur invité

Ecole Centrale des Arts et Manufactures
Grand Établissement sous tutelle
du Ministère de l'Éducation Nationale
Grande Voie des Vignes
92295 Châtenay-Malabry Cedex
Tél : 33 (1) 41 13 10 00
Télex : 634 991 F EC PARIS

**Laboratoire d'Énergétique
Moléculaire et Macroscopique,
Combustion (E.M2.C.)**
UPR 288, CNRS et Ecole Centrale Paris
Tél : 33 (1) 41 13 10 31
Fax : 33 (1) 47 02 80 35

2010ECAP0017

Remerciements

Cette thèse a été réalisée au sein de l’équipe de combustion du laboratoire EM2C de l’Ecole Centrale Paris. Je tiens tout d’abord à exprimer mes remerciements à Denis Veynante, qui m’a permis d’effectuer mes recherches en France en encadrant ce travail. Sa patience, gentillesse, et sa rigueur m’ont constamment guidé tout au long de ces 3 années.

Je voudrais également remercie Luc Vervisch d’avoir accepté de présider mon jury de soutenance, ainsi que Olivier Colin et Bénédicte Cuenot d’avoir consacré leur temps comme rapporteur.

Je remercie Nasser Darabiha pour m’avoir accueilli au laboratoire EM2C en tant que directeur, ainsi que pour sa participation à mon jury. Ses conseils judicieux m’ont beaucoup aidé tout au long de mon travail.

Je souhaite aussi remercier Mamoru Tanahashi qui a apporté de nombreuses idées au cours des discussions que nous avons eues chaque fois que je suis rentré au Japon, et qui a fait le voyage depuis le Japon pour ma soutenance.

J’ai également eu le plaisir de travailler directement ou indirectement avec Sébastien Ducruix, Olivier Gicquel, Benoît Fiorina, Matthieu Boileau, et Gaofeng Wang.

Je témoigne également ma reconnaissance à Frédéric Boudy et Carolyn Jacobs, qui m’ont énormément aidé au niveau des langues fran caise et anglaise.

Je n’oublie pas bien-sûr tous les autres aue j’ai pu rencontrer au cours de ces années d’études. Je pense en particulier á Anne Bourdon, Deanna Lacoste, Jean-Michel Lamet, Laetitia Pons Taliercio, Ruben Esteban, Gabi-Daniel Stancu, Zdenek Bonaventura, Philippe Berard, Nicolas Kahhali et Rogerio dos Santos.

Résumé

La simulation numérique est l’un des outils les plus puissants pour concevoir et optimiser les systèmes industriels. Dans le domaine de la Dynamique des Fluides Numériques (CFD, "Computational Fluid Dynamics"), la simulation aux grandes échelles (LES, "Large Eddy Simulation") est aujourd’hui largement utilisée pour calculer les écoulements turbulents réactifs, où les tourbillons de grande taille sont calculés explicitement, tandis que l’effet de ceux de petite taille est modelisé. Des modèles de sous-mailles sont requis pour fermer les équations de transport en LES, et dans le contexte de la simulation de la combustion turbulente, le plissement de la surface de flamme de sous-maille doit être modelisé.

En général, augmenter le plissement de la surface de flamme de sous-maille favorise la combustion. L’amplitude de la promotion est donnée par une fonction d’efficacité, qui est dérivée d’une hypothèse d’équilibre entre la production et la destruction de la surface de flamme. Dans les méthodes conventionnelles, le calcul de la fonction d’efficacité nécessite une constante qui dépend de la géométrie de la chambre de combustion, de l’intensité de turbulence, de la richesse du mélange de air-carburant etc, et cette constante doit être fixée au début de la simulation. Autrement dit, elle doit être déterminé empiriquement.

Cette thèse développe un modèle de sous-maille pour la LES en combustion turbulente, qui est appelé le modèle dynamique de flammelette épaissie (DTF, "dynamic thickened flamelet model"), qui détermine la valeur de la constante en fonction des conditions de l’écoulement sans utiliser des données empiriques.

Ce modèle est tout d’abord testé sur une flamme laminaire unidimensionnelle pour vérifier la convergence de la fonction d’efficacité vers l’unité (aucun plissement de la surface de flamme de sous-maille). Puis il est appliqué en combinaison avec le modèle dynamique de Smagorinsky (Dynamic Smagorinsky model) aux simulations multidimensionnelles d’une flamme en V, stabilisée en aval d’un dièdre. Les résultats de la simulation en trois dimensions sont alors comparés avec les données expérimentales obtenues sur une expérience de même géométrie. La comparaison montre la faisabilité de la formulation dynamique.

Mots clés: Modèle dynamique, Simulation aux grandes échelles, Flammes turbulentes prémélangées

Abstract

Numerical simulation is one of the most powerful tools to design and optimize industrial facilities. In the field of Computational Fluid Dynamics (CFD), Large Eddy Simulation (LES) is widely used to compute turbulent reacting flows, where larger turbulent motions are explicitly computed, while only the effect of smaller ones is modeled. Subgrid models are required to close the transport equations in LES, and in the context of the simulation of turbulent combustion, the subgrid-scale wrinkling of the flame front must be modeled.

In general, subgrid-scale flame wrinkling promotes the chemical reaction. The magnitude of the promotion is given through an efficiency function derived from an equilibrium assumption between production and destruction of flame surface. In conventional methods, the calculation of the efficiency function requires a constant which depends on the geometry of the combustion chamber, turbulence intensity, the equivalence ratio of the fuel-air mixture, and so on; this constant must be prescribed at the beginning of the simulation. In other words, empirical knowledge is required.

This thesis develops a subgrid-scale model for LES of turbulent combustion, called the dynamic thickened flamelet (DTF) model, which determines the value of the constant from the flow conditions without any empirical input.

The model is first tested in a one-dimensional laminar flame to verify the convergence of the efficiency function to unity (no subgrid-scale flame front wrinkling). Then it is applied to multi-dimensional simulations of V-shape flame stabilized downstream of a triangular flame holder in combination with the dynamic Smagorinsky model. The results of the three-dimensional simulation are then compared with the experimental data obtained through the experiment of the same geometry. The comparison proves the feasibility of the dynamic formulation.

Key words: Dynamic model, Large eddy simulation, Turbulent premixed combustion

Contents

Résumé **v**

Abstract **vii**

Introduction and motivation **1**

1 Theory and models for turbulent combustion simulations **5**
1.1 Conservation equations 5
1.2 Numerical method for turbulent simulations 9
1.3 Models of turbulent combustion 19
1.4 The Dynamic Thickened Flamelet Model 20

2 Mono-dimensional test case **25**
2.1 Introduction 25
2.2 Numerical configuration 26
2.3 Results 37
2.4 Conclusion 64

3 Implementation into the AVBP code **67**
3.1 Introduction 67
3.2 Application to laminar combustion 68
3.3 Application to a two-dimensional turbulent combustion 82
3.4 Test of the dynamic Smagorinsky model 93
3.5 Conclusion 98

4 Two-dimensional simulation **103**
4.1 Introduction 103
4.2 Numerical configuration 103
4.3 Simulations without the dynamic procedures 107
4.4 Simulation with the dynamic thickened flamelet model 109
4.5 Combination of the dynamic procedure with the dynamic Smagorinsky model 120
4.6 Conclusion 131

5 Three-dimensional simulation 133
5.1 Introduction 133
5.2 Configuration 133
5.3 Test cases 136
5.4 Result and discussion 142
5.5 Comparison with experimental results 159
5.6 Computational costs of the dynamic procedures 162
5.7 Conclusion 165

Conclusions and perspectives 167

References 171

A Characteristic boundary condition 179

B Implementation of the filtering process and the dynamic procedure 183

List of Figures

1.1 Shape of the cut-off filter in spectral space. 12
1.2 Shape of the cut-off filter in physical space 13
1.3 Shape of the top hat filter 13
1.4 Shape of the Gaussian filter 14

2.1 Reaction rate of Ferziger 30
2.2 Profiles of the progress variable c calculated with the reduced reaction model of Ferziger 31
2.3 Profile of a one-dimensional laminar flame calculated with Ferziger and Echekki's reduced reaction rate model. $c^* = 0.5$ 32
2.4 Reaction rate calculated with the Arrhenius law as a function of progress variable c. 33
2.5 Profile of one-dimensional laminar flame calculated with the Arrhenius law 34
2.6 Reaction rate of Boger et. al. (1998) 35
2.7 Profile of a one-dimensional laminar flame calculated with Boger's model 36
2.8 Reaction rates in the dynamic formulation 39
2.9 Influence of the combination of filters on the reaction rate ratio calculated with different chemical reaction model 44
2.10 Influence of the combination of filters on the reaction rate ratio calculated with different chemical reaction model 45
2.11 Influence of the combination of filters on the reaction rate ratio calculated with different chemical reaction model 46
2.12 Influence of the combination of filters on the reaction rate ratio calculated with different chemical reaction model 47
2.13 Intermediate terms in the calculation of the reaction rate ratio. 48
2.14 Influence of the combination of filters on the reaction rate ratio calculated with different chemical reaction model 49
2.15 Influence of the combination of filters on the reaction rate ratio calculated with different chemical reaction model 50
2.16 Thickness of a filtered flame 52

2.17 Definition of flame thicknesses 53
2.18 Analytically calculated subgrid-scale momentum flux through a laminar flame $-\overline{\rho}\,(\widetilde{uu} - \widetilde{u}\widetilde{u})$ 56
2.19 The ratio of the analytically calculated subgrid-scale momentum flux to the exact value of the convection transport of momentum 57
2.20 Analytically calculated subgrid-scale momentum flux $-\overline{\rho}\,(\widetilde{uu} - \widetilde{u}\widetilde{u})$ in a thickened laminar flame by a factor of 20 57
2.21 Analytically calculated subgrid-scale momentum flux in a thickened laminar flame $-\overline{\rho}\,(\widetilde{uu} - \widetilde{u}\widetilde{u})$ 58
2.22 Ratio of the analytically calculated subgrid-scale momentum flux to the exact value of the convection transport of momentum . . 59
2.23 The dynamically calculated Smagorinsky constant and the subgrid-scale momentum flux in a laminar flame 60
2.24 The dynamically calculated Smagorinsky constant and the subgrid-scale momentum flux calculated with Moin’s procedure in a laminar flame 62
2.25 Comparison of the intermediate terms in the calculation of the Smagorinsky constant C_S 63
2.26 Comparison of the intermediate terms in the calculation of the Smagorinsky constant C_S 64

3.1 Computational mesh 70
3.2 Inner flame structure. 74
3.3 Ratio of the thicknesses of resolved and test-filtered flames and the LES filter size to yield $\gamma =$ ratio as functions of the test-filter size $\widehat{\Delta}$ 76
3.4 Generic reaction rates calculated with Boger’s algebraic model . 77
3.5 Generic reaction rates calculated with the Arrhenius law 78
3.6 Comparison of the progress variables calculated with different field variables 78
3.7 Ratio of $\langle W(\widehat{\widetilde{\mathbf{q}}})\rangle/\langle\overbrace{W(\widetilde{\mathbf{q}})}\rangle$ and the LES filter size Δ_F to yield $\gamma\langle\overbrace{W(\widetilde{\mathbf{q}})}\rangle/\langle W(\widehat{\widetilde{\mathbf{q}}})\rangle = 1$ as functions of the test-filter size $\widehat{\Delta}$ . . . 80
3.8 Comparison of the generic reaction rates of thickened flame and filtered thickened flame 81
3.9 Configuration of computational domain: All scales are given in mm 83
3.10 Computational mesh for two-dimensional simulation 83
3.11 Instantaneous resolved fields of the flame computed using Colin’s model 84
3.12 Definition of the control volume for the integral operation . . . 85

3.13 Effect of the test-filter size on the principal reaction rate calculated with filtered variables. Top to bottom $\widehat{\Delta} = 1.0 \times 10^{-2}, \widehat{\Delta} = 1.5 \times 10^{-2}, \widehat{\Delta} = 2.0 \times 10^{-2}, \widehat{\Delta} = 3.0 \times 10^{-2}$ (m), the reaction rates were calculated with reduced Arrhenius law. 86
3.14 Effect of the control volume size on β and the efficiency E . . . 91
3.15 Influence of the chemical model used in the dynamic thickened flamelet model 92
3.16 Profiles in a laminar one-dimensional flame 95
3.17 The Smagorinsky constant C_S and the turbulent viscosity τ calculated with the dynamic Smagorinsky model and Moin's procedure in a laminar one-dimensional flame 96
3.18 Fields of the Smagorinsky constant C_S and the turbulent viscosity μ_t calculated with the standard dynamic Smagorinsky model 98
3.19 Cross sectional view of the Smagorinsky constant C_S calculated with the dynamic Smagorinsky model and Moin's procedure . . 99
3.20 Cross sectional view of the turbulent viscosity μ_t calculated with the dynamic Smagorinsky model and Moin's procedure 100

4.1 Temperature and chemical species distribution with the stream line for the initialization of the flame. 105
4.2 Time averaged stream lines obtained through a simulation using a constant efficiency constant β. 110
4.3 Time averaged reaction rate of the principal reaction obtained through a simulation using a constant efficiency constant β. . . 111
4.4 Comparison of the time averaged values and the root mean square values of the velocity in x direction on the center line of the combustion chamber 112
4.5 Instantaneous field of the principal reaction rate where the reaction zone came close to the flame holder with $\beta = 0$ 112
4.6 Instantaneous field of the principal reaction rate where the reaction zone came close to the flame holder with $\beta = 0.7$ 112
4.7 Time averaged temperature fields obtained through a simulation using a constant efficiency constant β. 113
4.8 Root mean square values of temperature obtained through a simulation using a constant efficiency constant β. 114
4.9 Time averaged fields of major variables calculated with dynamic model 116
4.10 Time averaged fields of major variables calculated with dynamic model 118
4.11 Instantaneous fields of the reaction rate, Charlette's constant β, and the efficiency function E obtained in the simulation using the dynamic thickened flamelet model. 119
4.12 Time evolution of reaction zone of the principal reaction 121

4.13 Time evolution of the constant β 122
4.14 Time evolution of the efficiency function 123
4.15 Time averaged values of the Smagorinsky constant, C_S 125
4.16 Time averaged values of the turbulent viscosity μ_t 125
4.17 Time averaged temperature field, its root mean square value, and the stream line of the time averaged field calculated with the dynamic thickened flamelet model and the dynamic Smagorinsky model 126
4.18 Time averaged temperature field, its root mean square value, and the stream line of the time averaged field calculated with the dynamic thickened flamelet model and the dynamic Smagorinsky model with Moin's procedure 127
4.19 Comparison of the time averaged values and the root mean square values of the velocity in x direction on the center line of the combustion chamber 127
4.20 Time averaged fields of the constant β, the value of the efficiency function, and the principal reaction rate obtained through the simulation with the dynamic thickened flamelet model and the dynamic Smagorinsky model 129
4.21 Time averaged fields of the constant β, the value of the efficiency function, and the principal reaction rate obtained through a simulation with the dynamic thickened flamelet model and the dynamic Smagorinsky model 130

5.1 Configuration of three-dimensional computational domain . . . 134
5.2 Temperature iso-surface of $800\,K$ of the initial condition 135
5.3 Initial fields of temperature (K) and reaction rate of the principal reaction $(kg/m^3 \cdot s)$ on the $z = 0$ plane. 136
5.4 Comparison of the β fields on $z = 0$ plane calculated with different averaging interval 139
5.5 Comparison of the distribution of β calculated with different averaging intervals 139
5.6 Comparison of β and efficiency fields calculated with different averaging intervals 140
5.7 Comparison of the C_S fields on $z = 0$ plane calculated with different averaging intervals 142
5.8 Comparison of the μ_t fields on $z = 0$ plane calculated with different averaging intervals 143
5.9 Comparison of the C_S distribution in z direction calculated with different averaging intervals 144
5.10 Comparison of the μ_t distribution in z direction calculated with different averaging intervals 145

5.11 Iso-surface of vorticity magnitude, $|\omega| = 12000$, of an instantaneous field 147
5.12 Iso-surfaces of relative helicity, $h = 0.9$ and $h = -0.9$ of an instantaneous field 147
5.13 Time averaged reaction rate on several z planes 148
5.14 Time averaged temperature on several z planes 149
5.15 Amplitude of the time averaged velocity in the x direction and the streamlines of the time averaged field based on the velocity components of the x and y directions 151
5.16 Amplitude of the time averaged velocity in the z direction and the streamlines of the time averaged field based on the velocity components of the z and y directions 152
5.17 Streamlines of the time averaged flow field in the recirculation motion 152
5.18 Temporal evolution of dynamically calculated Charlette's constant β on the $\widetilde{c} = 0.5$ surface 154
5.19 Temporal evolution of the value of the efficiency function on the $\widetilde{c} = 0.5$ surface 155
5.20 Time averaged field of Charlette's constant β 157
5.21 Time averaged field of the efficiency function 158
5.22 Time averaged field of the dynamically calculated Smagorinsky constant C_S 160
5.23 Time averaged fields of the turbulent viscosity μ_t 160
5.24 Comparison of the time averaged filtered progress variable $[\widetilde{c}]$ and its resolved variance with the experimental data 163

B.1 Shape of the Gaussian filter 184
B.2 Coupling of the AVBP code and the DTF-DS code. 185

List of Tables

2.1 Numerical parameter of the flame. 30
2.2 Combinations of the filter type 38
2.3 Effective filter size δ_e required to reproduce laminar conditions 42

3.1 Flame parameters 70
3.2 Chemical parameters for the reaction rate 71
3.3 Flame thickness of a filtered flame ($\widehat{\Delta} = 1.0 \times 10^{-2}$ m). 75
3.4 Flame thickness of a filtered flame ($\widehat{\Delta} = 1.5 \times 10^{-2}$ m). 75
3.5 Flame thickness of a filtered flame ($\widehat{\Delta} = 2.0 \times 10^{-2}$ m). 75
3.6 Flame thickness of a filtered flame ($\widehat{\Delta} = 3.0 \times 10^{-2}$ m). 75
3.7 Comparison of the integral of the generic reaction rate ($\int W\,dx$). $\widehat{\Delta} = 1.5 \times 10^{-2}$ (m). 79
3.8 Comparison of the integral of the generic reaction rate ($\int W/\alpha\,dx$). $\widehat{\Delta} = 1.5 \times 10^{-2}$ (m). 79
3.9 Comparison of $\langle W(\widehat{\widetilde{\mathbf{q}}})\rangle / \overbrace{\langle W(\widetilde{\mathbf{q}})\rangle}$ 80
3.10 Comparison of $\gamma\overbrace{\langle W(\widetilde{\mathbf{q}})\rangle} / \langle W(\widehat{\widetilde{\mathbf{q}}})\rangle$ calculated with the averaged variables in whole domain 88
3.11 Comparison of $(1 + \min\left[\gamma F, \Gamma_{\gamma\overline{\Delta}}\langle u'_{\gamma\overline{\Delta}}\rangle / S_L\right]) / (1 + \min\left[F, \Gamma_{\overline{\Delta}}\langle u'_{\overline{\Delta}}\rangle / S_L\right])$ in the denominator of the dynamic formulation calculated with the averaged variables in whole domain 88
3.12 Comparison of β calculated with the averaged variables in whole domain 88
3.13 Comparison of E calculated with the averaged variables in whole domain 88
3.14 Comparison of β calculated by the alternative formulation with the averaged variables in the whole domain 89
3.15 Comparison of E calculated by the alternative formulation with the averaged variables in the whole domain 89

4.1 Chemical parameters for the reaction rate. 104

5.1 Numerical parameters of the simulation. 164
5.2 Comparison of the computational costs of the simulation performed with the dynamic thickened flamelet (DTF) and the dynamic Smagorinsky (DS) models. 164
5.3 Comparison of the CPU time of the time evolution part and the part of the dynamic procedures. 164

Introduction and motivation

In our society the importance of combustion is inestimable. We utilize the energy generated through combustion not only in the domestic equipments such as heating systems, gas stoves, and vehicles, but also in large facilities like power plants, ironworks, and waste combustion facilities. Public transportation depends greatly on combustion through the use of buses, ships, and planes. Nobody lives without it.

In designing of these equipments and facilities, experimental studies with prototype models are indispensable for generating the optimal performance. Nowadays, the reduction of greenhouse gases is also an important topic. Careful designing of efficient facilities is then of huge importance. However, the construction of a prototype itself costs time and resources.

Numerical simulation is a powerful tool in this scene. It allows us to investigate the optimal configuration of the target facilities before the construction of the prototype. Though there are always some discrepancies between the results of simulations and practical systems, the optimization is done without consuming any resources.

In computational fluid mechanics, three major approaches have been proposed: Direct Numerical Simulation (DNS), Reynolds Averaged Navier-Stokes (RANS) simulation and Large Eddy Simulation (LES). DNS is the simplest method that simulates flows without any models. The precision of this method relies on the density of the computational mesh, which, in general, leads to a prohibitive computational costs for the sufficient resolution of turbulent structures. RANS calculates only the average field of the variables. It reduces the computational costs dramatically, but the information of the local structure is not taken into account and is lost. To describe these lost information, powerful models are required. In LES, larger turbulent structures are calculated explicitly similar to DNS, while smaller structures are modeled; the quality of models determines the reliability of the simulation. The advantage of this method is that the computational grid does not need to be as dense as in DNS, and the computational costs are reduced.

The combustion researchers also explore the advantages of LES for simulations of turbulent combustion. The difficult element in the LES of turbulent combustion is that the LES grids are generally larger than the flame structures and the evolution of the flame is not resolved on the mesh. To overcome this difficulty, a flame tracking technique is necessary, and, in addition, the subgrid-scale structure of the flame needs to be modeled.

Various models have been developed for the sub-grid scale flame wrinkling. Damköhler (1940) is the pioneer of the modeling of the flame propagation speed. Then numerical models derived from correlation of experimental data(Abdel-Gayed et al. (1987), Bradley (1992)) and based on the theoretical analysis such as the Renormalization Group Theory (RNG) (Yakhot (1988), Pocheau (1994)) have been proposed. An approach that considers the flame surface as a scale invariant surface has led to fractal models(Gouldin (1987), Gouldin et al. (1989), Gulder (1991)). However, no researcher has achieved to described the turbulent flame speed with a single universal model.

In the course of the development of the subgrid-scale models, dynamic procedures have been proposed. The applications of the dynamic procedure to the level set approach and to the fractal-similarity model have been performed by several authors (Im et al. (1997), Bourlioux (2000), Knundsen and Pitsch (2008), Knikker et al. (2002), Knikker et al. (2004)), but the application to the Thickened Flamelet (TF) model has not yet been done.

The present study aims to develop a dynamic subgrid-scale model for LES of turbulent combustion based on the TF model. In the context of the TF model, the thickened flame is known to be less sensitive to turbulence than the original flame; thus, an efficiency function E is introduced to counter balance the effect of thickening and to evaluate that of turbulence on the promotion of reaction rate. This function requires an empirical constant that must be presumed before the simulation depending on the configuration. However, the empirical input becomes no longer required by applying a dynamic procedure for the constant. This kind of a dynamic determination of the constant is common in computational fluid mechanics for the calculation of Reynolds stresses, (see, for example, the dynamic Smagorinsky model (Germano et al. 1991)), although few reports are found in the context of the simulations of turbulent combustion. The original version of the dynamic procedure investigated in the present study has been proposed by Charlette et al. (2002b). The authors have derived the procedure and tested its ability in a simple geometry of a flame evolving in statistically homogenous turbulence.

The present study targets more realistic turbulent flames: a V-shaped flame investigated by Boger and Veynante (2000), Knikker et al. (2000), Knikker et al. (2002), Knikker et al. (2004), and Giacomazzi et al. (2004).

Structure of the manuscript

The theoretical background of the simulation of turbulent combustion is presented in Chapter 1. This chapter introduces the transport equations of physical quantities and the LES models for turbulence and combustion. The concept of the dynamic thickened flamelet (DTF) model is also given in this chapter.

In the second chapter, one-dimensional tests of the DTF model are conducted. Because this model has not been tested strictly under a laminar condition where the efficiency function E should be unity, one-dimensional tests are performed to verify if the model returns correct output in laminar conditions. The dependence of the results on the choice of thickening factor, chemical model for reaction rate, and filtering process are discussed. Tests of the dynamic Smagorinsky model on a laminar flame are also presented. These tests aim to observe the existence of the unresolved fluxes opposite to the gradients and the ability of the dynamic Smagorinsky model to reproduce it.

The third chapter describes the implementation of the DTF model into the AVBP code, which has been developed by CERFACS and IFP. The same tests as performed in chapter 2 are performed to verify the conclusion of Chapter 2. Then the DTF model is applied to an instantaneous solution of a two-dimensional turbulent flame calculated with a fixed model constant, and the filter size and the interval of averaging for the calculation of the efficiency function are optimized. The Dynamic Smagorinsky model is also tested with the two-dimensional flame to observe the prediction of the model under turbulent conditions.

Two-dimensional simulations with and without the DTF model are performed in Chapter 4. Their results are compared to observe the performance of the DTF model of calculating turbulent combustion without any input. Then the DTF model is combined with the dynamic Smagorinsky model and two-dimensional simulations are conducted. Two types of the dynamic Smagorinsky models, both considering the density change across the flame and not, are tested and the effect of the density change is observed.

A three-dimensional simulation follows in Chapter 5. The simulation is performed with the DTF model and the dynamic Smagorinsky model retaining the same configuration as that of Chapter 4. The results are then compared to the experimental data. The comparison of results of simulations and experiments is not straightforward and is briefly discussed.

Lastly, general conclusions and perspectives are drawn in the final chapter.

Chapter 1

Theory and models for turbulent combustion simulations

This chapter aims to introduce the fundamental equations describing turbulent flow, the behavior of flame, and their interaction. Further information can be found in Poinsot and Veynante (2005), Ferziger and Perić (2002),Veynante and Vervisch (2002), and Pitsch (2006).

1.1 Conservation equations

Suppose that a control volume is defined in the middle of a flow of density ρ, and that a conserved scalar ϕ is defined for unit mass, the conservation law for this control volume is described as

$$\frac{\partial}{\partial t}\int_{\Omega}\rho\phi\,\mathrm{d}\Omega+\int_{S}\rho\phi\mathbf{u}\cdot\mathbf{n}\,\mathrm{d}S=\sum f_{\phi}\,, \tag{1.1}$$

where the first term represents the integral over the volume and the second term corresponds to the integral on the surface of the control volume, $\mathbf{n}$ is the unit vector normal to the surface and $\mathbf{u}$ is the flow velocity. The terms on the left-hand-side are the temporal change of the conserved scalar and the convective transfer through the surface of the control volume respectively. The right-hand-side is the sum of the source or sink term other than the convective term. The differential form of this equation is written as

$$\frac{\partial\left(\rho\phi\right)}{\partial t}+\operatorname{div}\left(\rho\phi\mathbf{u}\right)=q_{\phi}\,, \tag{1.2}$$

where q_{ϕ} is the source term of ϕ.

1.1.1 Conservation of mass and momentum

If we set $\phi = 1$, the equation above describes the conservation of mass,

$$\frac{\partial}{\partial t}\int_{\Omega} \rho \, \mathrm{d}\Omega + \int_{S} \rho \mathbf{u} \cdot \mathbf{n} \, \mathrm{d}S = Q \,, \tag{1.3}$$

$$\frac{\partial \rho}{\partial t} + \mathrm{div}\,(\rho \mathbf{u}) = q \,. \tag{1.4}$$

Considering that the source term of mass is equal to zero, the differential form leads to a well-known continuity equation,

$$\frac{\partial \rho}{\partial t} + \mathrm{div}\,(\rho \mathbf{u}) = 0 \,. \tag{1.5}$$

Setting $\phi = \mathbf{u}$, the integral form of the generic equation (Equation 1.1) writes

$$\frac{\partial}{\partial t}\int_{\Omega} \rho \mathbf{u} \, \mathrm{d}\Omega + \int_{S} \rho \mathbf{u}\mathbf{u} \cdot \mathbf{n} \, \mathrm{d}S = \sum f \,. \tag{1.6}$$

This equation describes the momentum conservation. The source term is due to the surface and the body forces which act on the control volume. For multi species flows, this force can be written as

$$\sum f = \rho \sum_{k=1}^{N} Y_k \mathbf{f}_k \,, \tag{1.7}$$

where Y_k is the mass fraction of species k, and $\mathbf{f}_k$ is the sum of surface and body forces which work on the species. The surface force is caused by pressure gradient, shear stress, surface tension, and so on; the body force is the sum of the gravity, centrifugal and Coriolis forces, electromagnetic force, etc. However considering that the effects of these forces are small and negligible, the equation yields

$$\frac{\partial}{\partial t}\int_{\Omega} \rho \mathbf{u} \, \mathrm{d}\Omega + \int_{S} \rho \mathbf{u}\mathbf{u} \cdot \mathbf{n} \, \mathrm{d}S = \int_{S} \mathbf{T} \cdot \mathbf{n} \, \mathrm{d}S \,, \tag{1.8}$$

where $\mathbf{T}$ represents the stress tensor on the surface of the control volume. For Newtonian fluids, which is a good representative of many actual fluids, the stress tensor $\mathbf{T}$ can be written as

$$\mathbf{T} = -\left(p + \frac{2}{3}\mu \, \mathrm{div}\, \mathbf{u}\right)\mathbf{I} + 2\mu \mathbf{D}, \tag{1.9}$$

where p is the static pressure, μ is the dynamic viscosity, $\mathbf{I}$ is the unit tensor and $\mathbf{D}$ is the deformation tensor,

$$\mathbf{D} = -\frac{1}{2}\left[\mathrm{grad}\, \mathbf{u} + (\mathrm{grad}\, \mathbf{u})^T\right] \,. \tag{1.10}$$

The differential form of the momentum conservation equation is given as

$$\frac{\partial (\rho \mathbf{u})}{\partial t} + \mathrm{div}\,(\rho \mathbf{u}\mathbf{u}) = \mathrm{div}\, \mathbf{T} \,. \tag{1.11}$$

1.1.2 Conservation of species and energy

For other conserved scalars, a gradient approximation is usually introduced for the diffusive transport. Fourier’s law for heat diffusion and Fick’s law for mass diffusion are the well-known examples. Representing diffusion velocity by $\mathbf{V}_\phi$, this approximation writes

$$\int_S \phi\, \mathbf{V}_\phi \cdot \mathbf{n}\, \mathrm{d}S = -\int_S \mathit{\Gamma}\, \mathrm{grad}\, \phi \cdot \mathbf{n}\, \mathrm{d}S\,, \tag{1.12}$$

where $\mathit{\Gamma}$ is the diffusion coefficient of ϕ. The conservation of species and that of energy can be described with this equation. In multi species flow, the gradient approximation gives the diffusion velocity $\mathbf{V}_k$ of species k,

$$Y_k \mathbf{V}_k = -D_k\, \mathrm{grad}\, Y_k\,, \tag{1.13}$$

and this velocity should satisfy

$$\sum_{k=1}^{N} Y_k V_{k,i} = 0\,. \tag{1.14}$$

where the subscript i represents the direction of the coordinate system. In general, the sum of the diffusion velocity approximated with the gradient as in Equation 1.13 does not satisfy Equation 1.14. To hold the relation of Equation 1.14, a correction convection velocity $\mathbf{V}^c$,

$$\mathbf{V}^c = \sum_{k=1}^{N} D_k\, \mathrm{grad}\, Y_k\,, \tag{1.15}$$

is introduced and the diffusion velocity is corrected as

$$Y_k \mathbf{V}_k = -D_k\, \mathrm{grad}\, Y_k + Y_k \mathbf{V}^c\,. \tag{1.16}$$

Substituting the mass fraction Y_k of species k into ϕ, the generic equation (Equation 1.1) gives

$$\frac{\partial}{\partial t}\int_\Omega \rho Y_k\, \mathrm{d}\Omega + \int_S \rho Y_k \mathbf{u} \cdot \mathbf{n}\, \mathrm{d}S = \sum S_{Y_k}\,. \tag{1.17}$$

The right-hand-side contains the source term caused by chemical reactions and the transport of Y_k due to mechanisms other than the convection transport; thus, the right-hand side is rewritten as

$$\sum S_{Y_k} = \int_S \rho D_k\, \mathrm{grad}\, Y_k\, \cdot \mathbf{n}\, \mathrm{d}S + \int_\Omega \dot{\omega}_k\, \mathrm{d}\Omega\,, \tag{1.18}$$

where D_k is called as the diffusivity of species k. Here the product ρD_k represents $\mathit{\Gamma}$ of the Equation 1.12. The equation then leads to

$$\frac{\partial}{\partial t}\int_\Omega \rho Y_k \,\mathrm{d}\Omega + \int_S \rho Y_k \mathbf{u}\cdot\mathbf{n}\,\mathrm{d}S = \int_S \rho D_k \,\mathrm{grad}\, Y_k \;\cdot\mathbf{n}\,\mathrm{d}S + \int_\Omega \dot{\omega}_k \,\mathrm{d}\Omega\,, \quad (1.19)$$

and its differential form is

$$\frac{\partial\left(\rho Y_k\right)}{\partial t} + \mathrm{div}\left(\rho \mathbf{u} Y_k\right) = \mathrm{div}\left[\,\rho D_k \,\left(\mathrm{grad}\, Y_k\right)\right] + \dot{\omega}_k\,. \quad (1.20)$$

For the conservation of energy, that of enthalpy is often considered. The equation can be derived following relation

$$h = h_t - E = e_t + p/\rho - E\,, \quad (1.21)$$

where e_t is total energy (t indicates "total"), h is enthalpy and E is kinetic energy. The derivation of the transport equations starts from the conservation of total energy e_t, whose differential form is written as

$$\frac{\partial \rho e_t}{\partial t} + \mathrm{div}\left(\rho \mathbf{u} e_t\right) = -\mathrm{div}\,\mathbf{q} + \mathrm{div}\left(\mathbf{T}\cdot\mathbf{u}\right) + \dot{Q}_e + \rho\sum_{k=1}^{N} Y_k \mathbf{f}_k\cdot\left(\mathbf{u}+\mathbf{V}_k\right)\;, \quad (1.22)$$

where $\dot{Q}_e$ is the source term of heat and the last term is the power produced by volume force $\mathbf{f}_k$ on species k, $\mathbf{q}$ is the energy flux given by

$$\mathbf{q} = -\lambda\,\mathrm{grad}\, T + \rho\sum_{k=1}^{N} h_k Y_k \mathbf{V}_k\;. \quad (1.23)$$

The first term is the heat diffusion approximated with Fourier's law and the second term is the energy diffusion due to the diffusion of species.
The equation for kinetic energy is obtained by taking the product of the equation of momentum (Equation 1.11) with $\mathbf{u}$.

$$\begin{aligned}\frac{\partial\left(\rho\mathbf{u}\right)}{\partial t}\cdot\mathbf{u} + \mathrm{div}\left(\rho\mathbf{u}\mathbf{u}\right)\cdot\mathbf{u} &= \frac{\partial}{\partial t}\left(\rho\,\frac{1}{2}\mathbf{u}\cdot\mathbf{u}\right) + \mathrm{div}\left[\rho\mathbf{u}\left(\frac{1}{2}\mathbf{u}\cdot\mathbf{u}\right)\right]\\ &= \frac{\partial \rho E}{\partial t} + \mathrm{div}\left(\rho\mathbf{u}E\right) = \mathrm{div}\,\mathbf{T}\cdot\mathbf{u} + \rho\sum_{k=1}^{N} Y_k \mathbf{f}_k\cdot\mathbf{u}\,. \quad (1.24)\end{aligned}$$

From the relation $h_t = e_t + p/\rho$, the left-hand side of Equation 1.22 leads to

$$\frac{\partial \rho e_t}{\partial t} + \mathrm{div}\left(\rho\mathbf{u}e_t\right) = \frac{\partial \rho h_t}{\partial t} + \mathrm{div}\left(\rho\mathbf{u}h_t\right) - \frac{\partial p}{\partial t} - \mathrm{div}\left(p\mathbf{u}\right)\;. \quad (1.25)$$

Then the equation for the total enthalpy, h_t, is written as

$$\frac{\partial \rho h_t}{\partial t} + \mathrm{div}\left(\rho\mathbf{u}h_t\right) = \frac{\partial p}{\partial t} - \mathrm{div}\,\mathbf{q} + \mathrm{div}\left[\left(\mathbf{T}+p\mathbf{I}\right)\cdot\mathbf{u}\right] + \dot{Q}_e + \rho\sum_{k=1}^{N} Y_k\mathbf{f}_k\cdot\left(\mathbf{u}+\mathbf{V}_k\right)\;. \quad (1.26)$$

Subtracting Equation 1.24 from this equation, the conservation equation for enthalpy is derived as

$$\frac{\partial \rho h}{\partial t}+\mathrm{div}\,(\rho \mathbf{u} h) = \frac{\partial p}{\partial t}-\mathrm{div}\,\mathbf{q}+\mathbf{u}\cdot\mathrm{grad}\,p+(\mathbf{T}+p\mathbf{I}):\mathrm{grad}\,\mathbf{u}+\dot{Q}_e+\rho\sum_{k=1}^{N} Y_k \mathbf{f}_k\cdot\mathbf{V}_k\,. \tag{1.27}$$

The integral form of this equation can also be derived through the same approach or directly from the differential form.

$$\begin{aligned}\frac{\partial}{\partial t}\int_\Omega \rho h\,\mathrm{d}\Omega + \int_S \rho h \mathbf{u}\cdot\mathbf{n}\,\mathrm{d}S = {} & \frac{\partial}{\partial t}\int_\Omega p\,\mathrm{d}\Omega - \int_S \mathbf{q}\cdot\mathbf{n}\,\mathrm{d}S \\ & + \int_\Omega \left[\mathbf{u}\cdot\mathrm{grad}\,p + (\mathbf{T}+p\mathbf{I}):\mathrm{grad}\,\mathbf{u}\right]\mathrm{d}\Omega \\ & + \int_\Omega \dot{Q}_e\,\mathrm{d}\Omega + \int_\Omega \left(\rho\sum_{k=1}^{N} Y_k \mathbf{f}_k\cdot\mathbf{V}_k\right)\mathrm{d}\Omega\,. \end{aligned} \tag{1.28}$$

In the AVBP code which is used in this study, this equation is further transformed to that of sensible enthalpy, h_s, as

$$h_s = h - \sum_{k=1}^{N} \Delta h_{f,k}^0 Y_k\,. \tag{1.29}$$

Combining this equation with that of species conservation (Equation 1.20), the transport equation of h_s becomes

$$\begin{aligned}\frac{\partial \rho h_s}{\partial t} + \mathrm{div}\,(\rho\mathbf{u}h_s) = {} & \dot{\omega}_T + \frac{\partial p}{\partial t} + \mathrm{div}\,(\lambda\,\mathrm{grad}\,T) - \mathrm{div}\left(\rho\sum_{k=1}^{N} h_{s,k} Y_k \mathbf{V}_k\right) \\ & + \mathbf{u}\cdot\mathrm{grad}\,p + (\mathbf{T}+p\mathbf{I}):\mathrm{grad}\,\mathbf{u} + \dot{Q}_e + \rho\sum_{k=1}^{N} Y_k\mathbf{f}_k\cdot\mathbf{V}_k\,, \end{aligned} \tag{1.30}$$

where Fick's law for diffusion velocities $\mathbf{V_k}$ is not substituted for the simplicity. Sensitive enthalpies for each species $h_{s,k}$ are tabulated as function of the temperature in the AVBP code.

1.2 Numerical method for turbulent simulations

1.2.1 Direct Numerical Simulation

Direct Numerical Simulation (DNS) is the simplest method of computational fluid mechanics, where the transport equations are directly descretized and the simulations are performed without any model. When sufficient computational resources are available, all variables are computed precisely. This is the reason why it is sometimes referred as "numerical experiment".

However, to obtain precise results, the mesh size must be fine enough to resolve the smallest eddies represented by the Kolmogrov scale (Kolmogorov 1941); required resources are proportional to $Re^{3/4}$ for each spatial direction (Tennekes and Lumley 1976). Besides this, in simulations of turbulent combustion, the grid size must be, at least, approximately tenth as small as the laminar flame thickness to resolve the flame front. The numerical scheme for the time-advance must also be chosen with great care, because DNS also requires high precision for time-advance; the time step must also be small, and the numerical scheme must be stable for the selected time step. Most simulations, therefore, use explicit methods. The use of DNS is, thus, limited to the low Reynolds number (Re) and simple geometry simulations.

In spite of the limitations above, DNS is a quite useful tool for understanding the turbulence structure and turbulence-combustion interaction; it allows us to obtain the information, which cannot be accessed through experiments. These results can also be used to develop numerical models.

1.2.2 Reynolds Averaged Navier Stokes equations

Reynolds Averaged Navier Stokes (RANS) equations are a method for calculating turbulent flows. This method considers only the averaged values of the variables. Consequently, the requirement of the computational resources is considerably reduced; turbulent flows under industrial conditions, represented by the high Reynolds numbers, can also be simulated.

Here, the philosophy of the RANS equations is explained using the momentum equation. Applying ensemble averaging, all variables are decomposed into an averaged part and a fluctuation part.

$$Q = [Q] + Q' \,, \tag{1.31}$$

where $[Q]$ is the averaged value of Q. Introducing Favre filtering, $\{Q\} = [\rho Q]/[\rho]$ and $Q = \{Q\} + Q''$, the momentum equation (Equation 1.11) becomes

$$\frac{\partial\left([\rho]\{\mathbf{u}\}\right)}{\partial t} + \operatorname{div}\left([\rho]\{\mathbf{u}\}\{\mathbf{u}\}\right) = \operatorname{div}[\mathbf{T}] + \operatorname{div}\tau \,, \tag{1.32}$$

where $[\mathbf{T}]$ is the mean viscous stress tensor,

$$[\mathbf{T}] = -\left([\,p\,] + \frac{2}{3}\mu \operatorname{div}\{\mathbf{u}\}\right)\mathbf{I} + \mu\left(\operatorname{grad}\{\mathbf{u}\} + (\operatorname{grad}\{\mathbf{u}\})^T\right) \,, \tag{1.33}$$

and τ is the Reynolds stresses,

$$\tau = -[\rho]\{\mathbf{u}''\mathbf{u}''\} = -[\rho]\left(\{\mathbf{uu}\} - \{\mathbf{u}\}\{\mathbf{u}\}\right) \,. \tag{1.34}$$

The existence of the Reynolds stresses makes the equation unclosed. This term is usually modeled based on the concept proposed by Boussinesq (1877),

$$\tau = -\frac{2}{3}\,\mu_t \operatorname{div}\{\mathbf{u}\}\mathbf{I} + \mu_t \left(\operatorname{grad}\{\mathbf{u}\} + (\operatorname{grad}\{\mathbf{u}\})^T\right) , \tag{1.35}$$

where μ_t is the turbulent viscosity. The most widely used model for the calculation of μ_t is the $k-\varepsilon$ model, where μ_t is obtained from the transport equations of turbulent kinetic energy k and its dissipation ε. The readers are referred to Wilcox (1998) and Menter (1993) for the details of the $k-\varepsilon$ model.

Though RANS is capable of simulating high Re flows, only the averaged information is available; simulations of transient flows, auto ignition, and flame instabilities can not be performed with RANS.

1.2.3 Large Eddy Simulation

Large Eddy Simulation (LES) is widely used for the simulation of non-reacting flows (Lesieur (1997), Ferziger (1997), Piomelli and Chasnov (1996), Lesieur and Métais (1996), Piomelli (1999), Sagaut (2000), and Meneveau and Katz (2000)). Turbulent flows are characterized by random velocity fluctuations and the eddy structures that cover a large range of sizes. Thus, a turbulent field is considered as a superposition of different scales of eddies. The perfect computation of turbulent flows demands perfect reproduction of these eddies; the grid scale must be smaller than that of the smallest eddies. Here comes a question: how large are the smallest eddies? From the Kolmogorov theory (Kolmogorov 1941), it is known that this smallest scale is written as $l_d = (\nu^3/\varepsilon)^{1/4}$. However, this scale is so small that makes it prohibitive to calculate all the eddies in turbulent flows except for simple geometries.

One of the solution is to calculate only large size eddies, which are dependent on the geometry, while small size eddies are considered to be more universal. The name Large Eddy Simulation comes from this idea. In this context the separation of small and large eddies is an important issue. To separate these two scales, the transport equations are modified by applying a so-called LES filter.

1.2.3.1 Filtering process and averages

In the context of Large Eddy Simulation, one of the following filters is applied to physical quantities.

- Cut-off filter (in the spectral space)

$$\hat{F}(k) = \begin{cases} 1 & k \leq k_c = \pi/\Delta \\ 0 & otherwise \end{cases} \tag{1.36}$$

This filter is applied in the spectral space and cancels any eddy lower than Δ. It can be rewritten in the physical space as

$$F(x_i) = \frac{1}{\Delta}\frac{\sin(k_c x_i)}{k_c x_i}\,. \tag{1.37}$$

- Box or Top hat filter

$$F(\mathbf{x}) = f(x_1, x_2, x_3) = \left\{ \begin{array}{ll} 1/\Delta^3 & |x_i| \leq \Delta/2 \\ 0 & otherwise \end{array} \right. \tag{1.38}$$

- Gaussian filter

$$F(\mathbf{x}) = f(x_1, x_2, x_3) = \left(\frac{6}{\pi\Delta^2}\right)^{3/2} \exp\left[-\frac{6}{\Delta^2}\left(x_1^2 + x_2^2 + x_3^2\right)\right] \tag{1.39}$$

Figures 1.1 to 1.4 show the shape of these filters. All the filters are normalized as,

$$\int_{-\infty}^{+\infty}\int_{-\infty}^{+\infty}\int_{-\infty}^{+\infty} F\left(x_1, x_2, x_3\right)\, dx_1 dx_2 dx_3 = 1\,. \tag{1.40}$$

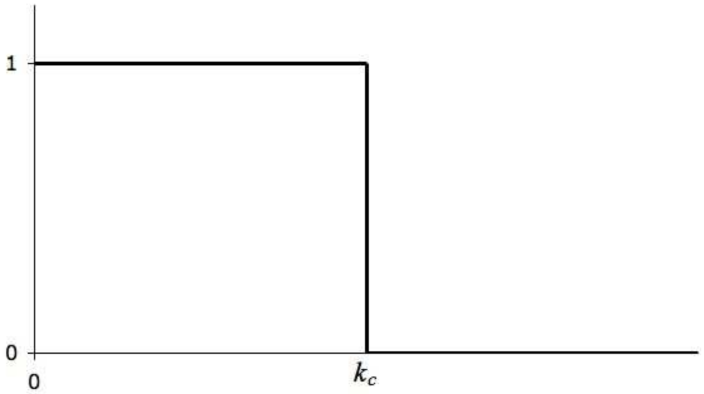

Figure 1.1 : *Shape of the cut-off filter in spectral space.*

The filtered quantity $\overline{Q}(\mathbf{x})$ of a physical quantity $Q(\mathbf{x})$ at the point $\mathbf{x} = (x_1, x_2, x_3)$ is defined as

$$\overline{Q}(\mathbf{x}) = \int Q(\mathbf{x}) F(\mathbf{x} - \mathbf{x}') d\mathbf{x}'\,. \tag{1.41}$$

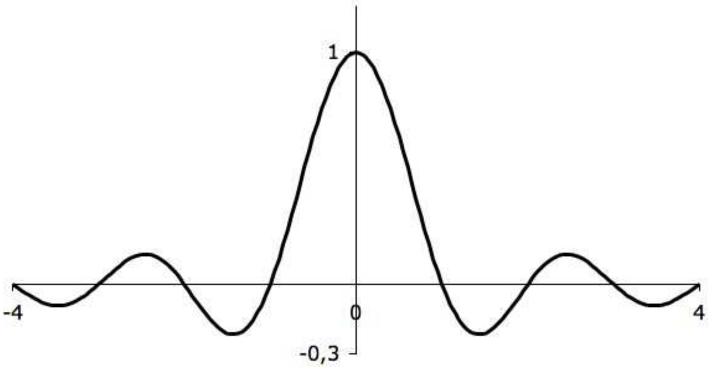

Figure 1.2 : *Shape of the cut-off filter in physical space. Horizontal axis was non-dimensioned by the filter size Δ.*

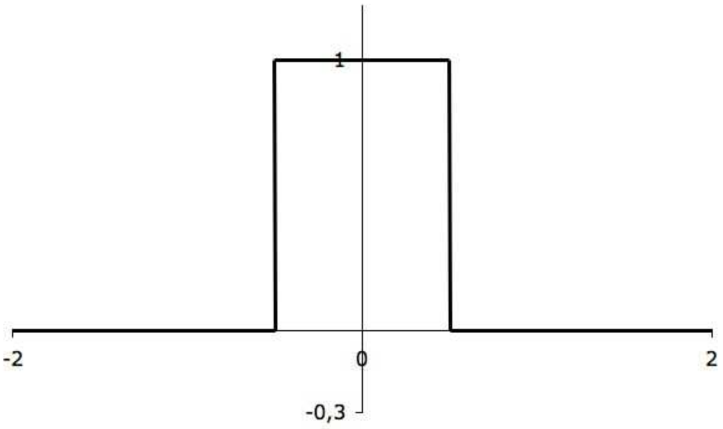

Figure 1.3 : *Shape of the top hat filter. Horizontal axis was non-dimensioned by the filter size Δ.*

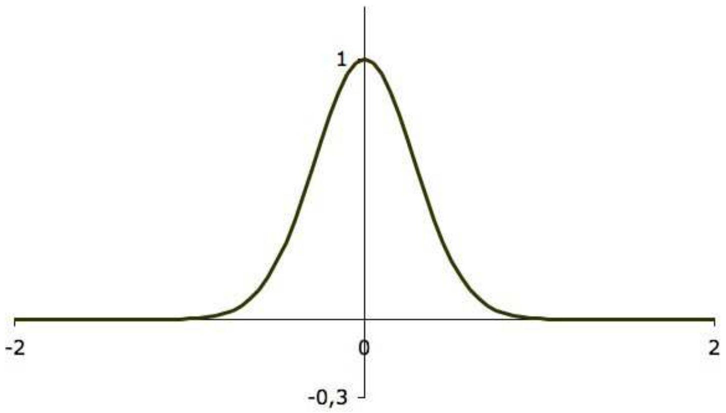

Figure 1.4 : *Shape of the Gaussian filter. Horizontal axis was non-dimensioned by the filter size Δ.*

Another way of filtering is the mass weighted, or Favre, filtering. This filtering simplifys the filtered transport equations. The definition of the Favre filtered quantity, $\widetilde{Q}(\mathbf{x})$, of $Q(\mathbf{x})$ is

$$\widetilde{Q}(\mathbf{x}) = \frac{\overline{\rho Q}}{\overline{\rho}} = \frac{\int \rho(\mathbf{x}')Q(\mathbf{x}')F(\mathbf{x}-\mathbf{x}')d\mathbf{x}'}{\int \rho(\mathbf{x}')F(\mathbf{x}-\mathbf{x}')d\mathbf{x}'} \, . \tag{1.42}$$

1.2.3.2 Filtered equations

In the present study, the transport equations are filtered with the Favre filter. Ignoring the volume force terms, they are written as follows:

- Conservation of mass

$$\frac{\partial \overline{\rho}}{\partial t} + \mathrm{div}\left(\overline{\rho}\tilde{\mathbf{u}}\right) = 0 \tag{1.43}$$

- Conservation of momentum

$$\frac{\partial\left(\overline{\rho}\tilde{\mathbf{u}}\right)}{\partial t} + \mathrm{div}\left(\overline{\rho}\tilde{\mathbf{u}}\tilde{\mathbf{u}}\right) = \mathrm{div}\,\overline{\mathbf{T}} - \mathrm{div}\left\{\overline{\rho}\left(\widetilde{\mathbf{u}\mathbf{u}} - \tilde{\mathbf{u}}\tilde{\mathbf{u}}\right)\right\} \tag{1.44}$$

- Conservation of species k

$$\frac{\partial \overline{\rho}\widetilde{Y_k}}{\partial t} + \mathrm{div}\left(\overline{\rho}\tilde{\mathbf{u}}\widetilde{Y_k}\right) = -\mathrm{div}\left(\overline{\rho}\widetilde{Y_k V_k}\right) - \mathrm{div}\left\{\overline{\rho}\left(\widetilde{\mathbf{u}Y_k} - \tilde{\mathbf{u}}\widetilde{Y_k}\right)\right\} + \overline{\dot{\omega}}_k \tag{1.45}$$

- Conservation of energy

$$\begin{aligned}\frac{\partial\overline{\rho}\tilde{h}_s}{\partial t}+\mathrm{div}\left(\overline{\rho}\tilde{\mathbf{u}}\tilde{h}_s\right) &= \overline{\dot{\omega}}_T+\frac{\partial\overline{p}}{\partial t}+\mathrm{div}\,\left(\lambda\,\mathrm{grad}\,\overline{T}\right)-\mathrm{div}\,\left(\overline{\rho}\sum_{k=1}^{N}h_{s,k}\widetilde{Y_k\mathbf{V}}_k\right)\\ &\quad+\overline{\mathbf{u}\cdot\mathrm{grad}\,p}+\overline{(\mathbf{T}+p\mathbf{I}):\mathrm{grad}\,\mathbf{u}}+\overline{\dot{Q}}_e\\ &\quad-\mathrm{div}\left\{\overline{\rho}\left(\widetilde{\mathbf{u}h_s}-\tilde{\mathbf{u}}\tilde{h}_s\right)\right\}\ . \qquad (1.46)\end{aligned}$$

The filtered equations cannot be solved directly, because filtering operation produces extra-terms due to unresolved motions, which are lost in the simulation. For example, the "subgrid-scale (SGS) Reynolds stresses",

$$\tau^s=-\overline{\rho}(\widetilde{\mathbf{uu}}-\tilde{\mathbf{u}}\tilde{\mathbf{u}})\,, \qquad (1.47)$$

corresponds to the filtered momentum flux due to unresolved small scales. The subgrid-scale Reynolds stress must be appropriately modeled to obtain realistic behavior of large scale eddies. A number of attempts have been made for this purpose. They are mostly based on the Smagorinsky model and the scale similarity model. The mixed model (Bardina et al. 1983) and the dynamic procedure (Germano et al. 1991) have been proposed in the course of the modeling attempts.

1.2.3.3 Reynolds stresses

Among several models for the Reynolds stresses, the details of the Smagorinsky model, the scale similarity model, and the dynamic procedure are given in the following.

The Smagorinsky model

The Smagorinsky model was proposed by Boussinesq (1877) as eddy-viscosity model based on the analogy of turbulent and laminar flows and extended to LES by Smagorinsky (1963). The anisotropic part of SGS Reynolds stress is assumed to be proportional to the strain rate of the large scale.

$$\tau^s_{ij}-\frac{1}{3}\tau^s_{kk}\delta_{ij}=\mu_t\left(\frac{\partial\overline{u}_i}{\partial x_j}+\frac{\partial\overline{u}_j}{\partial x_i}\right)=2\mu_t\overline{S}_{ij}\,, \qquad (1.48)$$

where μ_t is the eddy viscosity and $\overline{S}_{ij}$ is the strain rate. The form of the eddy viscosity is derived by dimensional arguments as

$$\mu_t=C_S\rho\Delta^2|\overline{S}|\,, \qquad (1.49)$$

where C_S is a model parameter and $C_S\approx 0.04$ for isotropic turbulence, Δ is the filter length scale, and $|\overline{S}|=(2\overline{S}_{ij}\overline{S}_{ij})^{1/2}$. However, the model parameter C_S

depends strongly on the flow configuration. It may be a function of Reynolds number and/or other parameters and may take different values in different flows: Deardorff (1970) used $C_S = 0.01$ in channel flow simulations, McMillan et al. (1980) found that C_S decreases with increasing strain rate in statistically homogeneous turbulence. Equation 1.48 contains the sum of the isotropic part in the left-hand-side. In incompressive flows, it may be neglected because its contribution is minute compared to the thermodynamic pressure (Erlebacher et al. 1990). The use of the subgrid-scale kinetic energy is also possible.
Defining the filtered kinetic energy $\widetilde{K}$ and the grid scale kinetic energy K_{GS} as

$$\widetilde{K} = \frac{1}{2}\,\rho \sum_{i=1}^{3} \widetilde{u_i u_i} \tag{1.50}$$

$$K_{GS} = \frac{1}{2}\,\rho \sum_{i=1}^{3} \widetilde{u}_i \widetilde{u}_i, \tag{1.51}$$

respectively, the subgrid-scale kinetic energy K_{SGS} is written as

$$K_{SGS} = \widetilde{K} - K_{GS} = \frac{1}{2}\,\rho \sum_{i=1}^{3} (\widetilde{u_i u_i} - \widetilde{u}_i \widetilde{u}_i) = \frac{1}{2} \tau^s_{kk}\ , \tag{1.52}$$

which is the half of the sum of the isotropic part of Reynolds stress.
From Yoshizawa’s expression (Yoshizawa 1986) the subgrid-scale kinetic energy K_{SGS} is given as

$$K_{SGS} = 2 C_I \Delta^2 |\overline{S}|^2\,, \tag{1.53}$$

where C_I is Yoshizawa’s constant given as $C_I = 0.045$ in statistically homogeneous turbulence. Then each term of the isotropic part of Reynolds stress is calculated as

$$\tau^s_{ij}|_{i=j} = 2\mu_t \overline{S}_{ij} + \frac{4}{3} C_I \Delta^2 |\overline{S}|^2\,. \tag{1.54}$$

In the present study, the flow is considered to be incompressible; the isotropic part may then be neglected since the effect is small as verified by Erlebacher et al. (1990) and Moin et al. (1991).

The scale similarity model

In the scale similarity model or Bardina’s model (Bardina et al. 1980), the smallest resolved eddies, which are slightly larger than the filter size, and the largest unresolved eddies, slightly smaller than the filter size, are assumed to behave similarly. This concept leads to

$$\tau^s_{ij} = -\rho(\overline{\overline{u}_i \overline{u}_j} - \overline{\overline{u}}_i \overline{\overline{u}}_j) \tag{1.55}$$

in constant density flows. Although this model is able to reproduce the backscatter of energy from smaller to larger scales, the model is known to be insufficiently dissipative. To cure this shortcoming, the model is often combined with the Smagorinsky model to form the so-called "mixed model" (Bardina et al. 1983).

The dynamic procedure

An alternative method for calculating the Reynolds stresses is to use a second filter of a size larger than that of the LES filter. This procedure was originally proposed by Germano et al. (1991) and modified by Lilly (1992). The dynamic procedure is usually combined with an eddy viscosity model like the Smagorinsky model. Thanks to the second filtering, the model constants, which are strongly affected by the configuration of flows, may be derived at every spatial point and every time step.
Here, we concentrate on the classical dynamic procedure of Lilly (1992) to avoid numerical complexities. Though this formulation is relatively simple, it yields a sufficiently accurate results, provided that the LES filter and test filter size lie in the inertial range.
Assuming that the density is constant, the Reynolds stresses at the LES filter scale, $\overline{\varDelta}$, are written as

$$\tau_{ij} = -\rho(\overline{u_i u_j} - \overline{u}_i \overline{u}_j)\,. \tag{1.56}$$

At the filter size of $\widehat{\overline{\Delta}}$, the Reynolds stresses are

$$T_{ij} = -\rho(\widehat{\overline{u_i u_j}} - \widehat{\overline{u}}_i \widehat{\overline{u}}_j)\,, \tag{1.57}$$

where $\widehat{\overline{\cdot}}$ represents the double filtering by filters of the size of $\overline{\varDelta}$ and $\widehat{\varDelta}$. Subtracting the first equation, after filtering by $\widehat{\varDelta}$, from the second, we get the Germano identity,

$$\widehat{\overline{u}_i \overline{u}_j} - \widehat{\overline{u}}_i \widehat{\overline{u}}_j = T_{ij} - \widehat{\tau_{ij}}\ , \tag{1.58}$$

where all quantities are known (left-hand-side from the resolved flow field, right-hand-side through the model).
Applying the Smagorinsky model, Reynolds stresses are written as

$$\tau_{ij}^s - \frac{1}{3}\tau_{kk}^s \delta_{ij} = 2\rho\, C_S \overline{\varDelta}^2 |\overline{S}| \overline{S}_{ij} \tag{1.59}$$

$$T_{ij}^s - \frac{1}{3}T_{kk}^s \delta_{ij} = 2\rho\, C_S \widehat{\varDelta}^2 |\widehat{\overline{S}}| \widehat{\overline{S}}_{ij} \tag{1.60}$$

with the same modeling constant. Substituting these relations into the Germano identity,

$$(\widehat{\overline{u}_i \overline{u}_j} - \widehat{\overline{u}}_i \widehat{\overline{u}}_j) - \frac{1}{3}(\widehat{\overline{u}_k \overline{u}_k} - \widehat{\overline{u}}_k \widehat{\overline{u}}_k)\delta_{ij} = 2C_S(\widehat{\overline{\varDelta}^2 |\overline{S}| \overline{S}_{ij}} - \widehat{\varDelta}^2 |\widehat{\overline{S}}| \widehat{\overline{S}}_{ij})\,. \tag{1.61}$$

This equation gives a set of equations, where the only unknown term is the model constant C_S. Solving this equation provides the value of the constant C_S. Lilly (1992) proposed a method that uses the least square method. For the simplicity, we rewrite this equation as

$$L_{ij} - \frac{1}{3}\delta_{ij}L_{kk} = 2C_S M_{ij}\,. \tag{1.62}$$

C_s is then calculated as

$$C_s = \frac{1}{2}(L_{ij}M_{ij}/M_{ij}^2)\,. \tag{1.63}$$

Moin et al. (1991) developed this procedure for the application to compressible flows. In the context of the dynamic procedure with density changes, the Reynolds stresses are calculated as

$$\tau_{ij}^s = -\overline{\rho}(\widetilde{u_i u_j} - \widetilde{u}_i\widetilde{u}_j) = \overline{\rho u_i u_j} - (\overline{\rho u_i}\,\overline{\rho u_j}/\overline{\rho})\,, \tag{1.64}$$

where $\widetilde{\cdot}$ represents the Favre filtering. The same equation at the double filter size $\widehat{\overline{\Delta}}$ is

$$T_{ij} = \widehat{\overline{\rho u_i u_j}} - (\widehat{\overline{\rho u_i}}\,\widehat{\overline{\rho u_j}}/\widehat{\overline{\rho}})\,. \tag{1.65}$$

Following the formalism of the standard dynamic procedure, the relation between the Reynolds stresses at two scales (the Germano identity) is deduced as

$$T_{ij} - \widehat{\tau_{ij}} = \left(\frac{\widehat{\overline{\rho u_i}\,\overline{\rho u_j}}}{\overline{\rho}}\right) - \frac{\widehat{\overline{\rho u_i}}\,\widehat{\overline{\rho u_j}}}{\widehat{\overline{\rho}}} = (\widehat{\overline{\rho}\widetilde{u}_i\widetilde{u}_j}) - \frac{1}{\widehat{\overline{\rho}}}\left(\widehat{\overline{\rho}\widetilde{u}_i}\widehat{\overline{\rho}\widetilde{u}_j}\right)\,. \tag{1.66}$$

Reynolds stresses are given with the Smagorinsky model:

$$\tau_{ij}^s - \frac{1}{3}\tau_{kk}^s\delta_{ij} = 2C_S\overline{\rho}\overline{\Delta}^2|\overline{S}|\overline{S}_{ij}\,, \tag{1.67}$$

$$T_{ij}^s - \frac{1}{3}T_{kk}^s\delta_{ij} = 2C_S\widehat{\overline{\rho}}\widehat{\Delta}^2|\widehat{\overline{S}}|\widehat{\overline{S}}_{ij}\,. \tag{1.68}$$

Substituting these relations into the Germano identity, we get

$$\begin{aligned}\left\{(\widehat{\overline{\rho}\widetilde{u}_i\widetilde{u}_j}) - \frac{1}{\widehat{\overline{\rho}}}\left(\widehat{\overline{\rho}\widetilde{u}_i}\widehat{\overline{\rho}\widetilde{u}_j}\right)\right\} - \left\{(\widehat{\overline{\rho}\widetilde{u}_k\widetilde{u}_k}) - \frac{1}{\widehat{\overline{\rho}}}\left(\widehat{\overline{\rho}\widetilde{u}_k}\widehat{\overline{\rho}\widetilde{u}_k}\right)\right\}\frac{\delta_{ij}}{3} \\ = 2C_S\left\{\left(\widehat{\overline{\rho}\overline{\Delta}^2|\overline{S}|\overline{S}_{ij}}\right) - \widehat{\overline{\rho}}\widehat{\Delta}^2|\widehat{\overline{S}}|\widehat{\overline{S}}_{ij}\right\}\,.\end{aligned} \tag{1.69}$$

This equation can be solved using the same procedure as that applied to Equations 1.62 and 1.63. However, the value of the Smagorinsky constant calculated by the models above shows strong oscillation in space. To avoid this, the terms in the formulation are usually averaged on the statistically homogeneous direction of turbulence.

$$C_s = \frac{1}{2}(\langle L_{ij}M_{ij}\rangle/\langle M_{ij}^2\rangle)\,, \tag{1.70}$$

where $\langle \cdot \rangle$ represents averaging in the direction. If such a direction does not exist, the terms can be averaged in time (Piomelli and Liu (1995), Ghosal et al. (1995), and Cheng et al. (2003)), or along streamlines (Meneveau et al. 1996). For more details of the dynamic procedure, the discussion about the test-filter size, $\widehat{\Delta}$, can be found in Meneveau and Lund (1997), Chester et al. (2001), Pope (2004), and Bou-Zeid et al. (2008). A developed version of the dynamic procedure, which has two constants is presented in Moin (1991) and Salvetti and Banerjee (1995).

1.3 Models of turbulent combustion

1.3.1 The level set approach

The level set approach is a technique for the localization of the flame front. Williams (1985) proposed the prototype of this method. In this context, the flame front is considered to be infinitely thin, and the inner structure of the flame is not resolved. Instead, a transport equation called as the G-equation is used to track the position of the flame front.

$$\rho \frac{\partial G}{\partial t} + \rho \mathbf{U} \cdot \nabla G = \rho S_L \left| \nabla G \right| , \tag{1.71}$$

where ρ is the density, $\mathbf{U}$ the fluid velocity, and S_L the laminar flame speed. The position of the flame front is represented by $G = G_0$ and other values of G are related to the distance from the flame front (Kerstein et al. 1988). In the context of LES, this equation is filtered with the LES filter;

$$\overline{\rho} \frac{\partial \overline{G}}{\partial t} + \overline{\rho} \mathbf{U} \cdot \nabla \overline{G} = \rho_0 S_T \left| \nabla \overline{G} \right| , \tag{1.72}$$

where ρ_0 is the density of unburned gas and S_T the turbulent flame speed that requires a model. Models for turbulent flame speed S_T for a corrugated flamelet and the thin reaction zone flames are found in Peters et al. (1997) and Peters (1999). Details for this approach are discussed in Peters (2000).

Utilization of the dynamic procedure for the determination of turbulent flame speed S_T in the G-equation was also proposed and tested in Im et al. (1997), Bourlioux (2000), and Knundsen and Pitsch (2008).

1.3.2 The Flame Surface Density model

The flame surface density model is based on the idea that the intensity of the reaction rate is proportional to the available flame surface, Σ, per unit volume; the reaction rate may be calculated by

$$\bar{\dot{\omega}} = \dot{\Omega} \Sigma \, , \tag{1.73}$$

where $\dot{\Omega}$ is the mean local burning rate per unit of flame area. This concept was first proposed by Marble and Broadwell (1977) in the RANS context. It allows the separation of the effects of turbulence from the reaction rate model; the reaction models need not to be modified to include turbulence effects. The flame surface density is calculated with a transport equation such as that found in Candel and Poinsot (1990).

For the modeling of the effect of turbulence on the flame surface density Σ, Trouvé and Poinsot (1994) divided the turbulence effects into unsteady straining and curvature effect. The authors also observed the dependence of the evolution of Σ on the Lewis number using DNS. Vervisch et al. (1995) demonstrated the relationship between Σ and the probability density function.

Based on these investigations, Boger et al. (1998) proposed an algebraic closure for Σ for LES. Richard et al. (2007) performed an engine cycle simulation using this model and demonstrated its feasibility. Chakraborty and Cant (2009) conducted simulations with the transport equation of Σ and compared LES result with that of DNS. The results were quite similar

A dynamic procedure was also proposed by Knikker et al. (2002) and Knikker et al. (2004), developing the fractal-similarity model. However, a full simulation is yet to be performed.

1.4 The Dynamic Thickened Flamelet Model

1.4.1 The thickened Flamelet model

The Thickened Flamelet model was proposed by Butler and O'Rourke (1977) and tested by O'Rourke and Bracco (1979) to resolve the extremely thin flame front of a laminar flame compared to the acceptable grid size. This model allows us to simulate turbulent combustion in combination with LES, whose computational mesh is relatively coarse.

The starting point of this model is the thickening of the flame without changing the propagating speed. From the theory of laminar premixed flame, the relation between the flame propagating speed S_L and the flame thickness δ_L are given as

$$S_L \propto \sqrt{a\overline{W}},\ \delta_L \propto \frac{a}{S_L}\,, \tag{1.74}$$

where a is the thermal diffusivity and $\overline{W}$ is the mean reaction rate. Then, thickening the flame without changing the laminar flame speed is achieved by multiplying a and $\overline{W}$ by F and $1/F$ respectively:

$$S_L \propto \sqrt{(Fa)\left(\frac{\overline{W}}{F}\right)},\ F\delta_L \propto \frac{(Fa)}{S_L}\,, \tag{1.75}$$

where F is called as the thickening factor. Following this, we get the transport equation of chemical species for a thickened flame,

$$\frac{\partial \overline{\rho}\widetilde{Y}_k}{\partial t} + \bigtriangledown \cdot (\overline{\rho}\widetilde{\mathbf{u}}\widetilde{Y}_k) = \bigtriangledown \cdot (\overline{\rho} F D_k \bigtriangledown \widetilde{Y}_k) + \frac{\dot{\omega}_k}{F} \tag{1.76}$$

Unfortunately, thickening the flame modifies the flame-turbulence interaction as the Damkohler number, Da, which compares the time scales of chemical reaction and turbulence ($Da = t_t/t_c$, where t_t and t_c are respectively the time scales of turbulence and chemical reaction), is decreased by a factor, F. For example, the flame becomes less sensitive to turbulent motions.
An efficiency function E is introduced to recover the lost flame surface wrinkling so that the thickened flamelet model propagates a flame of thickness $F\delta_L$ at the turbulent flame speed $S_T = ES_L$. Then the transport equation becomes

$$\frac{\partial \overline{\rho}\widetilde{Y}_k}{\partial t} + \bigtriangledown \cdot (\overline{\rho}\widetilde{\mathbf{u}}\widetilde{Y}_k) = \bigtriangledown \cdot (\overline{\rho} E F D_k \bigtriangledown \widetilde{Y}_k) + \frac{E}{F}\dot{\omega}_k \,. \tag{1.77}$$

Colin et al. (2000) proposed

$$E = 1 + \alpha \frac{2\ln(2)}{3c_{ms}(Re_t^{1/2} - 1)} \mathbf{\Gamma}\left(\frac{\mathit{\Delta}}{\delta_l^{0}}, \frac{u'_{\mathit{\Delta}}}{S_L^0}\right) \frac{u'_{\mathit{\Delta}}}{S_L^0} \,, \tag{1.78}$$

where $\mathbf{\Gamma}$ is an efficiency function that evaluates the increase in the flame surface area caused by the turbulence and $Re_t = u'L_t/\nu$ is the turbulent Reynolds number calculated with RMS velocity u' and integral length scale L_t. α is a model constant and $c_{ms} = 0.28$ was introduced based on the comparison to DNS data of Yeung et al. (1990). $\mathbf{\Gamma}$ is given by

$$\mathbf{\Gamma}\left(\frac{\mathit{\Delta}}{\delta_l^{0}}, \frac{u'_{\mathit{\Delta}}}{S_L^0}\right) = 0.75 \exp\left[-\frac{1.2}{(u'_{\mathit{\Delta}}/S_L^0)^{0.3}}\right] \left(\frac{\mathit{\Delta}}{\delta_l^{0}}\right)^{2/3} \,. \tag{1.79}$$

Charlette et al. (2002a) formed another model expression for E,

$$E = \left(1 + \min\left[\frac{\mathit{\Delta}}{\delta_l^{0}}, \mathbf{\Gamma}\frac{u'_{\mathit{\Delta}}}{S_L^0}\right]\right)^{\beta} \,, \tag{1.80}$$

where $\mathit{\Delta}$ is outer cut-off scale given as the LES filter size. β depends on the configuration of the turbulent flow; this must be presumed before the computation.
The advantage of this expression is to recover several situations. When $\beta = 0$, the value of efficiency is $E = 1$ and corresponds to laminar cases. $\beta = 1$ corresponds to the situation where the flame fills the volume (Catrakis and Dimotakis 1996). The case with β between 0 and 1 recovers the fractal model, where the fractal dimension $D = \beta + 2$. The readers are refered to Gouldin (1987), Gouldin et al. (1989) and Gulder (1991) for the fractal model.

1.4.2 Formulation of the Dynamic Thickened Flamelet model

The efficiency functions E mentioned above require to prescribe the model constant α or β. Similar to the case of the Smagorinsky model, the determination of the constant demands empirical knowledge, since the value may strongly depend on the configuration such as the shape of combustion chamber and the condition of turbulence. It is also possible to apply the dynamic procedure for the determination of turbulent flame speed. Charlette et al. (2002b) showed the feasibility of the dynamic procedure in combination with thickened flamelet model, but the authors used a quite simple geometry. The application to complex geometries has not yet been done.

In the present study, the Germano identity is applied to the reaction rate for the dynamic determination of β, following Charlette et al. (2002b). Estimation of the reaction rate requires information of the field such as temperature and mass density of chemical species. Representing these variables by $\widetilde{\mathbf{q}}$, we get $\dot{\omega}_k = \dot{\omega}_k(\widetilde{\mathbf{q}})$. In addition to this, the thickening factor F is defined as $F = \Delta/\delta_L$ in the LES context. Thus the Germano identity leads to

$$\widehat{E_{\overline{\Delta}}\,\dot{\omega}_k(\widetilde{\mathbf{q}})} = E_{\gamma\overline{\Delta}}\,\dot{\omega}_k(\widehat{\widetilde{\mathbf{q}}})\,, \tag{1.81}$$

where γ is the ratio of the second filter to the first filter size ($\gamma = \widehat{\Delta}/\overline{\Delta}$). Introducing the generic form of reaction rate, $\dot{\omega}_k(\mathbf{q}) = W(\mathbf{q})/\Delta$ (Charlette et al. 2002b),

$$\widehat{\frac{E_{\overline{\Delta}}}{\overline{\Delta}}W_k(\widetilde{\mathbf{q}})} = \frac{E_{\gamma\overline{\Delta}}}{\gamma\overline{\Delta}}W_k(\widehat{\widetilde{\mathbf{q}}})\,. \tag{1.82}$$

Substituting E (Equation 1.80),

$$\widehat{\frac{\left(1+\min\left[\frac{\overline{\Delta}}{\delta_l^0},\mathbf{\Gamma}\frac{u'_{\overline{\Delta}}}{S_L^0}\right]\right)^{\beta}}{\overline{\Delta}}W_k(\widetilde{\mathbf{q}})} = \frac{\left(1+\min\left[\frac{\gamma\overline{\Delta}}{\delta_l^0},\mathbf{\Gamma}\frac{u'_{\gamma\overline{\Delta}}}{S_L^0}\right]\right)^{\beta}}{\gamma\overline{\Delta}}W_k(\widehat{\widetilde{\mathbf{q}}})\,. \tag{1.83}$$

As all of the variables in this equation except β can be extracted from the calculated field, β can be obtained as

$$\beta = \frac{\log\left(\gamma\frac{\widehat{W_k\left(\widetilde{\mathbf{q}}\right)}}{W_k\left(\widehat{\widetilde{\mathbf{q}}}\right)}\right)}{\log\left(\frac{1+\min\left[\frac{\gamma\overline{\Delta}}{\delta_l^0},\mathbf{\Gamma}\frac{u'_{\gamma\overline{\Delta}}}{S_L^0}\right]}{\widehat{1+\min\left[\frac{\overline{\Delta}}{\delta_l^0},\mathbf{\Gamma}\frac{u'_{\overline{\Delta}}}{S_L^0}\right]}}\right)}\,. \tag{1.84}$$

The efficiency function E is then calculated substituting this value into Equation 1.80. If the turbulence is sufficiently strong, the expression of the efficiency function reduces to a simpler form,

$$E = \left(1 + \frac{\varDelta}{\delta_l^0}\right)^{\beta} \approx \left(\frac{\varDelta}{\delta_l^0}\right)^{\beta} . \tag{1.85}$$

It also reduces the expression for β as,

$$\beta = 1 + \frac{\log\left(\frac{\overbrace{W_{\overline{\varDelta}(\widetilde{\mathbf{q}})}}}{W_{\gamma\overline{\varDelta}}\left(\widehat{\widetilde{\mathbf{q}}}\right)}\right)}{\log\left(\gamma\right)} . \tag{1.86}$$

1.4.3 Strong and weak forms of the Dynamic model

The dynamic model is described through Equation 1.83. The advantage of this form is the local determination of β at each computational grid point. However, it gives a constant which changes even inside of a thin flame. This has no physical meaning because the objective of the dynamic procedure is to determine a single efficiency function that is constant across the flame front. For this reason, a weak form of the model is preferred. Averaging the both sides of the Equation 1.83 over a given volume results in

$$\left\langle \overbrace{\frac{\left(1 + \min\left[\frac{\overline{\varDelta}}{\delta_l^o}, \mathbf{\Gamma}\frac{u'_{\overline{\varDelta}}}{S_L^0}\right]\right)^{\beta}}{\overline{\varDelta}} W_k(\widetilde{\mathbf{q}})} \right\rangle = \left\langle \frac{\left(1 + \min\left[\frac{\gamma\overline{\varDelta}}{\delta_l^o}, \mathbf{\Gamma}\frac{u'_{\gamma\overline{\varDelta}}}{S_L^0}\right]\right)^{\beta}}{\gamma\overline{\varDelta}} W_k(\widehat{\widetilde{\mathbf{q}}}) \right\rangle , \tag{1.87}$$

where $\langle Q \rangle$ represents the average of Q over a sufficiently large domain for eliminating unphysical fluctuations. For practical applications, $u'_{\overline{\varDelta}}$ is presumed to be uncorrelated to the local raw reaction rate W_k over the averaging volume. Note that this assumption corresponds to a constant efficiency function over the averaging domain. Representing the volume average of $u'_{\varDelta}$ by $\langle u'_{\varDelta} \rangle$, the equation yields

$$\begin{aligned} &\left(1 + \min\left[\frac{\overline{\varDelta}}{\delta_l^o}, \mathbf{\Gamma}\frac{\left\langle u'_{\overline{\varDelta}}\right\rangle}{S_L^0}\right]\right)^{\beta} \left\langle \overbrace{W_k(\widetilde{\mathbf{q}})} \right\rangle \\ = \;& \gamma^{-1}\left(1 + \min\left[\frac{\gamma\overline{\varDelta}}{\delta_l^o}, \mathbf{\Gamma}\frac{\left\langle u'_{\gamma\overline{\varDelta}}\right\rangle}{S_L^0}\right]\right)^{\beta} \left\langle W_k(\widehat{\widetilde{\mathbf{q}}}) \right\rangle . \end{aligned} \tag{1.88}$$

Then

$$\beta = \frac{\log\left(\gamma \frac{\left\langle \overbrace{W_k\left(\widetilde{\mathbf{q}}\right)} \right\rangle}{\left\langle W_k\left(\widehat{\widetilde{\mathbf{q}}}\right)\right\rangle}\right)}{\log\left(\frac{1+\min\left[\frac{\gamma\overline{\Delta}}{\delta_l^0}, \mathbf{\Gamma}\frac{\left\langle u'_{\gamma\overline{\Delta}}\right\rangle}{S_L^0}\right]}{1+\min\left[\frac{\overline{\Delta}}{\delta_l^0}, \mathbf{\Gamma}\frac{\left\langle u'_{\overline{\Delta}}\right\rangle}{S_L^0}\right]}\right)} . \qquad (1.89)$$

This form of the dynamic procedure is referred as the weak form in the present study, while the original form is referred as the strong form.

Chapter 2

Mono-dimensional test case

This chapter presents the results of test cases of the LES models described in Chapter 1. LES models are based on several hypothesis and the validity of these hypothesis depends on the numerical configuration. The purpose of the tests performed in this chapter is to verify the model performances for the computation of laminar flames. These tests are mandatory for the cases, where the effect of subgrid-scale turbulence vanishes, i.g., due to a weak turbulence, fine grid meshes or laminar combustion. One-dimensional tests are chosen as the simplest procedure to verify the performance of the LES turbulence model and that of the power law dynamic thickened flamelet model.

2.1 Introduction

The dynamic procedures described in the previous chapter are constructed for simulations of turbulent regime. For the flexibility of the application, the models should also be able to represent laminar or weak turbulent combustion. In these conditions, β should approach zero. Since the denominator of Equation 1.84 also approaches zero, $\gamma \widehat{W_k\left(\widetilde{\mathbf{q}}\right)} / W_k\left(\widehat{\widetilde{\mathbf{q}}}\right)$ should converge to 1. In this term, the reaction rates are calculated using LES filtered and test-filtered variables, where several types of reaction models and filtering procedures can be used. The influences of the different combinations of the reaction model and the filtering procedure on the value of this term of are first tested.

In the context of the thickened flamelet model, the thickness of a flame is multiplied by a thickening factor F, and the LES filter size $\overline{\Delta}$ is not explicitly defined. Then the value for $\overline{\Delta}$ must be given depending on the thickening factor F. For this purpose, the relation between thickening and LES filtering of a laminar flame is also investigated.

Applications of the dynamic Smagorinsky model to a laminar flame is then tested. This model is widely used in turbulent flow simulations, but its combination with the thickened flamelet model is rare. The output of this model in a thickened flame should be observed before the implementation to multi-dimensional simulations. The outputs are compared by changing the filter sizes and the thickening factor F of the thickened flame.

2.2 Numerical configuration

2.2.1 1D laminar flame

In the case of a one-dimensional flame, the transport equations presented in the first chapter are simplified as follows:

- Conservation of mass
$$\frac{\partial \rho}{\partial t} + \frac{\partial \rho u}{\partial x} = 0 \tag{2.1}$$
- Conservation of species k
$$\frac{\partial \rho Y_k}{\partial t} + \frac{\partial \rho u Y_k}{\partial x} = -\frac{\partial}{\partial x}\left(\rho Y_k V_k\right) + \dot{\omega}_k \tag{2.2}$$
- Conservation of energy

$$\rho C_p \left(\frac{\partial T}{\partial t} + u\frac{\partial T}{\partial x}\right) = -\sum_{k=1}^{N} h_k \dot{\omega}_k + \frac{\partial}{\partial x}\left(\lambda \frac{\partial T}{\partial x}\right) - \rho \frac{\partial T}{\partial x}\sum_{k=1}^{N} C_{p,k} Y_k V_k \tag{2.3}$$

For a steady laminar flame, these equations are further reduced:

- Conservation of mass
$$\rho u = \text{constant} = \rho_u S_L\,, \tag{2.4}$$
where ρ_u and S_L are the density of unburned gas and the laminar flame speed respectively.
- Conservation of species of k
$$\rho_u S_L \frac{\mathrm{d}Y_k}{\mathrm{d}x} = -\frac{\mathrm{d}}{\mathrm{d}x}\left(\rho Y_k V_k\right) + \dot{\omega}_k \tag{2.5}$$
- Conservation of energy

$$\rho_u S_L C_p \frac{\mathrm{d}T}{\mathrm{d}x} = -\sum_{k=1}^{N} h_k \dot{\omega}_k + \frac{\mathrm{d}}{\mathrm{d}x}\left(\lambda \frac{\mathrm{d}T}{\mathrm{d}x}\right) - \rho \frac{\mathrm{d}T}{\mathrm{d}x}\left(\sum_{k=1}^{N} C_{p,k} Y_k V_k\right) \tag{2.6}$$

To get simple analytical solutions, several assumptions are introduced:

- Characteristic quantities such as molecular weights W_k, heat capacities $C_{p,k}$ and diffusivities D_k are identical for all species and Lewis numbers for all species are unity;

$$\begin{aligned} W_k &= W \\ C_{p,k} &= C_p \\ D_k &= D \\ Le_k &= \frac{\lambda}{\rho C_p D_k} = 1 \end{aligned} \tag{2.7}$$

- The chemical reaction is supposed to be one step without backward reaction;

$$\sum_{k=1}^{N} \nu'_k M_k \rightarrow \sum_{k=1}^{N} \nu''_k M_k \,, \tag{2.8}$$

  where M_k is the symbol of species k, ν'_k and ν''_k are its molar stoichiometric coefficients.

As the reaction is one step, the source terms of all species are linked through the single progress rate Q,

$$Q = \frac{\dot{\omega}_k}{W_k \nu_k} \,, \tag{2.9}$$

where $\nu_k = {\nu_k}'' - {\nu_k}'$. Then the heat source term is written as

$$\dot{\omega}_T = -\sum_{k=1}^{N} \Delta h^0_{f,k} \dot{\omega}_k = -Q \sum_{k=1}^{N} \Delta h^0_{f,k} W_k \nu_k \,. \tag{2.10}$$

The heat release through the complete burning of unit mass of fuel can be defined as

$$Q_{fuel} = \frac{\sum_{k=1}^{N} \Delta h^0_{f,k} W_k \nu_k}{W_F \nu_F} \,, \tag{2.11}$$

where the subscript F denotes fuel. Note that this quantity is the total enthalpy change through the combustion of unit mass fuel and not the heat release by a certain species. It is derived as

$$\dot{\omega}_T = -W_F \nu_F \, Q \, Q_{fuel} = -Q_{fuel} \, \dot{\omega}_F \tag{2.12}$$

Using this relation and Fick's law for the diffusion velocity, Equations 2.4 to 2.6 become

$$\rho u = \text{constant} = \rho_u S_L \tag{2.13}$$

$$\rho_u S_L \frac{\mathrm{d}Y_F}{\mathrm{d}x} = \frac{\mathrm{d}}{\mathrm{d}x}\left(\rho D \frac{\mathrm{d}Y_F}{\mathrm{d}x}\right) + \dot{\omega}_F \tag{2.14}$$

$$\rho_u C_p S_L \frac{\mathrm{d}T}{\mathrm{d}x} = \frac{\mathrm{d}}{\mathrm{d}x}\left(\lambda \frac{\mathrm{d}T}{\mathrm{d}x}\right) - Q_{fuel}\,\dot{\omega}_F \tag{2.15}$$

As the specific heat per unit mass for all species are considered to be equal, the last term of the heat transport equation is eliminated (see Equation 1.14). The mass fraction, Y_k, of species k can be derived from Y_F as

$$Y_k = Y_{k,u} - (Y_{F,u} - Y_F)\,\frac{W_k \nu_k}{W_F \nu_F}\,, \tag{2.16}$$

where $Y_{F,u}$ and $Y_{k,u}$ are the fuel mass fraction and the mass fraction of species k in unburned gas respectively.

2.2.2 Progress variable c

Introducing non-dimensional variables $Y = (Y_F - Y_{F,b}) \,/\, (Y_{F,u} - Y_{F,b})$ and $c = (T - T_u) \,/\, (T_b - T_u)$, Equations 2.14 and 2.15 can be rewritten as

$$\rho_u S_L \frac{\mathrm{d}Y}{\mathrm{d}x} = \frac{\mathrm{d}}{\mathrm{d}x}\left(\rho D \frac{\mathrm{d}Y}{\mathrm{d}x}\right) + \dot{\omega}_F / \left(Y_{F,u} - Y_{F,b}\right) \tag{2.17}$$

$$\rho_u S_L \frac{\mathrm{d}c}{\mathrm{d}x} = \frac{\mathrm{d}}{\mathrm{d}x}\left(\frac{\lambda}{C_p} \frac{\mathrm{d}c}{\mathrm{d}x}\right) - \dot{\omega}_F / \left(Y_{F,u} - Y_{F,b}\right)\,, \tag{2.18}$$

where $Y_{F,b}$ is the fuel mass fraction in burnt gas, T_u and T_b are the temperature of cold and burnt gas respectively. T_b is calculated by

$$T_b = T_u - Q_{fuel}\left(Y_{F,u} - Y_{F,b}\right)/C_p\,. \tag{2.19}$$

Because the Lewis numbers for all species are assumed to be unity, the sum of the two transport equations above becomes

$$\rho_u S_L \frac{\mathrm{d}}{\mathrm{d}x}(Y + c) = \frac{\mathrm{d}}{\mathrm{d}x}\left[\rho D \frac{\mathrm{d}}{\mathrm{d}x}(Y + c)\right]\,. \tag{2.20}$$

As $Y = 1$ and $c = 0$ in unburned gas and $Y = 0$ and $c = 1$ in burnt gas, the solution of this equation is

$$Y + c = 1\,. \tag{2.21}$$

Using this relation, the distribution of fuel Y_F and temperature field T can be calculated from the c field. This variable c is called the progress variable.

2.2.3 Closures for the reaction rate

Three different models of chemical reaction are tested. The details of each model are given in the following.

Reduced reaction model and analytical solution

A closure is required for the reaction rate to solve the equation of the progress variable c (Equation 2.18). For the first step, the simplified model for chemical reaction of Ferziger and Echekki (1993) was used. This model considers a one step chemistry of a mixture of fuel and oxidizer to the products and supposes that the reaction rate depends only on temperature. The temperature T is represented by the progress variable c. The reaction rate is given by

$$\dot{\omega}_c(c) = \dot{\omega}_F / \left(Y_{F,u} - Y_{F,b}\right) = \left\{ \begin{array}{ll} 0 & c < c^* \\ \rho_u R(1-c) & c \geq c^* \end{array} \right. , \tag{2.22}$$

where c^* is the threshold of the temperature at which the reaction starts, and R is a constant which is determined by the continuity of the curve of the progress variable c;

$$\left.\frac{\partial c}{\partial x}\right|_{x=-0} = \left.\frac{\partial c}{\partial x}\right|_{x=+0} \tag{2.23}$$

The equation of the progress variable (Equation 2.18) can now be solved. In the zone where $x < 0$, $c = 0$ at $x = -\infty$ and $c = c^*$ at $x = 0$, the general solution is

$$c = c^* \exp\left(\frac{S_L}{D_u} x\right) . \tag{2.24}$$

On the other side, where $x > 0$, the general solution writes

$$c = 1 + (c^* - 1) \exp\left(z_2 x\right) , \tag{2.25}$$

with

$$z_2 = \frac{S_L}{2D_u} - \left[\left(\frac{S_L}{2D_u}\right)^2 + \frac{R}{D_u}\right]^{1/2} . \tag{2.26}$$

where the boundary conditions $c = c^*$ at $x = 0$ and $c = 1$ at $x = \infty$ are applied. The solution of Equation 2.18 is then,

$$c\,(x) = \left\{ \begin{array}{ll} c^* \exp\left(\alpha x\right) & x \leq 0 \\ 1 + (c^* - 1) \exp\left(\beta x\right) & x > 0 \end{array} \right. \tag{2.27}$$

with

$$\alpha = \frac{S_L}{D_u} \tag{2.28}$$

$$\beta = \frac{S_L}{2D_u} - \left[\left(\frac{S_L}{2D_u}\right)^2 + \frac{R}{D_u}\right]^{1/2} . \tag{2.29}$$

Substituting these equations to Equation 2.23, R is given as

$$R = \frac{{S_L}^2}{D_u} \frac{c^*}{(c^* - 1)^2} \tag{2.30}$$

The reaction rate reproduced with this model is indicated in Figure 2.1.

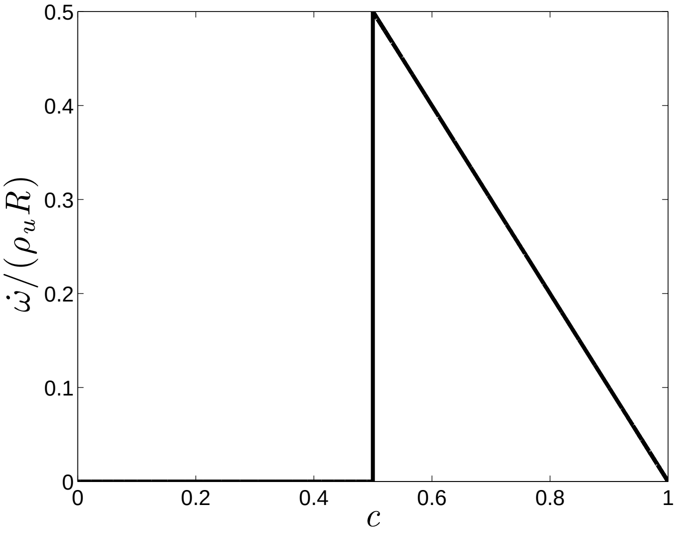

Figure 2.1 : *Reaction rate of Ferziger non-dimensioned by* $\rho_u R$ $(= 8.57 \times 10^3$ $kg/m^3 \cdot s)$ *as a function of progress variable c.* $c^* = 0.5$.

Figures 2.2 and 2.3 show the c fields of several values of c^* and the distributions of other major variables for $c^* = 0.5$. To compare the profile with the flame of other chemical reaction model, the length scale is non-dimensionalized with a laminar diffusive flame thickness $\delta_l^0 = D_u/S_L$.
Table 2.1 indicates the input parameters of the flame.

$S_L(m/s)$	$\delta_l^0(m)$	$T_u(K)$	$T_b(K)$	$\rho_u(kg/m^3)$
0.41	5.82×10^{-5}	300	2300	1.202

Table 2.1 : *Numerical parameter of the flame.*

Arrhenius law

For the one-dimensional test, the Arrhenius law is also implemented. As the inputs, the field of the progress variable c is obtained by filtering a Heaviside function with a Gaussian filter of filter size $\delta_f = \delta_l^0/c^* \sqrt{6/\pi}$, where $c* = 0.5$, to obtain the same flame thickness as that of the analytical solution calculated

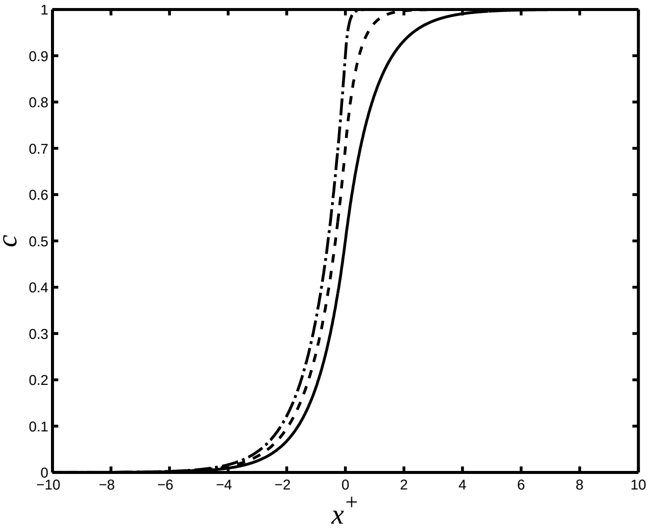

Figure 2.2 : *Profiles of the progress variable* c *calculated with the reduced reaction model of Ferziger as a function of the reduced spatial coordinate* $x^+ = x/\delta_l^0$. $c^* = 0.5(-)\,, c^* = 0.7\,(--)\ , c^* = 0.9\,(-\cdot-)$.

with Ferziger's model defined by $1/|\nabla c|_{max}$. The temperature field and the distribution of the chemical species in the flame are calculated with this progress variable. The constants of the Arrhenius law are first set to the values of one step combustion of propane and air mixture. Then the pre-exponential factor was adjusted for keeping the integral of the reaction rate over the flame to be $\rho_u S_L$. The same procedure is found in Trouvé and Poinsot (1994).
The reaction rate as a function of the progress variable and the profile of the flame are shown in Figures 2.4 and 2.5. Similar to Ferziger's reaction model, the chemical reaction occurs in the zone where the progress variable c takes relatively high values. As the maximum value of the reaction rate is slightly higher than Ferziger's reduced reaction model, the reaction zone shown in the bottom right figure of Figure 2.5 is thinner than that of Ferziger's reduced reaction model of Figure 2.3.

The algebraic model of Boger

Boger et al. (1998) developed an algebraic model for LES from DNS data and Boger (2000) validated this model using experimental data. They assumed that the flame surface density Σ takes a parabolic shape function of the filtered progress variable $\bar{c}$, given by

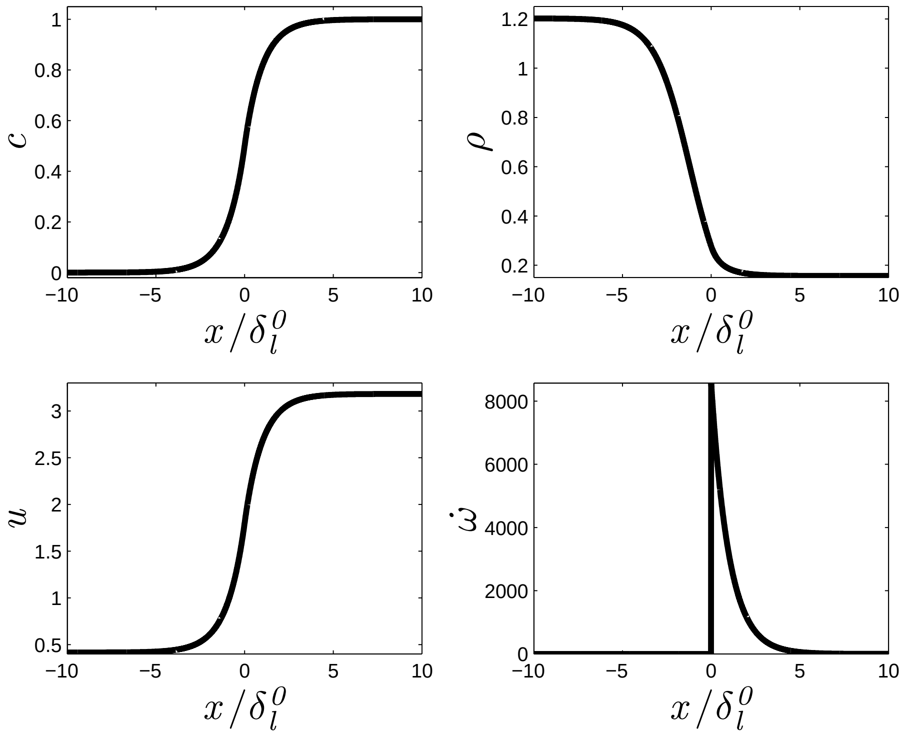

Figure 2.3 : *Profile of a one-dimensional laminar flame: $c^* = 0.5$, x axis is the distance non-dimensioned by diffusive laminar flame thickness $\delta_l^0 = D_u/S_L$.*

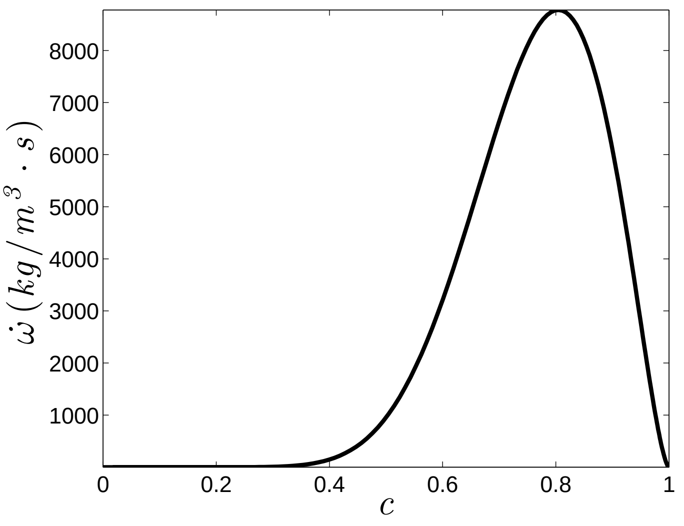

Figure 2.4 : *Reaction rate calculated with the Arrhenius law as a function of progress variable c.*

$$\Sigma = \frac{\alpha^+}{\Delta}\, 4\, \bar{c}(1-\bar{c})\,, \tag{2.31}$$

where α^+ is a model parameter and Δ is the filter dize. The factor 4 was introduced from the fact that the maximum of the parabolic function is 1/4. The value of α^+/Δ is evaluated from the arithmetic average of maximum and minimum values of Σ at the level of $\bar{c} = 0.5$ found in DNS data.
The value of α^+ for laminar cases may be calculated through a one-dimensional test case. The authors got

$$\alpha^+_{lam} = \sqrt{\frac{6}{\pi}} \approx 1.4\,. \tag{2.32}$$

Note that this value is obtained by the application of a Gaussian filter to an infinitely thin flame front. The value may be different for other types of filters. In laminar cases, the global reaction rate is $\rho_u S_L$. Thus the reaction rate in a filtered laminar flame can be described locally as a function of the filtered progress variable $\bar{c}$,

$$\bar{\dot{\omega}}_c \approx \rho_u S_L 4\sqrt{\frac{6}{\pi}}\, \frac{\bar{c}(1-\bar{c})}{\Delta} \tag{2.33}$$

For turbulent flames, the reaction rate is multiplied by a wrinkling factor Ξ, which is the ratio of the flame surface and its projection in the propagation

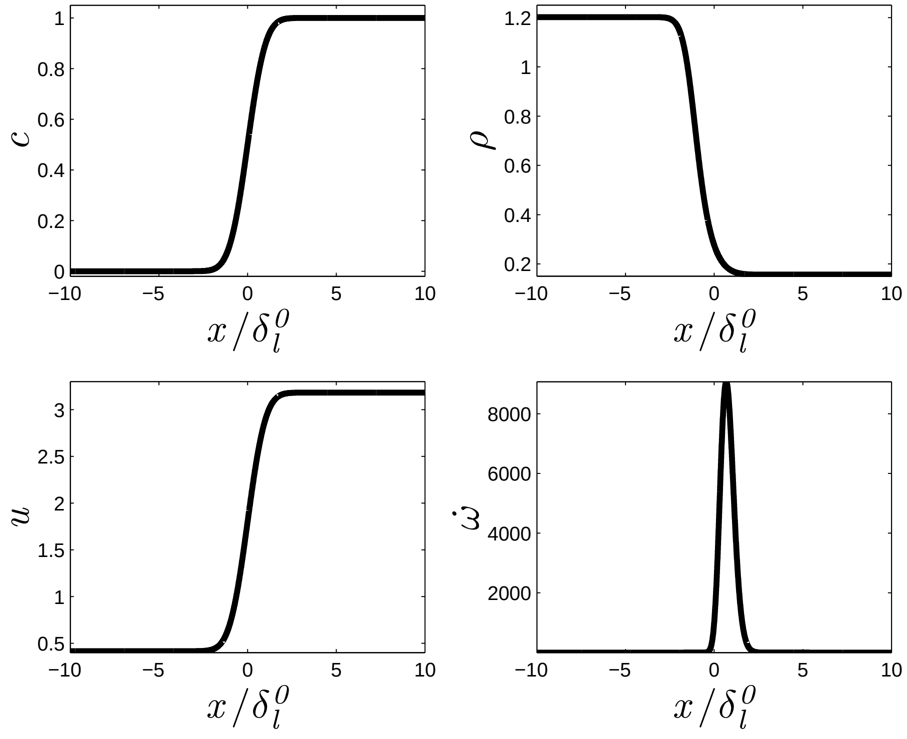

Figure 2.5 : *Profile of a one-dimensional laminar flame calculated with the Arrhenius law. x axis is the distance non-dimensioned by diffusive laminar flame thickness* δ_l.

direction,

$$\overline{\dot{\omega}}_c \approx \rho_u S_L 4\sqrt{\frac{6}{\pi}}\,\Xi\,\frac{\overline{c}(1-\overline{c})}{\mathit{\Delta}}\,, \tag{2.34}$$

where a model is required for Ξ. In practice, the reaction rate is written in terms of mass weighted filtered progress variable,

$$\overline{\dot{\omega}}_c \approx \rho_u S_L 4\sqrt{\frac{6}{\pi}}\,\Xi\,\frac{\widetilde{c}(1-\widetilde{c})}{\mathit{\Delta}}\,, \tag{2.35}$$

including the effect of the laminar transport.
The relation of the reaction rate and the filtered progress variable $\overline{c}$ and the profile of the flame calculated through this model are shown in Figures 2.6 and 2.7 respectively. The reaction rate is non-dimensioned by $\rho_u S_L/\overline{\mathit{\Delta}}$. The field of the filtered progress variable $\overline{c}$ is obtained by applying a Favre filter to a Heaviside function centered at $x = 0$ and the size of $\overline{\mathit{\Delta}}$.
Because the reaction rates depend only on the progress variable c in this chapter, $W(\widetilde{q})$ and $W(\widehat{\widetilde{q}})$ are written as $W(\widetilde{c})$ and $W(\widehat{\widetilde{c}})$ respectively. The reaction rates are referred in this form in the following.

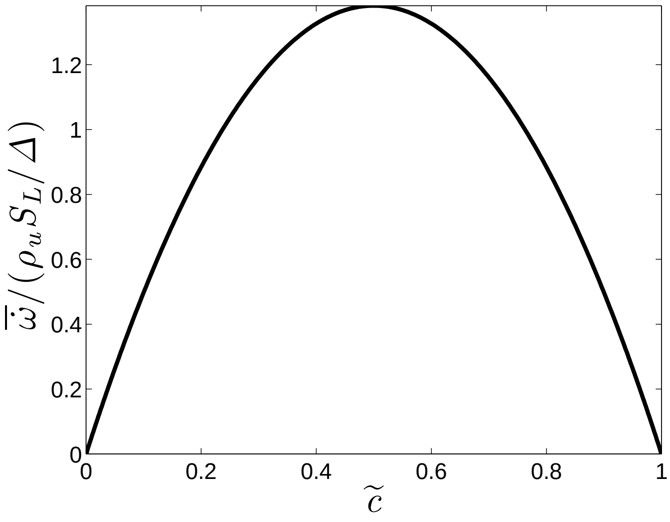

Figure 2.6 : *Reaction rate of Boger et al. (1998) as a function of filtered progress variable* $\overline{c}$.

2.2.4 LES filter

To investigate the influence of the filter type, three different combinations of the filters as shown in Table 2.2 are tested. Case 1 is the simplest combination

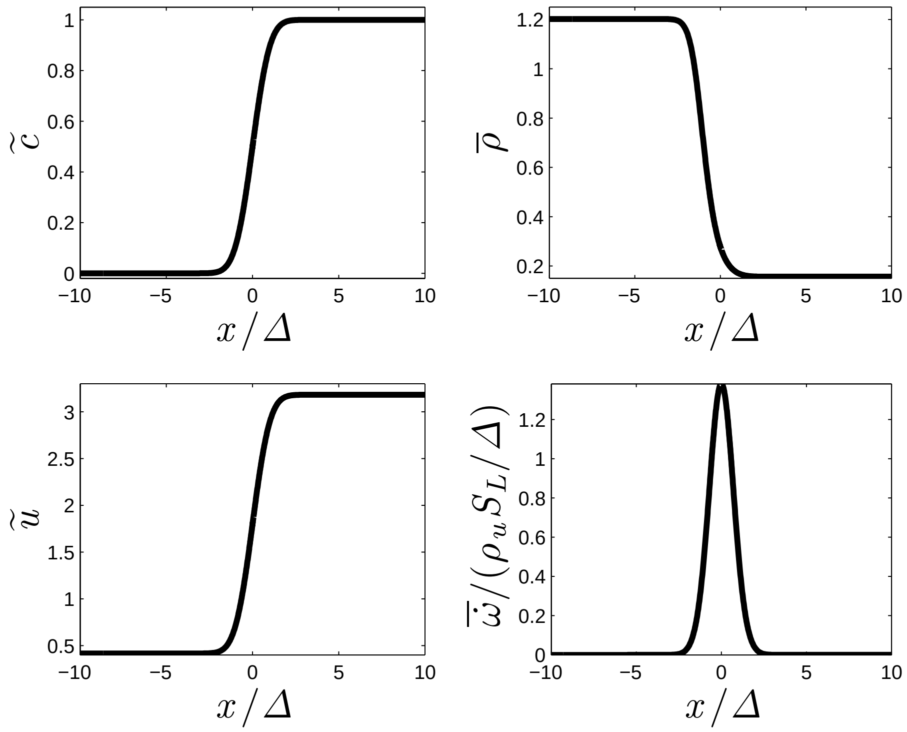

Figure 2.7 : *Profile of a one-dimensional laminar flame calculated with Boger's model. x axis is the distance non-dimensioned by diffusive laminar flame thickness* $\delta_l^0 = D_u/S_L$

where all filtering processes are done in a standard manner. Case 2 retains Favre filter as the LES filter but the test-filter remains standard. This combination imitates the application of the standard test-filter to the LES solution calculated with Favre averaged transport equations. Case 3 is essentially similar to Case 2, but a Favre type filter is applied to obtain double filtered terms. This is the method described in Moin et al. (1991) for the dynamic Smagorinsky model. Successive application of Favre filters of sizes $\overline{\Delta}$ and $\widehat{\Delta}$ is identical to a single application of Favre filter of the effective filter size $\widehat{\overline{\Delta}} = \sqrt{\overline{\Delta}^2 + \widehat{\Delta}^2}$, if the filters are Gaussian. The type of the filter is Gaussian throughout the tests of this study.

In practice, the combination of filters are limited to Case 3. The filtered transport equation of the chemical species (Equation 1.45) is written

$$\frac{\partial \overline{\rho}\tilde{Y}_k}{\partial t} + \mathrm{div}\left(\overline{\rho}\tilde{\mathbf{u}}\tilde{Y}_k\right) = -\mathrm{div}\left(\overline{\rho}\widetilde{Y_k V_k}\right) - \mathrm{div}\left\{\overline{\rho}\left(\widetilde{\mathbf{u}Y_k} - \tilde{\mathbf{u}}\tilde{Y}_k\right)\right\} + \overline{\dot{\omega}}_k \qquad (2.36)$$

This equation describes the transport of the Favre filtered mass fractions of the chemical species. The filtered equation yields the transport equation of the Favre filtered variables. The source term of the right-hand-side must, then, be calculated with Favre filtered variables. In the same manner, filtering the original transport equation by a filter of the size of $\widehat{\overline{\Delta}}$ yields a transport equation of the Favre filtered variables at $\widehat{\overline{\Delta}}$.

$$\frac{\partial \widehat{\overline{\rho}}\tilde{\tilde{Y}}_k}{\partial t} + \mathrm{div}\left(\widehat{\overline{\rho}}\tilde{\tilde{\mathbf{u}}}\tilde{\tilde{Y}}_k\right) = -\mathrm{div}\left(\widehat{\overline{\rho}}\widetilde{\widetilde{Y_k V_k}}\right) - \mathrm{div}\left\{\overline{\rho}\left(\widetilde{\widetilde{\mathbf{u}Y_k}} - \tilde{\tilde{\mathbf{u}}}\tilde{\tilde{Y}}_k\right)\right\} + \widehat{\overline{\dot{\omega}}}_k\,, \qquad (2.37)$$

where $\tilde{\tilde{\cdot}}$ represents Favre filtering by the filter of the size of $\widehat{\overline{\Delta}}$. The source term is then calculated by Favre filtered variables by a filter of size $\widehat{\overline{\Delta}}$. The dynamic formulation thus uses Favre filtered variables by the filers $\overline{\Delta}$ and $\widehat{\overline{\Delta}}$. This is identical to Case 3 where the single LES filter is the Favre filtering. Case 1 is performed as this is the most essential filter combination, and Case 2 is added to investigate the possibility of a simple test-filtering process.

The dynamic Smagorinsky model is also tested using the same combinations of the filters as indicated in Table 2.2. Dynamically calculated results are compared to analytical values of the subgrid stresses, that are obtained by filtering the analytical solution of a laminar flame and taking the difference of the analytical and the filtered solutions.

2.3 Results

2.3.1 Dynamic thickened flamelet model

Both strong and weak forms of the dynamic thickened flamelet model are tested on the one-dimensional flame. In the model formulation (Equations 1.84 and

Case	Single LES filter $\widetilde{(\cdot)}$	Double filter $\widehat{\widetilde{(\cdot)}}$
1	standard	twice standard
2	Favre	Favre + standard
3	Favre	Favre ($\widehat{\overline{\Delta}} = \sqrt{\overline{\Delta}^2 + \widehat{\Delta}^2}$)

Table 2.2 : *Combinations of the filter type*

1.89 for the strong and the weak forms, respectively), the LES filter was represented by the form of Favre averaging $\widetilde{(\cdot)}$. This may be replaced by a standard filter $\overline{(\cdot)}$ or other types of filters. The effect of the change in filter type and in reaction model is discussed in the following.

2.3.1.1 Strong form

The dynamic thickened flamelet model without averaging process was first tested. When the flame is close to a laminar state, the efficiency, E, should be about unity. In the case where u'_Δ is very low, $E \approx 1$ should correspond to $\gamma \overbrace{W(\widetilde{c})} / W\left(\widehat{\widetilde{c}}\right) \approx 1$. Figure 2.8 displays the reaction rates of this equation, $\overbrace{\dot{\omega}(\widetilde{c})} \left(= \overbrace{W(\widetilde{c})} / \overline{\Delta}\right)$ and $\dot{\omega}(\widehat{\widetilde{c}}) \left(= W\left(\widehat{\widetilde{c}}\right) / \widehat{\overline{\Delta}}\right)$ calculated using Ferziger's reduced reaction model. As it indicates, the two values were close at only one point in the front edge and at the rear side of the flame, and the relation $\gamma \overbrace{W(\widetilde{c})} / W\left(\widehat{\widetilde{c}}\right) = \overbrace{\dot{\omega}(\widetilde{c})} / \dot{\omega}(\widehat{\widetilde{c}}) = 1$ holds. Consequently β takes a large positive or negative values except in this region, as the denominator of Equation 1.83 is approximately zero when turbulence is weak. Then the efficiency, E, changes strongly across the flame. The same problem was also observed in the cases where Boger's algebraic model and Arrhenius law were used. Thus, the strong form of dynamic thickened flamelet model cannot be applied to a laminar flame. The relation $\gamma \overbrace{W(\widetilde{c})} = W\left(\widehat{\widetilde{c}}\right)$ should hold in the limit of the laminar case (see Equation 1.83), but again, this relation was not satisfied except at a few points, and the efficiency calculated through the dynamic procedure does not converge to unity. The weak form of the dynamic thickened flamelet model is required to overcome this difficulty. Thus the discussion is focused on the weak form in the following.

2.3.1.2 Weak form

As was described above, in the limit of laminar conditions,

$$\left\langle \gamma \overbrace{W(\widetilde{c})} \right\rangle = \left\langle W\left(\widehat{\widetilde{c}}\right) \right\rangle \tag{2.38}$$

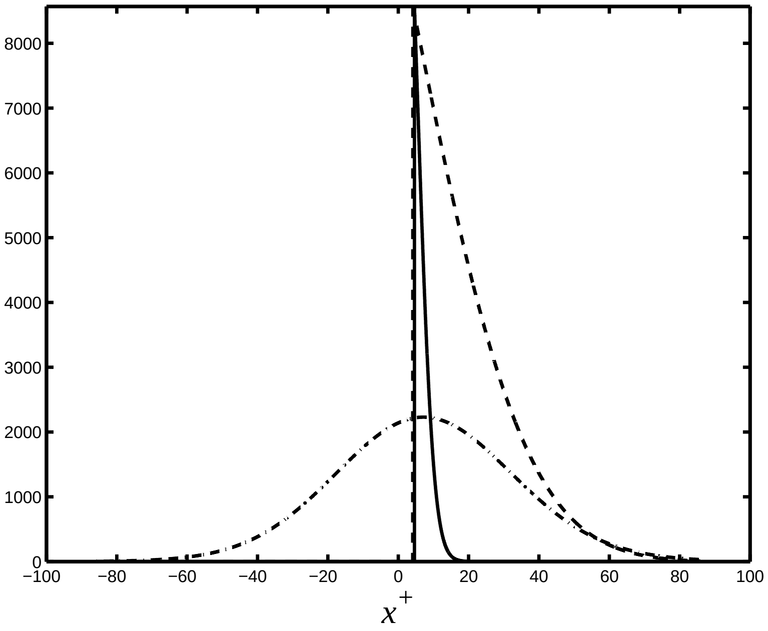

Figure 2.8 : *Reaction rates in the dynamic formulation (Equation 1.84):* $\dot{\omega}\,(c)$ $(-)$, $\widehat{\dot{\omega}(\widetilde{c})}$ $\left(=\widehat{W\,(\widetilde{c})}\,/\overline{\Delta}\right)$ $(--)$ *and* $\dot{\omega}(\widehat{\widetilde{c}})$ $\left(=\,W\left(\widehat{\widetilde{c}}\right)/\widehat{\overline{\Delta}}\right)$ $(-{\cdot}-)$ *(kg/$m^3\cdot s$) calculated with Ferziger's reduced reaction rate model.* $\overline{\Delta} = 2.0 \times 10^{-3}$*(m) and* $\widehat{\Delta} = 1.0 \times 10^{-2}$*(m)* $(\gamma = 5.10)$*, horizontal axis is the distance non-dimensioned by diffusion laminar flame thickness (*$x^+ = x/\delta_l^0$*).*

should hold. This formulation consists of two operators and one function: filtering, integration over a volume, and a function of reaction rate. The filtering operator needs filter sizes $\overline{\Delta}$ and $\widehat{\Delta}$ as inputs for LES and test-filtering respectively. The LES and test-filter sizes define the filter size ratio γ, which is generally calculate as $\gamma = \sqrt{\widehat{\Delta}^2 + \overline{\Delta}^2}/\overline{\Delta}$, when Gaussian filters are applied. The choice of the function for the chemical reaction is also important. Here we discuss Ferziger's reduced model, Boger's algebraic model and the Arrhenius law. Different combinations of the filter sizes and chemical reaction models clearly produces different values of the both sides of Equation 2.38, but they should be identical.

The flexibility of the dynamic thickened flamelet model in terms of the choices of filter sizes and the chemical reaction model was tested changing their combination. The tests were performed using two types of the field of the progress variable, c. The first one was the field obtained by applying a Gaussian filter of size $\delta_f = \delta_l^0/c^* \sqrt{6/\pi}$ to a Heaviside function, where $c^* = 0.5$. This filtering yields a field of the progress variable c that has the same laminar flame thickness defined as $1/\left|\nabla c\right|_{max}$ as that of the analytical solution of the reduced reaction model of Ferziger. When the filter combination of Case 1 was used, a standard filter was applied to a Heaviside function, while a Favre type filter was applied for Cases 2 and 3. In these conditions, the effective filter size ratio, γ was precisely calculated with $\gamma = \sqrt{\widehat{\Delta}^2 + \overline{\Delta}^2 + {\delta_f}^2}/\sqrt{\overline{\Delta}^2 + {\delta_f}^2}$ since Gaussian filters were applied. The second method used the c field of the analytical solution, calculated with the reduced reaction model of Ferziger, shown in Figure 2.3. In this case, δ_f was not defined explicitly, but the same value was used as a reference.

Influence of filter type

The filtering process plays an important role in the formulation of the dynamic model. Its choice is also crucial in the context of LES. To reduce the complexity of the filtered transport equations, Favre filtering, rather than standard filtering, is frequently applied to the original transport equations. This change in filtering is generally assumed not to alter the validity of the SGS models.

Shown in Figures 2.9 and 2.10 are the values of the reaction rate ratio $\left\langle \gamma \widetilde{W\left(\widetilde{c}\right)} \right\rangle / \left\langle W\left(\widehat{\widetilde{c}}\right) \right\rangle$ calculated with different combinations of filters, presented in Table 2.2, and different models for reaction rate. The c field was obtained by filtering a Heaviside function by a Gaussian filter of size δ_f. The horizontal axis is the LES filter size non-dimensioned by δ_f. The filter sizes were set to satisfy the relation $\widehat{\Delta}/\overline{\Delta} = 2$ in Figure 2.9 and $\widehat{\Delta}/\overline{\Delta} = 10$ in 2.10 respectively.

It is clearly seen that the reaction rate ratio was always unity with the filter combinations of Cases 1 and 3 (the solid and the dashdot lines, respectively). On the contrary, the combination of Case 2 (the dashed line) yielded the reaction rate ratio lower than unity independent from the choice of reaction model. These results show that the value of γ calculated with $\gamma = \sqrt{\widehat{\varDelta}^2 + \overline{\varDelta}^2 + {\delta_f}^2} / \sqrt{\overline{\varDelta}^2 + {\delta_f}^2}$ cannot be used with the filter combination of Case 2. This was due to the application of the non mass weighted filter after the mass weighted filtering, and that the filter size $\widehat{\varDelta}$ was not an appropriate value to calculate γ correctly. It was possible to correct $\widehat{\varDelta}$ by forcing,

$$\frac{\sqrt{\widehat{\varDelta}^2 + \overline{\varDelta}^2 + {\delta_f}^2}}{\sqrt{\overline{\varDelta}^2 + {\delta_f}^2}} = \frac{\left\langle W\left(\widehat{\widetilde{c}}\right)\right\rangle}{\left\langle \widehat{W\left(\widetilde{c}\right)}\right\rangle}, \tag{2.39}$$

but, as will be discussed below, the filter size used to obtain a laminar flame, δ_f, also needs to be corrected in a practical application of the dynamic model. Then, the correction of $\widehat{\varDelta}$ is not an attractive method. Thus, the filter combination of Case 2 was not preferable.

Figures 2.11 and 2.12 are the results of the tests, where the c field was analytically obtained with the reduced reaction model of Ferziger, for the cases of $\widehat{\varDelta}/\overline{\varDelta} = 2$ and $\widehat{\varDelta}/\overline{\varDelta} = 10$ respectively. All the results deviated from unity, when $\overline{\varDelta}/\delta_f$ was small. As shown in Figure 2.13, the increase in γ was stronger than the decrease in $\left\langle \widehat{W\left(\widetilde{c}\right)}\right\rangle / \left\langle W\left(\widehat{\widetilde{c}}\right)\right\rangle$ when $\widehat{\varDelta}/\overline{\varDelta} = 2$ and $\overline{\varDelta}/\delta_f < 3$, and the reaction rate ratio $\left\langle \gamma \widehat{W\left(\widetilde{c}\right)}\right\rangle / \left\langle W\left(\widehat{\widetilde{c}}\right)\right\rangle$ increased with $\overline{\varDelta}/\delta_f$, but it decreased when $\overline{\varDelta}/\delta_f > 3$, .

Similar to Figures 2.9 and 2.10, the lines in Figures 2.11 and 2.12 of the filter combinations of Cases 1 and 3 converged to unity with the increase of $\overline{\varDelta}/\delta_f$. The result of Case 2 also converged, but not to unity. The deviations of the results from those of Figures 2.9 and 2.10 found when $\overline{\varDelta}/\delta_f < 20$ were because of the fact that the effective filter size ratio γ was calculated with $\delta_f = \delta_l^0 / c^* \sqrt{6/\pi}$ considering that the analytical solution of the c field calculated with the reduced reaction model of Ferziger was close to the Gaussian filtered Heaviside function. However, the results show that the use of δ_f in the calculation of γ was inappropriate to obtain $\left\langle \gamma \widehat{W\left(\widetilde{c}\right)}\right\rangle / \left\langle W\left(\widehat{\widetilde{c}}\right)\right\rangle = 1$. An alternative filter size that reproduces the field of the progress variable c of the reduced reaction model of Ferziger from a Heaviside function was required for this relation.

Table 2.3 shows the values of the filter size that yield $\left\langle \gamma \widehat{W\left(\widetilde{c}\right)}\right\rangle / \left\langle W\left(\widehat{\widetilde{c}}\right)\right\rangle = 1$ when $\overline{\varDelta}/\delta_f = 2$ for different combinations of filters and reaction models. The values are referred as the effective filter size δ_e in the following. All values of δ_e were remarkably larger than $\delta_f (\approx 1.6 \times 10^{-4}\ (m))$. This is due to the fact that the field of the progress variable c obtained using the reduced reaction model of Ferziger takes longer distance to change from 0 to 1 than that obtained by applying a Gaussian filter of size δ_f to a Heaviside function, and a larger filter size than δ_f was required to retain the same integral of reaction rate as that calculated with the c field obtained with Ferziger's model.

Filter	Reaction model		
combination	Ferziger	Arrhenius	Boger
Case 1	5.4	5.4	5.8
Case 2	2.0	4.5	2.3
Case 3	6.2	5.9	6.7

Table 2.3 : *Effective filter size δ_e ($\times 10^{-4}$ m) that yields $\left\langle \gamma \widetilde{W\left(\widetilde{c}\right)} \right\rangle / \left\langle W\left(\widehat{\widetilde{c}}\right) \right\rangle = 1$ when $\overline{\Delta}/\delta_f = 2$ for different combinations of filter combination and reaction model.*

Using δ_e, the convergence of $\left\langle \gamma \widetilde{W\left(\widetilde{c}\right)} \right\rangle / \left\langle W\left(\widehat{\widetilde{c}}\right) \right\rangle$ was observed again and the results are presented in Figures 2.14 and 2.15. The lines of Cases 1 and 3 became close to those of Figures 2.9 and 2.10 and the values of $\left\langle \gamma \widetilde{W\left(\widetilde{c}\right)} \right\rangle / \left\langle W\left(\widehat{\widetilde{c}}\right) \right\rangle$ were approximately equal to unity, in spite of the use of the progress variable field calculated with the reduced reaction model of Ferziger. This means that the analytically obtained c field with this reaction model can be approximated with a Gaussian filtered Heaviside function of size δ_e, when the filter combination of Case 1 or Case 3 is chosen. However, the result obtained with Case 2 did not converge to unity, though δ_f was replaced by δ_e.

From the results presented here, the filter combinations of Cases 1 and 3 are verified to yield the reaction rate ratio $\left\langle \gamma \widetilde{W\left(\widetilde{c}\right)} \right\rangle / \left\langle W\left(\widehat{\widetilde{c}}\right) \right\rangle$ approximately equal to unity by correcting δ_f. These cases can reproduce a laminar condition, even if the field of the progress variable c was obtained with the reduced reaction model of Ferziger.

In a practical implementation of the dynamic procedure into combustion simulations, however, the density of the flow media changes considerably through combustion and only the filter combination of Case 3 can be retained. Case 2 represents the simplest way of implementation of the dynamic procedure using a standard filter to the Favre filtered transport equation. This method is attractive because of its simplicity, but it cannot be used as it breaks the relation described in Equation 2.38.

Choice of reaction model

It is also important to observe the differences caused by the chemical model selection since the reaction rates that appear in the dynamic formulation are calculated with it. The dynamic thickened flamelet model was tested in combination with Ferziger's model, Boger's model, or the Arrhenius law.
Top left plots of Figures 2.9 and 2.10 display the results calculated with the reduced reaction model of Ferziger, where the c field of a laminar flame was given as a Gaussian filtered Heaviside function. The values of $\left\langle \gamma \overbrace{W\left(\widetilde{c}\right)} \right\rangle$ and $\left\langle W\left(\widehat{\widetilde{c}}\right) \right\rangle$ were identical when the filter combinations of Cases 1 and 3 were applied. The line of Case 2 was always approximately 0.8 and lower than unity.
The results of Boger's algebraic model are presented in the top right plots of Figures 2.9 and 2.10. From the construction of this model, it is easily deduced that the integral value of the reaction rate is always equal to $\rho_0 S_L$, and the ratio should always be unity as long as the same types of filters are applied at the LES and test-filter scales. The formulation of $\gamma = \sqrt{\widehat{\Delta}^2 + \overline{\Delta}^2 + {\delta_f}^2} / \sqrt{\overline{\Delta}^2 + {\delta_f}^2}$ yielded the ideal values of the reaction rate ratio,
$\left\langle \gamma \overbrace{W\left(\widetilde{c}\right)} \right\rangle / \left\langle W\left(\widehat{\widetilde{c}}\right) \right\rangle$, when the filter combination of Cases 1 and 3 were applied. Even this reaction model did not give the desired result if the filter combination of Case 2 was applied.
The Arrhenius law yielded similar results to the reduced reaction model of Ferziger. The results calculated with filter combination of Cases 1 and 3 were always unity, but the result of Case 2 was about 0.8 and far from unity.
The comparisons in Figures 2.11 and 2.12, where the laminar flame was given as the analytical solution of the reduced reaction model of Ferziger, show that the deviation of the reaction rate ratio $\left\langle \gamma \overbrace{W\left(\widetilde{c}\right)} \right\rangle / \left\langle W\left(\widehat{\widetilde{c}}\right) \right\rangle$ from unity found when $\overline{\Delta}/\delta_f < 20$ depended on the reaction model, but the results were similar to Figures 2.9 and 2.10 when $\overline{\Delta}/\delta_f > 20$. The deviations found when $\overline{\Delta}/\delta_f < 20$ were suppressed by the use of δ_e instead of δ_f for the calculation of the effective filter size ratio γ, as shown in Figures 2.14 and 2.15.

From the comparison by the chemical reaction model, it is verified that the value of the reaction rate ratio, $\left\langle \gamma \overbrace{W\left(\widetilde{c}\right)} \right\rangle / \left\langle W\left(\widehat{\widetilde{c}}\right) \right\rangle$, is independent from the choice of the chemical reaction model, when δ_f is replaced by the effective filter size δ_e.

Influence of the filter size ratio $\widehat{\Delta}/\overline{\Delta}$

Another important parameter in the formulation is the filter size ratio $\widehat{\Delta}/\overline{\Delta}$. Before the application to the computational simulation, the condition of the

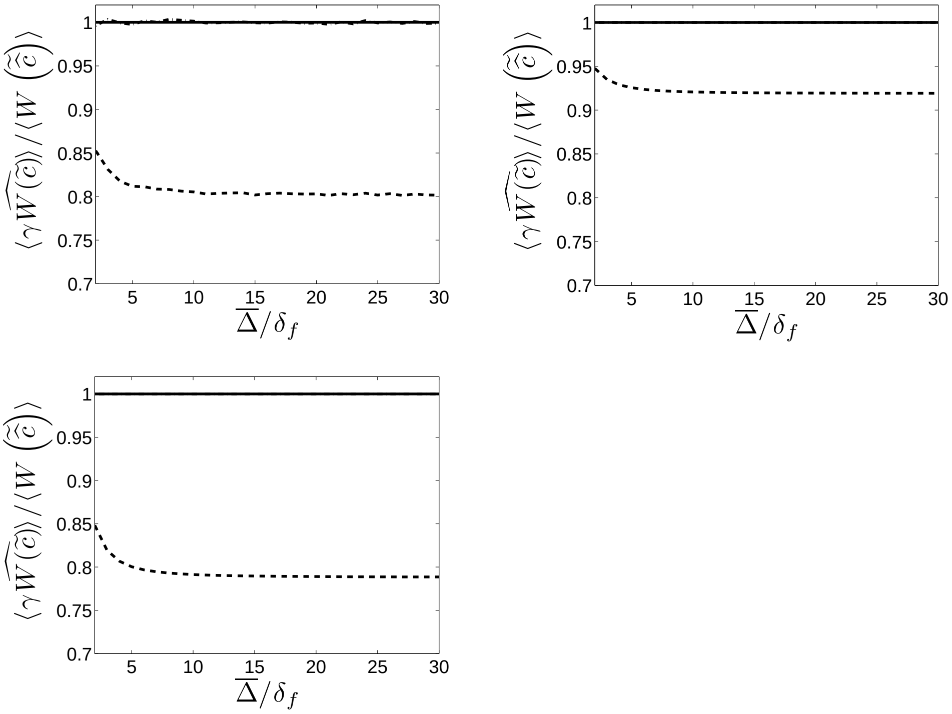

Figure 2.9 : *Influence of the combination of filters on the reaction rate ratio* $\left\langle \gamma \widehat{W(\widetilde{c})} \right\rangle / \left\langle W\left(\widehat{\widetilde{c}}\right) \right\rangle$ *as a function of the LES filter size, non-dimensioned by* $\delta_f = \delta_l^0/c^* \sqrt{6/\pi}$. *The field of the progress variable in a laminar flame was obtained by filtering a Heaviside function by a Gaussian filter of size* δ_f *and the effective filter size ratio* γ *was calculated with* δ_f. *Reaction rates were calculated with Ferziger's reduced chemical reaction model (top left,* $c^* = 0.5$*), Boger's algebraic model (top right) and the Arrhenius law (bottom).* $\widehat{\Delta}/\overline{\Delta} = 2$. *Filters were chosen as shown in Table 2.2, Case 1 (−), Case 2 (−−), and Case 3 (−·−).*

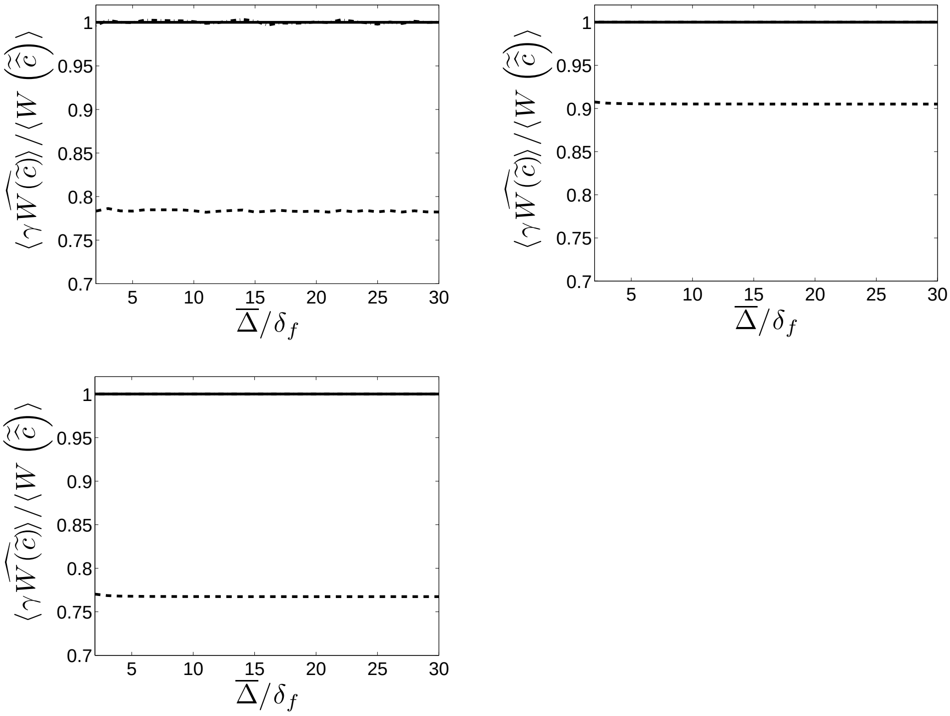

Figure 2.10 : *Influence of the combination of filters on the reaction rate ratio* $\left\langle \gamma \widehat{W(\widetilde{c})} \right\rangle / \left\langle W\left(\widehat{\widetilde{c}}\right) \right\rangle$ *as a function of the LES filter size, non-dimensioned by* $\delta_f = \delta_l^0 / c^* \sqrt{6/\pi}$. *The field of the progress variable in a laminar flame was obtained by filtering a Heaviside function by a Gaussian filter of size* δ_f *and the effective filter size ratio* γ *was calculated with* δ_f. *Reaction rates were calculated with Ferziger's reduced chemical reaction model (top left,* $c^* = 0.5$*), Boger's algebraic model (top right), and the Arrhenius law (bottom).* $\widehat{\Delta}/\overline{\Delta} = 10$. *Filters were chosen as shown in Table 2.2, Case 1 (–), Case 2 (– –), and Case 3 (–·–).*

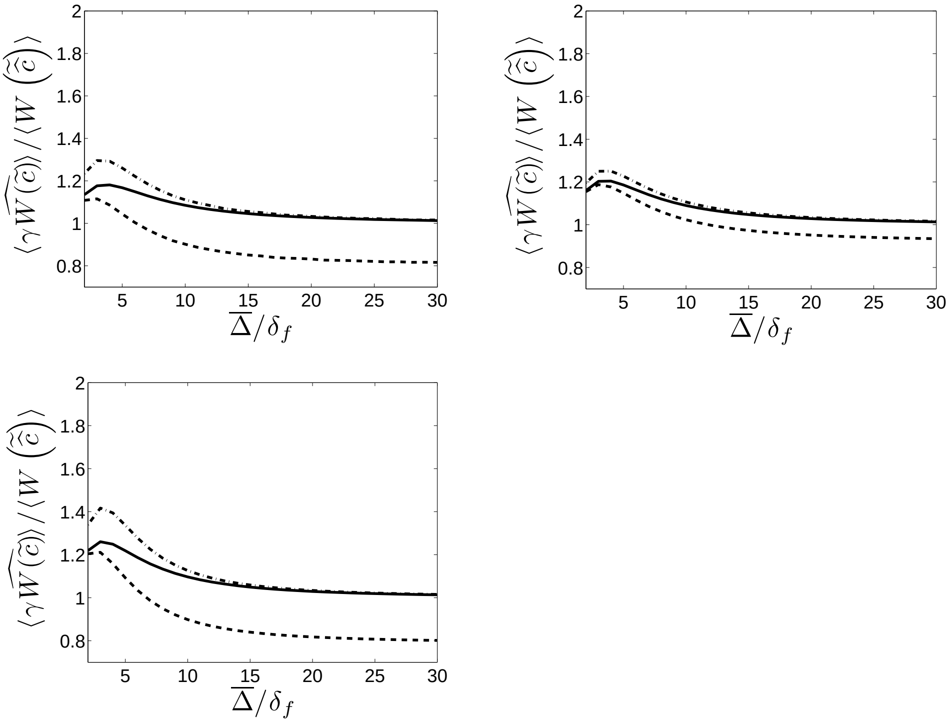

Figure 2.11 : *Influence of the combination of filters on the reaction rate ratio* $\left\langle \gamma \widehat{\overline{W\left(\widetilde{c}\right)}} \right\rangle / \left\langle W\left(\widehat{\widetilde{c}}\right) \right\rangle$ *as a function of the LES filter size, non-dimensioned by* $\delta_f = \delta_l^0/c^* \sqrt{6/\pi}$*. The field of the progress variable in a laminar flame was computed with the reduced reaction model of Ferziger. The effective filter size ratio* γ *was calculated with* δ_f*. Reaction rates are calculated with Ferziger's reduced chemical reaction model (top left,* $c^* = 0.5$*), Boger's algebraic model (top right) and Arrhenius law (bottom).* $\widehat{\Delta}/\overline{\Delta} = 2$*. Filters are chosen as shown in Table 2.2, Case 1 (−), Case 2 (−−), and Case 3 (−·−).*

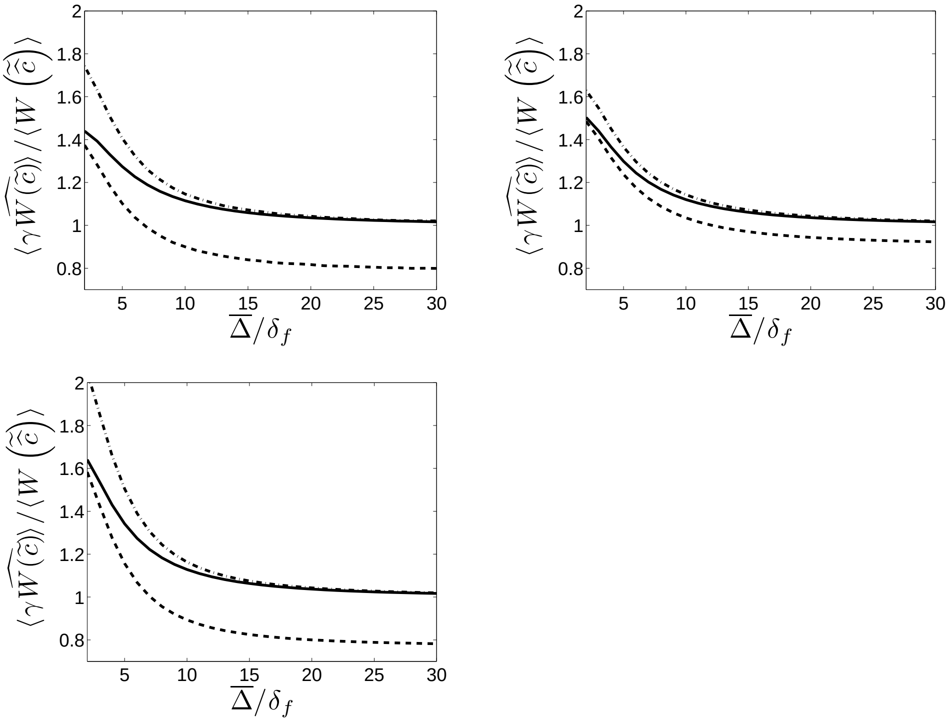

Figure 2.12 : *Influence of the combination of filters on the reaction rate ratio* $\left\langle \gamma \overbrace{W\left(\widetilde{c}\right)} \right\rangle / \left\langle W\left(\widehat{\widetilde{c}}\right) \right\rangle$ *as a function of the LES filter size, non-dimensioned by* $\delta_f = \delta_l^0/c^* \sqrt{6/\pi}$*. The field of the progress variable in a laminar flame was computed with the reduced reaction model of Ferziger. The effective filter size ratio* γ *was calculated with* δ_f*. Reaction rates are calculated with Ferziger's reduced chemical reaction model (top left,* $c^* = 0.5$*), Boger's algebraic model (top right) and Arrhenius law (bottom).* $\widehat{\Delta}/\overline{\Delta} = 10$*. Filters are chosen as shown in Table 2.2, Case 1 (*$-$*), Case 2 (*$--$*), and Case 3 (*$-\cdot-$*).*

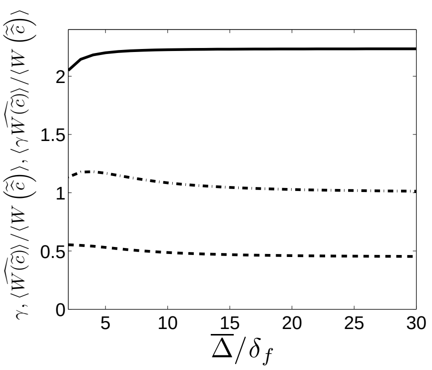

Figure 2.13 : *Intermediate terms in the calculation of the reaction rate ratio* $\left\langle \gamma \widehat{W(\widetilde{c})} \right\rangle / \left\langle W\left(\widehat{\widetilde{c}}\right) \right\rangle$*, as functions of the LES filter size, non-dimensioned by* $\delta_f = \delta_l^0 / c^* \sqrt{6/\pi}$*. A laminar flame was computed with the reduced reaction model of Ferziger. The effective filter size ratio* γ *was calculated with* δ_f*.* $\widehat{\Delta}/\overline{\Delta} = 2$*. The filter combination of Case 1 was used.* γ *(−),*$\left\langle \widehat{W(\widetilde{c})} \right\rangle / \left\langle W\left(\widehat{\widetilde{c}}\right) \right\rangle$ *(−−), and* $\left\langle \gamma \widehat{W(\widetilde{c})} \right\rangle / \left\langle W\left(\widehat{\widetilde{c}}\right) \right\rangle$ *(−·−).*

filter length scale that satisfies the formulation should be obtained. This test is extremely important because the filter length is also restricted by the size of the computational configuration.

Comparing Figures 2.9 and 2.10 which indicate the results calculated with $\widehat{\Delta}/\overline{\Delta} = 2$ and $\widehat{\Delta}/\overline{\Delta} = 10$ respectively, and the field of the progress variable c in a laminar flame was obtained by filtering a Heaviside function, the differences caused by change in $\widehat{\Delta}/\overline{\Delta}$ was not significant when the filter combinations of Cases 1 and 3 were used.

As shown in Figures 2.11 and 2.12, the differences between the results of $\widehat{\Delta}/\overline{\Delta} = 2$ and $\widehat{\Delta}/\overline{\Delta} = 10$ cases became more remarkable with low values of $\overline{\Delta}/\delta_f$, when the analytical solution of the progress variable field of the reduced reaction model of Ferziger was used as a laminar flame. However, as observed in Figures 2.14 and 2.15, they were eliminated by introducing the effective filter size δ_e presented in Table 2.3.

The filter size ratio, thus, does not significantly affect the reaction rate ratio, when the effective filter size ratio γ is calculated using appropriate value for δ_f and appropriate filter combination is chosen (Case 1 or Case 3 in Table 2.2).

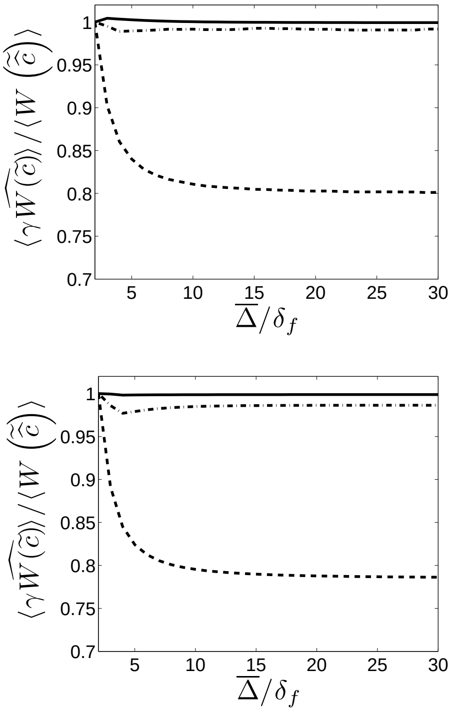

Figure 2.14 : *Influence of the combination of filters on the reaction rate ratio* $\left\langle \gamma \widehat{W\left(\widetilde{c}\right)} \right\rangle / \left\langle W\left(\widehat{\widetilde{c}}\right) \right\rangle$ *as a function of the LES filter size, non-dimensioned by* $\delta_f = \delta_l^0 / c^* \sqrt{6/\pi}$*. The field of the progress variable in a laminar flame was computed with the reduced reaction model of Ferziger. The effective filter size ratio* γ *was calculated with the effective filter size* δ_e *presented in Table 2.3. Reaction rates are calculated with Ferziger's reduced chemical reaction model (top left,* $c^* = 0.5$*), Boger's algebraic model (top right) and Arrhenius law (bottom).* $\widehat{\Delta}/\overline{\Delta} = 2$*. Filters are chosen as shown in Table 2.2, Case 1 (—), Case 2 (– –), and Case 3 (–·–).*

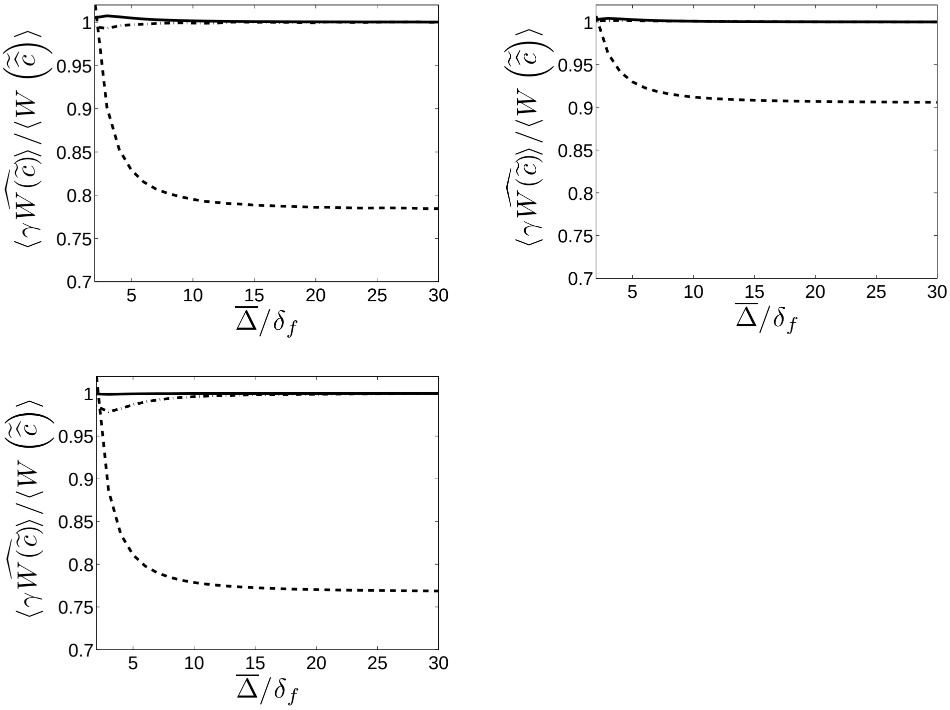

Figure 2.15 : *Influence of the combination of filters on the reaction rate ratio* $\left\langle \gamma \widehat{W\left(\widetilde{c}\right)} \right\rangle / \left\langle W\left(\widehat{\widetilde{c}}\right) \right\rangle$ *as a function of the LES filter size, non-dimensioned by* $\delta_f = \delta_l^0 / c^* \sqrt{6/\pi}$*. The field of the progress variable in a laminar flame was computed with the reduced reaction model of Ferziger. The effective filter size ratio* γ *was calculated with the effective filter size* δ_e *presented in Table 2.3. Reaction rates are calculated with Ferziger's reduced chemical reaction model (top left,* $c^* = 0.5$*), Boger's algebraic model (top right) and Arrhenius law (bottom).* $\widehat{\Delta}/\overline{\Delta} = 10$*. Filters are chosen as shown in Table 2.2, Case 1 (—), Case 2 (– –), and Case 3 (–·–).*

Summary

According to the results obtained through the tests, the influence of choices of chemical reaction model, filter type and the filter size ratio can be summarized as follows:

- In the tests, where a laminar flame was obtained by applying a Gaussian filter to a Heaviside function, the filter combinations of Cases 1 and 3, indicated in Table 2.2, yielded reasonable results independent from the choice of the chemical reaction model and the filter size ratio between the LES and test-filter sizes. Application of the standard type filter to the Favre filtered variables (filter combination of Case 2) resulted in a breakdown of the relation described in Equation 2.38.
- When a laminar flame was analytically obtained with the reduced reaction model of Ferziger, the effective filter size δ_e that reproduces the field of the progress variable c in a laminar flame from a Heaviside function must be calculated to obtain the correct effective filter size ratio γ for $\left\langle \gamma \widehat{W\left(\widetilde{c}\right)} \right\rangle / \left\langle W\left(\widehat{\widetilde{c}}\right) \right\rangle = 1$. This method works well with the filter combinations of Cases 1 and 3, but not with the combination of Case 2, showing the difficulty of the use of this filter combination.
- The choice of the reaction rate model has little influence on the validity of Equation 2.38. All chemical reaction models tested here yield reasonable results when the filter combination of Case 1 or Case 3 is applied and δ_f was corrected.
- The filter size ratio between the LES and test-filter sizes is not a significant factor - at least in a one-dimensional case. Its impact should be investigated in multi-dimensional cases, as this term also appears in the denominator of the formulation (Equation 1.89).

The change of the density is not negligible in combustion simulations and the filter combination of Case 3 should be applied to them.

2.3.2 Relation between thickening and filtering of a laminar flame

In the previous tests, the LES filter size $\overline{\Delta}$ and the test-filter size $\widehat{\Delta}$ were explicitly defined and the effective filter size ratio γ was calculated using these values. However, in the context of the thickened flamelet model, the flame is thickened by a thickening factor F, and the LES filter size $\overline{\Delta}$ is not defined. An equivalent filter size Δ_F to thickening by a factor F must be given to the dynamic procedure to calculate γ.

Figure 2.16 displays the ratio of thicknesses of the LES filtered laminar flame δ_L and the laminar flame δ_l^0 as functions of the LES filter size non-dimensioned by $\delta_f = \delta_l^0 / c^* \sqrt{6/\pi}$, which is the filter size that yields a laminar flame whose thickness, defined by $1/\left|\nabla c\right|_{max}$, is identical to that of the flame calculated with the reduced reaction model of Ferziger. c^* was set to 0.5. The results of four combinations of filter type and the definition of the flame thickness are presented.

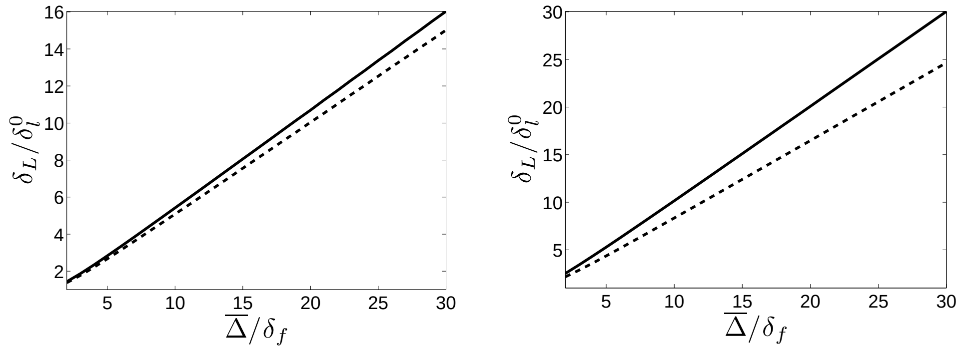

Figure 2.16 : *Thickness of a filtered flame δ_L/δ_l^0 as functions of the LES filter size, non-dimensioned by $\delta_f = \delta_l^0 / c^* \sqrt{6/\pi}$, where c^* is set to 0.5. Flame thickness was defined as the distance where the progress variable changes from 0.01 to 0.99 (left) and the maximum value of the progress variable gradient ($\delta_L = 1/\left|\nabla \overline{c}\right|_{max}$, right). Application of a standard filter (−) and a mass weighted (Favre) filter (−−).*

All lines were almost straight, but the values of δ_L/δ_l^0 and $\overline{\Delta}/\delta_f$ were not identical except when a standard filter was applied, the flame thickness was defined as $\delta_L = 1/\left|\nabla \overline{c}\right|_{max}$, and the $\overline{\Delta}$ was sufficiently large.

When the flame thickness was defined as the distance that the progress variable takes to change from 0.01 to 0.99 ($\delta_{0.01}^{0.99}$, left plot of Figure 2.16), the ratio δ_L/δ_l^0 was approximately half of $\overline{\Delta}/\delta_f$. The lines can be approximated as

$$\frac{\delta_L}{\delta_l^0} = 0.5143 \frac{\overline{\Delta}}{\delta_f} + 0.5987 \ , \tag{2.40}$$

when a standard filter was applied (solid line), and

$$\frac{\delta_L}{\delta_l^0} = 0.4800 \frac{\overline{\Delta}}{\delta_f} + 0.6165 \ , \tag{2.41}$$

when a Favre filter was applied (dashed line).

The lines of the right plot, where the flame thickness was defined as $\delta_L = 1/\left|\nabla \overline{c}\right|_{max}$, were closer to the line of $\delta_L/\delta_l^0 = \overline{\Delta}/\delta_f$ than those in the left plot. This was due to the fact that the thickness $\delta_{0.01}^{0.99}$ of a laminar flame is larger than the thickness defined as $1/\left|\nabla c\right|_{max}$ as displayed in Figure 2.17, and less influenced by filtering. They are approximately

$$\frac{\delta_L}{\delta_l^0} = 0.9772\frac{\overline{\Delta}}{\delta_f} + 0.7345 \; , \tag{2.42}$$

when a standard filter was applied (solid line), and

$$\frac{\delta_L}{\delta_l^0} = 0.7967\frac{\overline{\Delta}}{\delta_f} + 0.7578 \; , \tag{2.43}$$

when a Favre filter was applied (dashed line).

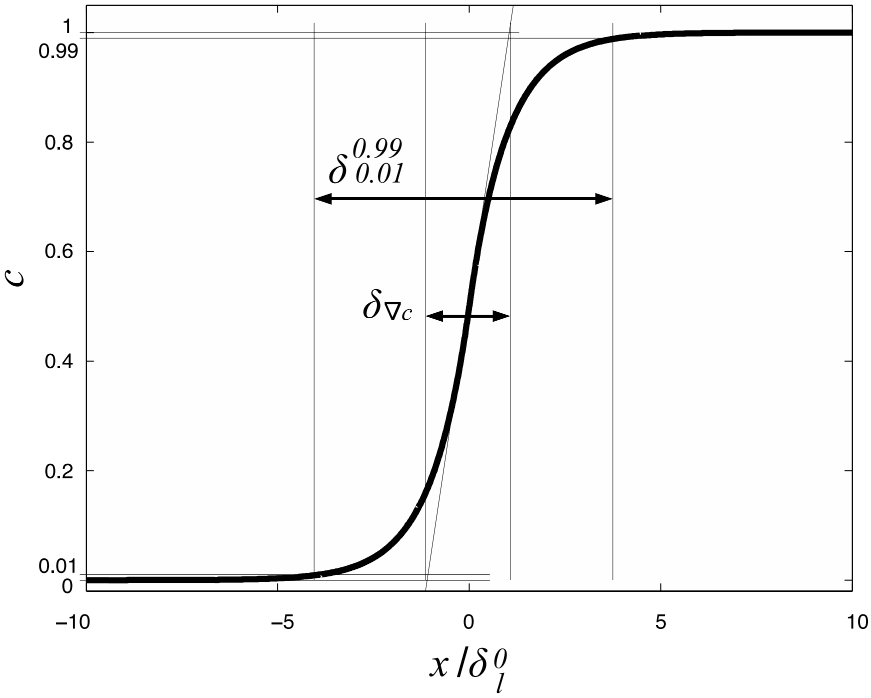

Figure 2.17 : *Definition of flame thicknesses. $\delta_{0.01}^{0.99}$ is the flame thickness defined as the distance, where the progress variable changes from* 0.01 *to* 0.99*, and $\delta_{\nabla c}$ is the thickness defined as the inverse of the maximum value of the progress variable gradient. δ_l^0 is the diffusion flame thickness D_u/S_L.*

Thus, the thickness ratio δ_L/δ_l^0 was approximately proportional to the filter size $\overline{\Delta}$, when $\overline{\Delta}$ is sufficiently large, but the proportionality coefficient depended on the filter type and the definition of the flame thickness. Representing the proportionality coefficient by a, and suppose that the filter size $\overline{\Delta}$ is large enough, the relation between δ_L/δ_l^0 and $\overline{\Delta}/\delta_f$ reduces to

$$\frac{\delta_L}{\delta_l^0} = a\frac{\overline{\Delta}}{\delta_f} \; . \tag{2.44}$$

Then, the filter size Δ_F to yield a flame of thickness $F\delta_l^0$ is written as

$$\Delta_F = \frac{1}{a}F\delta_f = \frac{1}{a}F\frac{\delta_l^0}{c^*}\sqrt{\frac{6}{\pi}} = \alpha F\delta_l^0 \; , \tag{2.45}$$

where the product of terms other than $F\delta_l^0$ was represented by α for the clarity. In previous tests, the value of δ_f was corrected for a laminar flame calculated with the reduced reaction model of Ferziger, using $\overline{\Delta}$ and $\widehat{\Delta}$. In the context of the thickened flamelet model, however, $\overline{\Delta}$ is not defined, and it must be obtained for the calculation of γ, i.e., the value of α in Equation 2.45 has to be determined. This calculation of α will be conducted in the next chapter through a test similar to that performed above.

Summary

From the test performed here, the thickness of a filtered laminar flame δ_L was verified to be approximately proportional to the filter size $\overline{\Delta}$. The proportionality coefficient of δ_L to $\overline{\Delta}$, which is represented by a in Equation 2.44, depends on the definition of the flame thickness and the filter type. In the context of the thickened flamelet model, an equivalent filter size Δ_F that yields the field of the progress variable c in a thickened flame of thickness $F\delta_l^0$ from a Heaviside function must be calculated by determining the proportionality coefficients a of Equation 2.44 and corresponding α of Equation 2.45. This test will be conducted in the next chapter.

2.3.3 The dynamic Smagorinsky model

The subgrid-scale flux

In the LES context, the subgrid-scale flux of a filtered quantity, $\widetilde{Q}$, is usually modeled by using the gradient assumption,

$$\overline{\rho}(\widetilde{\mathbf{u}Q} - \widetilde{\mathbf{u}}\widetilde{Q}) = -\frac{\mu_t}{\sigma_t}\nabla\widetilde{Q} \, , \tag{2.46}$$

where μ_t and σ_t are the turbulent viscosity and the turbulent Schmidt number respectively.

When the direction of the subgrid-scale flux is opposite to that predicted by Equation 2.46, the counter-gradient-like transport occurs, and μ_t becomes negative. The effect of the subgrid-scale fluxes is limited in the LES context than

in RANS simulations, because, unlike to RANS, most part of the convection transport of the scalar quantities are resolved in LES. However, it is worth observing the magnitude of subgrid-scale flux that takes place in a laminar flame. For the details of the counter gradient transport in the RANS context, the readers are referred to Bray et al. (1981), Shepherd et al. (1982), Libby and Bray (1981), Bray et al. (1989). Bray (1996), and Veynante et al. (1997).
In this section, the subgrid-scale momentum flux (Reynolds stresses) across a laminar flame is calculated by applying a LES filter to the flame obtained in the previous section, and its magnitude is observed. This subgrid-scale momentum flux is also calculated with the dynamic Smagorinsky model to assess the validity of this model.
The dynamic Smagorinsky model is designed to calculate the subgrid-scale momentum flux, which remains unclosed in the equation after the filtering operation. This term is called Reynolds stresses, τ, and is usually modeled as follows:

$$\tau = -\overline{\rho}(\overline{\mathbf{uu}} - \bar{\mathbf{u}}\bar{\mathbf{u}}) = 2\mu_t \overline{S} \equiv 2C_S \overline{\rho} \mathit{\Delta}^2 |\overline{S}| \overline{S} \tag{2.47}$$

where μ_t is the turbulent viscosity, C_S is a model parameter to be determined, $\mathit{\Delta}$ is the filter length scale, S is the strain rate defined as

$$\overline{S} = \left(\frac{\partial \overline{u}_i}{\partial x_j} + \frac{\partial \overline{u}_j}{\partial x_i} \right) , \tag{2.48}$$

and $|\overline{S}| = (2\overline{S}_{ij}\overline{S}_{ij})^{1/2}$. This formulation may be rewritten using Favre averaged variables.

$$\tau = -\overline{\rho}(\widetilde{\mathbf{uu}} - \tilde{\mathbf{u}}\tilde{\mathbf{u}}) = 2\mu_t \widetilde{S} \equiv 2C_S \overline{\rho} \mathit{\Delta}^2 |\widetilde{S}| \widetilde{S} \,, \tag{2.49}$$

where

$$\widetilde{S} = \left(\frac{\partial \widetilde{u}_i}{\partial x_j} + \frac{\partial \widetilde{u}_j}{\partial x_i} \right) . \tag{2.50}$$

Analytical values of the subgrid-scale transport

The subgrid-scale momentum flux was obtained analytically by filtering the analytical solution of a laminar flame, which was obtained in the previous section, and by calculating with the equation below.

$$-\overline{\rho}\left(\widetilde{uu} - \widetilde{u}\widetilde{u}\right) \tag{2.51}$$

Figure 2.18 shows the analytical subgrid-scale momentum flux obtained by filtering variables of a flame calculated with Ferziger's reaction rate ($c^* = 0.5$) displayed in Figure 2.3. The horizontal axis of the left plot is the position from the flame surface non-dimensioned by the laminar diffusion flame thickness $\delta_l^0 = 5.82 \times 10^{-5}$ (m). Even though the flame was laminar, subgrid-scale momentum flux existed and took negative values, i.e. in the direction opposite to the gradient assumption (Equation 2.46). As explained in Poinsot and Veynante (2005), this was caused by the thermal expansion of the burnt gas through the flame. The intensity of the peak value of the subgrid-scale momentum flux increased with the filter size $\widehat{\Delta}$. This was because of that a larger filter made the field smoother, and the effect of the subgrid-scale became more important.

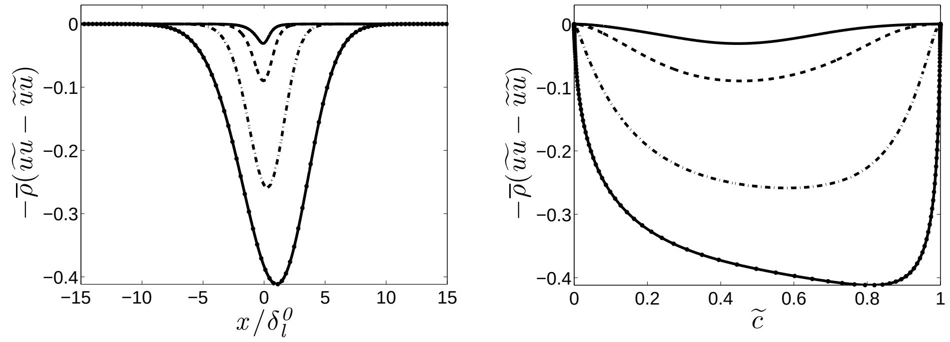

Figure 2.18 : *Analytically calculated subgrid-scale momentum flux through a laminar flame* $-\overline{\rho}\,(\widetilde{uu} - \widetilde{u}\widetilde{u})$. $\overline{\Delta} = \delta_l^0 (= D_u/S_L)(-)$, $\overline{\Delta} = 2\delta_l^0\,(--)$, $\overline{\Delta} = 5\delta_l^0\,(-\cdot-)$ *and* $\overline{\Delta} = 10\delta_l^0\,(-$ *with* $\bullet)$. *The horizontal axis of the left plot was non-dimensioned by the laminar diffusion flame thickness,* $\delta_l^0 = D_u/S_L = 5.82 \times 10^{-5}$ *m*

Figure 2.19 represents the ratio of the subgrid-scale momentum flux to the exact value of the convection transport of momentum $\overline{\rho}\widetilde{uu}$. As expected, this ratio increased with the filter size. The value stayed small when the LES filter size was δ_l^0 and $2\delta_l^0$, but it was not negligible when the LES filter size is larger than $5\delta_l^0$. The same test with a flame thickened by a factor of 20 and a filter size of $20\delta_l^0$, $40\delta_l^0$, $100\delta_l^0$, and $200\delta_l^0$ yielded exactly same results, and it was well verified that thickening of a laminar flame did not alter the nature of the subgrid-scale momentum flux as far as the relation of the flame thickness and the LES filter size stayed the same (Figure 2.20).

Additional one-dimensional tests were performed by setting the configuration similar to the multi-dimensional simulations that will be performed in Chapters 4 and 5. The computational mesh for the two-dimensional simulation is presented in Figure 3.10 in the next chapter. The LES filter size of this test was set to 5.0×10^{-4} m corresponding to the computational mesh size used in the two-dimensional simulation, and the flame was thickened by a factor of 5, 10, 20 and 30. The results are indicated in Figures 2.21 and 2.22.

It is clearly shown that the subgrid-scale momentum flux opposite to the gradient assumption existed in a thickened laminar flame and its amplitude depended on the thickening factor. When the thickening factor was 5, the ratio of the subgrid-scale momentum flux to the exact convection transport was approximately 9 %. This value decreased as the thickening factor increased. With the

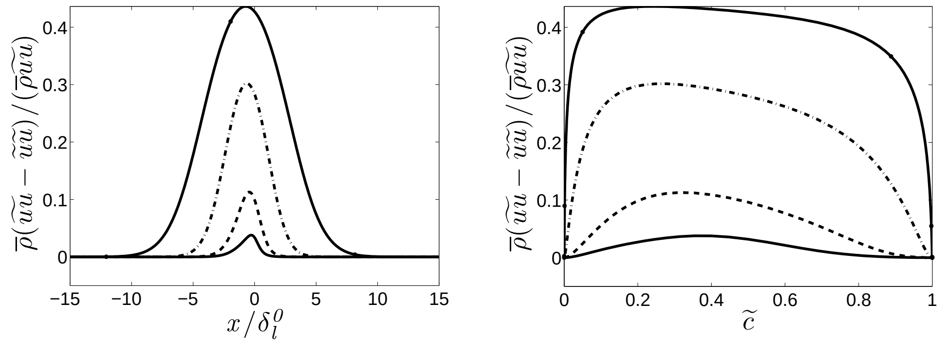

Figure 2.19 : *The ratio of the analytically calculated subgrid-scale momentum flux to the exact value of the convection transport of momentum.* $-\overline{\rho}\,(\widetilde{uu}-\widetilde{u}\widetilde{u})\,/-\overline{\rho}\,(\widetilde{u}\widetilde{u})$: $\overline{\Delta}=\delta_l^0(=D_u/S_L)(-)$, $\overline{\Delta}=2\delta_l^0\,(--)$, $\overline{\Delta}=5\delta_l^0\,(-\cdot-)$ *and* $\overline{\Delta}=10\delta_l^0\,(-$ *with* $\bullet)$. *The horizontal axis of the left plot was non-dimensioned by the laminar diffusion flame thickness,* $\delta_l^0=D_u/S_L=5.82\times10^{-5}\ m$

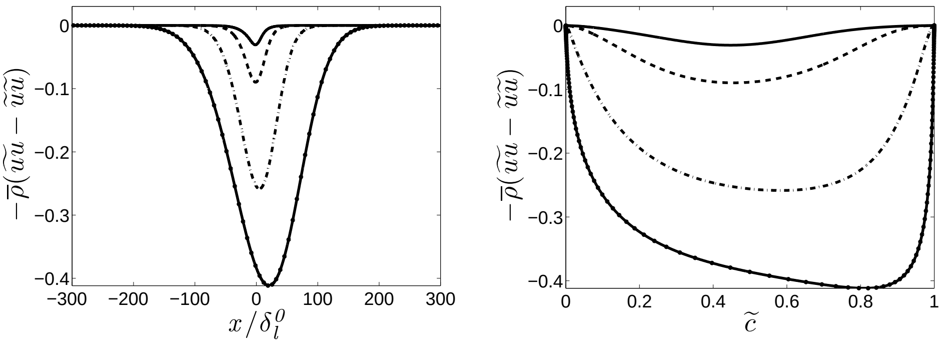

Figure 2.20 : *Analytically calculated subgrid-scale momentum flux* $-\overline{\rho}\,(\widetilde{uu}-\widetilde{u}\widetilde{u})$ *in a thickened laminar flame by the factor of* 20. $\overline{\Delta}=20\,\delta_l^0(=20D_u/S_L)(-)$, $\overline{\Delta}=40\,\delta_l^0\,(--)$, $\overline{\Delta}=100\,\delta_l^0\,(-\cdot-)$ *and* $\overline{\Delta}=200\,\delta_l^0\,(-$ *with* $\bullet)$. *The horizontal axis of the left plot was non-dimensioned by the laminar diffusion flame thickness,* $\delta_l^0=D_u/S_L=5.82\times10^{-5}\ m$

thickening factor of 20, it was lower than 1 % and with that of 30, it became negligible.

These results suggest that, in the two-dimensional simulations performed in Chapter 4, the subgrid-scale momentum flux in the flame is opposite to the gradient assumption (Equation 2.46), if the turbulence is weak. However, the amplitude can be decreased by changing the thickening factor. It is thus expected that the subgrid-scale momentum flux opposite to the gradient assumption is also negligible in the simulations of Chapter 4, if the flame is thickened more than 20 times.

In the case of the three-dimensional simulation performed in Chapter 5, whose computational mesh is represented in Figure 5.1 of Chapter 5, the computational grid size at the flame holder is 1.0 mm. This condition approximately corresponds to the $\overline{\Delta} = 20\delta_l^0$ case shown in Figure 2.20. Then the subgrid-scale momentum flux is approximately 4% of the exact convection transport of momentum as is represented in Figure 2.19 with the solid line. Thus the subgrid-scale momentum flux in the flame is also negligibly small in the three-dimensional simulations of Chapter 5.

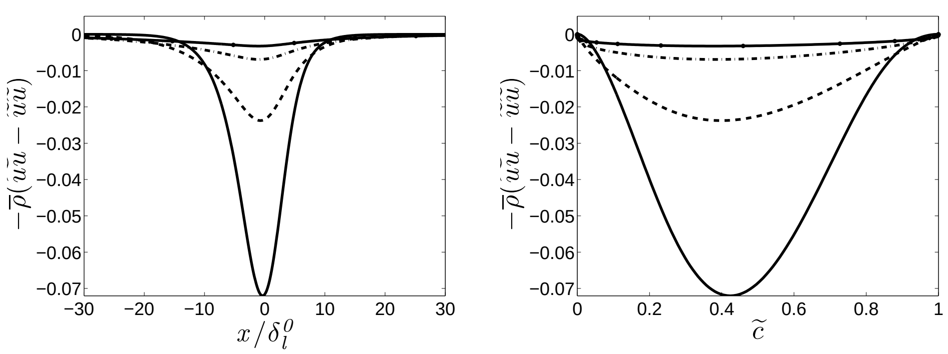

Figure 2.21 : *Analytically calculated subgrid-scale momentum flux in a thickened laminar flame* $-\overline{\rho}\,(\widetilde{uu} - \widetilde{u}\widetilde{u})$. $\overline{\Delta} = 5.0 \times 10^{-4}$ *m. The flame was thickened by a factor of* 5 (−), 10(−−), 20(−·−), *and* 30(− *with* ●). *The horizontal axis of the left plot was non-dimensioned by the laminar diffusion flame thickness,* $\delta_l^0 = D_u/S_L = 5.82 \times 10^{-5}$ *m*

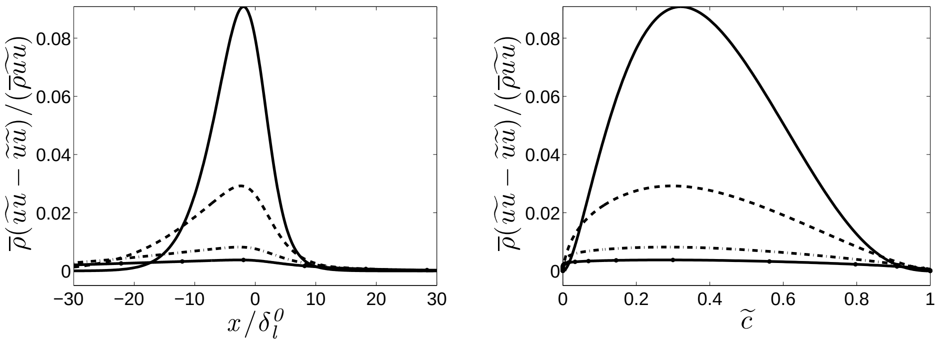

Figure 2.22 : *Ratio of analytically calculated subgrid-scale momentum flux to the exact value of the convection transport of momentum* $-\overline{\rho}\,(\widetilde{uu}-\widetilde{u}\widetilde{u})\,/-\overline{\rho}\,(\widetilde{uu})$. $\overline{\Delta} = 5.0\times10^{-4}$ *m. The flame is thickened by the factor of* 5 (−), 10(−−) , 20(−·−), *and* 30(− *with* ●). *The horizontal axis of the left plot was non-dimensioned by the laminar diffusion flame thickness,* $\delta_l^0 = D_u/S_L = 5.82\times10^{-5}$ *m*

Subgrid transport calculated with the dynamic Smagorinsky model

Figure 2.23 compares the subgrid-scale momentum flux calculated by the dynamic Smagorinsky model and the analytical value. The results of the dynamic Smagorinsky model were calculated with different test-filter sizes; $\widehat{\Delta}/\overline{\Delta}=2$, $\widehat{\Delta}/\overline{\Delta}=5$ and $\widehat{\Delta}/\overline{\Delta}=10$, where $\overline{\Delta}=\delta_l^0$. The analytical value of subgrid-scale momentum flux $\overline{\rho}(\widetilde{uu}-\widetilde{u}\widetilde{u})$ was obtained in the same manner that was described above and the Smagorinsky constant C_S was calculated by using this value;

$$C_S = \tau_{ij}/\left(2\overline{\rho}\overline{\Delta}^2|\widetilde{S}|\widetilde{S}_{ij}\right) \tag{2.52}$$

$$= -\overline{\rho}(\widetilde{uu}-\widetilde{u}\widetilde{u})/\left\{2\overline{\rho}\overline{\Delta}^2\sqrt{2\left(\frac{d\widetilde{u}}{dx}\right)^2}\frac{d\widetilde{u}}{dx}\right\}. \tag{2.53}$$

The dynamic Smagorinsky model predicted relatively well the subgrid-scale momentum fluxes. Even though some discrepancies existed in the middle of the flame, it reproduced the same tendency as that of the analytically calculated subgrid-scale momentum flux.

At both edges of the flame, the Smagorinsky constant took a large negative values. This was caused by small values of the velocity derivative used as the strain rate in this test. As the strain rate was close to zero, $\widehat{\overline{\Delta}^2|\widetilde{S}|\widetilde{S}_{ij}} \approx \widehat{\Delta}^2|\widehat{\widetilde{S}}|\widehat{\widetilde{S}}_{ij} \approx 0$, and the value of the Smagorinsky constant diverged (see Equation 1.61). In spite of this divergence of the constant, predicted subgrid-scale momentum flux

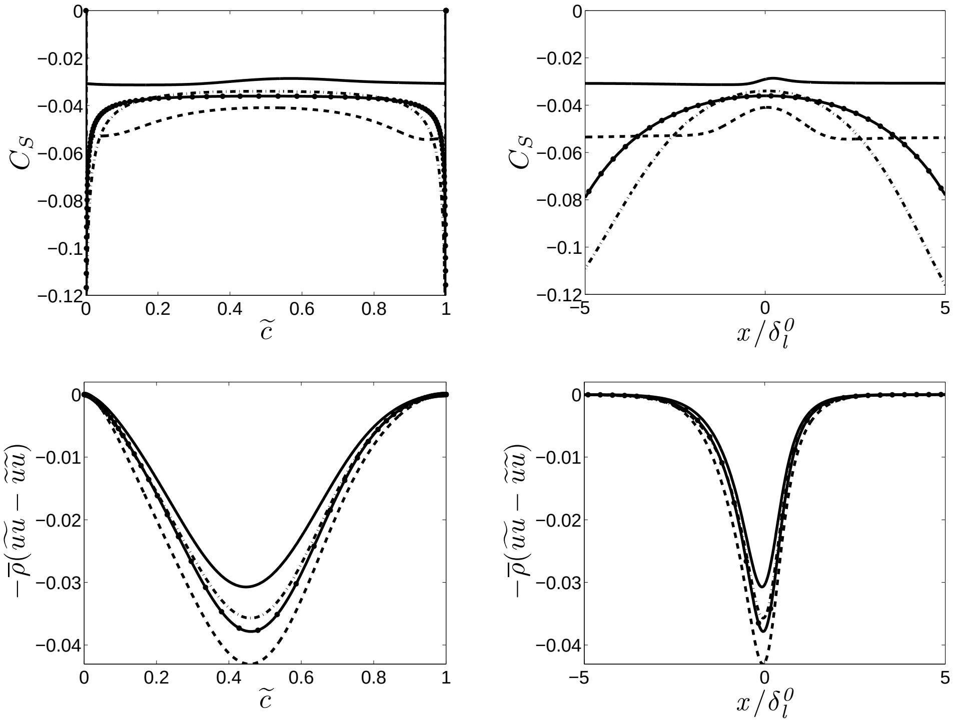

Figure 2.23 : *The dynamically calculated Smagorinsky constant and the subgrid-scale momentum flux in a laminar flame. The horizontal axes of the right plots were non-dimensioned by the laminar diffusion flame thickness* $\delta_l^0 = 5.82 \times 10^{-5}$ *(m).* $\overline{\Delta} = \delta_l^0$. *The lines correspond to the analytical value* $(-)$ *and dynamically calculated values with* $\widehat{\Delta}/\overline{\Delta} = 2\,(--)$, $\widehat{\Delta}/\overline{\Delta} = 5\,(-\cdot-)$, *and* $\widehat{\Delta}/\overline{\Delta} = 10\,(-$ *with* $\bullet)$.

did not diverge. This was because the strain rates were close to zero and the values calculated with Equation 1.48 converged to zero.

The influence of the test-filter size was verified to be weak. The results calculated with different test-filter sizes did not change in order of magnitude. Also, the result did not vary linearly with the test-filter size. A test-filter size, double of the LES filter size ($= \delta_l^0$), produced the largest difference from the analytical value of the subgrid-scale momentum flux, and when the test-filter size was five times of the LES filter size, the results were the closest.

Application of the Moin's procedure (Moin et al. 1991) was also tested. It writes

$$\left\{\widehat{(\overline{\rho}\widetilde{u}_i\widetilde{u}_j)} - \frac{1}{\widehat{\overline{\rho}}}\left(\widehat{\overline{\rho}\widetilde{u}_i}\,\widehat{\overline{\rho}\widetilde{u}_j}\right)\right\} - \left\{\widehat{(\overline{\rho}\widetilde{u}_k\widetilde{u}_k)} - \frac{1}{\widehat{\overline{\rho}}}\left(\widehat{\overline{\rho}\widetilde{u}_k}\,\widehat{\overline{\rho}\widetilde{u}_k}\right)\right\}\frac{\delta_{ij}}{3}$$
$$= 2C_S\left\{\left(\widehat{\overline{\rho}\overline{\Delta}^2|\overline{S}|\overline{S}_{ij}}\right) - \widehat{\overline{\rho}}\widehat{\Delta}^2|\widehat{\overline{S}}|\widehat{\overline{S}}_{ij}\right\}, \qquad (2.54)$$

and in one-dimensional case, it reduces to

$$\begin{aligned}
&\widehat{(\overline{\rho}\widetilde{u}\widetilde{u})} - \frac{1}{\widehat{\overline{\rho}}}\left(\widehat{\overline{\rho}\widetilde{u}}\widehat{\overline{\rho}\widetilde{u}}\right) \\
= \quad & 2C_S\left\{\left(\overbrace{\overline{\rho}\overline{\mathit{\Delta}}^2\sqrt{2\left(\frac{d\widetilde{u}}{dx}\right)^2}\frac{d\widetilde{u}}{dx}}\right) - \widehat{\overline{\rho}}\widehat{\mathit{\Delta}}^2\sqrt{2\left(\frac{d\widehat{\widetilde{u}}}{dx}\right)^2}\frac{d\widehat{\widetilde{u}}}{dx}\right\}. \qquad (2.55)
\end{aligned}$$

For the following discussion, we represent this equation as,

$$Term1 - Term2 = 2C_S\left(Term3 - Term4\right). \qquad (2.56)$$

In the case of the standard dynamic Smagorinsky model, they correspond to

$$\begin{aligned}
Term1 &= \overline{\rho}\widehat{\widetilde{uu}} \\
Term2 &= \overline{\rho}\widehat{\widetilde{u}}\widehat{\widetilde{u}} \\
Term3 &= \overline{\rho}\overline{\mathit{\Delta}}^2\overbrace{\sqrt{2\left(\frac{d\widetilde{u}}{dx}\right)^2}\frac{d\widetilde{u}}{dx}} \\
Term4 &= \overline{\rho}\widehat{\mathit{\Delta}}^2\sqrt{2\left(\frac{d\widehat{\widetilde{u}}}{dx}\right)^2}\frac{d\widehat{\widetilde{u}}}{dx}.
\end{aligned}$$

The results are presented in Figure 2.24. The analytical value represented by the solid line is the same data as that presented in Figure 2.23. The position of the peak value was slightly different from analytical result as shown in the bottom right plot of Figure 2.24. The position of the peak in the results of the standard dynamic Smagorinsky model was at the same x coordinate as the analytical subgrid-scale transport. This deviation was due to the sensitivity of this procedure to the density change through the flame.

Figures 2.25 and 2.26 compare the intermediate terms in the calculation of the Smagorinsky constant. As is seen in Figure 2.25 the terms of Moin's model were smaller on unburned side ($x < 0$) and larger on burnt side ($x > 0$). Since the density was included in the filtering, the filtered values were more strongly influenced by the values of a high density zone, i.e. on the unburned side, than by those of a low density zone, i.e. on the burnt side. This trend was noticeable in zones where the density gradients took large values (see Figure 2.3). The $Term1 - Term2$ and $Term3 - Term4$ yielded the fields as indicated in Figure 2.26. The field of $Term1 - Term2$ preserved the influence of density change, and it made the dynamically calculated subgrid stress field deviate towards the burnt gas side.

The amplitude of the calculated stress field was similar to that of the standard model. However, unlike to the result of standard model, the result with filter

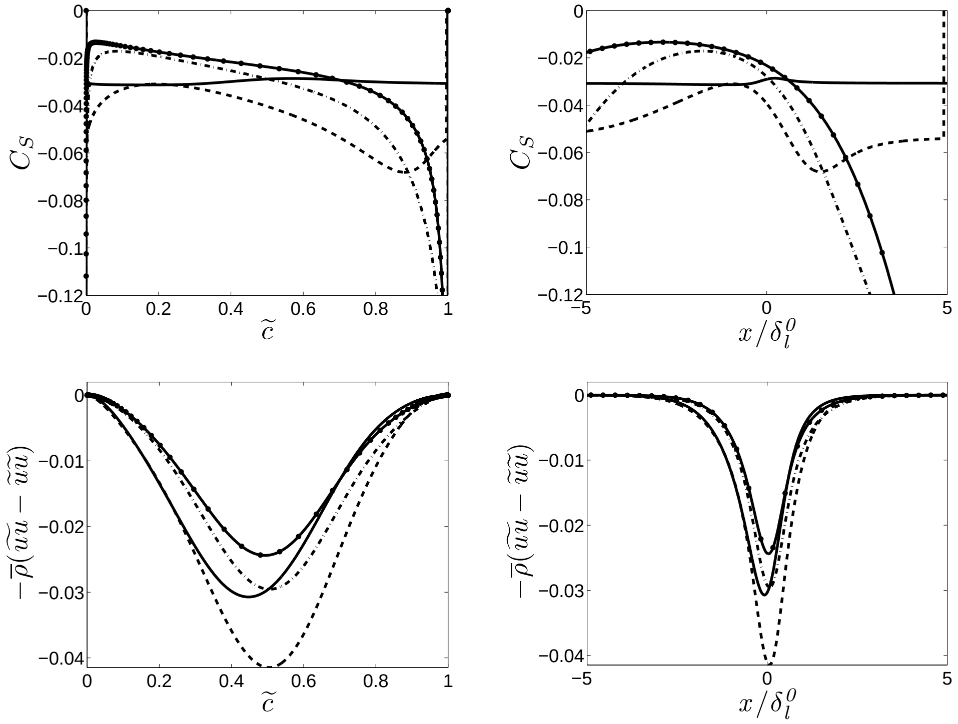

Figure 2.24 : *The dynamically calculated Smagorinsky constant and the subgrid-scale momentum flux calculated with Moin's procedure in a laminar flame. The horizontal axes of the right plots were non-dimensioned by the laminar diffusion flame thickness,* $\delta_l^0 = 5.82\times 10^{-5}$ *(m).* $\overline{\Delta} = \delta_l^0$*. The lines correspond to the analytical value* $(-)$ *and the dynamically calculated values with* $\widehat{\Delta}/\overline{\Delta} = 2\,(--)$*,* $\widehat{\Delta}/\overline{\Delta} = 5\,(-\cdot-)$ *and* $\widehat{\Delta}/\overline{\Delta} = 10\,(-$ *with* $\bullet)$*.*

size $\widehat{\Delta} = 5\overline{\Delta}$ had the same height of peak as that of the analytical value, and the peak of the $\widehat{\Delta} = 10\overline{\Delta}$ result was closer to zero than the analytical value. It may be said that Moin's model yields, potentially, better approximation of the subgrid-scale momentum flux in a one-dimensional laminar flame.

In this section, the existence of the subgrid-scale momentum flux opposite to the gradient assumption in a laminar flame was verified and both the standard dynamic Smagorinsky model and Moin's procedure succeeded in predicting its emergence.

However, the subgrid stress opposite to the ones predicted from the usual gradient assumption may cause numerical instabilities in practical simulations. Furthermore, because the reaction zone is amplified in the use of the thickened flamelet model, and the region where the subgrid stress takes negative value is also enlarged, the possibility of numerical instabilites increases. In this study, the negative values of the subgrid stresses will be set to zero in

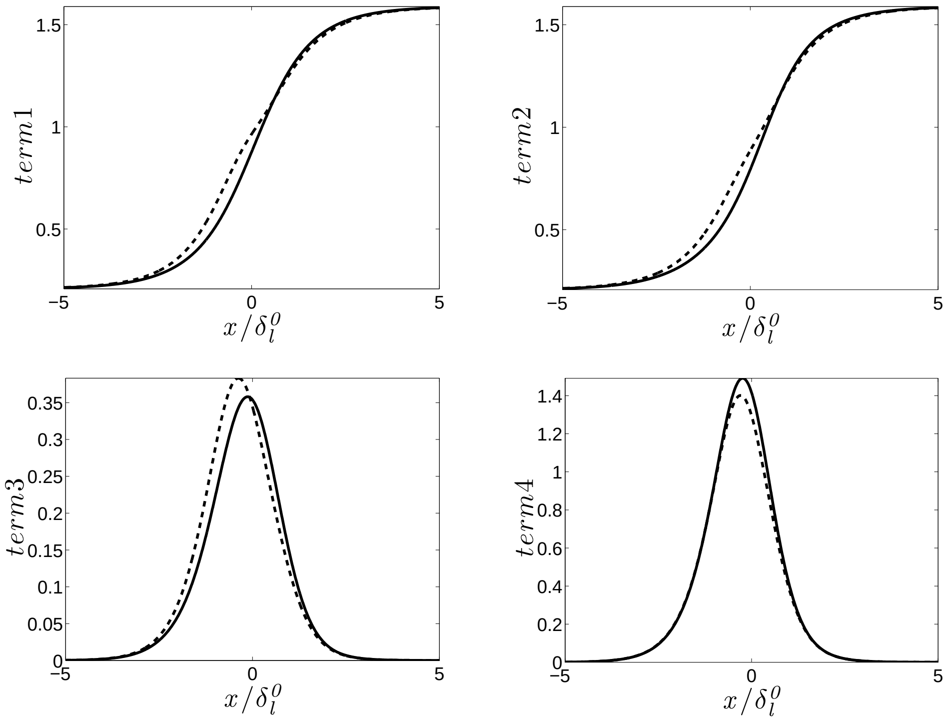

Figure 2.25 : *Comparison of the intermediate terms in the calculation of the Smagorinsky constant C_S. The horizontal axes were non-dimensioned by the laminar diffusion flame thickness, $\delta_l^0 = 5.82 \times 10^{-5}$ (m). $\overline{\Delta} = \delta_l^0$. The lines correspond to the terms of Moin's model (−) and standard dynamic Smagorinsky model using Favre filtering (−−), Term1 to Term4 correspond to $\widehat{\overline{\rho}\widetilde{uu}}$, $(1/\widehat{\overline{\rho}})\widehat{\overline{\rho}\widetilde{u}}\widehat{\overline{\rho}\widetilde{u}}$, $\overbrace{\overline{\rho}\overline{\Delta}^2|\widetilde{S}|\widetilde{S}}$ and $\widehat{\overline{\rho}}\widehat{\Delta}^2|\widehat{\widetilde{S}}|\widehat{\widetilde{S}}$ for the Moin's model (solid line) and $\overline{\rho}\widehat{\widetilde{uu}}$, $\overline{\rho}\widehat{\widetilde{u}}\widehat{\widetilde{u}}$, $\overline{\rho}\overline{\Delta}^2\widehat{|\widetilde{S}|\widetilde{S}}$ and $\overline{\rho}\widehat{\Delta}^2|\widehat{\widetilde{S}}|\widehat{\widetilde{S}}$ for the standard model (dashed line).*

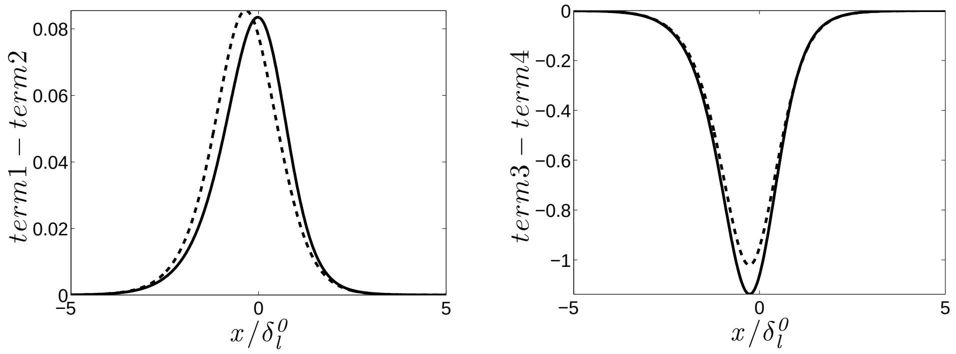

Figure 2.26 : *Comparison of the intermediate terms in the calculation of the Smagorinsky constant C_S. The horizontal axes were non-dimensioned by the laminar diffusion flame thickness $\delta_l^0 = 5.82 \times 10^{-5}$ (m). $\overline{\Delta} = \delta_l^0$. The lines correspond to the terms of Moin's model (−) and standard dynamic Smagorinsky model using Favre filtering (−−), term1 to term4 correspond to $\widehat{\overline{\rho}\widetilde{uu}}$, $(1/\widehat{\overline{\rho}})\widehat{\overline{\rho}\widetilde{u}}\widehat{\overline{\rho}\widetilde{u}}$, $\overbrace{\overline{\rho}\overline{\Delta}^2|\widetilde{S}|\widetilde{S}}$ and $\widehat{\overline{\rho}}\widehat{\Delta}^2|\widehat{\widetilde{S}}|\widehat{\widetilde{S}}$ for the Moin's model (solid line) and $\overline{\rho}\widehat{\widetilde{uu}}$, $\overline{\rho}\widehat{\widetilde{u}}\widehat{\widetilde{u}}$, $\overline{\rho}\overline{\Delta}^2\widehat{|\widetilde{S}|\widetilde{S}}$ and $\overline{\rho}\widehat{\Delta}^2|\widehat{\widetilde{S}}|\widehat{\widetilde{S}}$ for the standard model (dashed line).*

the multi-dimensional simulations considering the fact that the influence of the subgrid-scale momentum flux opposite to the gradient assumption is small and to avoid numerical instabilities.

2.4 Conclusion

Following the tests performed in this chapter, several remarks can be made:

- The strong form of the dynamic thickened flamelet model cannot be applied to the present study because it results in a negative/positive infinite value of the constant β and a strong variation of the efficiency in the flame. For this reason, the weak form is chosen in this study.

- Moin's filtering process, described in Moin et al. (1991) for the double filtered terms in the formulation of the dynamic procedure (combination of two Favre filters), yields ideal convergence of the constant β in the limit of the weak turbulence, unlike to the combination of Favre filtering and simple filtering. It does not depend on the choice of the reaction model.

- The change in filter size ratio between the LES and the test-filters $\widehat{\Delta}/\overline{\Delta}$ does not significantly affect the value of the reaction rate ratio $\left\langle \gamma \overbrace{W(\widetilde{\mathbf{q}})} \right\rangle / \left\langle W\left(\widehat{\widetilde{\mathbf{q}}}\right) \right\rangle$.

- The thicknesses of filtered laminar flames δ_L were proportional to the filter size $\mathit{\Delta}$, when $\mathit{\Delta}$ is sufficiently large compared to the filter size δ_f, which was used to obtain the progress variable field in a laminar flame from a Heaviside function.

- For the dynamic Smagorinsky model, both the standard and Moin's procedure were tested on a laminar flame. All of the results show the existence of the subgrid stresses opposite to the ones predicted from usual gradient assumption that is caused by the thermal expansion of the flow media, but the influence have been shown to be small. Thus, it will be neglected in multi-dimensional simulations in the following chapters to avoid numerical instabilities.

Chapter 3

Implementation into the AVBP code

In this chapter, the implementation of the dynamic model into the AVBP code is performed and tested. In the previous chapter, the dynamic model was applied to a one-dimensional flame and the filtering procedure was discussed. Here the validity of the conclusion of Chapter 2 is investigated in the AVBP code and the numerical configurations, such as the test-filter length and the integral interval for the averaging, are discussed in view of multi-dimensional simulations.

3.1 Introduction

Before simulations of turbulent combustion with the dynamic models, tests to assess their application are mandatory. In this chapter, the assessment is done through two simple tests.

In the first test, the dynamic thickened flamelet model is applied to a laminar one-dimensional flame. The results are compared with those of the previous chapter.

In the second test, the calculation of the constant β is analyzed through the application of the model to a two-dimensional turbulent flame, computed with Colin's efficiency function (Colin et al. 2000). The influence of the filter size and the size of integral volume is also examined.

Using the same geometry, the dynamic Smagorinsky model is also tested. This test is performed to examine the effect of the dynamic Smagorinsky model on a flame, and to determine the test-filter size for its application to multi-dimensional simulations.

The AVBP code has been developed by CERFACS (European Centre for Research and Advanced Training in Scientific Computation) and IFP (French Institute of Petrol) in France for simulations of laminar and turbulent compressible combustion. This solver uses cell-vertex finite volume discretization method so that unstructured grids for complex geometries can also be treated (see Selle et al. (2004)). Several schemes for the time evolution are available, such as Runge-Kutta method of several orders, Lax-Wendroff (Hirsch 1989), and Two step Taylor-Galerkin schemes (Donea (1984), Quartapelle and Selmin (1993), and Colin and Rudgyard (2000)).

3.2 Application to laminar combustion

This test has two major objectives:

- Determination of the proportionality coefficient α that gives an equivalent filter size $\overline{\Delta} = \alpha F \delta_l^0$ to obtain a thickened flame of thickness $F\delta_l^0$.
- Verification of the convergence of the term to unity,

$$\frac{\gamma \langle \overbrace{W(\widetilde{\mathbf{q}})} \rangle}{\langle W(\widehat{\widetilde{\mathbf{q}}}) \rangle} \, . \tag{3.1}$$

In the previous chapter, two tests were performed on a laminar flame. In the first test, a laminar flame was produced by applying a Gaussian filter of size $\delta_f = \delta_l^0/c^* \sqrt{6/\pi}$, to a Heaviside function, and the thickness was clearly defined by $\delta_l^0 = D_u/S_L c^*$, where c^* was set to 0.5. Then thickened flames were obtained by applying filters of size $\overline{\Delta} = F\delta_f$, where F changed from 2 to 30, to the laminar flame. In this test, all the filters were Gaussian type, and the expression, $\widehat{\overline{\Delta}} = \sqrt{\widehat{\Delta}^2 + \overline{\Delta}^2}$ was true. The convergence of the reaction rate ratio $\gamma \langle \overbrace{W(\widetilde{c})} \rangle / \langle W(\widehat{\widetilde{c}}) \rangle$ to unity was, therefore, well verified.

However, in the second test, where the laminar flame was obtained with the reduced reaction model of Ferziger, the value of $\delta_f = \delta_l^0/c^* \sqrt{6/\pi}$ was no longer valid, and a "corrected" value for δ_f was calculated to satisfy $\gamma \langle \overbrace{W(\widetilde{c})} \rangle / \langle W(\widehat{\widetilde{c}}) \rangle = 1$.

In practical simulations thickened flame is not obtained by filtering but by thickening, and the LES filter size $\overline{\Delta}$ is not explicitly defined. $\overline{\Delta}$ must be determined through a test to calculate the filter size ratio γ for multi-dimensional simulations performed in Chapter 4 and Chapter 5.

As verified in the previous chapter, the thickness of the filtered laminar flame δ_L is proportional to the filter size $\overline{\Delta}$ (see Figure 2.16 of Chapter 2). Then the effective filter size ratio $\gamma = \sqrt{\widehat{\Delta}^2 + \overline{\Delta}^2}/\overline{\Delta}$ is identical to the ratio of test-filtered laminar flame thickness δ_T and resolved laminar flame thickness δ_F $(= F\delta_l^0)$,

$$\gamma = \frac{\delta_T}{\delta_F} \, . \tag{3.2}$$

Simultaneously, $\overline{\Delta}$ is given as $\alpha\delta_F$, then,

$$\gamma = \frac{\delta_T}{\delta_F} = \sqrt{\left(\frac{\widehat{\Delta}}{\alpha\delta_F}\right)^2 + 1}\,. \tag{3.3}$$

Both γ and α are, thus, computable from the observation of flame thicknesses of resolved and test-filtered flames.
The thickness of the thickened laminar flame and that of the test-filtered thickened laminar flame are calculated by two methods, based on the distance that the progress variable c takes to change from 0.01 to 0.99 and the inverse of the maximum gradient of the progress variable. See Section 2.3.2 of Chapter 2 for detailed description.
As in the one-dimensional case, the value of Equation 3.1 should be unity for one-dimensional laminar flames. If not, the constant β of the dynamic procedure diverges. This point is verified again in the AVBP code. The reaction rates $W(\widehat{\mathbf{q}})$ and $W(\tilde{\mathbf{q}})$ in Equation 3.1 are calculated using the progress variables, $\widetilde{c}$ and $\widehat{\widetilde{c}}$, defined with resolved and test-filtered variables for Boger's algebraic model and the reduced Arrhenius law, and directly using filtered variables for the Arrhenius law. The details of reaction rate models are given in the following section. This reaction rate is substituted into Equation 3.1 and the value of γ to satisfy $\gamma\langle\widehat{W(\widetilde{\mathbf{q}})}\rangle/\langle W(\widehat{\mathbf{q}})\rangle$ and the value of α, which gives this γ, are calculated. In this test, the term $\langle\widehat{W(\widetilde{\mathbf{q}})}\rangle$ reduces to $\langle W(\widetilde{\mathbf{q}})\rangle$ by integrating the reaction rate across the flame front since the filtering process conserves the integral.

3.2.1 Configuration

This test is based on a simple configuration of long, narrow channel that has the length of $0.3\,m$ and the width of $0.001\,m$. Figure 3.1 is a close up of the mesh near $x = 0$. The same uniform mesh continues from $x = -0.15$ to $x = 0.15$, a distance sufficient to start and finish combustion. The left-hand-side and the right-hand-side are the inlet and the outlet respectively. The inlet velocity is set to 0.41 m/s, which is the laminar flame speed of the fuel of methane-air at stoichiometry. The equivalence ratio of the incoming methane-air mixture is stoichiometric. The upper and bottom boundaries are treated as symmetric boundaries. An analytical solution of a one-dimensional laminar flame is given as the initial condition and the flame is stabilized by TTGC scheme along two million iterations using two step chemical reaction.

$$\begin{aligned} C_3H_8 + 5O_2 &\implies 3CO + 4H_2O \\ CO + 1/2O_2 &\iff CO_2 \end{aligned} \tag{3.4}$$

The detail of this two step reaction is given in Section 4.2. The thickening factor F is set to 20. This value will be used in the multi-dimensional simulations in chapter 4 and chapter 5. The inputs are shown in table 3.1. The laminar flame thickness is obtained using the proposition of Blint (1986).

$s_L(m/s)$	$\delta_l^0(m)$	$T_u(K)$	$T_b(K)$	$\rho_u(kg/m^3)$	F	$\widehat{\Delta}(m)$
0.41	4.84×10^{-4}	300	2300	1.202	20	0.015

Table 3.1 : *Flame parameters*

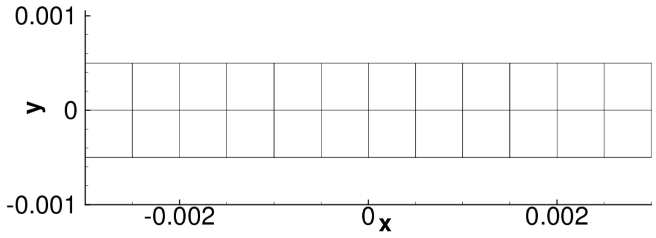

Figure 3.1 : *Computational mesh*

Three reaction rate models are employed in this test:

- Boger's algebraic model

$$\dot{\omega} = 4\rho_u s_l^0 \sqrt{\frac{6}{\pi}} \frac{\widetilde{c}(1-\widetilde{c})}{\Delta} \tag{3.5}$$

  In generic form (Charlette et al. 2002b), it writes

$$W_{\Delta}(\widetilde{c}) = 4\rho_u s_l^0 \sqrt{\frac{6}{\pi}} \widetilde{c}(1-\widetilde{c}) \tag{3.6}$$

  then

$$\dot{\omega} = \frac{W_{\Delta}(\widetilde{c})}{\Delta} . \tag{3.7}$$

- Arrhenius law using the progress variable (reduced Arrhenius law)

$$\dot{\omega} = \frac{A}{F}\rho_u(1-\widetilde{c}) \exp\left(-\frac{E_a}{R(300+2000\times\widetilde{c})}\right) \tag{3.8}$$

$$W_{\Delta}(\widetilde{c}) = A\alpha\delta_l^0\rho_u(1-\widetilde{c}) \exp\left(-\frac{E_a}{R(300+2000\times\widetilde{c})}\right) \tag{3.9}$$

  where E_a is the activation energy, R is the gas constant, A is the pre-exponential factor determined according to the laminar flame speed, and

α is a constant that gives the filter size $\varDelta$ to obtain a flame of thickness $F\delta_l^0$ ($\varDelta = \alpha F \delta_l^0$). $\dot{\omega}$ and $W_\varDelta(\widetilde{c})$ are related as:

$$\dot{\omega} = \frac{W_\varDelta(\widetilde{c})}{\varDelta} = \frac{W_\varDelta(\widetilde{c})}{\alpha F \delta_l^0} \,. \qquad (3.10)$$

- Arrhenius law using filtered variables

$$\begin{aligned} \dot{\omega} &= \frac{A}{F}\bar{\rho}\widetilde{X}^a_{C_3H_8}\widetilde{X}^b_{O_2}\exp\left(-\frac{E_a}{R\widetilde{T}}\right) && (3.11) \\ W_\varDelta(\widetilde{X}_{C_3H_8}, \widetilde{X}_{O_2}, \widetilde{T}) &= A\alpha\delta_l^0\bar{\rho}\widetilde{X}^a_{C_3H_8}\widetilde{X}^b_{O_2}\exp\left(-\frac{E_a}{R\widetilde{T}}\right) && (3.12) \end{aligned}$$

where X_k are molar fractions of species k. a and b are the specific constants of the reaction respectively. These values are summarized in Table 3.2. Here again

$$\dot{\omega} = \frac{W_\varDelta(\widetilde{c})}{\varDelta} = \frac{W_\varDelta(\widetilde{c})}{\alpha F \delta_l^0} \,. \qquad (3.13)$$

a	b	A(cgs)	$E_a(cal.mol^{-1})$
0.9028	0.6855	2.0×10^{12}	33000

Table 3.2 : *Chemical parameters for the reaction rate*

Boger's algebraic model and the reduced Arrhenius law need the calculation of the progress variable. Several definitions of the progress variable are possible.

$$\begin{aligned} c &= \frac{T - T_u}{T_b - T_u} && (3.14) \\ c &= \frac{Y_i - Y_{ib}}{Y_{ib} - Y_{iu}} && (3.15) \end{aligned}$$

The definition of the progress variable plays an important role. The most common method is to use the temperature for the definition of the progress variable as in Equation 3.14. The use of mass fractions of chemical species participating in the reaction, i.e. of C_3H_8, O_2 and $CO + CO_2$ is also possible. The former should be used carefully since in non-adiabatic case the maximum temperature of the burnt gas depends on the configuration and it is not a fixed parameter. Consequently, the progress variable might not reach unity even if all the fuel is burnt. In this study, the temperature of burnt gas is verified to be 2300 K and the progress variable defined with temperature can be employed.
In the case of the Arrhenius law, the definition of the progress variable is not required: the reaction rate can also be calculated with the test-filtered variables.

Calculation of the filtered variables

In the previous chapter, filtering procedure was also discussed. Here we implement the third combination of Table 2.2, as the density of the flow media changes significantly across the flame and the simulation code is written with Favre averaging.

To calculate the reaction rate at the test-filter scale, test-filtered fields of the variables are necessary. When employing the Arrhenius law, filtered fields of temperature and concentration of chemical species need to be calculated. As conservative transport equations are discretized in the AVBP code, the variables $\overline{Q}$ are multiplied by density $\overline{\rho}$. The $\bar{\cdot}$ indicates the LES filtered quantity. They are divided by density to obtain the primitive variables and the values take the Favre averaged form ($\widetilde{Q} = \overline{\rho Q}/\overline{\rho}$). To obtain the test-filtered variable of Q, both of the terms $\overline{\rho Q}$ and $\overline{\rho}$ are filtered and the test-filtered variable is calculated as $\widehat{\overline{\rho Q}}/\widehat{\overline{\rho}}$. This operator is represented by $\widetilde{\widetilde{Q}}$ in the following.

The field of the test-filtered temperature is calculated from the test-filtered enthalpy field. This is because, in the AVBP code, the energy transport equation is written using total enthalpy. The enthalpy field is first test-filtered and the kinetic energy that is calculated with the test-filtered velocity is subtracted to obtain the total sensible enthalpy of all species.

$$\widetilde{\widetilde{h}}_s = \widetilde{\widetilde{H}} - \widetilde{\widetilde{E}} = \widetilde{\widetilde{H}} - \frac{1}{2}\widetilde{\widetilde{u}}_i\widetilde{\widetilde{u}}_i \tag{3.16}$$

Then, using the test-filtered concentration of chemical species, the temperature is calculated from the following relation,

$$\widetilde{\widetilde{h}}_s = \sum_i \int_{T_0}^{\widetilde{\widetilde{T}}} \widetilde{\widetilde{Y}}_i C_{v,i} dT \tag{3.17}$$

The values of the specific heat of each chemical species are tabulated and given to the code as input data.

3.2.2 Results

Test for flame thickness

Figure 3.2 shows the fields of resolved temperature, mass fractions of C_3H_8 and O_2 and the corresponding test-filtered fields. The reaction rates calculated through the Arrhenius law using the variables of the thickened and the filtered thickened flame are shown as references of the flame positions. The flame thicknesses calculated with these fields are indicated in Tables 3.3 to 3.6. The thickening factor is set to $F = 20$, and the test-filter size varies from $\widehat{\Delta} = 1.0 \times 10^{-2}$ to $\widehat{\Delta} = 3.0 \times 10^{-2}\,(m)$. The last two rows of these tables are the LES filter size $\Delta_F (= \alpha F \delta_l^0)$ and the coefficient α that provide γ equal to the thickness ratios, calculated with Equation 3.3. The ratio of the resolved and test-filtered flame thicknesses and Δ_F are plotted in Figure 3.3 as functions of the test-filter size $\widehat{\Delta}$.

The results indicate that the proportionality coefficient α of LES filter size Δ_F against the resolved laminar flame thickness δ_F ($\Delta_F = \alpha\delta_F$) to yield γ that is equal to the ratio of thickened and filtered thickened flame thicknesses decreased as the test-filter size increased. This comes from the fact that the profiles of the resolved variables in a thickened flame are not identical to that of a Gaussian filtered Heaviside function. As Equation 3.3 implicitly suppose that the profiles of resolved variables in a thickened flame are identical to the Gaussian filtered Heaviside function, test-filter size $\widehat{\Delta}$ affected the value of α.

α also depended on the variable, which is used in the calculation of the progress variable and the definition of the flame thickness. This is because of the dependence of the resolved flame thicknesses δ_F on the choice of the variable and the definition of the thickness. The larger the flame thickness is, the less α becomes, as α is defined as $\alpha = \overline{\Delta}/\delta_L$, where $\overline{\Delta}$ is the LES filter size and δ_L is the flame thickness of the filtered laminar flame by this filter. The discrepancy of the flame thicknesses due to the different variables chosen for the calculation of α was caused by the use of different Schmidt numbers Sc for each chemical species. Consequently, the diffusion properties of C_3H_8 and O_2 were different from conduction property of temperature, and resulted in the dependence of the flame thickness on the choice of the variable.

Unlike to the proportionality coefficient α, the value of Δ_F did not depend much on the definition of flame thickness as shown in Figure 3.3. It slightly decreased with the increase of $\widehat{\Delta}$, but the value was always around 0.009 m. Thus, the thickened flame by a factor of 20 was verified to be approximated by a Gaussian filtered laminar flame by a filter size of 0.009 m in the AVBP code.

Test for the selection of reaction models

Figures 3.4 and 3.5 compare the reaction rates calculated with variables of thickened flame and those calculated with test-filtered variables, and Figure 3.6 displays the fields of the progress variables, $\widetilde{c}$, and the test-filtered progress variable, $\widehat{\widetilde{c}}$, obtained from different resolved and test-filtered variables. In Figure 3.5, the reaction rates are divided by α to exclude the dependence of reaction rates on this term. Boger's algebraic model made no difference between the maximum value of the two reaction rates, because the reaction rate only depends on the progress variable c. The value does not depend on the choice of variable ($Y_{C_3H_8}$, Y_{O_2} or T) for the calculation of the progress variable. Since It does not change even in the case where the reduced Arrhenius law is applied, only the field of the reaction rate calculated with the progress variables based on temperature is displayed for the reduced Arrhenius law in Figure 3.5. When the reaction rate was calculated with the Arrhenius law using the test-

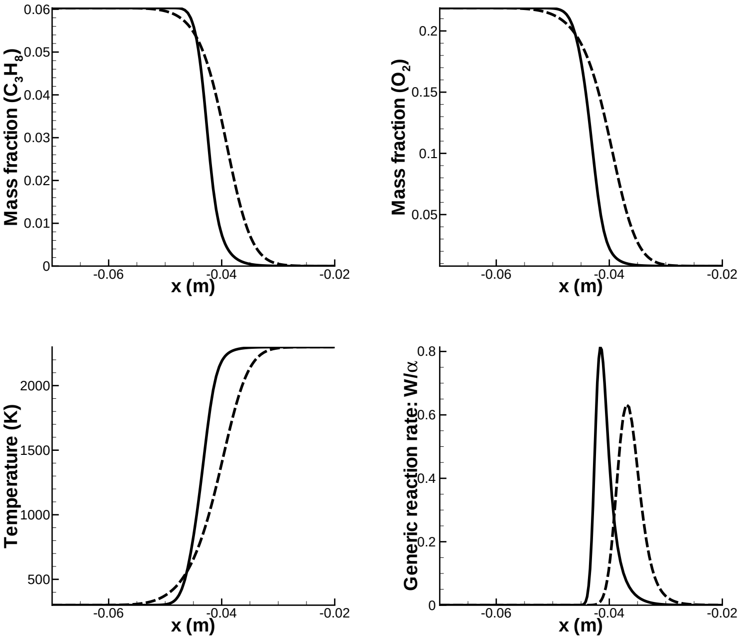

Figure 3.2 : *Inner flame structure of thickened flame (solid line) and filtered flame after thickening (dashed line). The reaction rates are calculated with the variables of thickened flame (solid line) and filtered variables after thickening (dashed line).* $\widehat{\Delta} = 1.5 \times 10^{-2}$ *(m).*

variable used	$Y_{C_3H_8}$	Y_{O_2}	T	$\nabla Y_{C_3H_8}$	∇Y_{O_2}	∇T
thickened flame (mm)	9.90	10.35	10.27	4.85	5.26	5.64
filtered thickened flame (mm)	14.26	15.31	15.58	7.18	7.57	8.16
ratio	1.44	1.48	1.52	1.48	1.44	1.45
Δ_F for $\gamma =$ ratio (mm)	9.65	9.17	8.77	9.16	9.66	9.56
α	0.974	0.886	0.854	1.889	1.837	1.696

Table 3.3 : *Flame thickness calculated with the variables indicated in the first row.* $\widehat{\Delta} = 1.0 \times 10^{-2}\ m$.

variable used	$Y_{C_3H_8}$	Y_{O_2}	T	$\nabla Y_{C_3H_8}$	∇Y_{O_2}	∇T
thickened flame (mm)	9.90	10.35	10.27	4.85	5.26	5.64
filtered thickened flame (mm)	19.07	20.15	20.66	9.35	9.80	10.55
ratio	1.93	1.95	2.01	1.93	1.86	1.87
Δ_F for $\gamma =$ ratio (mm)	9.11	8.98	8.59	9.10	9.54	9.49
α	0.920	0.868	0.837	1.876	1.814	1.682

Table 3.4 : *Flame thickness calculated from the variables indicated in the first row.* $\widehat{\Delta} = 1.5 \times 10^{-2}\ m$.

variable used	$Y_{C_3H_8}$	Y_{O_2}	T	$\nabla Y_{C_3H_8}$	∇Y_{O_2}	∇T
thickened flame (mm)	9.90	10.35	10.27	4.85	5.26	5.64
filtered thickened flame (mm)	24.16	25.77	26.54	11.85	12.33	13.26
ratio	2.44	2.49	2.58	2.44	2.34	2.35
Δ_F for $\gamma =$ ratio (mm)	8.98	8.77	8.39	8.97	9.43	9.40
α	0.908	0.847	0.817	1.850	1.793	1.667

Table 3.5 : *Flame thickness calculated with the variables indicated in the first row.* $\widehat{\Delta} = 2.0 \times 10^{-2}\ m$.

variable used	$Y_{C_3H_8}$	Y_{O_2}	T	$\nabla Y_{C_3H_8}$	∇Y_{O_2}	∇T
thickened flame (mm)	9.90	10.35	10.27	4.85	5.26	5.64
filtered thickened flame (mm)	35.84	37.87	39.07	17.32	17.85	19.15
ratio	3.62	3.66	3.81	3.57	3.39	3.39
Δ_F for $\gamma =$ ratio (mm)	8.62	8.52	8.17	8.75	9.25	9.25
α	0.871	0.824	0.796	1.804	1.759	1.639

Table 3.6 : *Flame thickness calculated with the variables indicated in the first row.* $\widehat{\Delta} = 3.0 \times 10^{-2}\ m$.

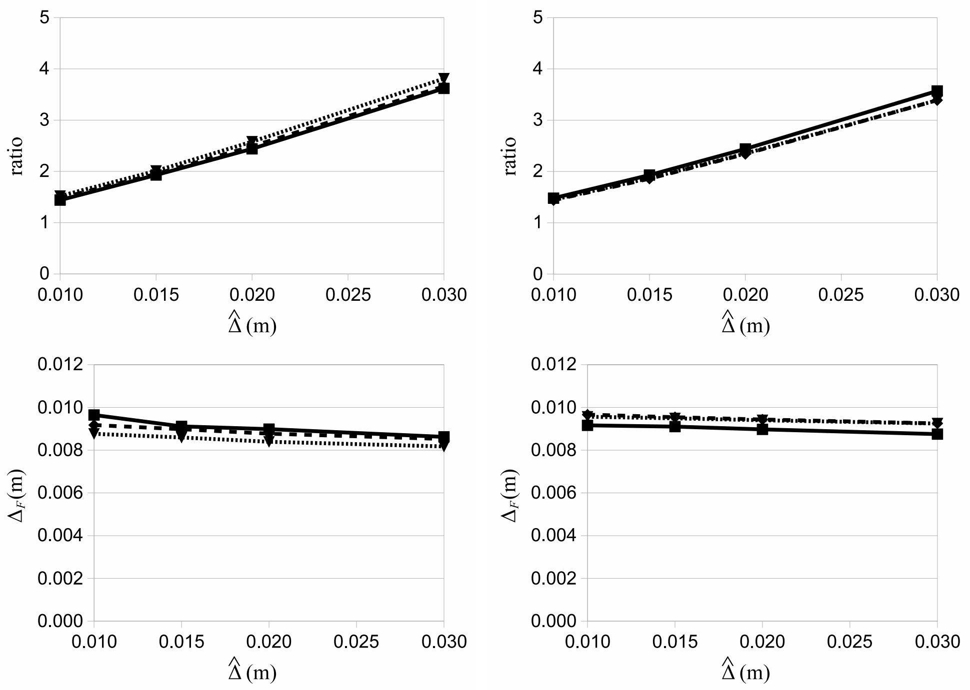

Figure 3.3 : *Ratio of the thicknesses of thickened and test-filtered flames (top) (δ_T/δ_F) and the LES filter size Δ_F to yield γ that is equal to the ratio of thickened and filtered thickened flame thicknesses (bottom) as functions of the test-filter size $\widehat{\Delta}$. The flame thicknesses were calculated as the distances that the resolved variables change from 1 to 99 % (left) and from the maximum gradient of resolved variables (right). The results were obtained from C_3H_8 (solid line), O_2 (dashed line), and temperature fields (dotted line).*

filtered variables, the reaction rate calculated with resolved variables exceeded the other, as indicated in Figure 3.5.

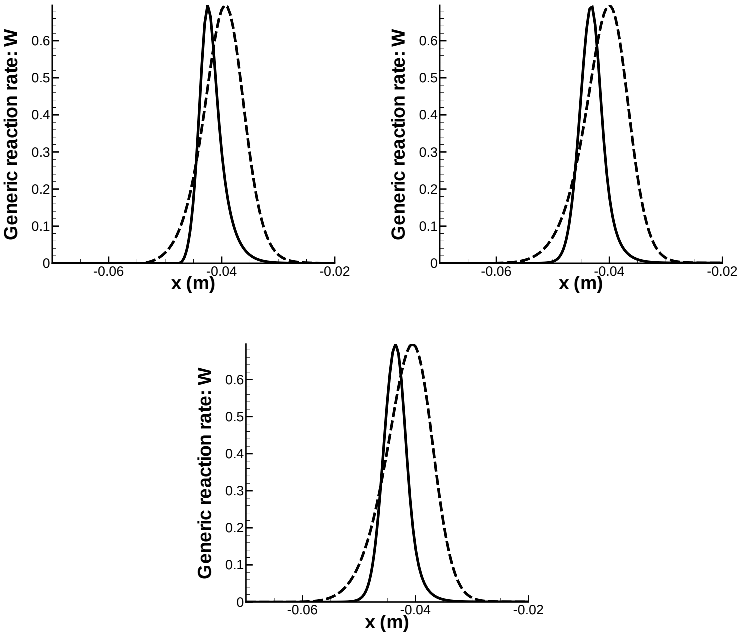

Figure 3.4 : *Generic reaction rates calculated with Boger's algebraic model. Reaction rates are calculated with the resolved variables (solid line) and the test-filtered variables (dashed line). The progress variable is calculated from mass fractions of C_3H_8 (upper left), that of O_2 (upper right), and temperature (bottom).* $\widehat{\Delta} = 1.5 \times 10^{-2}$ *(m).*

Tables 3.7 and 3.8 show the integral values of the generic reaction rates and their ratios, providing the values of γ required to ensure the relation $\gamma \int W(\widetilde{\mathbf{q}})dx = \int W(\widehat{\widetilde{\mathbf{q}}})dx$. In this study, integration from negative to positive infinity is equivalent to the operation indicated as $\langle \cdot \rangle$, the relation is rewritten as $\gamma \langle W(\widetilde{\mathbf{q}}) \rangle = \overbrace{\langle W(\widehat{\widetilde{\mathbf{q}}})\rangle}$. The difference of the integral values comes from the difference of the flame thickness and the maximum value. In the case of Boger's algebraic model, the maximum values of the reaction rates were always the same, but the distances that the progress variable needs to become unity from zero were slightly different as shown in Figure 3.6. Thus, the integrals of the reaction rates took somewhat different values.

The ratios $\langle W(\widehat{\widetilde{\mathbf{q}}})\rangle / \overbrace{\langle W(\widetilde{\mathbf{q}})\rangle}$ and the LES filter size $\overline{\Delta}$ to obtain γ equal to these ratios calculated through Equation 3.3 are plotted in Figure 3.7 as functions of the test-filter size $\widehat{\Delta}$ for different chemical models. Again, these ratios are the values of γ required to obtain $\gamma \overbrace{\langle W(\widetilde{\mathbf{q}})\rangle} / \langle W(\widehat{\widetilde{\mathbf{q}}})\rangle = 1$. The lines of the reac-

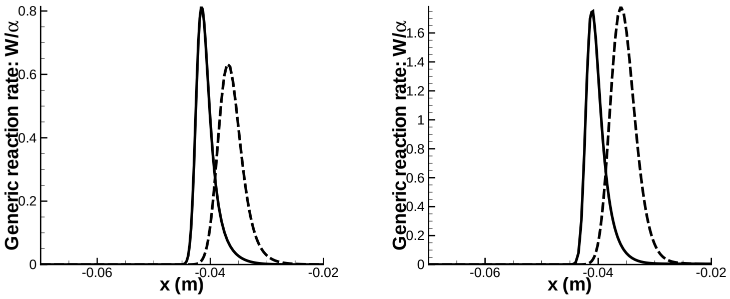

Figure 3.5 : *Generic reaction rates calculated with the Arrhenius law (left) and the reduced Arrhenius law (right). Reaction rates are calculated with the resolved variables (solid line) and the test-filtered variables (dashed line). The progress variable for the reduced Arrhenius law is calculated from temperature.* $\widehat{\Delta} = 1.5 \times 10^{-2}$

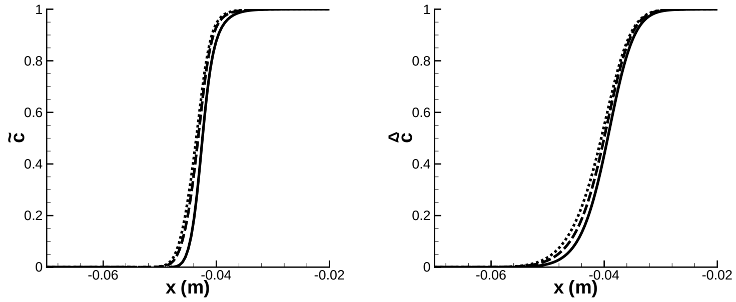

Figure 3.6 : *Comparison of the progress variables calculated with different field variables. Use of* $Y_{C_3H_8}$ *(solid line),* Y_{O_2} *(dashed line) and temperature (dotted line)*

Reaction model	Boger ($Y_{C_3H_8}$)	Boger (Y_{O_2})	Boger (T)
thickened flame ($\times 10^{-3}$)	3.17	3.45	3.54
filtered thickened flame ($\times 10^{-3}$)	6.17	6.60	6.87
ratio	1.95	1.91	1.94

Table 3.7 : *Comparison of the integral of the generic reaction rate ($\int W\,dx$). $\widehat{\Delta} = 1.5 \times 10^{-2}$ (m).*

Reaction model	reduced Arrhenius	Arrhenius
thickened flame ($\times 10^{-3}$)	4.82	2.79
filtered thickened flame ($\times 10^{-3}$)	9.06	3.27
ratio	1.88	1.17

Table 3.8 : *Comparison of the integral of the generic reaction rate ($\int W/\alpha\,dx$). $\widehat{\Delta} = 1.5 \times 10^{-2}$ (m).*

tion rate ratios obtained with the reduced Arrhenius law and Boger's algebraic model were close to those obtained in the test for flame thickness as displayed in the left plot of Figure 3.7. (see also Figure 3.3). However, the Arrhenius law always yielded the reaction rate ratio smaller than those obtained in this test. This deviation resulted in the difference of $\overline{\Delta}$ plotted in the right figure of Figure 3.7. The values of $\overline{\Delta}$ with Boger's algebraic model and the reduced Arrhenius law were close to the values of Δ_F obtained from the observation of the flame thicknesses (see again Figure 3.3), but the values of $\overline{\Delta}$ with the Arrhenius law was more than twice as large as Δ_F obtained through the thickness observation. This shows that the thickening of a laminar flame can be approximated by a Gaussian filtering with a filter size of Δ_F, when the reaction rate is calculated with Boger's algebraic model or the reduced Arrhenius law, but the application of the Arrhenius law requires the LES filter size of $\overline{\Delta}$ different from Δ_F obtained from the observation of the flame thickness, thus, the thickened and test-filtered flame thicknesses require different values of the proportionality coefficient α and, the thickening cannot be approximated by the filtering. To assure $\gamma\langle\widehat{W(\widetilde{\mathbf{q}})}\rangle/\langle W(\widehat{\widetilde{\mathbf{q}}})\rangle = 1$, the value of reaction rate ratio obtained here are used as the effective filter size ratio γ in the two-dimensional test in the next section. These values are given in Table 3.9.

The deviation of $\langle W(\widehat{\widetilde{\mathbf{q}}})\rangle/\langle\widehat{W(\widetilde{\mathbf{q}})}\rangle$ with the use of the Arrhenius law was caused by the different Schmidt numbers Sc for each chemical species. The difference of Sc resulted in the difference of the diffusion properties of C_3H_8 and O_2 from that of conduction heat transfer, and the profiles of these variables became different from that of temperature. The deviation among the variables became larger after the application of the test-filter, because the test-filter was mass weighted and contained density that changes with temperature. This causes the difference in the progress variables $\widetilde{c}$ and $\widehat{\widetilde{c}}$ based on the different resolved variables as figure 3.6 displays. Because Arrhenius law uses all of these three resolved variables, temperature, mass fractions of C_3H_8 and O_2, this chemical model was more sensitive to the discrepancy than the other two models tested here. Consequently $\langle W(\widehat{\widetilde{\mathbf{q}}})\rangle$ depended more strongly on the filter size $\widehat{\Delta}$ than the others and it resulted in the discrepancy of the ratio $\langle W(\widehat{\widetilde{\mathbf{q}}})\rangle / \widehat{\langle W(\widetilde{\mathbf{q}})\rangle}$ from the value calculated with other chemical models.

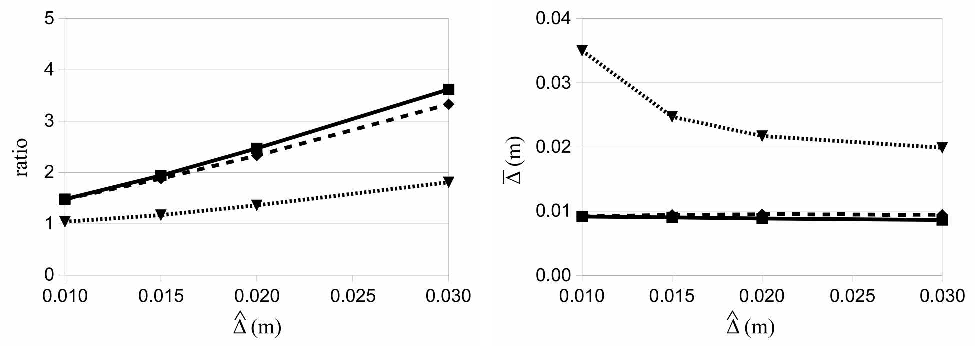

Figure 3.7 : *Ratio of* $\langle W(\widehat{\widetilde{\mathbf{q}}})\rangle / \widehat{\langle W(\widetilde{\mathbf{q}})\rangle}$ *(left) and the LES filter size* Δ_F *(right) to yield* $\gamma \widehat{\langle W(\widetilde{\mathbf{q}})\rangle} / \langle W(\widehat{\widetilde{\mathbf{q}}})\rangle = 1$ *as functions of the test-filter size* $\widehat{\Delta}$*. The reaction rate was calculated with Boger's algebraic model (solid line), the reduced Arrhenius law (dashed line), and the Arrhenius law (dotted line).*

$\widehat{\Delta}$ (m)	1.0×10^{-2}	1.5×10^{-2}	2.0×10^{-2}	3.0×10^{-2}
Boger	1.48	1.94	2.47	3.62
reduced Arrhenius law	1.48	1.88	2.33	3.33
Arrhenius law	1.04	1.17	1.36	1.81

Table 3.9 : *Comparison of* $\langle W(\widehat{\widetilde{\mathbf{q}}})\rangle / \widehat{\langle W(\widetilde{\mathbf{q}})\rangle}$ *calculated with different chemical models and different test-filter size: These ratios are the values of* γ *to obtain* $\gamma \widehat{\langle W(\widetilde{\mathbf{q}})\rangle} / \langle W(\widehat{\widetilde{\mathbf{q}}})\rangle = 1$

Figure 3.8 compares the generic reaction rates of thickened flame and filtered thickened flame as functions of resolved and test-filtered temperature respectively. It can be seen that the maximum value of the reaction rate changes with the Arrhenius law but stays identical with the reduced Arrhenius law. This is because the combination of the values of field variables to yield the maximum reaction rate was different for the thickened and the test-filtered thickened flame in the case of the Arrhenius law. The combinations are $(T(K) \;\; Y_{C_3H_8} \;\; Y_{O_2}) = (1946.87 \;\; 0.0196688 \;\; 0.0513303)$ for non-filtered variables and $(1976.67 \;\; 0.0133326 \;\; 0.0459647)$ for filtered variables.

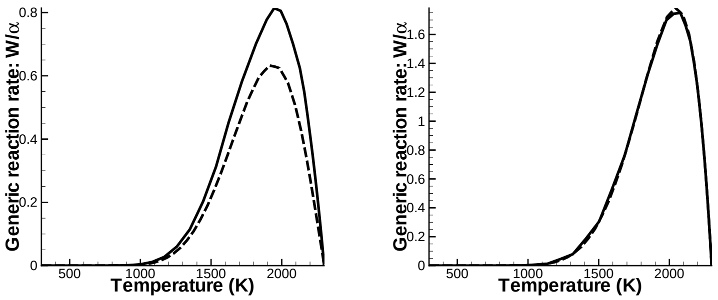

Figure 3.8 : *Comparison of the generic reaction rates of thickened flame and filtered thickened flame: Arrhenius law (left) and reduced Arrhenius law (right): thickened flame (solid line) and filtered flame after thickening (dashed line):* $\widehat{\Delta} = 1.5 \times 10^{-2}$ (m)

3.2.3 Summary

From the obtained results, the observations can be summarized as follows.

- From the observation of the thickness of the thickened and the filtered thickened flame, the thickening of flame and the application of Gaussian filter are not identical. Consequently Equation 3.3, that is based on the application of Gaussian filter, does not yield the exact filter size ratio γ. To obtain a correct γ, an appropriate laminar flame thickness, which depends on the test-filter size $\widehat{\Delta}$, is required.

- For Boger's algebraic model and the Arrhenius law with the progress variable, the value of the laminar flame thickness, δ_l^0, obtained from the comparison of reaction rates of the thickened and the filtered thickened flames gives γ close to the thickness ratio of the thickened and the filtered thickened flames, and also assures the convergence of reaction rate ratio $\gamma\langle\overbrace{W(\widetilde{\mathbf{q}})}\rangle/\langle W(\widehat{\widetilde{\mathbf{q}}})\rangle$ to unity.

- The Arrhenius law is quite sensitive to the difference of the diffusion properties of chemical species and temperature, which is due to the difference in the Schmidt number Sc. γ for $\gamma\langle\overbrace{W(\widetilde{\mathbf{q}})}\rangle/\langle W(\widehat{\widetilde{\mathbf{q}}})\rangle = 1$ was obtained from the test performed in this section, but the value is approximately twice as large as that obtained from the thickness observation.

In the two-dimensional test of the next section, the value of γ is taken from Table 3.9 for each reaction model and each test-filter size.

3.3 Application to a two-dimensional turbulent combustion

The purposes of this test are:

- Observation of the effect of the filter size on the output of the dynamic model
- Observation of the effect of control volume size for the weak form of the dynamic model
- Comparison of the results given by different reaction models

As for the one-dimensional case, the effect of the filter size is an important factor. Since the choice of the filter size affects the calculation of not only the numerator but also the denominator of the formulation (Equation 1.89), its effect on the denominator should be analyzed with a special attention. This test is not possible in the one-dimensional cases where the flow is considered to be laminar.

To apply the weak form of the dynamic model, a control volume must be defined for the calculation of the integral and average. In the one-dimensional cases, the integration is performed across the whole flame front. But in multi-dimensional simulations of a combustion chamber, the integration volume must be clearly defined.

The choice of the reaction model also plays an important role. The dynamic model is theoretically applicable to any kind of reaction model, but it does not mean that the result is independent from the choice of the reaction model. The comparison of the results of different chemical models provides tips for the choice of the reaction model.

3.3.1 Configuration

As an initial test of the implementation of the dynamic procedure to turbulent combustion, a flame was first calculated with Colin's efficiency function (Colin et al. 2000) for reference. Figures 3.9 and 3.10 display the configuration of the computational domain and the computational mesh used in this test respectively. Flow speed at the inlet was set to 5 m/s and that of the coflow was 20 m/s. The flame was stabilized behind a flame holder. Figure 3.11 presents instantaneous resolved fields of this flame. The computation provided the distribution of the resolved variables that enter the dynamic procedure, such as the temperature and the chemical species mass fractions.

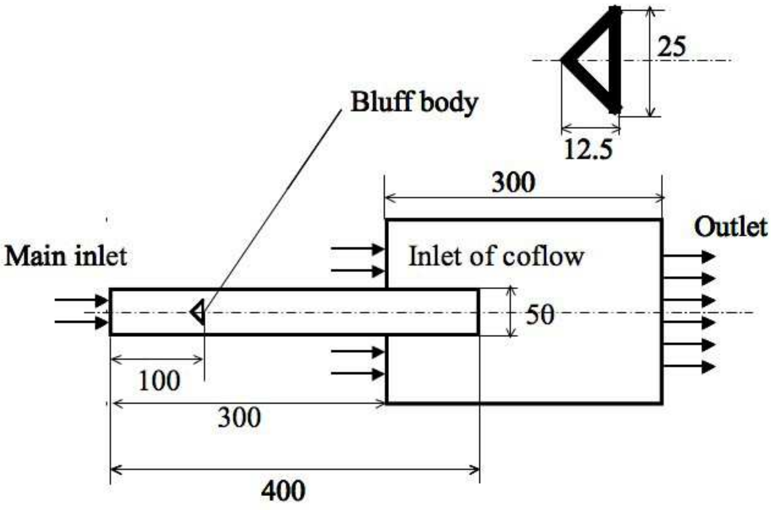

Figure 3.9 : *Configuration of computational domain: All scales are given in mm*

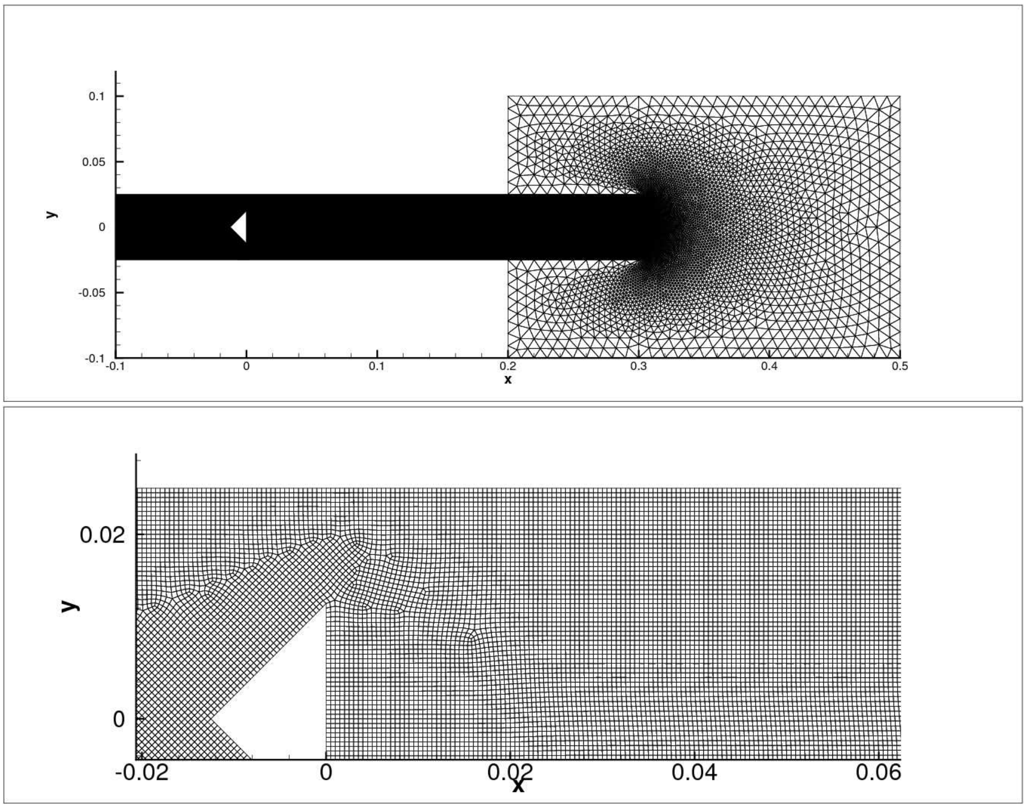

Figure 3.10 : *Computational mesh for two-dimensional simulation (top) and its zoom in the vicinity of the flame holder (bottom). Scales are given in m*

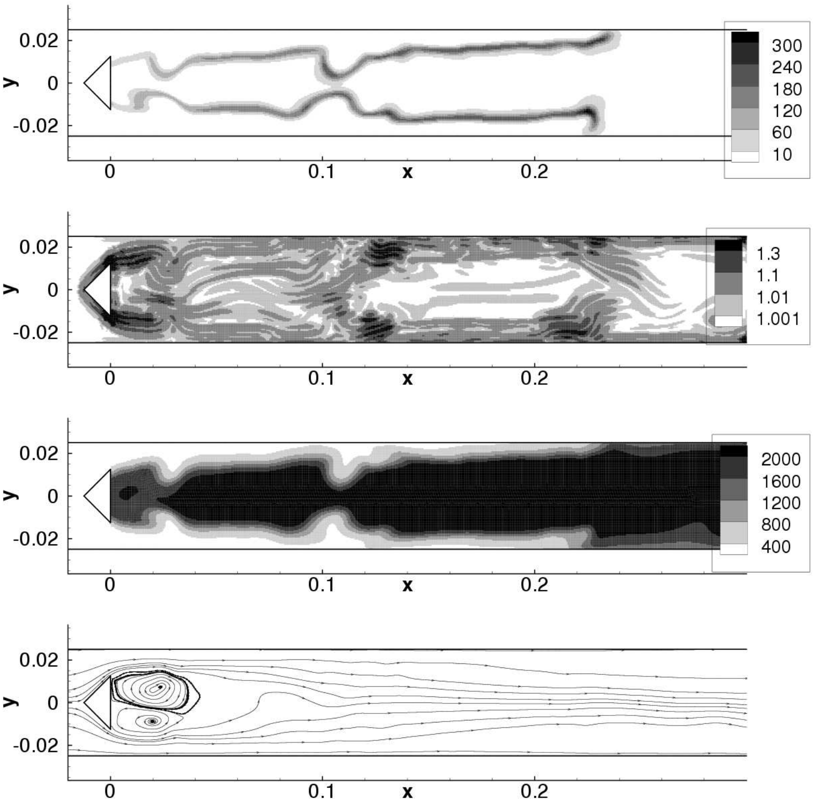

Figure 3.11 : *Instantaneous resolved fields of the flame computed using Colin's model. First reaction rate ($kg/m^3 \cdot s$), efficiency function, temperature (K) and the stream line (top to the bottom) thickening factor $F = 20$.*

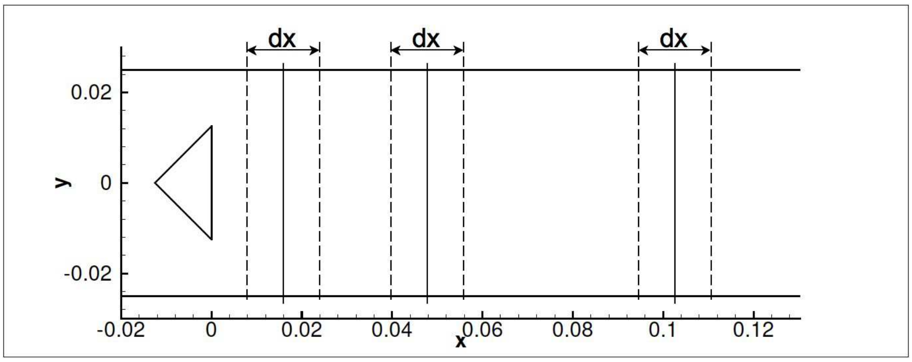

Figure 3.12 : *Definition of the control volume for the integral operation*

The control volume in this test was defined as displayed in Figure 3.12, and contains all the points which is within $[x - dx/2, x + dx/2]$. Accordingly model parameter will depend only on the downstream location..

3.3.2 Results

Effect of filter size

The influence of the filter size was investigated setting the length of the control volume to $0.3\,m$, i.e. the integral operation was completed using the whole combustion chamber downstream of the flame holder. This definition of the control volume allows to evaluate the statistical tendencies of the terms that emerge in the formulation of the dynamic model.

The test-tilter size $\widehat{\Delta}$ has upper and lower limits. The distributions of the generic reaction rate calculated with the reduced Arrhenius law using the filtered variables $W(\widehat{\mathbf{q}})$ are shown in Figure 3.13. The filter size was increased from $\widehat{\Delta} = 1.0 \times 10^{-2}$ m to $\widehat{\Delta} = 3.0 \times 10^{-2}$ m. As the filter size became larger, the distance between the two flame surfaces became shorter and then the surfaces disappear. This makes $\gamma\langle\widehat{W(\widetilde{\mathbf{q}})}\rangle/\langle W(\widehat{\widetilde{\mathbf{q}}})\rangle$ calculated with the reduced Arrhenius law larger and the value of β becomes unphysical large value. So the upper limit of the test-filter size $\widehat{\Delta}$ is about $2.0 \times 10^{-2}\,m$.

The lower limit is restricted by the assumption made in the construction of the dynamic model, $\widehat{\Delta}$ is larger than the flame thickness. Considering the thickness of flame presented in Tables 3.3 to 3.6, the value $\widehat{\Delta} = 1.0 \times 10^{-2}$ m is close to the resolved flame thickness and the assumption is not valid. It is to say that $\widehat{\Delta} = 1.0 \times 10^{-2}$ m is around the lower limit of the test-filter size.

The value of the major terms in the formulation, Equation 1.89, are given in Table 3.10 to 3.13. The subgrid-scale velocity fluctuation at the test-filter level, $u'_{\gamma\Delta}$ is estimated from

$$u'_{\gamma\Delta} = \gamma^{1/3} u'_{\Delta} \tag{3.18}$$

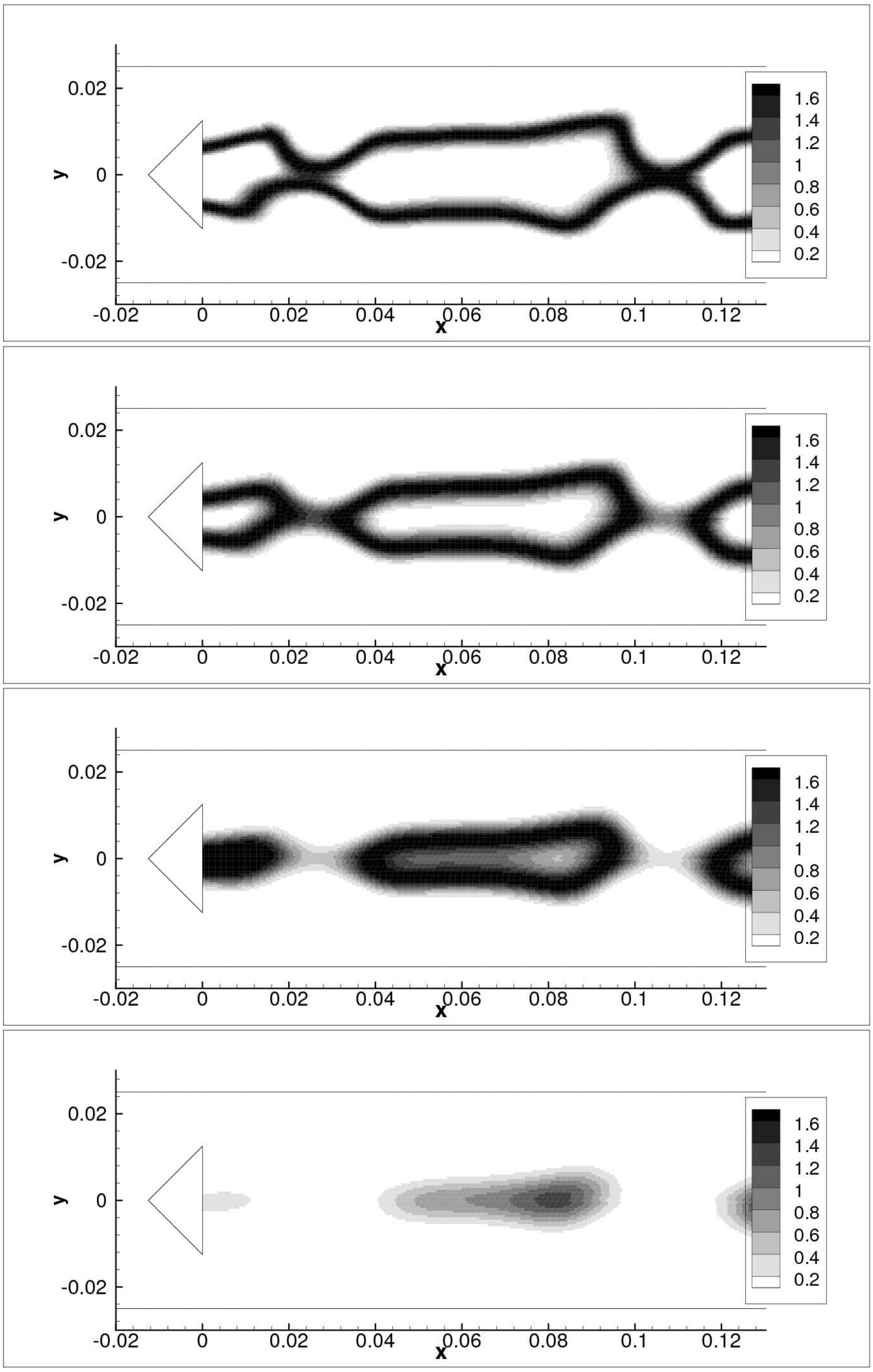

Figure 3.13 : *Effect of the test-filter size on the principal reaction rate calculated with filtered variables. Top to bottom* $\widehat{\Delta} = 1.0 \times 10^{-2}$, $\widehat{\Delta} = 1.5 \times 10^{-2}$, $\widehat{\Delta} = 2.0 \times 10^{-2}$, $\widehat{\Delta} = 3.0 \times 10^{-2}$ *(m), the reaction rates were calculated with reduced Arrhenius law.*

assuming the constant turbulence dissipation rate (Kolmogorov theory, Kolmogorov (1941)),

$$\epsilon = \frac{{u'_{\mathit{\Delta}}}^3}{\mathit{\Delta}} = \frac{{u'_{\gamma\mathit{\Delta}}}^3}{\gamma\mathit{\Delta}}\,. \tag{3.19}$$

All of the intermediate terms presented in Tables 3.10 and 3.11 increased in value with the filter size. The value of the constant β depended on the chemical model. The Arrhenius law yielded negative β when $\widehat{\mathit{\Delta}} \leq 2.0 \times 10^{-2}\,m$. This is because of the low γ value due to the different Schmidt numbers of chemical species as discussed in the previous section. Boger's algebraic model gave β in between five and ten and the value decreased with the filter size $\widehat{\mathit{\Delta}}$. The result of the reduced Arrhenius law also indicated the decreasing tendency of β with $\widehat{\mathit{\Delta}}$. The value changes between 15 and 20. The transition of the efficiency E was similar to that of β. The results of the standard Arrhenius law indicated as 1.00 were actually slightly smaller than unity because β is negative, but they are larger than 0.995 and indicated as 1.00.

Alternative formulation

Although some tendencies were observed in the results presented above, the values of β were extremely high. β is theoretically of the order of $D-2$, where D is the fractal dimension of the flame surface. This was caused by the fact that the ratio of $1+\min[F, \Gamma_{\underline{\mathit{\Delta}}}\langle u'_{\underline{\mathit{\Delta}}}\rangle/S_L]$ and $1+\min[\gamma F, \Gamma_{\gamma\underline{\mathit{\Delta}}}\langle u'_{\gamma\underline{\mathit{\Delta}}}\rangle/S_L]$ was close to unity (see Table 3.11). Then, the log operator in Equation 1.89, provided a value approximately zero and the value of β became large. In fact $u'_{\gamma\underline{\mathit{\Delta}}}$ was probably poorly estimated. To avoid this problem, an alternative formulation is tested. This formulation suppose that the ratio of the turbulence strengths at the two scales is approximated by the filter size ratio.

$$\frac{1+\min\left[\frac{\gamma\mathit{\Delta}}{\delta_l^{\mathrm{o}}}, \mathbf{\Gamma}\frac{\langle u'_{\gamma\mathit{\Delta}}\rangle}{s_l^0}\right]}{1+\min\left[\frac{\mathit{\Delta}}{\delta_l^{\mathrm{o}}}, \mathbf{\Gamma}\frac{\langle u'_{\mathit{\Delta}}\rangle}{s_l^0}\right]} \approx \gamma\,. \tag{3.20}$$

and β is calculated as

$$\beta = 1 + \frac{\log\left(\dfrac{\overbrace{W_{\mathit{\Delta}}(\widetilde{\mathbf{q}})}}{W_{\gamma\mathit{\Delta}}\left(\widehat{\widetilde{\mathbf{q}}}\right)}\right)}{\log(\gamma)}\,, \tag{3.21}$$

which is the same expression as Equation 1.86, and the efficiency E is obtained from

$$E = \left(1+\min\left[\frac{\mathit{\Delta}}{\delta_l^{\mathrm{o}}}, \mathbf{\Gamma}\frac{u'_{\mathit{\Delta}}}{s_l^0}\right]\right)^{\beta}\,. \tag{3.22}$$

$\widehat{\Delta}$ (m)	1.0×10^{-2}	1.5×10^{-2}	2.0×10^{-2}
Boger (C_3H_8)	1.082	1.135	1.178
Reduced Arrhenius law	1.160	1.280	1.430
Arrhenius law	0.850	0.831	0.844

Table 3.10 : *Comparison of* $\gamma\langle\overbrace{W(\widetilde{\mathbf{q}})}\rangle/\langle W(\widehat{\mathbf{q}})\rangle$ *calculated with the averaged variables in whole domain with different chemical models and different test-filter size:* γ *was taken from table 3.9 for each chemical reaction model.*

$\widehat{\Delta}$ (m)	1.0×10^{-2}	1.5×10^{-2}	2.0×10^{-2}
Boger (C_3H_8)	1.008	1.017	1.026
Reduced Arrhenius law	1.008	1.015	1.023
Arrhenius law	1.000	1.001	1.003

Table 3.11 : *Comparison of* $(1+\min\left[\gamma F, \Gamma_{\gamma\overline{\Delta}}\langle u'_{\gamma\overline{\Delta}}\rangle/S_L\right])/(1+\min\left[F, \Gamma_{\overline{\Delta}}\langle u'_{\overline{\Delta}}\rangle/S_L\right])$ *in the denominator of the dynamic formulation (Equation 1.89) calculated with the averaged variables in whole domain.* $1+\min[F, \Gamma_{\overline{\Delta}}\langle u'_{\overline{\Delta}}\rangle/S_L] = 1.017$, $u'_{\overline{\Delta}}$ *was calculated from* $u'_{\gamma\overline{\Delta}} = \gamma^{1/3}u'_{\overline{\Delta}}$, γ *was taken from table 3.9 for each chemical reaction model.*

$\widehat{\Delta}$ (m)	1.0×10^{-2}	1.5×10^{-2}	2.0×10^{-2}
Boger (C_3H_8)	9.45	7.66	6.37
Reduced Arrhenius law	17.56	16.03	15.40
Arrhenius law	−0.16	−0.19	−0.17

Table 3.12 : *Comparison of* β *calculated with the averaged variables in whole domain.* γ *was taken from table 3.9 for each chemical reaction model.*

$\widehat{\Delta}$ (m)	1.0×10^{-2}	1.5×10^{-2}	2.0×10^{-2}
Boger (C_3H_8)	1.18	1.14	1.12
Reduced Arrhenius law	1.35	1.32	1.30
Arrhenius law	1.00	1.00	1.00

Table 3.13 : *Comparison of* E *calculated with the averaged variables in whole domain.* γ *was taken from table 3.9 for each chemical reaction model.*

Tables 3.14 and 3.15 are the values of β and the efficiency, E, calculated with the averaged variables in the whole combustion chamber. The value of β remained lower than unity and the order was similar to the value reported by Charlette et al. (2002b) except when using the Arrhenius law. This unexpected negative values of β with Arrhenius law was caused by low γ obtained in the one-dimensional test. The value of β did not significantly change with the test-filter size $\widehat{\Delta}$ compared to the results of the original formulation and the values of the efficiency were almost constant when $\widehat{\Delta} \leq 2.0 \times 10^{-2}\, m$.

$\widehat{\Delta}$ (m)	1.0×10^{-2}	1.5×10^{-2}	2.0×10^{-2}
Boger (C_3H_8)	0.202 (1.48)	0.190 (1.94)	0.181 (2.47)
reduced Arrhenius law	0.376 (1.48)	0.390 (1.88)	0.423 (2.33)
Arrhenius law	−4.148 (1.04)	−1.200 (1.17)	−0.540 (1.36)

Table 3.14 : *Comparison of β calculated by the alternative formulation with the averaged variables in the whole domain. The values of γ used in the calculation are shown in brackets. They were taken from Table 3.9 for each chemical reaction model.*

$\widehat{\Delta}$ (m)	1.0×10^{-2}	1.5×10^{-2}	2.0×10^{-2}
Boger (C_3H_8)	1.003	1.003	1.003
reduced Arrhenius law	1.007	1.007	1.007
Arrhenius law	0.970	0.991	0.996

Table 3.15 : *Comparison of E calculated by the alternative formulation with the averaged variables in the whole domain. γ was taken from Table 3.9 for each chemical reaction model.*

Effect of the control volume size for integration

The control volume should be broader than the flame thickness calculated with filtered variables. Since the thickness is verified to be around 2.0×10^{-2} m when $\widehat{\Delta} = 1.5 \times 10^{-2}$ m (see Table 3.4) in laminar case, the minimum width of the control volume with this test-filter size is, then, expected to be at least 4.0×10^{-2} m.

The influence of the control volume size is shown in Figure 3.14, which displays the constant β and the efficiency E as functions of the x coordinate. On the left are the results calculated with Boger's algebraic model and on the right are those calculated with the reduced Arrhenius law. $\widehat{\Delta}$ was set to 1.5×10^{-2} m. The fluctuations of β and the efficiency decay with the increase of the control volume size, but the general tendency that β increases with x and the positions of undulations are not altered.

In the results from tests of small control volume sizes ($dx \leq 1.0 \times 10^{-2}\, m$), several minor peaks can be seen. This is a typical result that occurs when the control volume size is not large enough. They decreased in the result of $dx = 4.0 \times 10^{-2}\,m$.

At $x \approx 0.11\,m$, the values of β calculated with the reduced Arrhenius law have a major peak when the control volume size is small, but no longer exist in the result of $dx > 4.0 \times 10^{-2}$ m. These peaks stand at the position where the two flame surfaces approach each other, and $W(\widehat{\mathbf{q}})$ takes small value. Though it is not so steep, a peak is also found in the result calculated with Boger's algebraic model at the same position. The use of a large control volume suppresses the emergence of such peaks caused by the approaching surfaces.

In spite of the different control volume sizes, all results indicate the same order of the efficiency E and the same tendency that it gradually increases with the distance from the flame holder. Considering the fact that the result of small control volume contains oscillations of β and E, and that that of a large control volume loses the local information, $dx = 4.0 \times 10^{-2}\,m$ is a reasonable control volume width. Though β takes slightly negative values at some points, it is limited in the zones, where the flame wrinkling is weak (see Figure 3.11), and the values of E are quite close to unity. In the simulations of the following chapters, $dx = 4.0 \times 10^{-2}\,m$ is then chosen for the control volume size.

Comparison of the chemical models

As shown in Tables 3.14 and 3.15, the Arrhenius law yields negative values of β and the efficiency becomes lower than unity. Boger's algebraic model yielded smaller values of the constant β than the reduced Arrhenius law did.

The negative value of β calculated by the Arrhenius law was caused by small γ obtained in the one-dimensional tests. The value obtained in the one-dimensional test was too small to be used in turbulent simulations, and resulted in the negative β values. This infers that the condition of diffusion of chemical species in the two-dimensional turbulent case differed from that in the laminar one-dimensional case. The value of γ obtained in the previous section is not the "correct" value for the test performed in this section.

The difference of β between the results obtained by using Boger's model and the reduced Arrhenius law is due to the smaller value of $\gamma\langle\overbrace{W(\widetilde{\mathbf{q}})}\rangle/\langle W(\widehat{\mathbf{q}})\rangle$ as presented in Table 3.10. Though the value of γ for the reduced Arrhenius law, taken from Table 3.9, was smaller than that for Boger's algebraic model, the reduced Arrhenius law yielded larger ratio of $\gamma\langle\overbrace{W(\widetilde{\mathbf{q}})}\rangle/\langle W(\widehat{\mathbf{q}})\rangle$, and provided larger β. This is related to the geometry of the flame surface.

As shown in Figures 2.6 and 2.4 of Chapter 2, the reaction rate calculated through the reduced Arrhenius law leans towards the side of higher progress variable, compared to that calculate through Boger's algebraic model. Then the ratio $\langle\overbrace{W(\widetilde{\mathbf{q}})}\rangle/\langle W(\widehat{\mathbf{q}})\rangle$ becomes large when the flame surface is convex against the unburned gas, and small when it is concave, because, as Figure 3.15 shows,

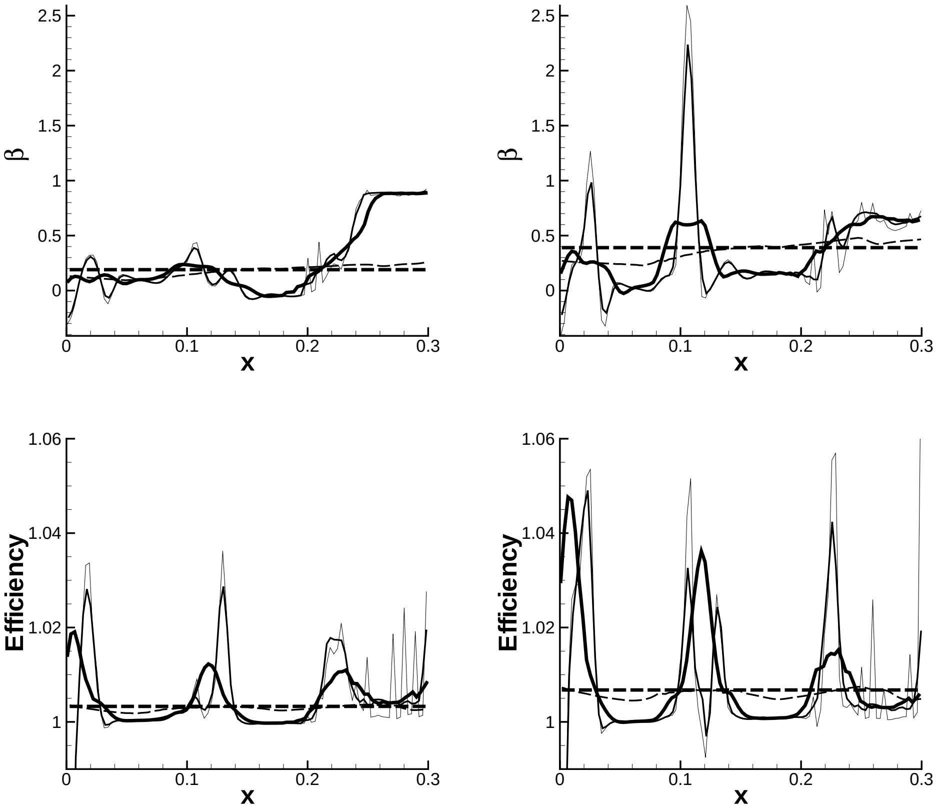

Figure 3.14 : *Effect of the control volume size on* β *and the efficiency* E*. The reaction rates are calculated with Boger's algebraic model (left) and the reduced Arrhenius law (right).* $dx = 2.0 \times 10^{-3}$ *m (narrow solid line),* $dx = 1.0 \times 10^{-2}$ *m (solid line),* $dx = 4.0 \times 10^{-2}$ *m (bold solid line),* $dx = 1.5 \times 10^{-1}$ *m (narrow dashed line), and the result of the use of the whole zone behind flame holder as one control volume (bold dashed line).*

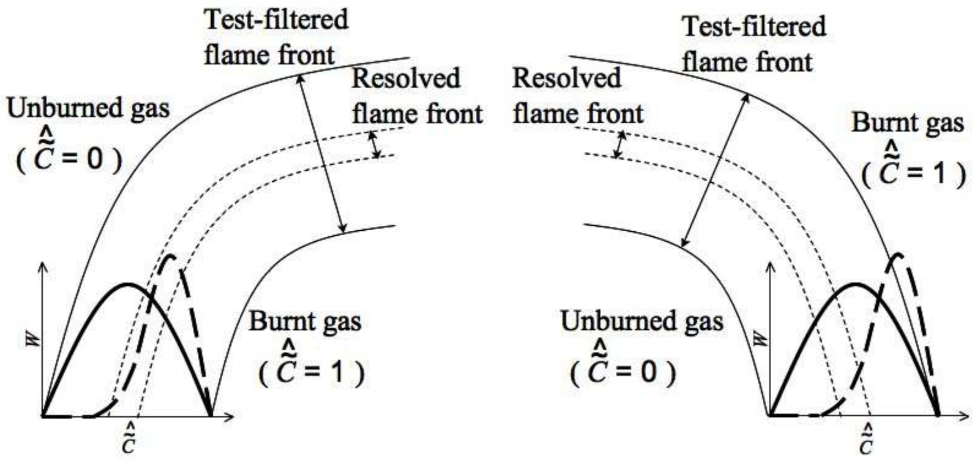

Figure 3.15 : *Influence of the chemical model used in the dynamic thickened flamelet model. Convex (left) and concave (right) to fresh gas cases. The two bold lines represent the reaction rate calculated with Boger's algebraic model (solid line) and the reduced Arrhenius law (dashed line).*

the area, where the filtered progress variable is high, becomes smaller/larger when the flame surface is convex/concave and $\langle W(\widehat{\widetilde{\mathbf{q}}})\rangle$ becomes smaller/larger than a planar flame surface per unit length along the surface. This effect of the geometry of the flame surface is not significant with Boger's algebraic model, because the distribution of the reaction rate against the progress variable is centered at $\overline{c} = 0.5$.

In the flame used for the two-dimensional test, the flame surface was rather convex against the unburned gas, and the reaction rate ratio, $\gamma\langle\widehat{W(\widetilde{\mathbf{q}})}\rangle/\langle W(\widehat{\widetilde{\mathbf{q}}})\rangle$, calculated through the reduced Arrhenius law became larger than that calculated through Boger's algebraic model as shown in Table 3.10. The sensitivity of the reduced Arrhenius law to the geometry of the flame surface can also be seen in Figure 3.14. The oscillation of β and the efficiency are more significant in the results calculated with the reduced Arrhenius law than in those calculated with Boger's algebraic model.

Summary

The results of two-dimensional test case are summarized as follows.

- The test-filter size $\widehat{\Delta}$ must be in the range of $1.0 \times 10^{-2} < \widehat{\Delta} < 2.0 \times 10^{-2}$ (m) in the configuration of this study. If the test-filter size is smaller than this range, it is close to the thickness of flame calculated with test-filtered variables. This condition is out of the assumption of $\widehat{\Delta} > F\delta_l^0$. A test-filter size larger than this range let the two flame surfaces approach to each other and make them into one flame or the flame surfaces disappear. The test-filter size $\widehat{\Delta}$ is then fixed at $\widehat{\Delta} = 1.5 \times 10^{-2}$ (m) in the multi-dimensional simulations in the following chapters.

- The control volume size for the integration and the averaging is fixed to 2.0×10^{-2} (m). The volume smaller than this size causes strong oscillation of the constant β and the larger volume loses local information.

- Application of the Arrhenius law in the calculation of the constant of Charlette, β, is not preferred. The dynamic procedure with this chemical model predicts negative values of the constant β. It is related to the low γ obtained in the one-dimensional tests due to the difference of the Schmidt number Sc. Boger's algebraic model and reduced Arrhenius law are, then, implemented in the multi-dimensional simulation.

- The reduced Arrhenius law is more sensitive to the geometry of the flame surface than Boger's algebraic model. It causes the oscillation of β and the efficiency, which is more remarkable than that observed in the results of Boger's algebraic model.

3.4 Test of the dynamic Smagorinsky model

Test for the dynamic Smagorinsky model

To observe the impact of the dynamic Smagorinsky model, the standard dynamic Smagorinsky model and that with Moin's procedure (Moin et al. 1991) are applied to the one-dimensional thickened laminar flame and the two-dimensional turbulent flame presented in the previous chapters. The tests are performed by changing the filter size for the filtering process, employed in the model.

Figure 3.16 displays profiles of the one-dimensional thickened laminar flame. The profiles are similar to those obtained in Chapter 2 (see Figures 2.3, 2.7, and 2.5). The reaction rate is lower than in the profiles of the previous chapter because the flame is thickened by a factor of 20, and the reaction rate is divided by 20.

Both the standard dynamic Smagorinsky model and that based on Moin's procedure are applied to this flame. To suppress the oscillation and to avoid the divergence of the Smagorinsky constant, a small damping factor $D = 1.0 \times 10^{-3} (m^4/s^4)$ is added to the denominator of Equation 1.63.

$$C_S = \frac{1}{2} L_{ij} M_{ij} / (M_{ij}^2 + D) \tag{3.23}$$

This value selected is the minimum required to suppress the oscillation of the Smagorinsky constant, C_S, outside of the reaction zone, where the flow is laminar and C_S is zero. The value of D is kept the same for all cases tested here. A comparison of the output of the two models is displayed in Figure 3.17. The test-filter size, $\widehat{\Delta}_S$, was changed from 1.0×10^{-3}, 2.5×10^{-3}, to 5.0×10^{-3} (m), corresponding to $\widehat{\Delta}_S = 2\overline{\Delta}$, $\widehat{\Delta}_S = 5\overline{\Delta}$, and $\widehat{\Delta}_S = 10\overline{\Delta}$, where $\overline{\Delta}$ is the grid size of the computational mesh. As for the one-dimensional test of the previous chapter, both models yielded negative constant C_S, i.e. the unresolved momentum transport occurs in the direction opposite to its gradient. The absolute value of the Smagorinsky constant is larger than in Chapter 2, but turbulent stresses are smaller. This is caused by the thickening of the flame that decreased the velocity gradient. This effect is also observed in the previous chapter as displayed in Figure 2.21.

Except for the result of $\widehat{\Delta}_S = 1.0 \times 10^{-3}$ (m), the outputs of the standard dynamic Smagorinsky and that of Moin's procedure do not notably differ. The width of the zone where negative C_S was predicted grows with the test-filter size $\widehat{\Delta}_S$, but the absolute value of the Smagorinsky constant did not change significantly with it. The results for $\widehat{\Delta}_S = 2.5 \times 10^{-3}$ (m) are very similar in both cases.

The difference between the two models was considerable when $\widehat{\Delta}_S = 1.0 \times 10^{-3}$ (m). Both results show large C_S values in the middle of the flame compared to the other $\widehat{\Delta}_S$. This is due to the fact that the terms L_{ij} and M_{ij} contain density $\overline{\rho}$ when Moin's procedure is applied. As the density decreases by a factor of about six across the flame, the orders of M_ij and L_ij also reduce to one sixth through the flame, and those of the products, $L_{ij}M_{ij}$ and M_{ij}^2 reduce to approximately 1/36. When the filter size $\widehat{\Delta}_S$ is small, the values of $L_{ij}M_{ij}$ and M_{ij}^2 in the burnt side become of the same order of the magnitude as the values calculated in the laminar zone, then damped by D.

The results presented here show that the standard dynamic Smagorinsky model and Moin's procedure predict similar values of the turbulent stresses in the flame. If negative turbulent stresses are clipped at zero in simulations to avoid numerical instabilities, the two models are expected to yield quite similar results.

To observe the effect of the filter size $\widehat{\Delta}_S$ in a configuration similar to the simulation of turbulent combustion, the models were applied to the two-dimensional turbulent flame displayed in Figure 3.11. The prediction of the Smagorinsky constant C_S and the turbulent viscosity μ_t given by the standard dynamic Smagorinsky model in the two-dimensional turbulent combustion is presented in Figure 3.18. This result is calculated with $\widehat{\Delta}_S = 2.5 \times 10^{-3}$ (m). It indicates that the negative C_S zone widely exists around the reaction zone. Similar distribution of C_S were obtained by changing the filter size $\widehat{\Delta}_S$ and also by applying Moin's procedure. To compare the results of the standard dynamic

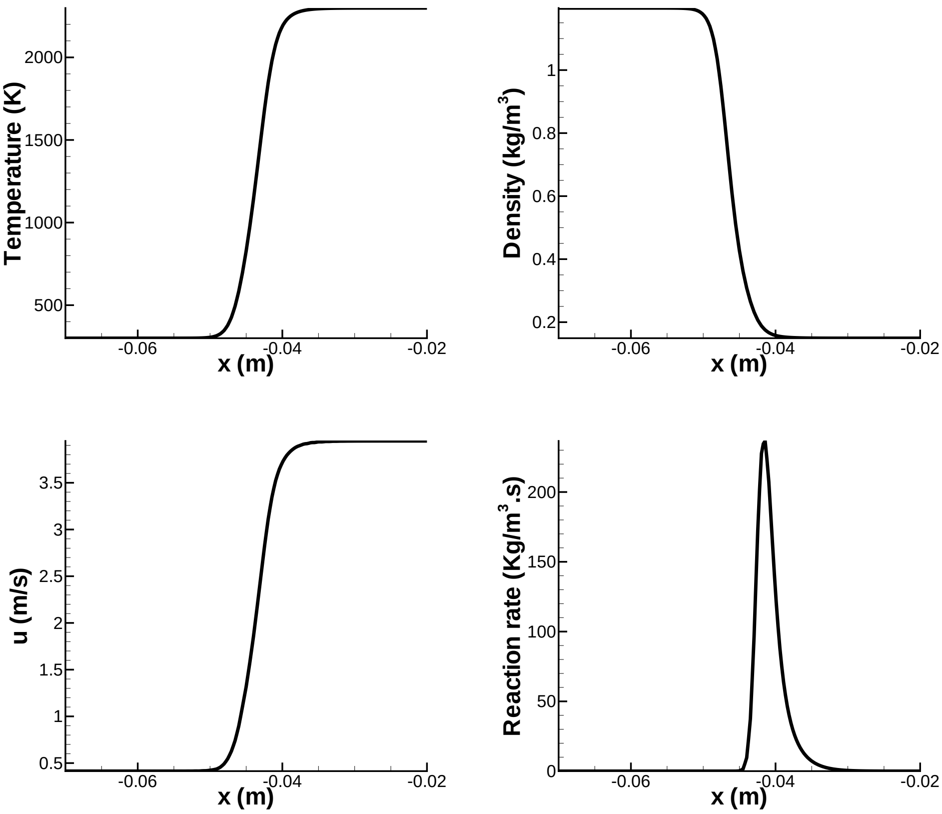

Figure 3.16 : *Profiles in a laminar one-dimension flame. Temperature, density, velocity, and the reaction rate. Thickening factor* $F = 20$.

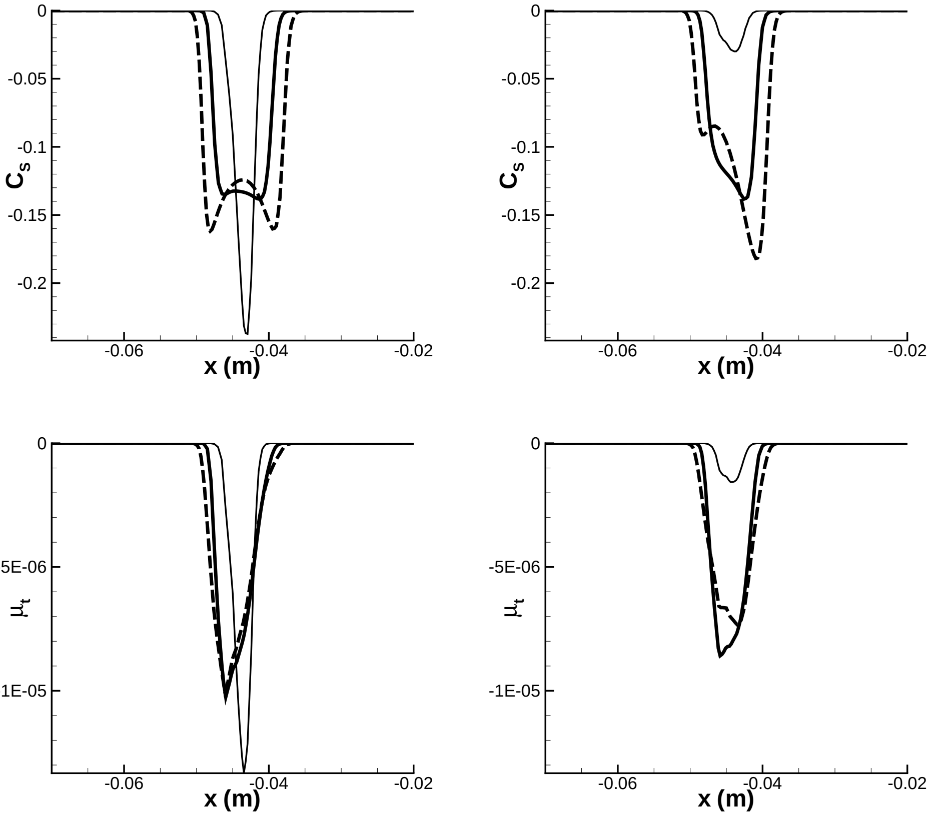

Figure 3.17 : *The Smagorinsky constant C_S and the turbulent viscosity μ_t calculated with the Smagorinsky model (left) and Moin's procedure (right) in a laminar one-dimensional flame. $\widehat{\Delta}_S = 1.0 \times 10^{-3}$ m (narrow solid line), $\widehat{\Delta}_S = 2.5 \times 10^{-3}$ m (bold solid line), and $\widehat{\Delta}_S = 5.0 \times 10^{-3}$ m (dashed line).*

Smagorinsky model and that of Moin's procedure, cross sections at several x coordinate are presented in Figures 3.19 and 3.20.
In the case of $\widehat{\Delta}_S = 1.0 \times 10^{-3}$ (m), a strong oscillation of the Smagorinsky constant C_S was observed in both cases of the standard Smagorinsky model and Moin's model. It is hard to distinguish a specific trend due to the difference in the formulation, however, the oscillation was sharper with the standard model. This oscillation declined as the test-filter size $\widehat{\Delta}_S$ increased. When the test-filter size, $\widehat{\Delta}_S$, was larger than $\widehat{\Delta}_S > 1.25 \times 10^{-3}$ (m), a negative constant C_S was found only in the area where density change occurred. $\widehat{\Delta}_S = 2.5 \times 10^{-3}$ (m) gave approximately same results with both models, with the main discrepancy being the height of the negative peaks observed in the result of Moin's procedure. Similar to the result of the laminar case shown in Figure 3.17, these peaks were found at the edges of the zone where the density change started or finished. These peaks affected the field of the turbulent viscosity μ_t, however, the middle row of Figure 3.20 shows the effect to be mild.
The use of $\widehat{\Delta}_S = 5.0 \times 10^{-3}$ (m) increased the difference between the two models. In the result of the standard model, the variations of the C_S field were more gentle, and the widths of each "cavity" were larger than the case of $\widehat{\Delta}_S = 2.5 \times 10^{-3}$ (m). The result of Moin's procedure also showed the expansion of the "cavity" size, but also indicated the apparition of negative peaks that did not exist in the result of $\widehat{\Delta}_S = 2.5 \times 10^{-3}$ (m).
These results infer that the density change through the flame does not significantly affect the dynamic calculation of the Smagorinsky constant, if $\widehat{\Delta}_S = 2.5 \times 10^{-3}$ (m) is applied. This can be explained by the relation of test-filter size $\widehat{\Delta}_S$ and the flame thickness. If the density change in the range of the test-filter size is not large, $\overline{\rho}$ may be considered to be constant and the formulation of Moin's model reduces to the standard dynamic Smagorinsky model. This case corresponds to the result calculated with $\widehat{\Delta}_S = 2.5 \times 10^{-3}$ (m). If $\widehat{\Delta}_S$ is larger than the flame thickness, $\overline{\rho}$ is no longer constant in the range of the test-filter size, and the outputs of the two models are different. This is observed in the result of $\widehat{\Delta}_S = 5.0 \times 10^{-3}$ (m), and typically occurs if the dynamic Smagorinsky model is applied to a flame without thickening. In that situation Moin's model is more appropriate than the standard model. In our study, however, the flame is thickened by a factor of 20 and the dilatation effect was not significant in terms of the calculation of the Smagorinsky constant.

Summary

As mentioned above, a small test-filter, $\widehat{\Delta}_S$, causes a strong oscillation in the C_S field and a large test-filter enlarges the zone where C_S takes negative values. Conventionally, the oscillation of the dynamically determined Smagorinsky constant is eliminated by, a) averaging in the direction where the turbulence is considered to be homogeneous, or b) filtering if such a direction does not exist.

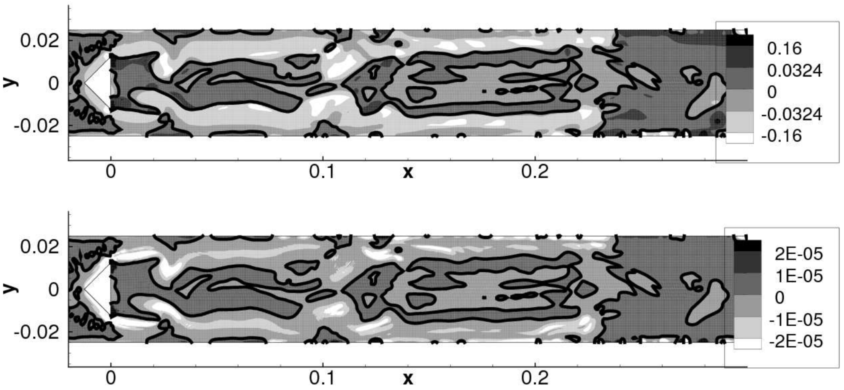

Figure 3.18 : *Fields of the Smagorinsky constant* C_S *(top) and the turbulent viscosity* μ_t *(bottom) calculated with the standard dynamic Smagorinsky model. Test-filter size* $\widehat{\Delta}_S$ *is set to* 2.5×10^{-3} *(m). The solid lines correspond to the contours of* 0.

In the present study, averaging is possible in three-dimensional simulations in the depth direction (on z axis), but in two-dimensional simulations, the z axis does not exist and the filtering is the sole choice. The result of the filtering depends on the filter size. The test-filter is commonly applied several times until the oscillation reduces to a reasonable level, but this procedure is not siginificantly different from using a large test-filter for the calculation of the constant C_S. The only limitation of the test-filter size is that $\widehat{\Delta}_S < l_t$, where l_t is the integral length scale and $l_t \sim 1.0 \times 10^{-2}$ (m) in our configuration. Then $\widehat{\Delta}_S = 2.5 \times 10^{-3}$ (m) is a reasonable value.
It is well verified that the subgrid-scale flux of momentum opposite to its gradient takes place in the flame and that dynamic Smagorinsky model is able to predict it. However, it is not desirable and should be avoided in the simulation because the implementation of negative turbulent stresses may cause numerical instabilities. For this reason, negative values of the Smagorinsky constant are set to zero in the multi-dimensional simulations of the following chapters.

3.5 Conclusion

From the test cases performed in this chapter, following points came to light:

- For the dynamic thickened flamelet model, the equation that gives the filter size ratio of Gaussian filter,

$$\gamma = \sqrt{\left(\frac{\widehat{\Delta}}{F\delta_l^0}\right)^2 + 1} \tag{3.24}$$

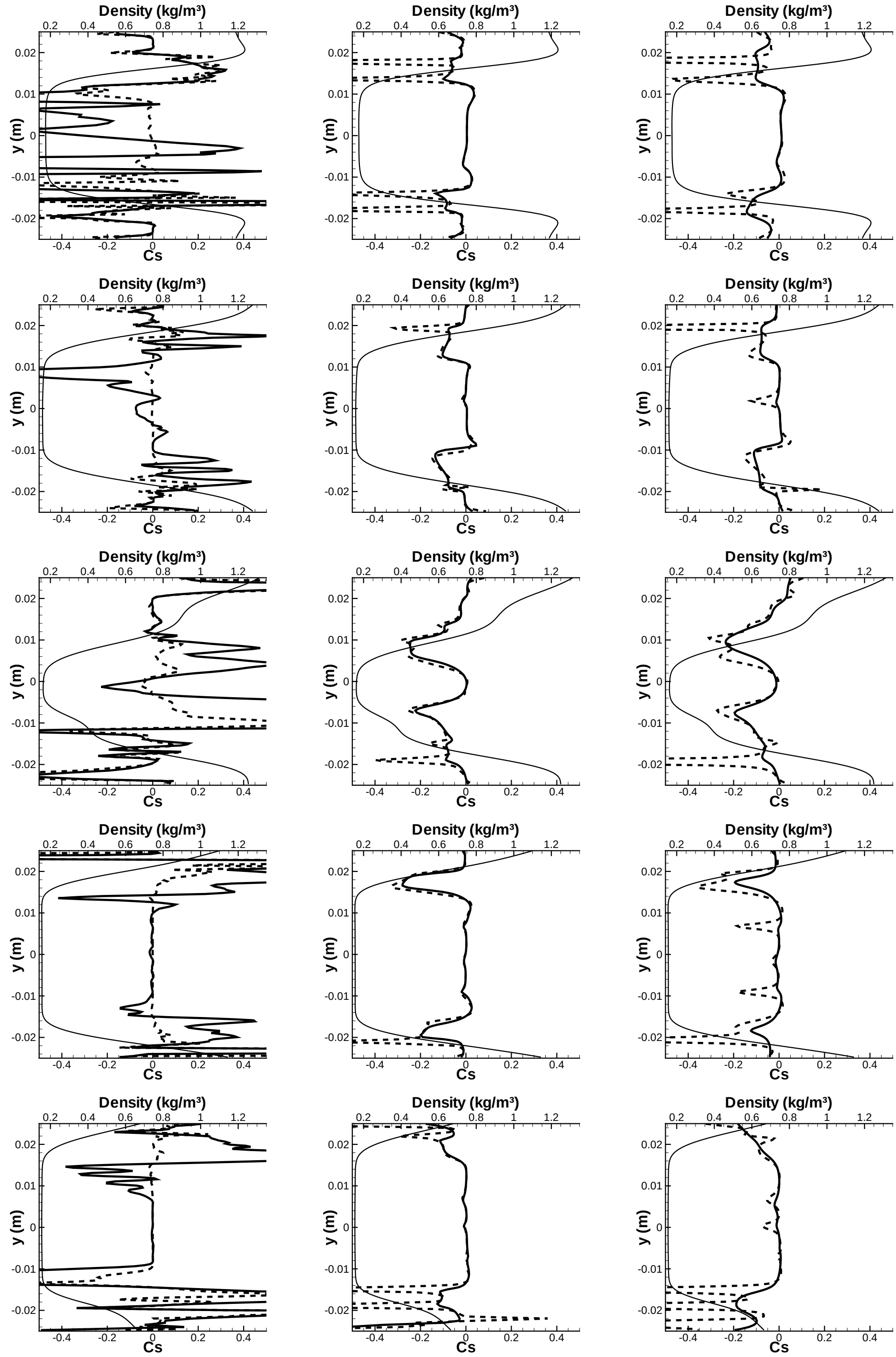

Figure 3.19 : *Cross sectional view of the Smagorinsky constant C_S calculated with the dynamic Smagorinsky model (bold solid line) and Moin's procedure (dashed line).* $\widehat{\Delta}_S = 1.0 \times 10^{-3}$ *(m) (left),* $\widehat{\Delta}_S = 2.5 \times 10^{-3}$ *(m) (center), and* $\widehat{\Delta}_S = 5.0 \times 10^{-3}$ *(m) (right) at* $x = 0.01$, $x = 0.06$, $x = 0.11$, $x = 0.16$, *and* $x = 0.21$ *from top to bottom. Density (narrow solid line) is added to visualize the density change.*

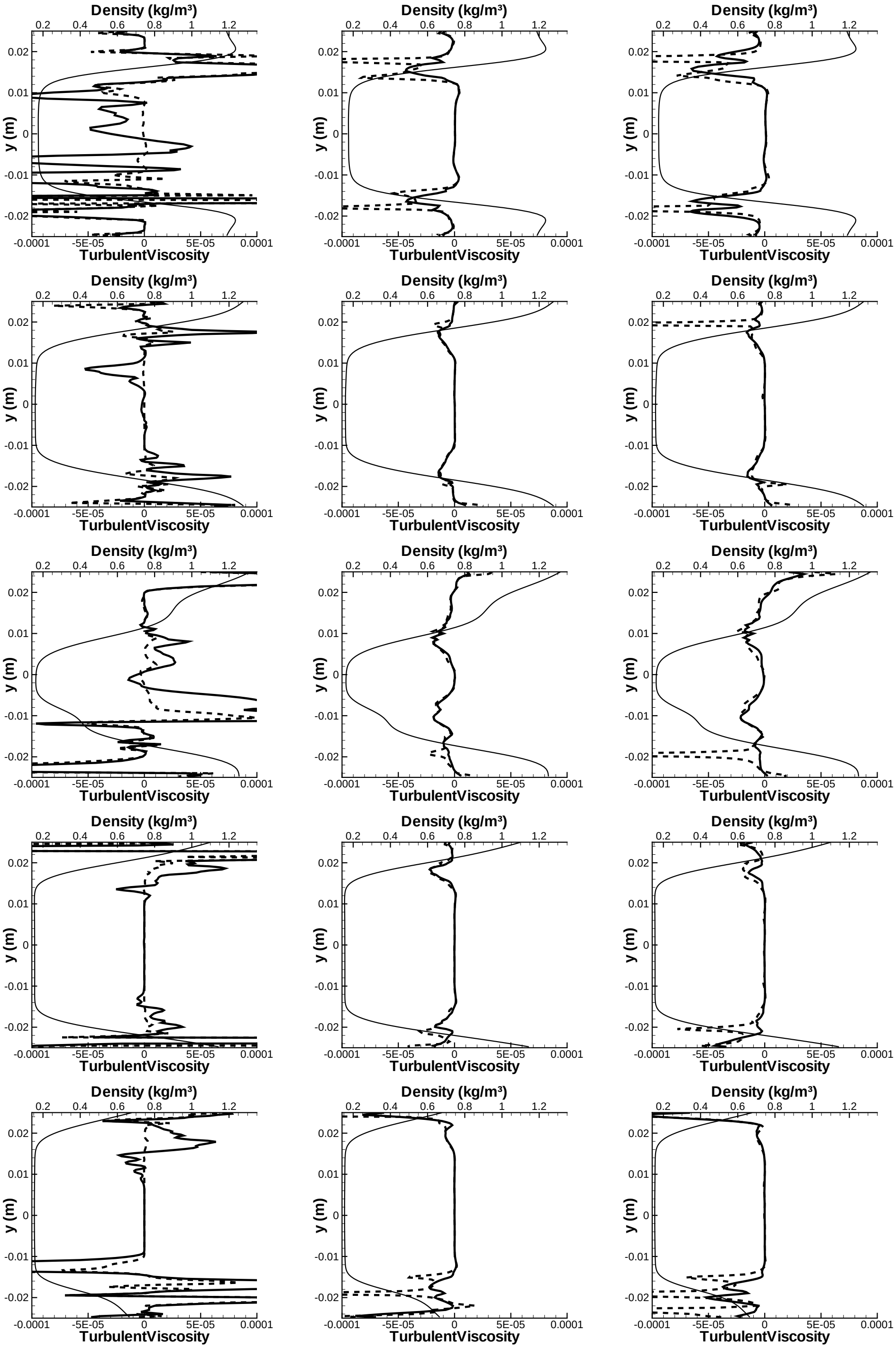

Figure 3.20 : *Cross sectional view of the turbulent viscosity* μ_t *calculated with the dynamic Smagorinsky model (bold solid line) and Moin's procedure (dashed line):* $\widehat{\Delta}_S = 1.0 \times 10^{-3}$ *m (left),* $\widehat{\Delta}_S = 2.5 \times 10^{-3}$ *m (center), and* $\widehat{\Delta}_S = 5.0 \times 10^{-3}$ *m (right) at* $x = 0.01$, $x = 0.06$, $x = 0.11$, $x = 0.16$, *and* $x = 0.21$ *from top to bottom. Density (narrow solid line) is added to visualize the density change.*

is not exact, but gives a good approximation, when a correct value of δ_l^0, which depends on the test-filter size and the chemical reaction model, is given. The value for γ obtained from the observation in this chapter is used in the multi-dimensional simulations of the following chapter.

- The Arrhenius law is too sensitive to the difference of diffusion properties of the resolved variables due to the use of different Schmidt numbers, and causes difficulties in the dynamic thickened flamelet model. Boger's algebraic model or the reduced Arrhenius law are preferred.
- The application of the reduced Arrhenius law yields stronger oscillation of the value of the Charlette's constant β than that calculated through the application of Boger's algebraic model. This is due to the sensitivity of the reduced Arrhenius law to the geometry of the flame surface.
- The test-filter size $\widehat{\Delta} = 1.5 \times 10^{-2}$ (m) and the control volume size $dx = 2.0 \times 10^{-2}$ (m) were shown to be the optimal values for the configurations of this study. These values are used in the multi-dimensional simulation.
- For the dynamic Smagorinsky model, the results of the standard model and that of Moin's procedure were not significantly different. They are expected to yield similar results when a negative Smagorinsky constant is clipped to zero. This point is discussed again in the next chapter by applying them to the two-dimensional simulations.
- The test-filter size $\widehat{\Delta}_S = 2.5 \times 10^{-3}$ (m) reduces the oscillation of the C_S field considerably and is smaller than the integral length scale, l_t. This value is, thus, applied to the multi-dimensional simulation.

Chapter 4

Two-dimensional simulation

This chapter presents the results of the two-dimensional simulations performed with the models tested in Chapter 3. Because three-dimensional simulations are numerically too expensive to perform with different numerical conditions, the effect caused by the difference in models is investigated through two-dimensional simulations as a first step in this chapter.

4.1 Introduction

Two-dimensional simulations are a first step towards three-dimensional simulations. Although the structure of the turbulence is three-dimensional and the turbulence energy does not sufficiently dissipate, the low computational costs allows fast comparisons between results of different numerical configurations. This is an important step in the elimination of possible errors, and to determine the best configuration for obtaining realistic results in three-dimensional simulations.

In the next section, the numerical configuration for the two-dimensional simulations is presented. The results of the non-dynamic simulations, i.e., constant β cases are discussed in Section 4.3. This is followed by those of dynamic thickened flamelet model in Section 4.4 and of the combination of dynamic thickened flamelet model and dynamic Smagorinsky model in Section 4.5. The conclusions of this chapter are given in Section 4.6.

4.2 Numerical configuration

In this study, a V-shaped flame anchored behind a triangle flame holder is investigated. For the presentation of the geometry and the computational mesh, the readers are referred to Figures 3.9 and 3.10 in Section 3.3.1. The flame is a premixed flame of propane and air at stoichiometric conditions with a two-step chemical reaction,

$$\begin{aligned} C_3H_8 + 5O_2 &\Longrightarrow 3CO + 4H_2O \\ CO + 1/2O_2 &\Longleftrightarrow CO_2 \end{aligned} \tag{4.1}$$

The reaction rates are calculated through Arrhenius law;

$$\begin{aligned} \dot{\omega}_1 &= A_1 \rho X_{C_3H_8}{}^{\alpha_1} X_{O_2}{}^{\beta_1} \exp\left(-\frac{E_{a_1}}{RT}\right) \\ \dot{\omega}_2 &= A_2 \rho X_{CO_2}{}^{\alpha_2} X_{O_2}{}^{\beta_2} \exp\left(-\frac{E_{a_2}}{RT}\right). \end{aligned} \tag{4.2}$$

The parameters of each reaction are given in Table 4.2.

Parameters	α_i	β_i	A_i(cgs)	$E_{a_i}(cal.mol^{-1})$
Reaction (1)	0.9028	0.6855	2.0×10^{12}	33000
Reaction (2)	1.0	0.5	4.51×10^{10}	12000

Table 4.1 : *Chemical parameters for the reaction rate.*

To reduce the influence of boundary conditions, two co-flows are introduced above and below the outlet of the main flow. The temperature of the inlet gas and the walls of main chamber are set to 300 K. That of the co-flow is 2200 K. The computational mesh consists of two parts, one for the combustion chamber and the other for the inlet of co-flows. The former is filled with relatively fine cells where the maximum cell size is $\Delta \approx 6.0 \times 10^{-4}\ m$, and this part contains about 50,000 cells. In the second part, the cell size is kept fine in the vicinity of the conjunction area with the primary chamber, but the resolution is gradually reduced from this area to the other boundaries to decrease computational costs.

Initial condition

For all simulations performed in this chapter, the initial condition is the same as the one presented in the previous chapter (see Section 3.3.1). The flame was initially defined as a jumping boundary of temperature and chemical species beside the flame holder. This initial flame is superimposed on the flow field that is calculated separately without the flame (Figure 4.1). The flame is then stabilized using Colin's efficiency model (Equation 1.78, Colin et al. (2000)) with a thickening factor of $F = 20$ and a constant of $\alpha = 0.3$, which has been obtained empirically (Gonçalves dos Santos 2007). The initial condition is presented in Figure 3.11 of the previous chapter.

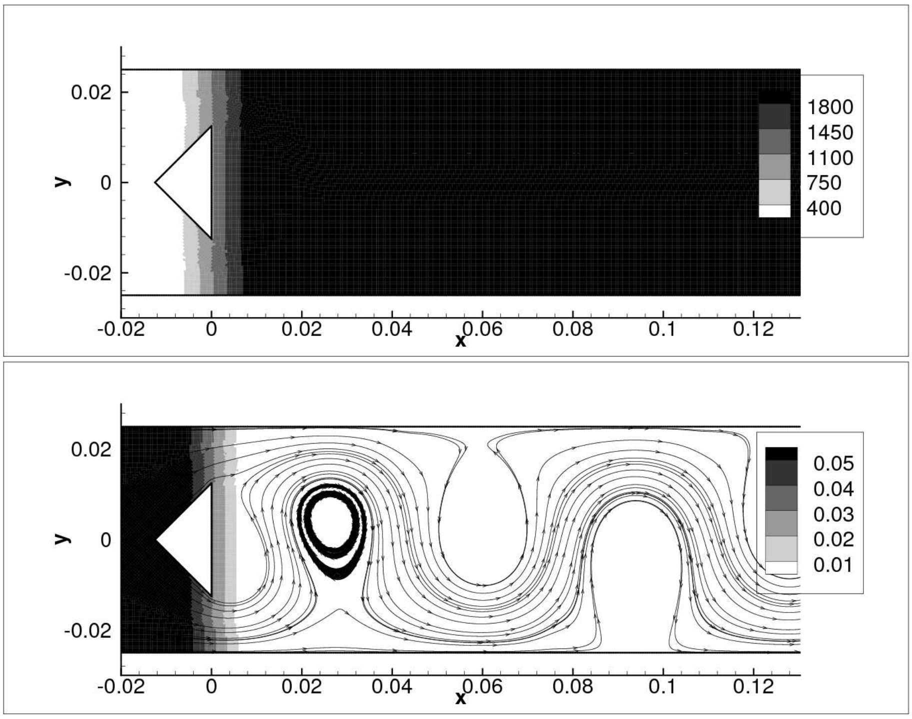

Figure 4.1 : *Temperature (K) (above) and mass fraction of C_3H_8 (kg/kg) (below) with the stream line for the initialization of the flame.*

Boundary conditions

In the main combustion chamber, the boundary condition at the walls is given by a logarithmic wall law (Schmitt 2005) with heat losses. The wall heat flux is calculated through

$$q_{wall} = \frac{1}{R_{wall}}(T_{ref} - T_{wall}) \tag{4.3}$$

where the thermal resistance of the wall is set to $R_{wall} = 0.1\,Km^2/W$ taking the value retained by Varoquié (2004) and Gonçalves dos Santos (2007) and T_{ref} is equal to $T_{ref} = 300\,K$. At the flame holder, a no-slip adiabatic condition is chosen and the walls of secondary chamber are modeled as slip and adiabatic. The characteristic boundary conditions (Poinsot and Lele 1992) are applied to the inlet and outlet to release the acoustic energy from the computational domain. For the description of the philosophy of the characteristic boundary condition, readers are refered to Appendix A. At the main inlet, the incoming velocity, temperature, and the mass fractions of the chemical species are respectively set to $5.0\,m/s$, $300\,K$, and at stoichiometry. At the inlet of the co-flows, the same physical quantities are set to $20\,m/s$, $2000\,K$, and 1.00 for N_2 and 0 for other chemical species. Only the pressure is set to the $101325\,Pa$ at the outlet.

The Reynolds number based on the dimension of the flame holder and on the maximum velocity beside the flame holder ($10\,m/s$) is of the order 10^4.

Determination of the thickening factor

Flame thickening is performed by multiplying the diffusion coefficient and dividing the reaction rate by the thickening factor F in the transport equation of chemical species (see Equation 1.77). This is a deliberated manner for amplifying the flame thickness without changing the flame speed. On the contrary, if the flame is absent, this modification of the equation simply changes the diffusive properties of the chemical species, and it has no sense. The thickening factor is, thus, determined, depending on the reaction rate, according to Légier et al. (2000),

$$F = 1 + (F_{max} - 1)\,\theta\,, \tag{4.4}$$

where F_{max} is given as an input and θ is a sensor function which detects the existence of the reaction zone. This equation allows to set a thickening factor equal to unity in the zone where the reaction does not take place and to F_{max} in the reaction zone. The sensor function is written

$$\theta = \tanh\left(C_f \frac{\Omega}{\Omega_0}\right)\,. \tag{4.5}$$

Ω_0 is the max value of Ω that the sensor function is expected to take in the reaction zone. C_f is a coefficient introduced for setting the thickening factor

F to be F_{max} in the whole reaction zone. F does not reach F_{max} without this coefficient as $tanh(1) \approx 0.762$. An over-large value of C_f leads to the Heaviside function-like distribution of F between the reaction and non-reaction zone. C_f is set to 500, taking the value of Truffin (2005). This method was also tested and verified in Gonçalves dos Santos (2007).

One of the variations of this method can be found in Schmitt et al. (2007), where the authors varied F depending on the grid resolution. It is a sophisticated method for assuring the good resolution of the flame front on the LES grid. The variation of F in the reaction zone, however, may affect the results of dynamic thickened flamelet model, and its effect is expected not to be simple to understand. In this study the former method is therefore adopted.

Variations of the thickened flamelet model and the turbulence model

The simulations of this chapter are performed with the thickened flamelet model and the Smagorinsky model. Both models have the dynamic version for the determination of the constants. Firstly, the simulations are conducted with fixed constants for both the thickened flamelet model and the Smagorinsky model. The constant β for the thickened flamelet model is varied from zero to 0.7, while the Smagorinsky constant, C_S, is set to $C_S = 0.0324\,(= 0.18^2)$. The results are presented in Section 4.3. Then, the dynamic thickened flamelet model is applied to the simulation with constant C_S in Section 4.4, and full dynamic simulations with the dynamic thickened flamelet model and the dynamic Smagorinsky model are completed in Section 4.5.

4.3 Simulations without the dynamic procedures

A series of simulations without the dynamic procedures are performed before their application to the simulations. The value of the constant β is given at the beginning and kept constant during the simulation. C_S is set to 0.0364. The objective of these simulations is to investigate the influence of the value of β on the flame and to obtain a reference flame to compare with the results calculated with the dynamic models. All simulations are performed over 500,000 iterations, which corresponds to approximately 0.1 s. This time interval is sufficiently long to eliminate the influence of initial conditions and to obtain a statistically steady flame.

In Figures 4.2 and 4.3, the stream lines of the time averaged fields and the time averaged reaction rates of the principal reaction ($C_3H_8+5O_2 \Longrightarrow 3CO+4H_2O$) are respectively presented. It is clearly shown that the size of the recirculation zone decreased when the constant β increased for $\beta \geq 0.3$, while it did not change much when $\beta < 0.3$. The increase of the efficiency function E due to the increase of β enhanced the reaction, and the time averaged reaction zone came close to the flame holder as displayed in Figure 4.3. This caused the acceleration of the flow due to the thermal expansion to occur closer to the flame holder, and the size of the recirculation zone reduced with the increase of β. Figure 4.4 compares the x component of the time averaged velocity calculated with different β. The time averaged velocity did not change while β was smaller than 0.3. The result of $\beta = 0.5$ deviated from those of $\beta \leq 0.3$ at $x > 0.1$, indicating the promotion of chemical reaction due to the higher value of β. That of $\beta = 0.7$ was remarkably different from the others. The recirculating speed was higher than the others and the value of u became positive at a position considerably closer to the flame holder. The acceleration also occurred quite closer to the flame holder than the other results, but u converged to around 40 m/s independent from the value of β, because the amounts of the incoming fuel and air were kept constant, and then, the integral of chemical reactions did not change.

In Figure 4.3, the zone, where the time averaged reaction rate was smaller than $20\, kg/m^3 \cdot s$ downstream of the flame holder, became larger when the value of β changed from 0 to 0.3, and returned to be small as it changed from 0.3 to 0.7. When $\beta \leq 0.3$, the increase of β made the efficiency function larger immediately downstream of the flame holder and the flame turned to be less sensitive to the resolved flow motions. Then the wrinkling of the flame surface became weak and the time averaged reaction zone became narrower and longer in this zone as Figure 4.3 displays. Consequently the size of the area, where the time averaged reaction rate was smaller than $20 kg/m^3 \cdot s$, became larger. As β further increased, however, the reaction rate close to the flame holder became high, and the area reduced again. Figures 4.5 and 4.6 display representative instantaneous fields of the reaction zone that came close to the flame holder for $\beta = 0$ and $\beta = 0.7$ respectively.

The comparison of the time averaged reaction zone (Figure 4.3) also gives the information about the length of the flame from the flame holder. The length was not so different when β was smaller than 0.3. This shows that the values of the efficiency function stayed at a same level and, a priori, they were close to unity despite of the increase in the constant β from 0 to 0.3, i.e., turbulence was weak except immediately downstream of the flame holder. Figures 4.7 and 4.8 respectively display the time averaged temperature fields and their root mean square values for different values of β. The latter can be interpreted to be the time averaged strength of the resolved wrinkling. When $\beta \leq 0.3$, the zones, where the root mean square values were larger than 600 K, at approximately $x = [0.05, 0.15]$ (m) became narrower with the increase of β, showing that the resolved wrinkling reduced when β increased. As β further increased, the high wrinkling zone approached to the flame holder, and the flame length became shorter. In Figure 4.3, the case of $\beta = 0.7$ clearly shows shorter flame length than the case of $\beta = 0.5$ does.

The time averaged temperature fields indicate the relation between the reaction rate and the resolved flame wrinkling. The higher the heat release is, the higher the temperature becomes immediately downstream of the flame holder. At the same time, the more the flame is wrinkled, the smaller the high temperature zone becomes, because high wrinkling of the resolved flame surface let the cold unburned gas come into this zone.

In the results with $\beta \leq 0.5$, the zones, where the time averaged temperature was higher than 2000 K, were approximately identical to the zones, where the time averaged reaction rate was smaller than 20 $kg/m^3 \cdot s$ (see also Figure 4.3). The size of this high temperature zone of $\beta = 0.7$ case was considerably larger than the corresponding low reaction rate zone, because of the high reaction rate due to the high efficiency function. High values of the efficiency function with $\beta = 0.7$ also made the position of the second high temperature zone, which started at $x \approx 0.15$ (m) and where temperature was higher than 2000 K, significantly closer to the flame holder than the other results.

Summary

In this section, the simulations without dynamic procedures were performed. The results revealed that the flame came closer to the flame holder when higher values of β was used. This is because of the increase in the efficiency function and the reaction rate also increased with β immediately downstream of the flame holder. The increase of the reaction rate in this zone caused the acceleration of flow to occur close to the flame holder and resulted in the reduction of the recirculation zone in size. It was also verified that the length of the flame from the flame holder did not change much when $\beta \leq 0.3$, showing that the turbulence was weak, while the flame was shortened as β further increased.

4.4 Simulation with the dynamic thickened flamelet model

The simulation presented above for the non-dynamic simulation is also performed with the dynamic thickened flamelet model. The configuration is identical to the two-dimensional test of the previous chapter. For the definition of the control volume used in the formulation, see Section 3.3.1. In the previous chapter, the Arrhenius law was shown to be very sensitive to the use of different Schmidt numbers Sc for each chemical species. The simulations, then, retain Boger's algebraic model and the Arrhenius law using the progress variable. The mass fraction of propane, $Y_{C_3H_8}$, is used for the calculation of the progress variable $\widetilde{c}$.

In Figure 4.9, time averaged temperature fields and root mean square values

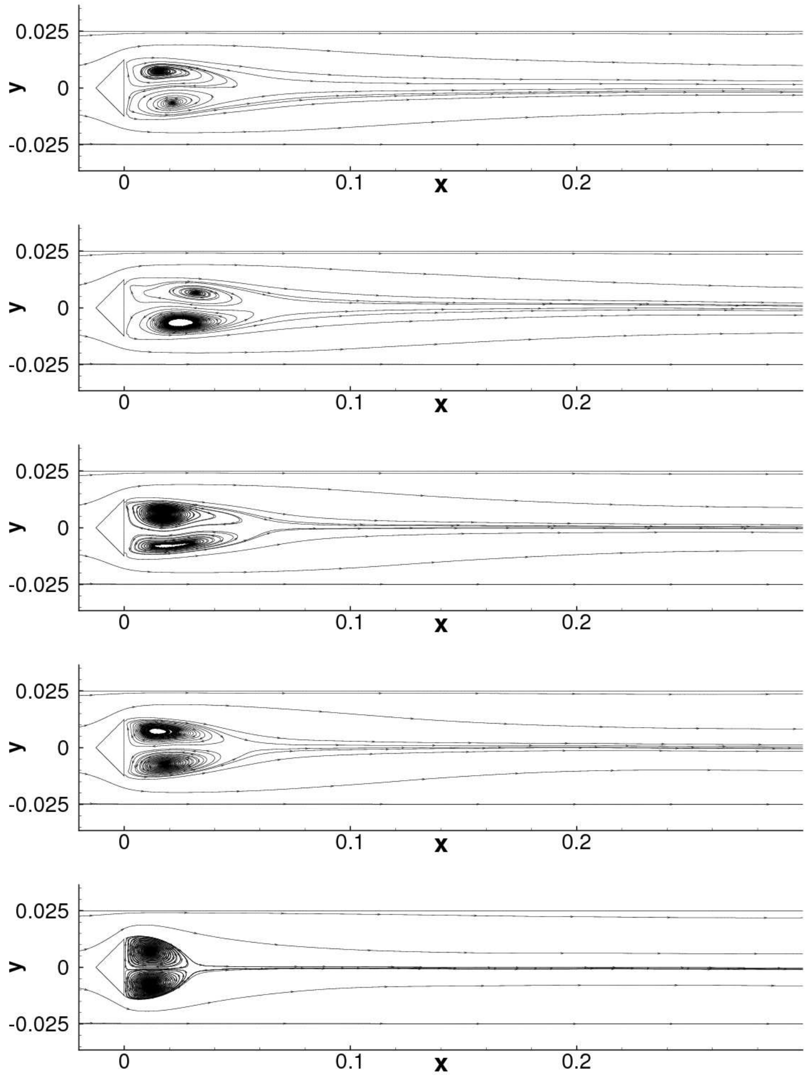

Figure 4.2 : *Time averaged stream lines obtained through a simulation using a constant efficiency constant β. β is set to* 0.0, 0.1, 0.3, 0.5 *and* 0.7 *from the top to the bottom.*

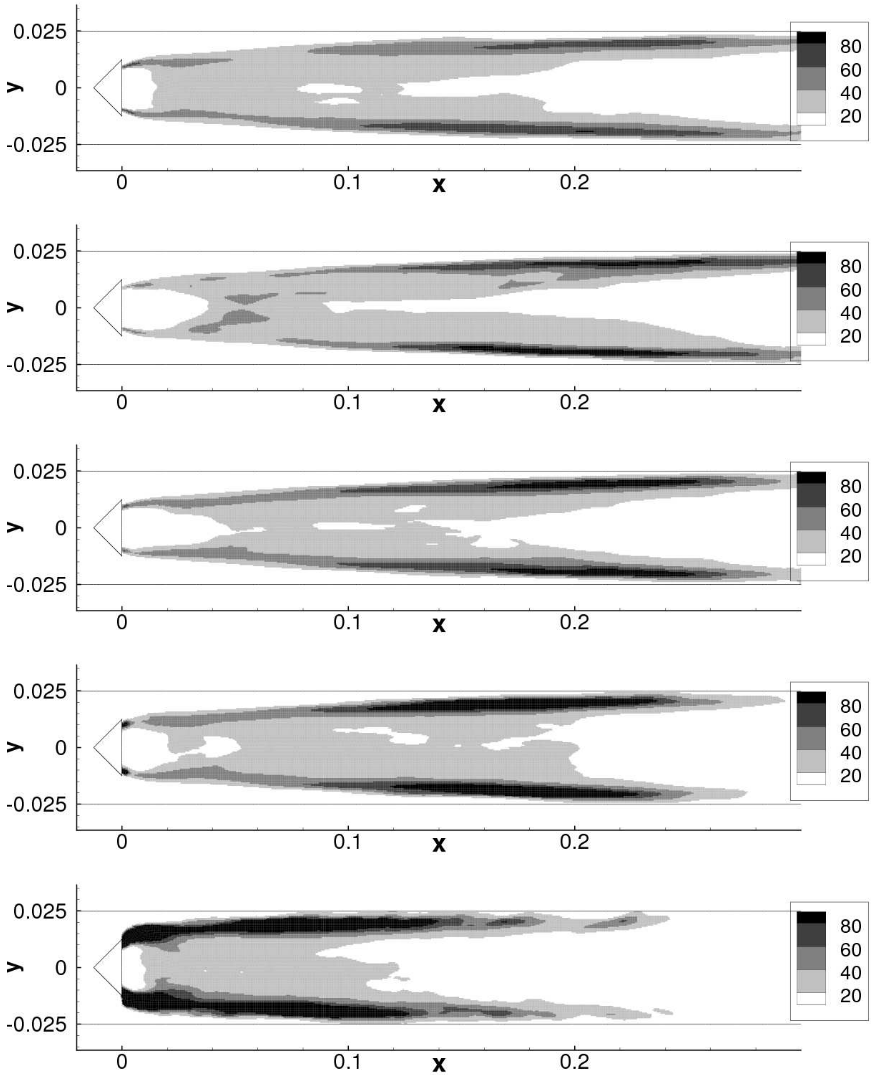

Figure 4.3 : *Time averaged reaction rate of the principal reaction ($kg/m^3 \cdot s$) obtained through a simulation using a constant efficiency constant β. β is set to* 0.0, 0.1, 0.3, 0.5 *and* 0.7 *from the top to the bottom*

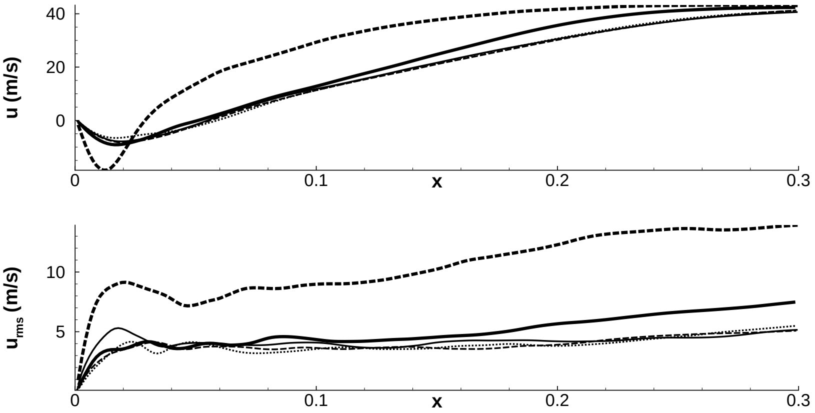

Figure 4.4 : *Comparison of the time averaged values and the root mean square values of the velocity in x direction on the center line of the combustion chamber* ($y = 0$)*:* β *was set to* 0 *(narrow solid line),* 0.1 *(narrow dashed line),* 0.3 *(narrow dotted line),* 0.5 *(bold solid line), and* 0.7 *(bold dashed line).*

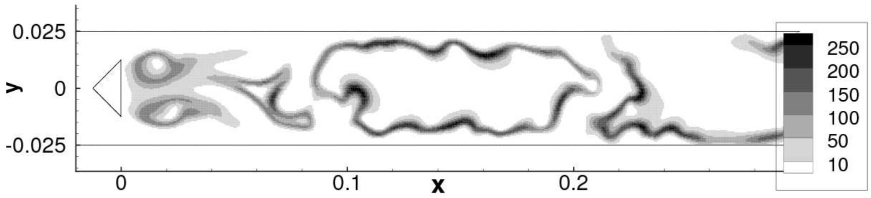

Figure 4.5 : *Instantaneous field of the principal reaction rate (kg/*$m^3 \cdot s$*) where the reaction zone came close to the flame holder.* $\beta = 0$

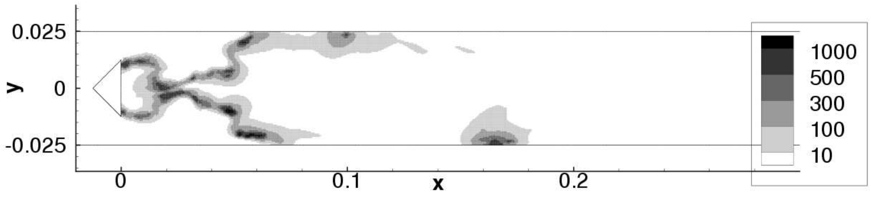

Figure 4.6 : *Instantaneous field of the principal reaction rate (kg/*$m^3 \cdot s$*) where the reaction zone came close to the flame holder.* $\beta = 0.7$

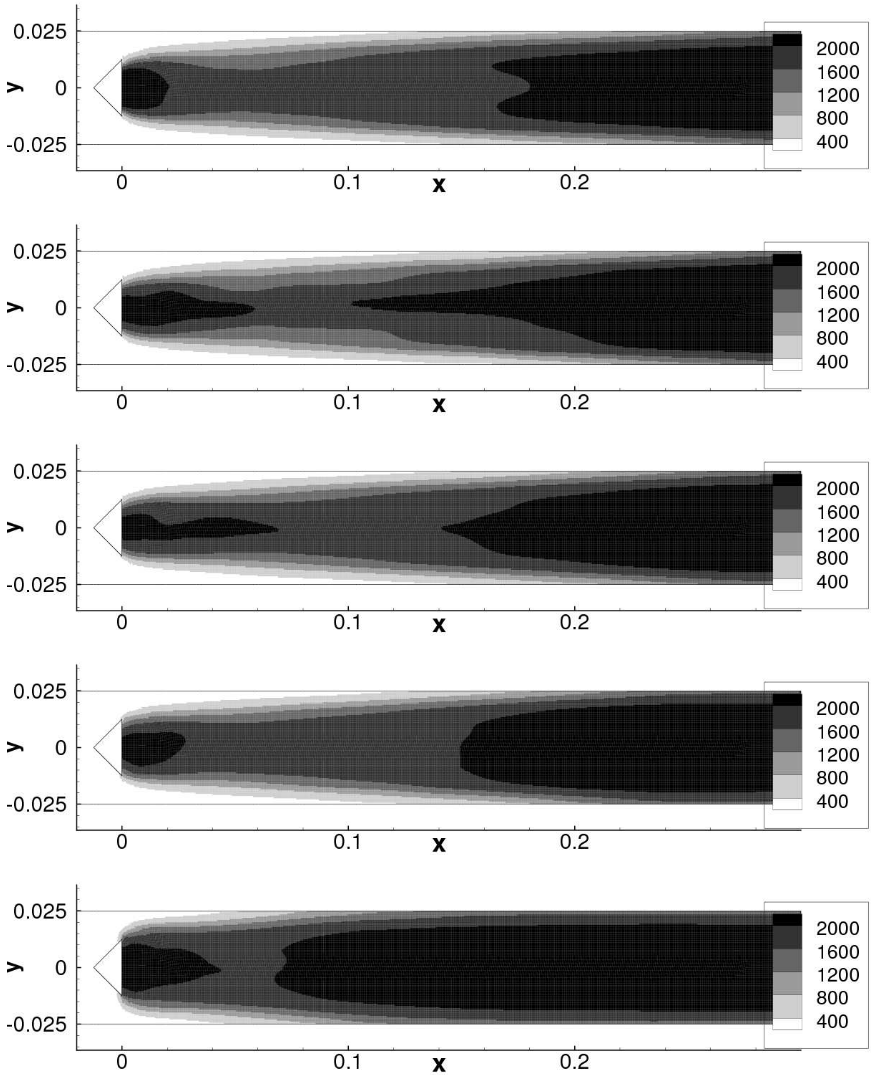

Figure 4.7 : *Time averaged temperature fields (K) obtained through a simulation using a constant efficiency constant* β*.* β *is set to* 0.0, 0.1, 0.3, 0.5*, and* 0.7 *from the top to the bottom*

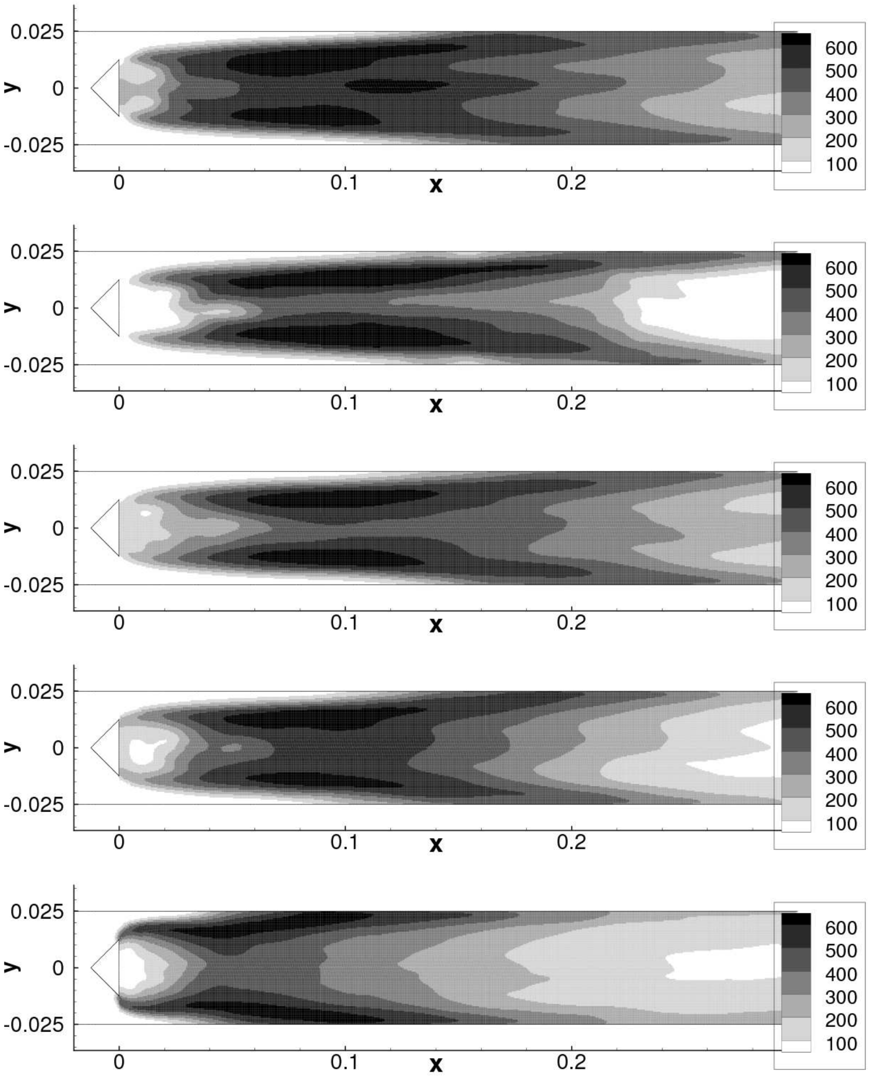

Figure 4.8 : *Root mean square values of temperature (K) obtained through a simulation using a constant efficiency constant* β. β *is set to* 0.0, 0.1, 0.3, 0.5, *and* 0.7 *from the top to the bottom*

of temperature, stream lines of the time averaged fields, time averaged values of β, time averaged values of the efficiency function E, and time averaged reaction rates of the principal reaction obtained through the simulation with the dynamic thickened flamelet model are displayed. The constant β was calculated using Boger's algebraic model in the dynamic procedure. Since the constant β and the efficiency function E were calculated only in the reaction zone, the time averaged values of β and E were obtained only using the values in the presence of the reaction zone. The use of Boger's algebraic model in the calculation of the constant β succeeded in computing the flame without any input for β, and yielded reasonable results similar to the constant β case. The result was close to those of $\beta = 0.3$ and $\beta = 0.5$.

The time averaged field of β shows the statistical trend of the distribution of β. In the result obtained with Boger's algebraic model displayed in Figure 4.9, β was smaller than 0.1 immediately downstream of the flame holder. In the middle of the combustion chamber, there was a zone, where β was higher than 0.3, but outside of this zone, it stayed between 0.1 and 0.3. Downstream of $x = 0.2$ (m), β increased up to the outlet of the chamber. The value of β was lower than 0.5 except close to the outlet of the chamber.

A low value of β found downstream of the flame holder indicates that the flame was not significantly wrinkled. The flame was strained by the shear flow linked to the sudden expansion, but the flame surface remained planar, and the value of β was low. The emergence of the high β zone in the middle of the chamber was caused by the approach of the two flame surfaces. As was seen in Figure 3.13 of the previous chapter, when the two flame surfaces approach, the reaction rate of the test-filtered flame decreases and the product $\gamma\langle\widehat{W_{\Delta}(\widetilde{\mathbf{q}})}\rangle/\langle W_{\gamma\Delta}(\widehat{\widetilde{\mathbf{q}}})\rangle$ increases. Thus the value of β also becomes high.

Figure 4.10 displays the time averaged fields of the major variables obtained through the simulation with the dynamic procedure using the reduced Arrhenius law in the calculation of β. Compared with the results obtained using the Boger's algebraic model, presented in Figure 4.9, the values of β were remarkably high, and the time averaged field of the principal reaction rate, indicated in the last figure of Figure 4.10, shows that the flame was stabilized, not behind, but rather beside the flame holder.

In fact the flame was not stable throughout the simulation. Figure 4.11 shows instantaneous fields of the reaction rate, β, and the efficiency function E at a typical occurrence of the instability, observed at 175 ms after the simulation started. As discussed in the previous chapter, the dynamic thickened flamelet model is sensitive to the geometry of the flame surface, when the Arrhenius law is implemented in the dynamic procedure. Although the curvature is the same, the model yields a higher constant β when it is convex to the unburned gas than when it is concave. This led to the extreme growth of the convex flame surface in the simulation performed here, and resulted in the flame that

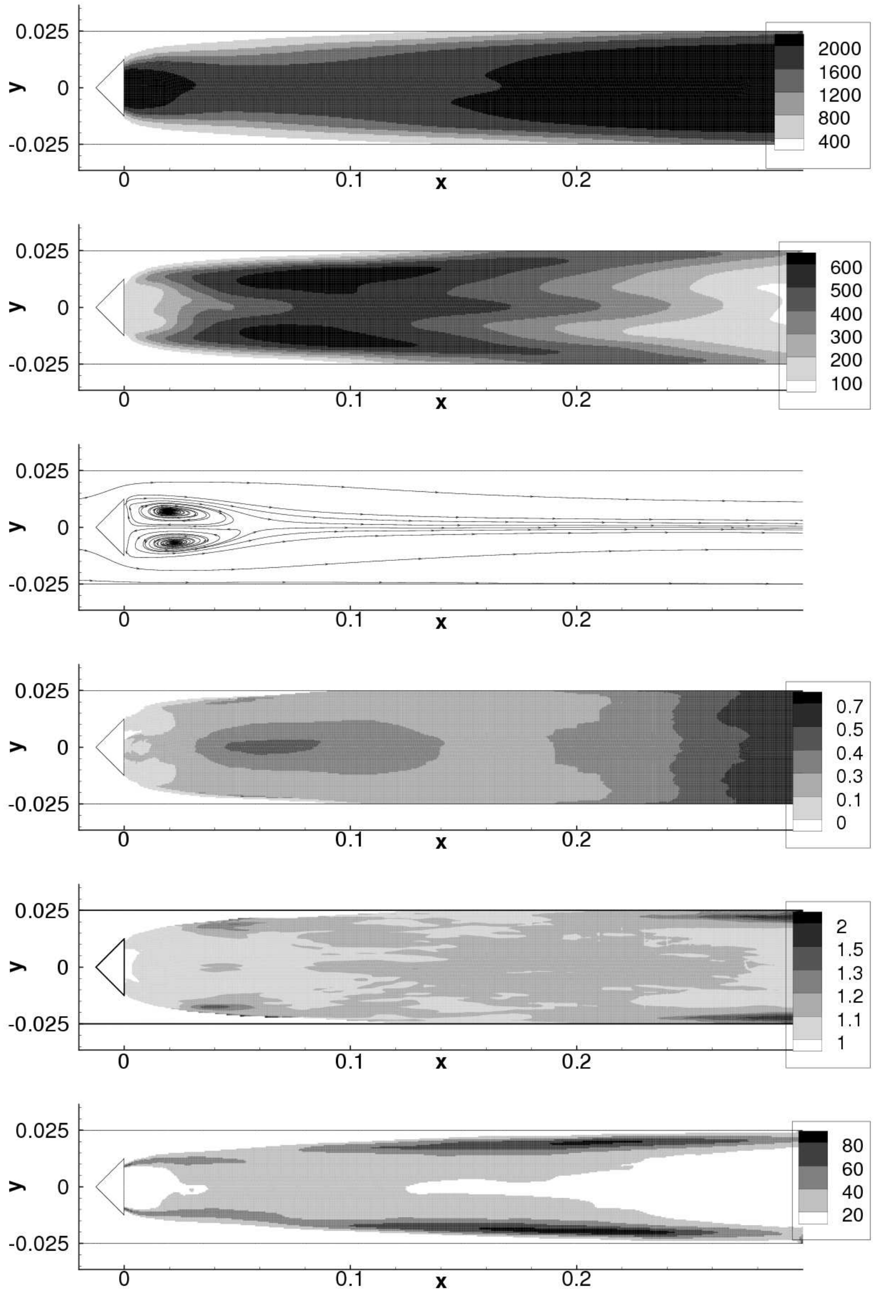

Figure 4.9 : *Time averaged fields of major variables calculated with dynamic model. Top to bottom: time averaged temperature field (K), root mean square value of temperature (K), streamline of the time averaged field, time averaged β field, time averaged field of the efficiency function, and time averaged reaction rate field ($kg/m^3 \cdot s$). The value of β was calculated using Boger's algebraic model in the dynamic procedure, while the Arrhenius law was used for the time evolution. The test-filter size $\widehat{\Delta}$, the effective filter size ratio γ and the width of the control volume for integration dx were respectively set to $\widehat{\Delta} = 1.5 \times 10^{-2}$ (m), $\gamma = 1.94$, and $dx = 4.0 \times 10^{-2}$ (m)*

climbed up the incoming flow. Only Boger’s algebraic model is, therefore, used in the calculation of the constant β in simulations in the next section and also in the next chapter.

Figures 4.12 to 4.14 display the temporal evolution of the reaction zone, the constant β and the efficiency function E respectively. The values of β and E were calculated only in the reaction zone, and set to zero and unity respectively outside of this zone. As the control volume for the calculation of integrals and the averages in the dynamic procedure was defined as a rectangular zone (see Section 3.3.1) having a width of 0.04 m, the values of β are constant on a $x = const$ line in the reaction zone of an instantaneous field, and the instantaneous distribution of the constant β inside the reaction zone can be plotted as a function of x coordinate. Comparison of the instantaneous field of the reaction zone, the plots of β, and the distribution of the efficiency function, shows the dependence of β on the shape of the flame surface. The top figures of Figures 4.12 to 4.14 indicate the instantaneous fields at 70 ms after the simulation started ($400,000$th iteration). The reaction zone was not significantly wrinkled immediately downstream of the flame holder. β was, then, zero and the value of the efficiency function was unity. The wrinkling started at $x \approx 0.01$ (m) and β also started increasing. The existence of the wrinkling kept the values of β non-zero up to $x = 0.14$ (m). Then β became 0 again in $[0.14, 0.17]$. Note that the strength of the wrinkling at a certain x coordinate is the average of upper and lower reaction surfaces in the control volume. Besides this, the wrinkling greater than the test-filter size, $\widehat{\Delta} = 0.015$ (m) is considered to be fully resolved and it does not enhance the increase of β. At $x \approx 0.17\,(m)$, β started increasing again. This transition of β corresponded to the apparition of high wrinkling at $x \approx 0.19$ (m). The values of β stayed at the same level while the flame surfaces exists, but started increasing at $x \approx 0.23$ (m) toward unity. This is because combustion had almost finished before $x \approx 0.23$ and the reaction rates in the formulation,

$$\beta = 1 + \frac{\log\left(\dfrac{\widehat{W_{\Delta}(\widetilde{\mathbf{q}})}}{W_{\gamma\Delta}\left(\widehat{\widetilde{\mathbf{q}}}\right)}\right)}{\log(\gamma)}, \tag{4.6}$$

$\widehat{W_{\Delta}(\widetilde{\mathbf{q}})}$ and $W_{\gamma\Delta}\left(\widehat{\widetilde{\mathbf{q}}}\right)$ were almost equal, but non-zero.

A peak of β emerged at $x \approx 0.04$ (m) in the plot at 77 ms. This peak grew with time and the value of β reached 0.6 at 105 ms. This growth corresponded to a local flame extinction observed at 98 ms, which was induced by the interaction of the two flame surfaces. During this process, the wrinkling of the flame surface increased continuously, and the value of β also increased.

It is also worth discussing the evolution of the second peak of β corresponding to the position of a peninsula-like structure and a small cusp, found in the top figure of Figure 4.12 at $x \approx 0.13$ (m) in the upper and lower surfaces

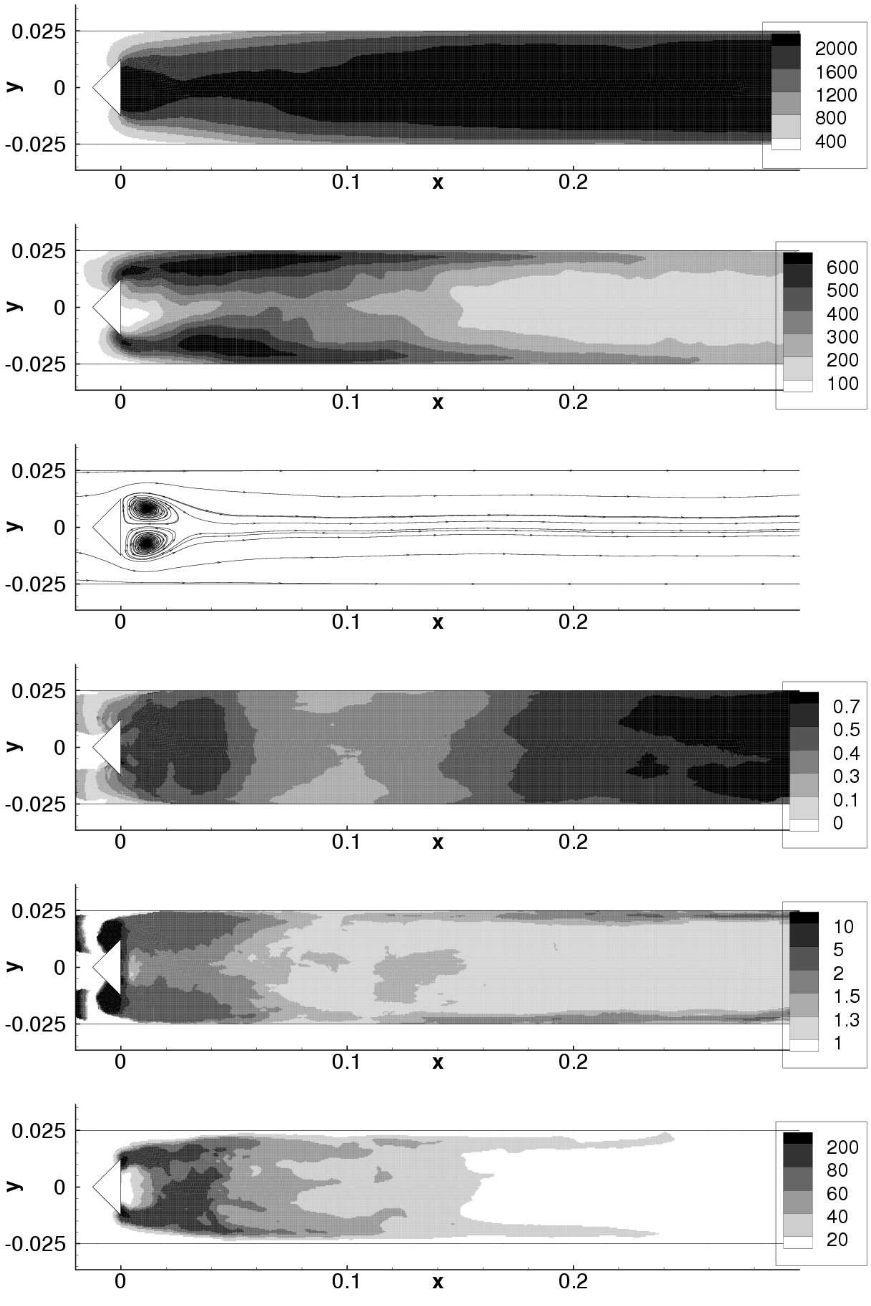

Figure 4.10 : *Time averaged fields of major variables calculated with dynamic model. Top to bottom: time averaged temperature field (K), root mean square value of temperature (K), streamline of the time averaged field, time averaged β field, time averaged field of the efficiency function, and time averaged reaction rate field ($kg/m^3/sec$). The value of β was calculated using the reduced Arrhenius law, while the Arrhenius law was used for the time evolution. The test-filter size $\widehat{\Delta}$, the effective filter size ratio γ and the width of the control volume for integration dx were respectively set to $\widehat{\Delta} = 1.5 \times 10^{-2}$ (m), $\gamma = 1.88$, and $dx = 4.0 \times 10^{-2}$ (m)*

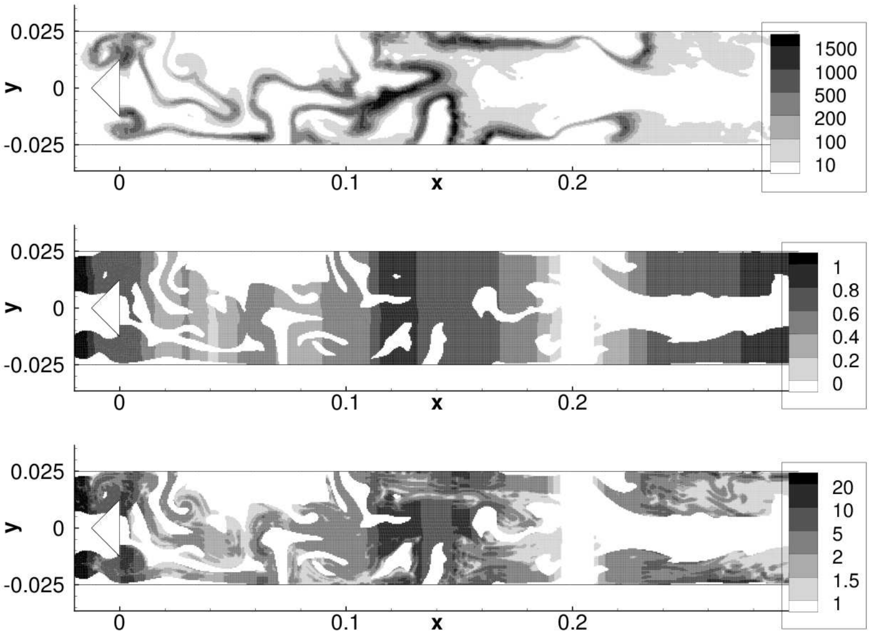

Figure 4.11 : *Instantaneous fields of the reaction rate (kg/m^3·s), Charlette's constant* β*, and the efficiency function* E *obtained in the simulation using the dynamic thickened flamelet model at* 175 *ms after the start of the simulation. The value of* β *was calculated using the reduced Arrhenius law in the dynamic procedure, while the Arrhenius law was used for the time evolution.*

respectively. The peak was still not remarkable at 70 ms, but the low peak grew with time and reached 0.5 at 105 ms.
At 70 ms, the cusp in the lower flame surface was small, and the value of β was raised by the wrinkling around the peninsula. The effect was averaged out in the control volume and β remained small. At 77 ms, the cusp became shaper, but was still small. At 84 ms, it became smaller and the value of β also declined. From 91 ms, the growth restarted and continued until 105 ms, increasing the value of β.

Summary

In this section, the simulations with the dynamic thickened flamelet model were conducted in combination with the Smagorinsky model of $C_S = 0.0324$. The results show the dependence of the output of the dynamic thickened flamelet model on the choice of the chemical model used in the calculation of β. The sensitivity of the use of the reduced Arrhenius law in the dynamic thickened flamelet model resulted in an extremely high values of the efficiency function, that the flame was not stabilized by the flame holder and climbed up the incoming flow. Boger' s algebraic model is then chosen for the calculation of β in the following simulations.
The results with Boger's algebraic model have been investigated in detail. The value of the dynamically determined β was the same order as the empirical value such as $\beta = 0.5$ and the efficiency function E was at the reasonable level. The transition of β and E with the wrinkling of the reaction zone proves the ability of this model of calculating the efficiency function E dynamically without any empirical input for β.

4.5 Combination of the dynamic procedure with the dynamic Smagorinsky model

In the previous section, the simulation with the dynamic thickened flamelet model succeeded in computing a realistic combustion using Boger's algebraic model in the calculation of β. In this section, the dynamic procedure is combined with the dynamic Smagorinsky model. Two types of the dynamic Smagorinsky model are applied to the simulation. One is the standard dynamic Smagorinsky model and the other uses Moin's procedure (see Section 1.2.3.2). The Smagorinsky constant C_S is set to zero when the dynamic Smagorinsky model returns negative values of C_S.
Figures 4.15 and 4.16 compare the time averaged values of the Smagorinsky constant C_S and that of the turbulent viscosity μ_t calculated with the standard dynamic Smagorinsky model and with Moin's procedure. In figure 4.16, the result calculated with constant C_S ($= 0.0324$) is also indicated for the com-

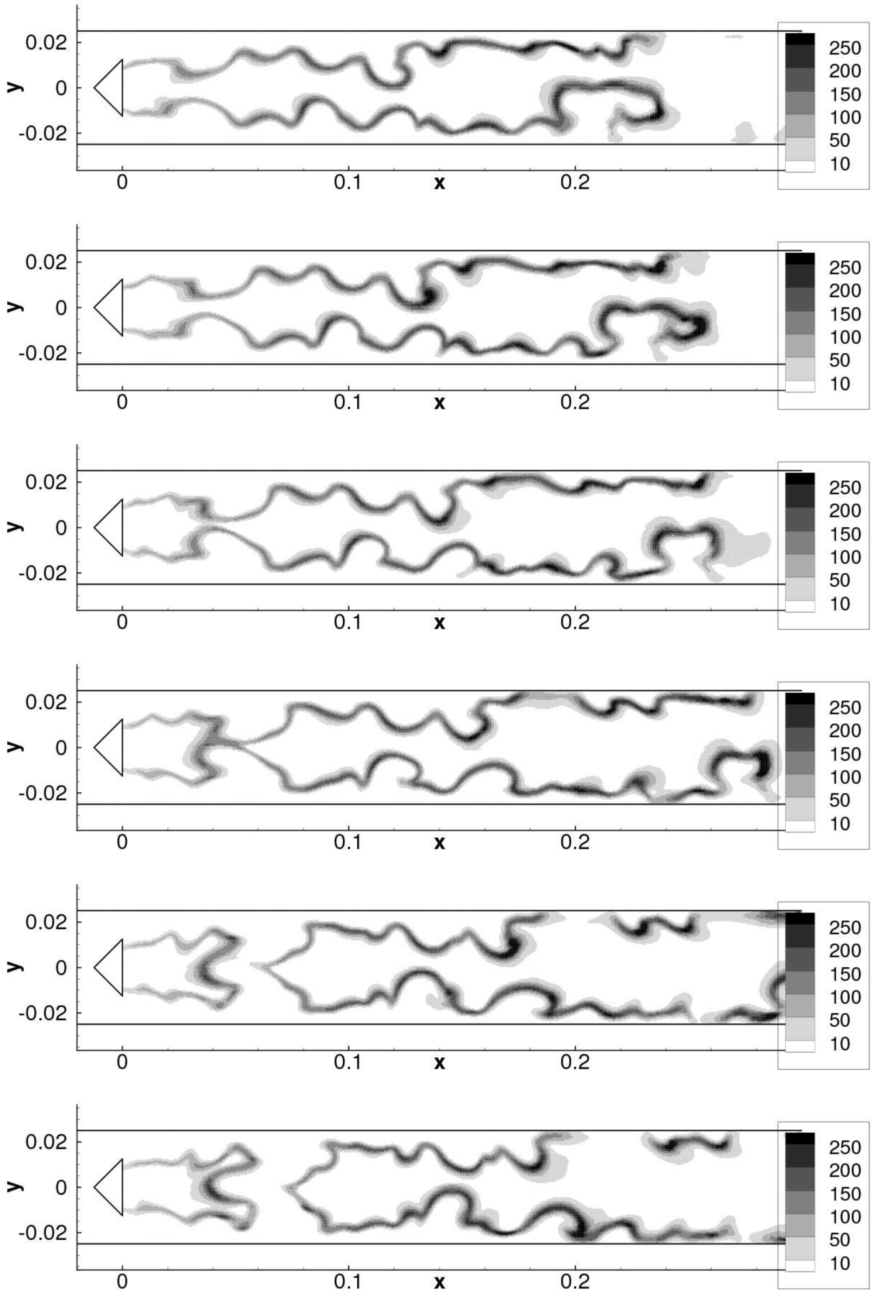

Figure 4.12 : *Time evolution of reaction zone of the principal reaction from 70 ms (900,000th iteration) to 105 ms (920,000th iteration). The Arrhenius law was used for the calculation of the reaction rate, while Boger's algebraic model was used in the dynamic procedure to calculate* β*. The test-filter size* $\widehat{\Delta}$*, the effective filter size ratio* γ *and the width of the control volume for integration* dx *were respectively set to* $\widehat{\Delta} = 1.5 \times 10^{-2}$ (m), $\gamma = 1.94$, *and* $dx = 4.0 \times 10^{-2}$ (m)*. Each figure shows the instantaneous field at 70, 77, 84, 91, 98, 105 ms top to bottom.*

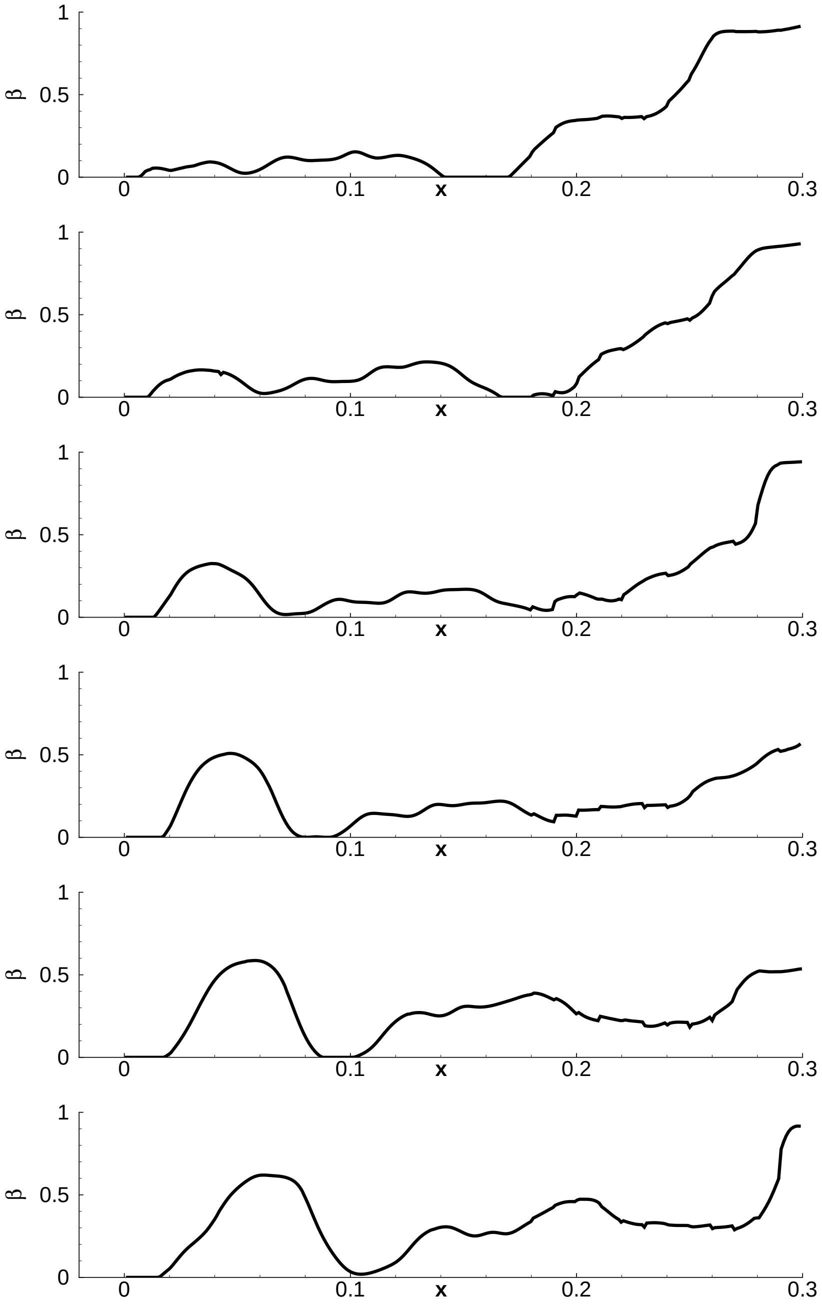

Figure 4.13 : *Time evolution of the constant* β *plotted as a function of the downstream coordinate from 70 ms (900,000th iteration) to 105 ms (920,000th iteration). The Arrhenius law was used for the calculation of the reaction rate, while Boger's algebraic model was used in the dynamic procedure to calculate* β*. The test-filter size* $\widehat{\Delta}$*, the effective filter size ratio* γ *and the width of the control volume for integration* dx *were respectively set to* $\widehat{\Delta} = 1.5 \times 10^{-2}$ (m), $\gamma = 1.94$, *and* $dx = 4.0 \times 10^{-2}$ (m). *Each figure shows the instantaneous field at 70, 77, 84, 91, 98, 105 ms top to bottom.*

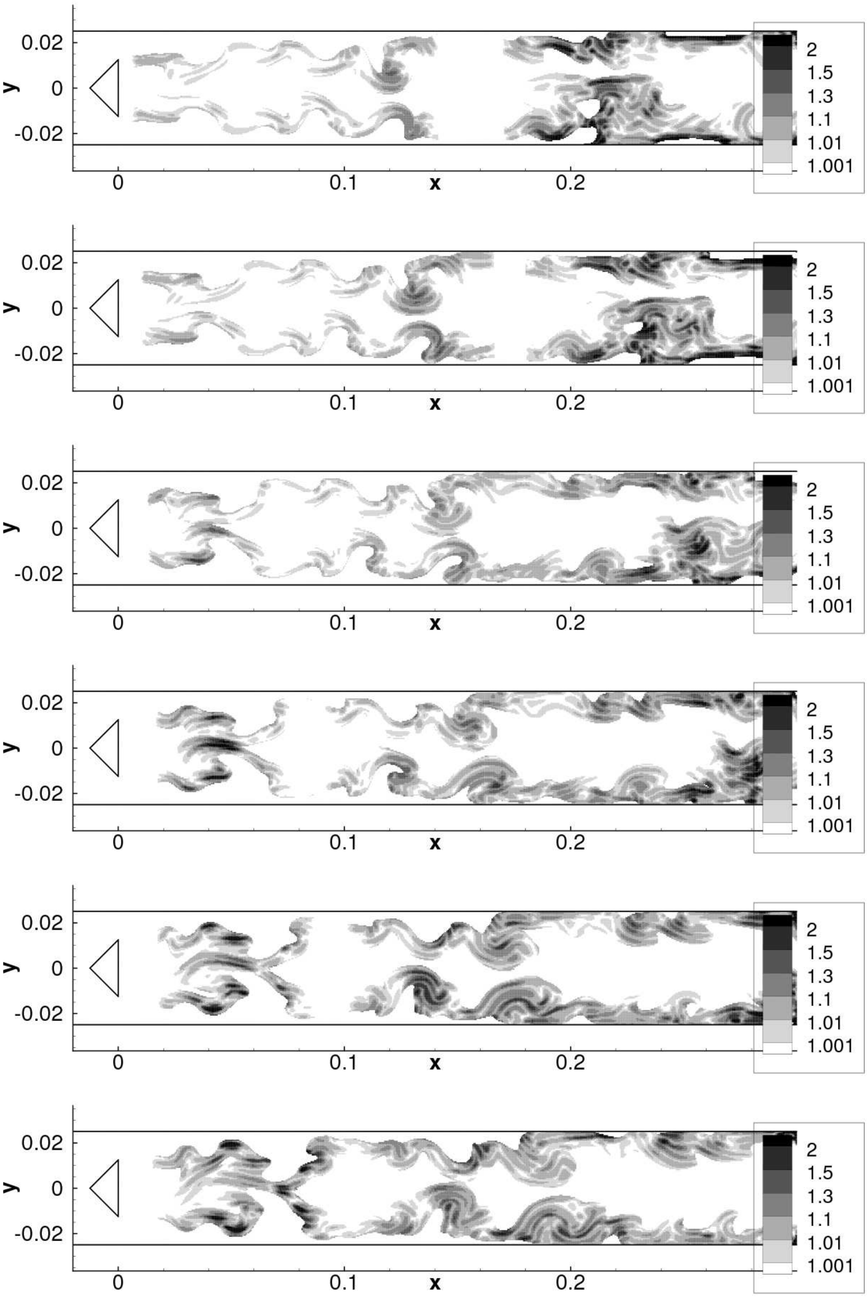

Figure 4.14 : *Time evolution of the efficiency function from 70 ms (900,000th iteration) to 105 ms (920,000th iteration). The Arrhenius law was used for the calculation of the reaction rate, while Boger's algebraic model was used in the dynamic procedure to calculate* β. *The test-filter size* $\widehat{\Delta}$, *the effective filter size ratio* γ *and the width of the control volume for integration* dx *were respectively set to* $\widehat{\Delta} = 1.5 \times 10^{-2}$ (m), $\gamma = 1.94$, *and* $dx = 4.0 \times 10^{-2}$ (m). *Each figure shows the instantaneous field at 70, 77, 84, 91, 98, 105 ms top to bottom.*

parison. Unlike to the results of the test performed in Chapter 3, the fields of time averaged C_S were considerably different, when different types of the dynamic Smagorinsky model were applied. C_S of the standard Smagorinsky model was smaller than 0.01 almost everywhere in the combustion chamber except immediately downstream of the flame holder. This value is quite small compared to the reference value of $C_S = 0.0324\,(= 0.18^2)$, which was used in the constant C_S simulations. The output of Moin's procedure was closer to the reference than that of the standard dynamic Smagorinsky model, but smaller than the reference value too.

Observing more in detail, the outputs of both models in burnt gas had the same tendency and they were of the same order. Behind the flame holder ($x < 0.02$) the incoming and the recirculating flows encounter and a shear flow takes place. It makes the terms of deformation tensor high and increases the value of C_S. Both models predicted high values of C_S here. In the zone inside or close to the recirculation zone, C_S of both models were between 0.0025 and 0.01, then, lower than the reference value.

The most remarkable difference of these results was found along the unburned side edge of the time averaged reaction zone. These zones corresponded to the position where the time averaged values of temperature started to increase as Figures 4.17 and 4.18 display for the standard Smagorinsky model and that with Moin's procedure respectively. The standard dynamic Smagorinsky model returned the values of C_S less than 0.0025 here, while Moin's procedure yielded the values between 0.01 and 0.0324. This shows the impact of the density change on the determination of C_S, which was not observed in the test case of the previous chapter and proves the requirement to consider the density change.

The differences of the Smagorinsky constant reflected in the time averaged fields of the turbulent viscosity μ_t, as Figure 4.16 displays. The same discrepancy of the time averaged C_S fields can also be found in those of μ_t calculated with the dynamic Smagorinsky models. The field of μ_t calculated with constant C_S showed higher values than that calculated with the dynamic Smagorinsky models almost everwhere in the computational domain. In front of the flame holder the two dynamic Smagorinsky models predicted remarkably smaller turbulent viscosity μ_t than the non-dynamic Smagorinsky model did. Both in the unburned and the burnt gases, μ_t calculated with the non-dynamic Smagorinsky model was considerably higher than the values obtained with the dynamic Smagorinsky models. However, downstream of the flame holder, where the sudden expansion induced a shear flow, μ_t in the non-dynamic Smagorinsky model became lower than the value predicted by the dynamic Smagorinsky models.

To observe the effect of the dynamic Smagorinsky models on the combustion, the time averaged temperature field, its root mean square values and the stream lines of the time averaged fields are presented in Figures 4.17 and 4.18 for the combination of the dynamic thickened flamelet model and the dynamic

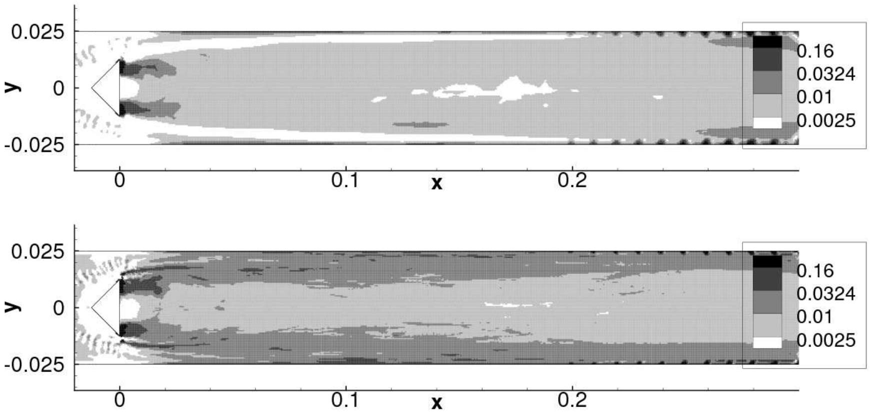

Figure 4.15 : *Time averaged values of the Smagorinsky constant, C_S calculated with the standard dynamic Smagorinsky model (top) and with Moin's procedure (bottom). The test-filter size $\widehat{\Delta}_S$ for the calculation of the Smagorinsky constant C_S was set to 2.5×10^{-3} m.*

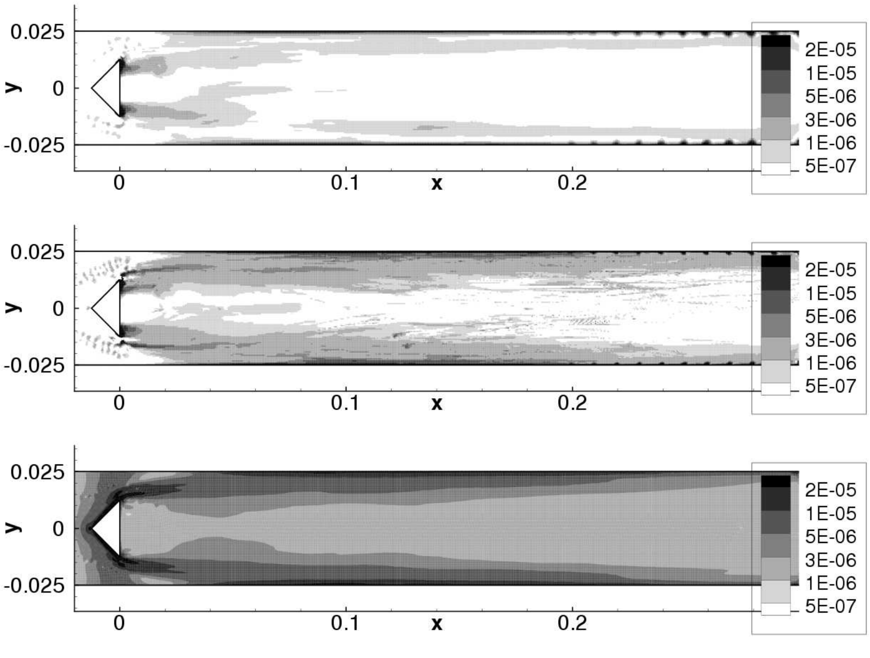

Figure 4.16 : *Time averaged values of the turbulent viscosity, μ_t calculated with the standard dynamic Smagorinsky model (top), Moin's procedure (middle), and the Smagorinsky model with constant C_S ($= 0.0324$). The test-filter size $\widehat{\Delta}_S$ for the calculation of the Smagorinsky constant C_S was set to 2.5×10^{-3} m for the use of the dynamic Smagorinsky models.*

Smagorinsky model and for that of the dynamic thickened flamelet model and the dynamic Smagorinsky model with Moin's procedure, respectively. The values of β were calculated using Boger's algebraic model in the dynamic procedure. The differences due to the introduction of Moin's procedure was not significant and these results were quite similar to that of the constant C_S case displayed in the top three figures of Figure 4.9.

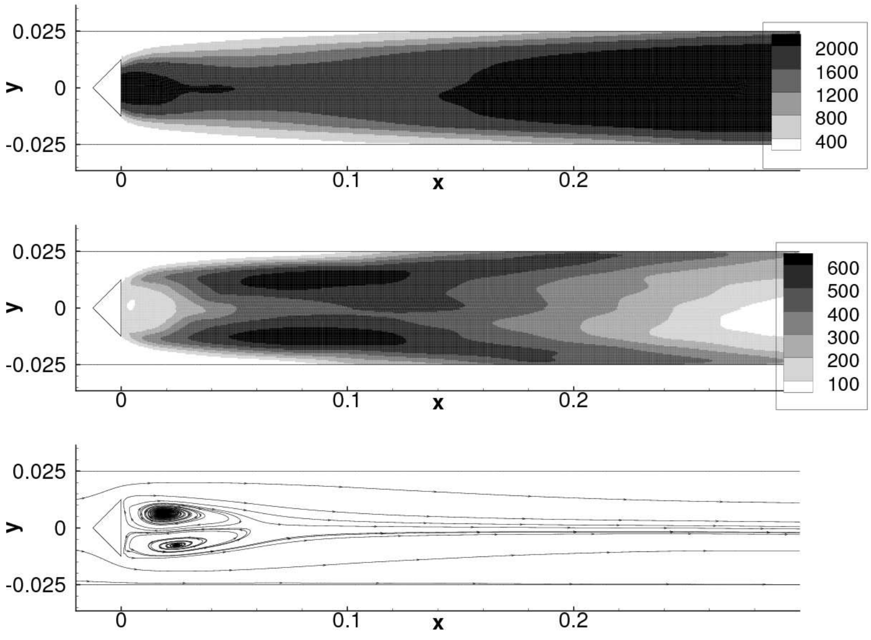

Figure 4.17 : *Time averaged temperature field (K), its root mean square value, and the stream line of the time averaged field calculated with the dynamic thickened flamelet model and the dynamic Smagorinsky model. The value of β was calculated using Boger's algebraic model in the dynamic procedure.*

Figure 4.19 displays the time averaged velocity in x direction on the center line ($y = 0$) of the combustion chamber and its root mean square values. The time averaged velocity is related to the the total reaction rate in the upstream, as the acceleration of the flow media occurs through the density change across the flame. This plot indicates that the time averaged velocity on this line did not change much. However, a slight deviations are observed in the plot of the root mean square value of velocity in x direction. This resulted from the low turbulent viscosity μ_t calculated with the standard dynamic Smagorinsky model, but the difference between the results calculated with Moin's procedure and the Smagorinsky model with constant C_S were not significant.
Though the difference of the time averaged fields of temperature and the stream-

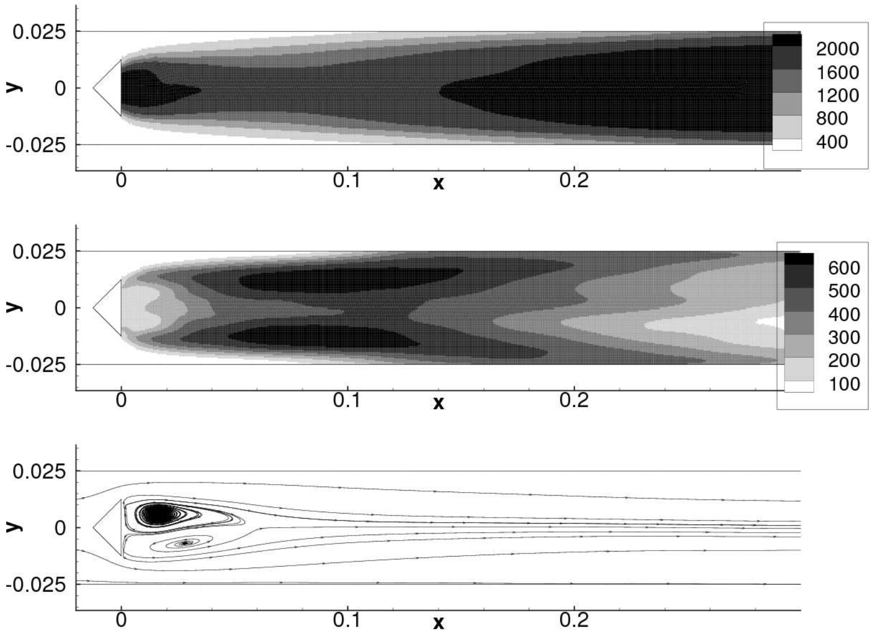

Figure 4.18 : *Time averaged temperature field (K), its root mean square value and the stream line of the time averaged field calculated with the dynamic thickened flamelet model and the dynamic Smagorinsky model with Moin's procedure. The value of β was calculated using Boger's algebraic model in the dynamic procedure.*

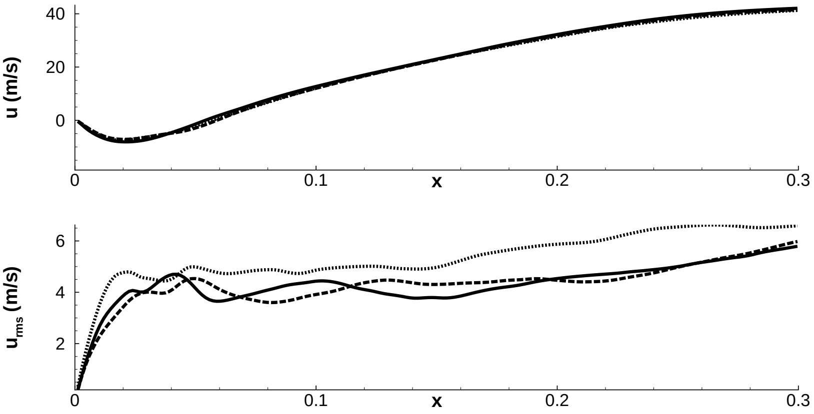

Figure 4.19 : *Comparison of the time averaged values and the root mean square values of the velocity in x direction on the center line of the combustion chamber (y = 0): C_S = 0.0324 (solid line), the result of the standard dynamic Smagorinsky model (dashed line) and the result of Moin's procedure (long dashed line)*

line were not significant, the discrepancies of the fields of the Charlette's constant β and that of the efficiency function are clearly shown in Figures 4.20 and 4.21, which display the fields of the time averaged values of β and the efficiency function E conditioned by the presence of the reaction zone and that of the reaction rate of the principal reaction obtained through the simulation with the standard dynamic Smagorinsky model (Figure 4.20) and that with Moin's procedure (Figure 4.21). These fields indicate that the value of β calculated in combination with the standard dynamic Smagorinsky model was higher than that calculated with Moin's procedure especially on the centerline of the combustion chamber, and the efficiency function E did so at the edge of the zone, where β took non-zero values downstream of the flame holder. The difference in β came from the difference of the magnitude of the flame wrinkling between the scale of flame thickness $F\delta_0^l$ and that of the test-filter size $\widehat{\Delta}$, i.e. the wrinkling between these scales was stronger when the standard dynamic Smagorinsky model was applied than when the dynamic Smagorinsky model with Moin's procedure was used. On the other hand, the difference of the efficiency function E on the edges of the non-zero β zone was due to the difference of the fluctuating velocity u', as the values of β here were similar in both cases.
These changes were due to the dynamic determination of the Smagorinsky constant C_S. As displayed in Figures 4.15 and 4.16, time averaged values of C_S and μ_t were smaller in the case when the standard dynamic Smagorinsky model was applied everywhere in the computational domain than in the case where Moin's procedure was applied. This smaller C_S led to less dissipation of the resolved turbulence, which increases the resolved flame wrinkling and the fluctuating velocity u', then, β and E also increased. The increased values of β and E made the time averaged reaction rate slightly higher than that calculated with Moin's procedure. However, the fields were almost identical. This fact proves the robustness of the dynamic thickened flamelet model that it corrects the eventual distrust of the fluctuating velocity u' due to the use of different models for C_S. Since the value of the Smagorinsky constant C_S predicted using the dynamic Smagorinsky model with Moin's procedure was closer to the reference value of $C_S = 0.0324$ than when standard dynamic Smagorinsky model was used, the fields of β and the efficiency function E obtained using the Moin's procedure were closer to those of the constant C_S case than those calculated using the standard dynamic Smagorinsky model (see the last three figures of Figure 4.9).

Summary

Contrary to the test case performed in the previous chapter, the results of the simulations performed with the standard dynamic Smagorinsky model and that of Moin's procedure clearly showed difference due to the density change across the flame. The standard dynamic Smagorinsky model predicted considerably

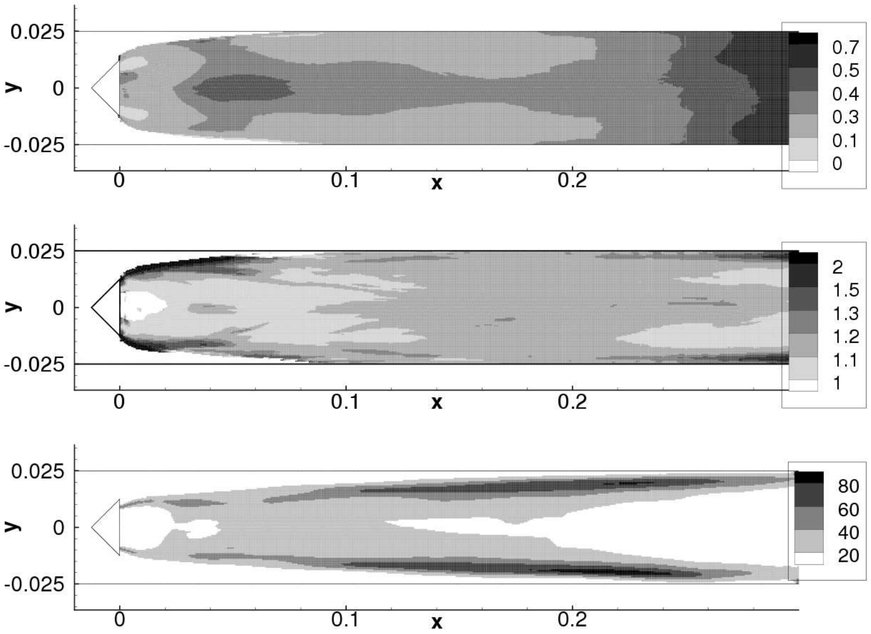

Figure 4.20 : *Time averaged fields of the constant β, the value of the efficiency function, and the principal reaction rate obtained through the simulation with the dynamic thickened flamelet model and the dynamic Smagorinsky model. The value of β was calculated using Boger's algebraic model in the dynamic procedure.*

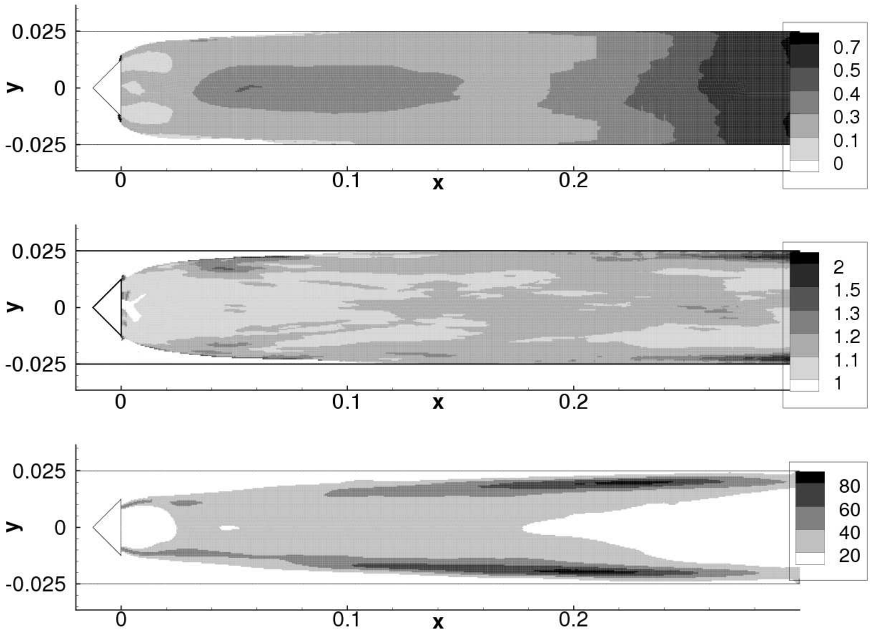

Figure 4.21 : *Time averaged fields of the constant β, the value of the efficiency function, and the principal reaction rate obtained through the simulation with the dynamic thickened flamelet model and the dynamic Smagorinsky model with Moin's procedure. The value of β was calculated using Boger's algebraic model in the dynamic procedure.*

low values of the Smagorinsky constant C_S, while the prediction of Moin's procedure was of the same order as that of the conventional value $C_S = 0.0324$. The discrepancy in C_S led to the difference of the intermediate values, such as Charlette's constant β and the efficiency function E. However the time averaged values of physical quantities such as temperature and reaction rate obtained through the simulations performed with these two models were almost identical and similar to the constant C_S case. This fact shows the robustness of the dynamic thickened flamelet model that it corrects the eventual distrust of the fluctuating velocity u' caused by the use of different types of the Smagorinsky model.

Because Moin's procedure is a method adapted to flows with density change, it is chosen for the three-dimensional simulation performed in the next chapter.

4.6 Conclusion

In this chapter, two-dimensional simulations of the V-flame using the dynamic thickened flamelet model and the dynamic Smagorinsky model were performed and the ability of the dynamic thickened flamelet model of calculating the efficiency function without any input for Charlette's constant β was demonstrated. At the same time, the optimal combination of models was determined for the three-dimensional simulation of the next chapter.

For the calculation of the constant β in the dynamic thickened flamelet model, Boger's algebraic model rather than Arrhenius law with the progress variable was chosen, because the Arrhenius law was very sensitive to the geometry of the flame surface, and the flame was not stabilized downstream of the flame holder.

Contrary to the result of test case in the previous chapter, the standard dynamic Smagorinsky model and the dynamic Smagorinsky model with Moin's procedure yielded remarkably different results in terms of the Smagorinsky constant C_S and the turbulent viscosity μ_t. It shows the importance of density change across the flame for the determination of C_S.

In spite of the discrepancy of C_S predicted by the standard dynamic Smagorinsky model and that with Moin's procedure, the time averaged fields of physical quantities such as temperature and reaction rate were almost identical to those of the constant C_S case. This fact demonstrates the robustness of the dynamic thickened flamelet model, that it corrects the eventual distrust of the fluctuating velocity due to the use of different Smagorinsky models, even if unsteady flow characteristics remains to be compared.

Since Moin's procedure is a method adapted to flows with density change, it will be retained for the three-dimensional simulations in the next chapter.

Chapter 5

Three-dimensional simulation

In this chapter, a three dimensional full dynamic simulation is performed using the dynamic thickened flamelet model and the dynamic Smagorinsky model. From the simulations conducted in the previous chapter, Boger's algebraic model and Moin's procedure were chosen for dynamic thickened flamelet model and for the dynamic Smagorinsky model respectively. The results of the simulation of this chapter are compared to the experimental results obtained at E.M2.C. laboratory.

5.1 Introduction

In the previous chapter, two-dimensional simulations with and without dynamic models were performed and the results proved the capability of the dynamic thickened flamelet model and the dynamic Smagorinsky model of calculating the V-flame combustion. In this chapter, the models are applied to a simulation of a V-flame in a three dimensional configuration.

5.2 Configuration

The configuration of the computational domain is presented in Figure 5.1. As for the two-dimensional simulations, the flame is stabilized behind a triangular flame holder. The origin of the coordinates is set at the front edge of the flame holder on the centerline of the combustion chamber. To reduce the influence of the boundary conditions, a co-flow is injected into a secondary domain surrounding the burner inlet. The mesh contains approximately 4.7 million cells. The grid size is $\Delta = 1.0 \times 10^{-3}\,(m)$ from the inlet ($x = -0.1\,(m)$) to $x = 0.15\,(m)$, then it gradually increases.

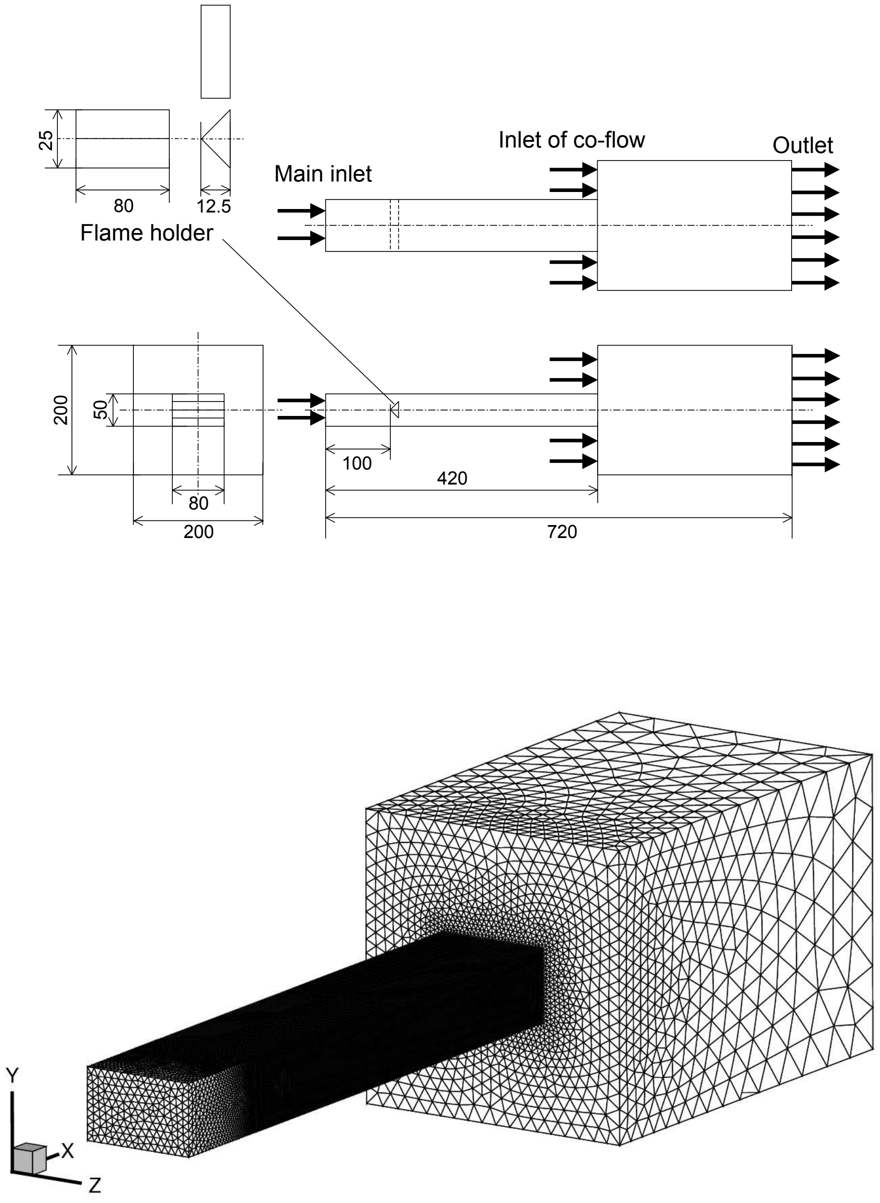

Figure 5.1 : *Configuration of computational domain: All scales are given in mm*

Initial condition

Similar to the two-dimensional case, the flame was at first given as a jumping boundary of temperature and mass fraction of chemical species beside the flame holder. This jump was superimposed to the velocity field obtained through a simulation without flame. Then the flame was stabilized using the dynamic thickened flamelet model and the Smagorinsky model with $C_S = 0.0324$ through $300,000$ iterations corresponding to approximately 0.08 seconds sufficient to obtain a statistically steady flame. The temperature iso-surface of $800\,K$, the fields of temperature and the reaction rate of the principal reaction ($C_3H_8 + 5O_2 \Longrightarrow 3CO + 4H_2O$) on the $z = 0$ plane, are presented in Figures 5.2 and 5.3 respectively.

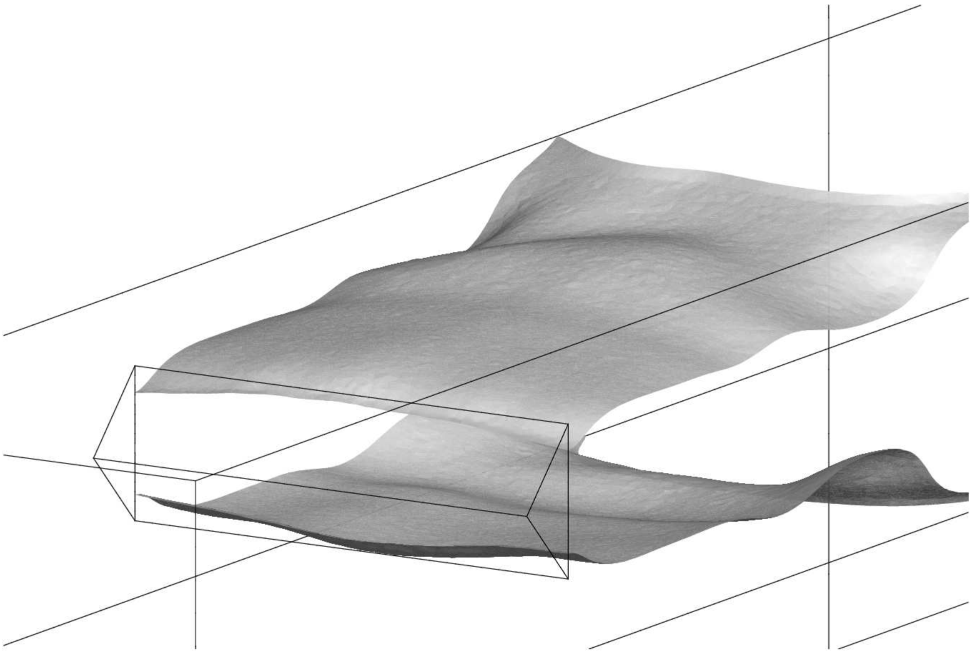

Figure 5.2 : *Temperature iso-surface of* $800\,K$ *of the initial condition*

Boundary condition

The boundary conditions are similar to those of the two-dimensional simulations. At the main inlet of the primary combustion chamber, the stoichiometric mixture of air and propane enters at $5\,m/s$ and $300\,K$. Nitrogen is injected from the co-flow inlet at a speed of $22\,m/s$ and temperature of $2000\,K$. To these inlets and the outlet, characteristic boundary conditions (Poinsot and Lele, 1992, see also Appendix A for the detail) are applied. The flame holder is considered

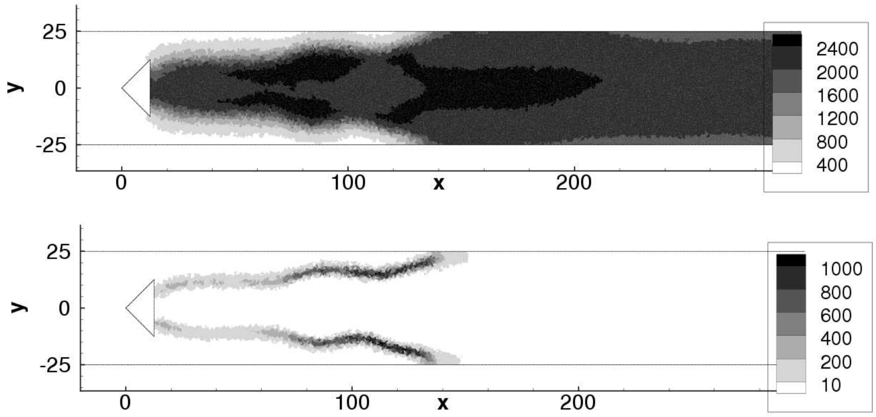

Figure 5.3 : *Initial fields of temperature (K) and reaction rate of the principal reaction ($kg/m^3 \cdot s$) on the $z = 0$ plane.*

as a no-slip adiabatic wall, while the other walls are described as slip wall with heat losses. The reference temperature is set to $300\,K$ at these walls. A slip and adiabatic condition is applied to the sides of the secondary domain, where the co-flow is injected.

Description of the dynamic models

Following the investigations of the previous chapter, Boger's algebraic model and Moin's procedure are retained for the dynamic thickened flamelet model and the dynamic Smagorinsky model respectively. A modified formulation, Equations 3.21 and 3.22 in Chapter 3, of the dynamic thickened flamelet model is used in this chapter. For the detail of this modified formulation, see Section 3.3.2 in Chapter 3.

5.3 Test cases

In the context of the dynamic Smagorinsky model, it is widely done to average the intermediate terms in the calculation of the Smagorinsky constant C_S in the direction, where the turbulence is considered to be homogeneous, to suppress numerical instabilities (Germano et al. (1991), Moin et al. (1991), Piomelli et al. (1991) and Pope (2004)). Equation 1.63 is then rewritten as

$$C_s = \frac{1}{2}(\langle L_{ij}M_{ij}\rangle / \langle M_{ij}^2\rangle)\,, \tag{5.1}$$

where $\langle\cdot\rangle$ represents averaging in the direction, where the turbulence is homogeneous. In the simulation of this chapter, for example, the condition of turbulence is supposed to be statistically similar in z direction. However the existences of the flame and the lateral walls make this assumption questionable. The conditions of turbulence are not the same close to the wall and in the middle of the chamber. In addition to this, the flame surface is three dimensional and not always parallel to the z axis. Then a line parallel to the z axis can intersect with the flame surface and contains both unburned and burnt gases, where the characteristics of the turbulence are different. Then the length for the averaging should be as short as possible to conserve the local information, and long enough to suppress oscillations of C_S.

The same thing can be said in the calculation of the efficiency constant β. In the two-dimensional simulations, the interval for the averaging (dx) was determined in the manner that the interval always contains both unburned and burnt sides of the flame. It was also verified that too short intervals lead to strong oscillations of β and the efficiency function (see Section 3.3 in Chapter 3). In this section, a test for the interval in z direction is performed before the three-dimensional simulation.

For the dynamic Smagorinsky model, three types of averaging are tested. In the first case, no averaging is done and C_S is calculated locally. The second case is the averaging on the whole line that is parallel to the z axis, defined between the two lateral walls and contains the target point. In the third case C_S is averaged using the data on the points, which is on the line defined in the second case and whose distance from the target point is lower than $0.02\,m$. Then the interval is $0.04\,m$ if the target point is farther than $0.02\,m$ from the wall. If it is closer than $0.02\,m$, the interval reduces to the sum of $0.02\,m$ and the distance to the wall.

The test of the dynamic thickened flamelet model is conducted using the same widths of the averaging interval. Other intervals for the averaging are $dx = 0.04\,m$ and $dy = 0.05\,m$ (whole height of the combustion chamber). These values are retained from the two-dimensional tests and assure that the averaging interval contains both unburned and burnt sides of the flame.

5.3.1 Results of the test on the dynamic thickened flamelet model

Figures 5.4 and 5.5 respectively compare the fields of β in the $z = 0$ plane and transversal cuts at $x = 0.06$ and $x = 0.12$ in this plane calculated with different dz. In Figure 5.4, dz increases from the top to the bottom. The differences between the three results are not significant, but they slightly differ as shown in Figure 5.5. The results calculated locally in terms of the z direction contains small oscillations. This is due to the use of non-structured grid in the simulation. The plotted values were calculated by interpolating the node values of cells that contain the line where the values are plotted.

Immediately downstream of the flame holder, the value of β is $0.4 < \beta < 0.6$, when β is calculated locally in terms of the z direction. The use of the averaging induced $0.6 < \beta < 0.8$ in this zone, and it was greater when the averaging was performed using the whole span-wise length of the chamber than with $dz = 0.02$ (m). This means that the value of β was larger at other z position than at $z = 0$ immediately downstream of the flame holder. On the contrary, in the zone, where the value of β was not significantly different in the three results, for example at $x \approx 0.11$ (m), where β is around 0.4, the difference of β in the z direction was small.

Figure 5.6 compares the distribution of β and the efficiency function in z direction calculated with different values of dz at $(x, y) = (0.06, 0.01)$ (m) and $(x, y) = (0.12, 0.02)$(m). β was set to zero outside of the flame, then the values of the efficiency function E were 1. It is clearly shown that the oscillations of β and E were effectively suppressed using larger dz. The plot of $dz = 0$ displays large oscillations both in β and E. The use of $dz = 0.04$ reduced it, but, conserved the general tendency. On the contrary, the averaging over the whole span-wise distance of the chamber eliminated local trends and gave single values for β and E.

It is not obvious whether the oscillations found in the result of $dz = 0$ are unphysical. Because the oscillations are not strong compared to the results of the two-dimensional test case (see Figure 3.14 of Chapter 3), they do not cause numerical problems at least on these lines. However, the use of $dz = 0$ implicitly excludes the effect of the resolved flame surface curvatures in the z direction. In this study, therefore, the averaging with $dz = 0.04$ is chosen as for dx, which was set to $0.04\,(m)$.

Interestingly the values of β were higher in the results at $(x, y) = (0.06, 0.01)$ (m) than at $(x, y) = (0.12, 0.02)$(m), but the values of the efficiency function were higher at $(x, y) = (0.12, 0.02)$(m). β is influenced by the term $\gamma \overbrace{W_{\Delta}(\widetilde{\mathbf{q}})} / W_{\widehat{\Delta}}(\widehat{\widetilde{\mathbf{q}}})$, which expresses the difference of the strength of flame surface wrinkling at the scales of the flame thickness $\Delta = F\delta_l^0$ and at the test-filter size $\widehat{\Delta}$, and the value of β contains the information related to the strength of the unresolved wrinkling against that resolved on the computational mesh. The efficiency function E is calculated using the value of β and the turbulent strength, that is expressed using the fluctuating velocity u'_{Δ}. The value of E, thus, may become low (high), when u'_{Δ} is low (high), even if the value of β is high (low).

From this test, the interval for the averaging in the z direction is set to $dz = 0.04$ to conserve the local trend of β and that of the efficiency as found in Figure 5.6. It is also verified that the efficiency increases with the turbulence, although the value of β may decrease with it.

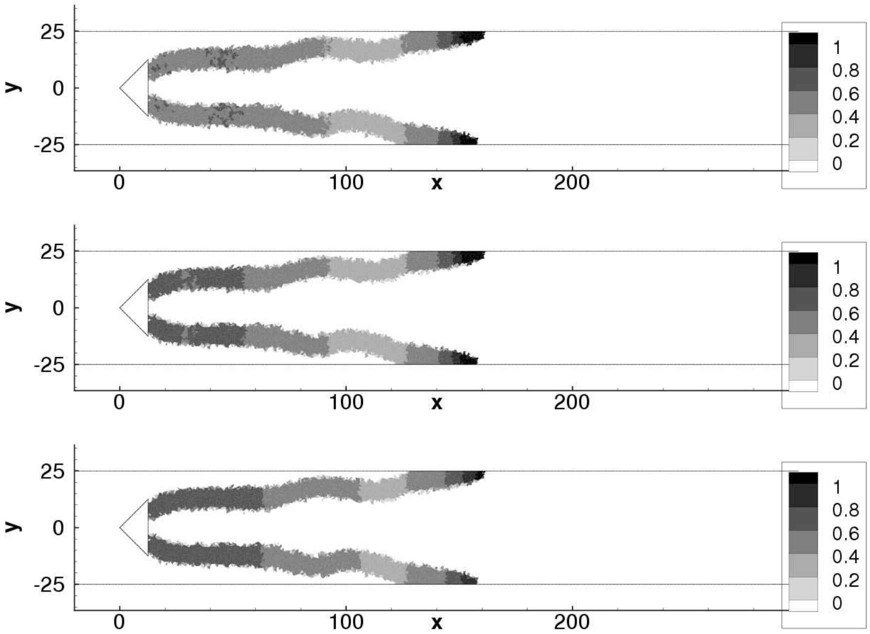

Figure 5.4 : *Comparison of the β fields on $z = 0$ plane calculated with different averaging interval. Top to bottom, local calculation, $l_z = 4.0 \times 10^{-2}$ m and the use of the whole span-wise dimension of the combustion chamber. Scales are given in mm*

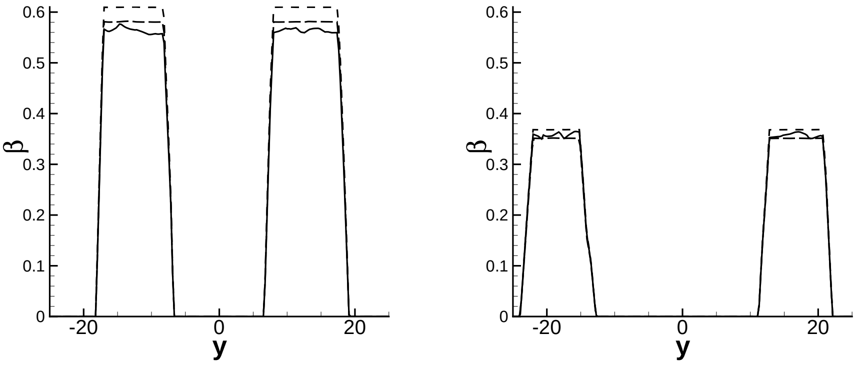

Figure 5.5 : *Comparison of the distribution of β calculated with different averaging intervals at $(x, z) = (0.06, 0)$(m, left) and $(x, z) = (0.12, 0)$(m, right): $dz = 0$ (solid line), $dz = 4.0 \times 10^{-2}$ m (bold dashed line) and the use of the whole span-wise dimension of the combustion chamber (dashed line)*

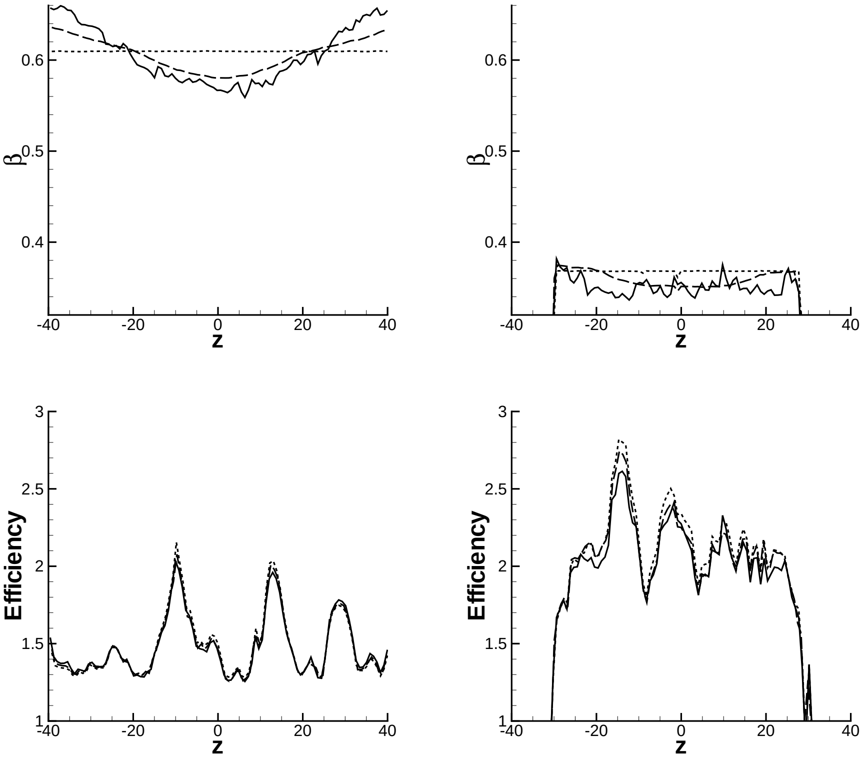

Figure 5.6 : *Comparison of β and efficiency field calculated with different averaging intervals at $(x, y) = (0.06, 0.01)$(m, left) and $(x, y) = (0.12, 0.02)$(m, right): $dz = 0$ (solid line), $dz = 4.0 \times 10^{-2}$ m (dashed line) and the use of the whole span-wise dimension of the combustion chamber (dotted line)*

5.3.2 Results of the test on the dynamic Smagorinsky model

Figure 5.7 compares the C_S fields calculated with different averaging intervals in the z direction. On the top is the result of local application of the dynamic Smagorinsky model with Moin's procedure. The averaging interval in z direction, which is represented by l_z, is zero. In the middle, l_z is $0.02\,m$, and on the bottom, l_z is the whole span-wise dimension of the chamber.

The C_S field was effectively smoothed, and the reduction of the oscillation of C_S was more remarkable than in the case of β. Contrary to the two-dimensional case, C_S was not zero in the reaction zone. The values were greater than 0.16 and considerably larger than the reference value $C_S = 0.0324$ in homogeneous turbulence. This is because of the three-dimensional structure of the turbulence. Though the thermal expansion of the flow media is likely to cause the negative Smagorinsky constant, the effect was weaker than the turbulence in the z direction. As C_S was calculated with the norm of the deformation rate $|\overline{S_{ij}}| = \sqrt{2\overline{S_{ij}}^2}$, C_S was not zero if the terms, corresponding to the deformation related to z direction, was dominant.

The distributions of C_S and μ_t in z direction are indicated in Figures 5.9 and 5.10 respectively. As in Figure 5.7, the oscillation of C_S decreased with the increase of l_z. Small oscillation existed also in the results calculated with averaging on the whole span-wise dimension of the combustion chamber. This is because of the use of an unstructured computational mesh. The values plotted in the figure was obtained through the interpolation using the values at the node points of cells that contain the line, where C_S was plotted. In the test case of dz conducted above for the calculation of β, the averaging was performed in a volume, and not on a line. The oscillation of the result was, therefore, clearly eliminated when dz was set as the whole span-wise dimension of the combustion chamber.

The levels of the oscillation observed in the results of $l_z = 0.02\,m$ and the whole span-wise length were of the same order of the magnitude. It implies that the $l_z = 0.02\,m$ is sufficient to reduce the oscillation of C_S and the use of longer interval eliminates the local information, such as the upheaval found in the results at $y = 0.01$ (in the middle) of $l_z = 0.02$. However, the value found at the upheaval was considerably large, and might cause unreasonable dissipation of momentum in the simulation conducted in the next section.

When the Smagorinsky constant C_S was locally calculated, the fields of the turbulent viscosity μ_t also oscillated following the distribution of C_S as shown in Figure 5.10. The occurrence of peaks is especially remarkable in the second and last figures in the left and right columns respectively. The discrepancies between the results calculated with $l_z = 0.02\,m$ and the use of the whole span-wise dimension of the combustion chamber as the averaging interval were not significant. However, as observed in the second figure in the left column, the value of μ_t in the middle of the chamber was approximately twice higher and it oscillated more strongly when it was calculated with $l_z = 0.02\,m$ than when it was done using the whole span-wise dimension as the averaging interval. This fact indicates the effect of the C_S values calculated with $l_z = 0.02\,m$ which may lead to an immoderate local dissipation of momentum and to numerical problems.

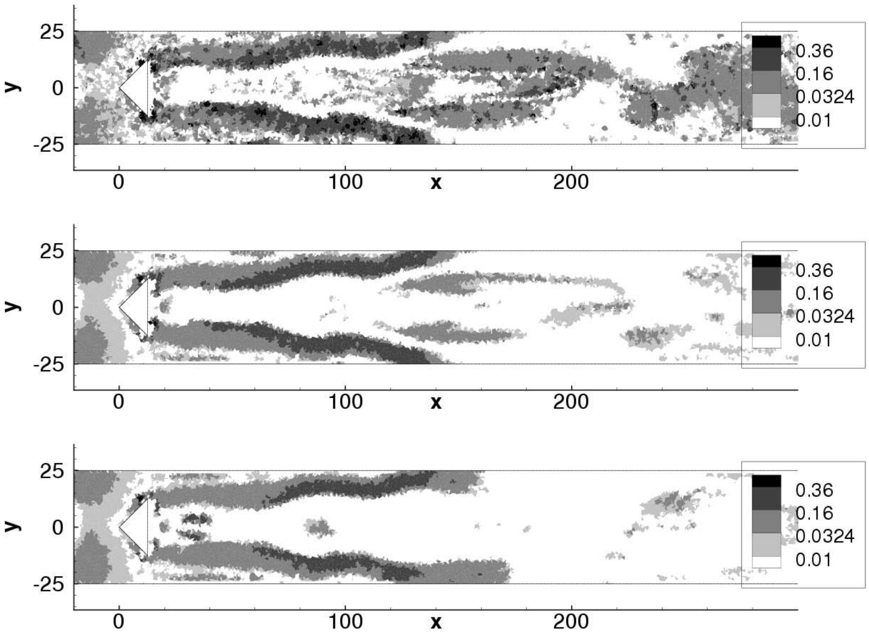

Figure 5.7 : *Comparison of the C_S fields on $z = 0$ plane calculated with different averaging intervals. Top to bottom, local calculation, $l_z = 4.0 \times 10^{-2}\ m$ and the use of the whole span-wise dimension of the combustion chamber. Scales are given in mm*

Through the test conducted here, it is verified that the use of larger l_z eliminates the oscillation of the Smagorinsky constant C_S effectively. In the simulations of this chapter, l_z is then set to the whole length of the combustion chamber. Note again that the negative values of C_S are clipped at $C_S = 0$ to avoid numerical problems.

5.4 Result and discussion

5.4.1 Three-dimensional effect of turbulence

Contrary to the two-dimensional simulations, results of three-dimensional simulations contain complex turbulent structures due to the existence of the third dimension, which enhances the dissipation of kinetic energy. To observe the effect of three-dimensional turbulence, instantaneous vorticity iso-surfaces of

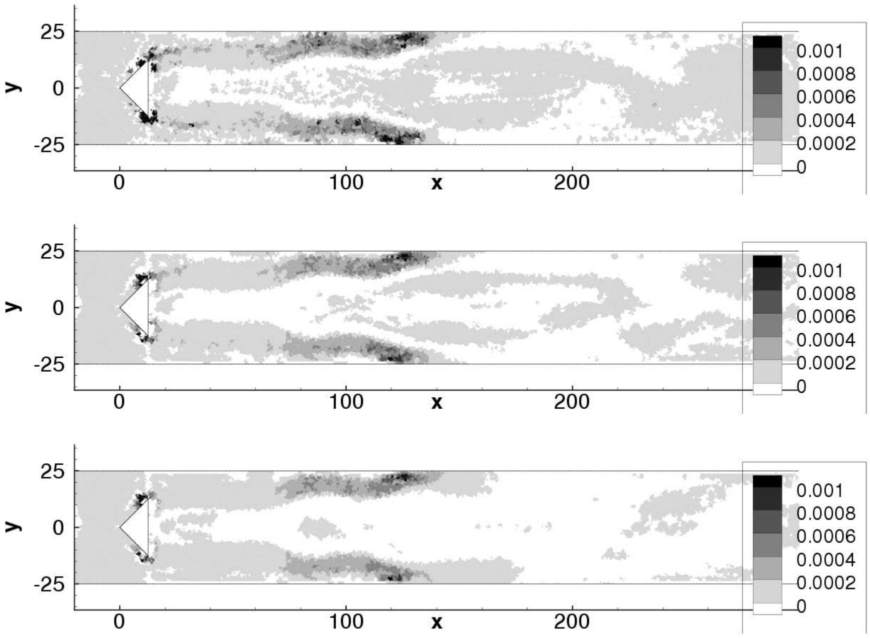

Figure 5.8 : *Comparison of the μ_t fields on $z = 0$ plane calculated with different averaging intervals. Top to bottom, local calculation, $l_z = 4.0 \times 10^{-2}$ m and the use of the whole span-wise dimension of the combustion chamber. Scales are given in mm*

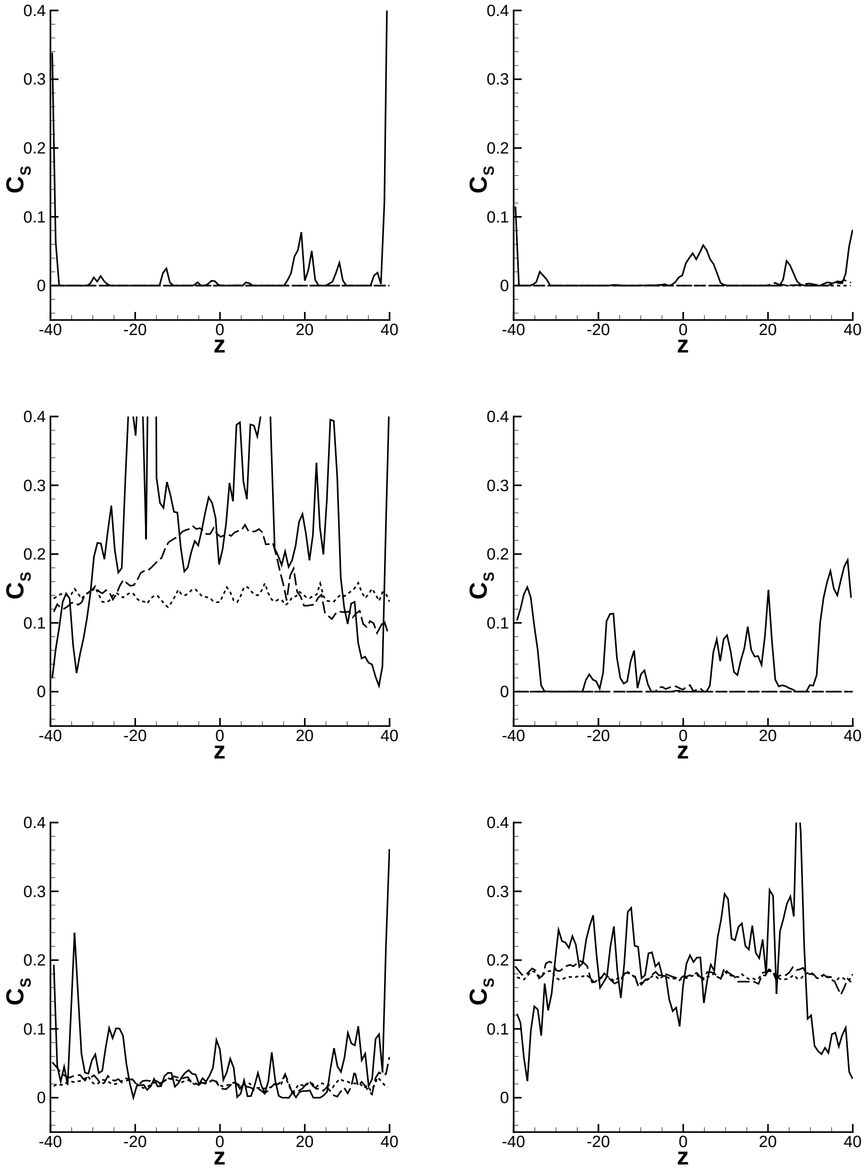

Figure 5.9 : *Comparison of the* C_S *distribution in z direction calculated with different averaging intervals at* $(x, y) = (0.06, 0)(0.06, 0.01)(0.06, 0.02)$*(m, left) and* $(x, y) = (0.12, 0)(0.12, 0.01)(0.06, 0.02)$*(m, right). Local calculation (solid line),* $l_z = 4.0 \times 10^{-2}$ *m (dashed line) and the use of the whole span-wise dimension of the combustion chamber (dotted line).*

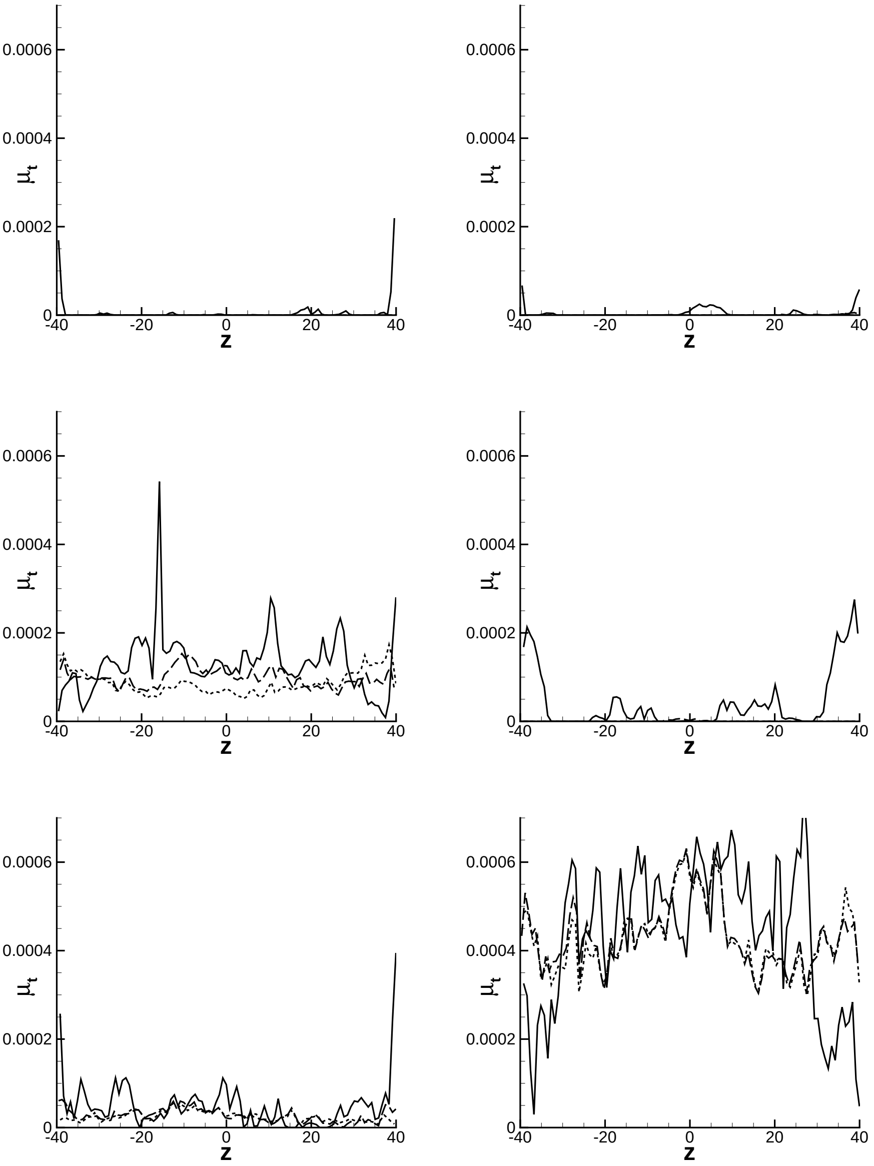

Figure 5.10 : *Comparison of the μ_t distribution in z direction calculated with different averaging intervals at $(x, y) = (0.06, 0)(0.06, 0.01)(0.06, 0.02)$(m, left) and $(x, y) = (0.12, 0)(0.12, 0.01)(0.06, 0.02)$(m, right). Local calculation (solid line), $l_z = 4.0 \times 10^{-2}$ m (dashed line) and the use of the whole span-wise dimension of the combustion chamber (dotted line).*

$|\omega| = 12000$ at $47\,ms$ after the simulation started ($t - t_0 = 47\ ms$), are presented in Figure 5.11. To distinguish different surfaces, the iso-surfaces are coloured by temperature. The sheet-like structure of the vorticity iso-surface indicates the existence of a shear flow. In this instantaneous field, a shear flow takes place downstream of the flame holder and the rear half of the combustion chamber. In these zones, the turbulent structures are two-dimentsional and three-dimensional effect of turbulence is weak. Between these zones, the sheet of the iso-vorticy surface is disturbed, because of the existence of eddy structures.

Figure 5.12 is the relative helicity iso-surfaces of $h = 0.9$ and $h = -0.9$ of the same instantaneous field as that presented in Figure 5.11. Helicity, H, and relative helicity, h, are quantities defined as the inner product of the velocity $\mathbf{u}$ and the vorticity $\omega = \nabla \times \mathbf{u}$, and its direction cosine, respectively,

$$H = \mathbf{u} \cdot \omega\,, \tag{5.2}$$

$$h = \frac{\mathbf{u} \cdot \omega}{|\mathbf{u}||\omega|}\,. \tag{5.3}$$

Then, H is non-zero when the directions of vorticity and the flow velocity are not orthogonal. High absolute values of relative helicity indicates the existence of a corkscrew-like motion around a streamline, then, that of the three-dimensional turbulent structure. It takes positive (negative) values when the corkscrew-like motion by the vorticity is clockwise (counter clockwise) viewed from the downstream in the flow. In two-dimensional simulations, helicity is always zero.

Effect on combustion

Figure 5.13 are the cross-sectional fields of the time averaged reaction rate of the principal reaction, $C_3H_8 + 5O_2 \Longrightarrow 3CO + 4H_2O$, at the center of the chamber ($z = 0$) and close to the lateral walls ($z = 0.035$ and $z = -0.035\ m$). Immediately downstream of the flame holder, the distance between the two flame surfaces was shorter close to the lateral walls than at the center of the chamber. The positions, where the flame reached the upper and lower walls, were also different. Near the lateral walls, the position was farther from the flame holder than at the center of the chamber. These deviations of the reaction zones were due to the existence of the lateral walls.

On the walls of the combustion chamber, heat loss boundary conditions were applied. Thus, temperature became lower near the wall than in the middle of the chamber as shown in Figure 5.14, and the reaction rate of the principal reaction was also reduced. The reduction of the reaction rate made the flame surfaces retreat, and the distance of the two flame surfaces reduced. As observed in Chapter 4, the increase of the reaction rate makes the acceleration of the flow occur closer to the flame holder. The discrepancy of the reaction rates

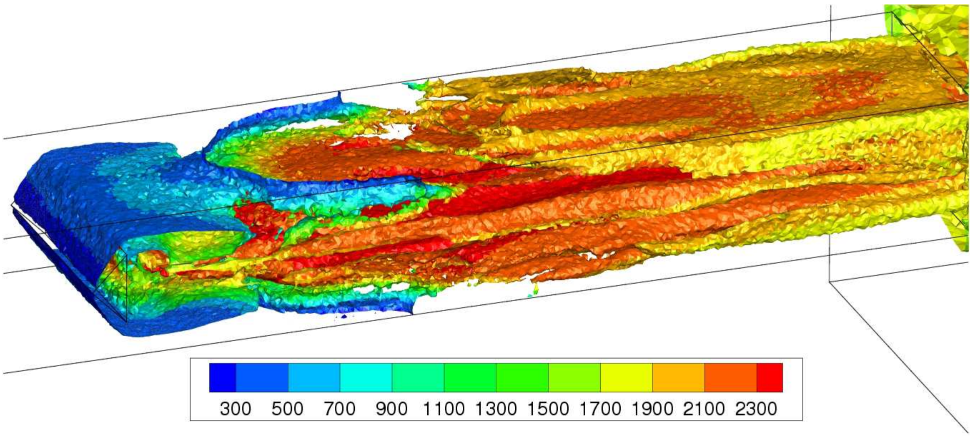

Figure 5.11 : *Iso-surface of vorticity magnitude, $|\omega| = 12000$, of an instantaneous field, 47 ms after the simulation started. To distinguish the different surfaces, the iso-surfaces are coloured by temperature (K).*

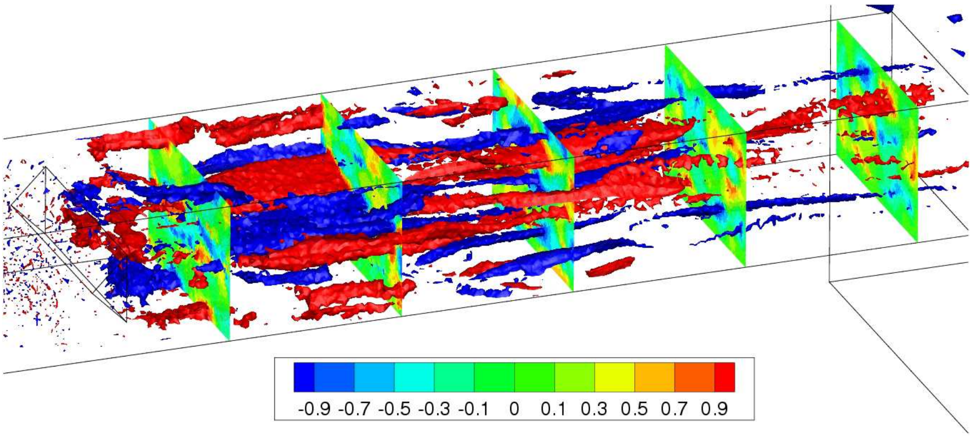

Figure 5.12 : *Iso-surfaces of relative helicity, $h = 0.9$ and $h = -0.9$, of an instantaneous field, 47 ms after the simulation started.*

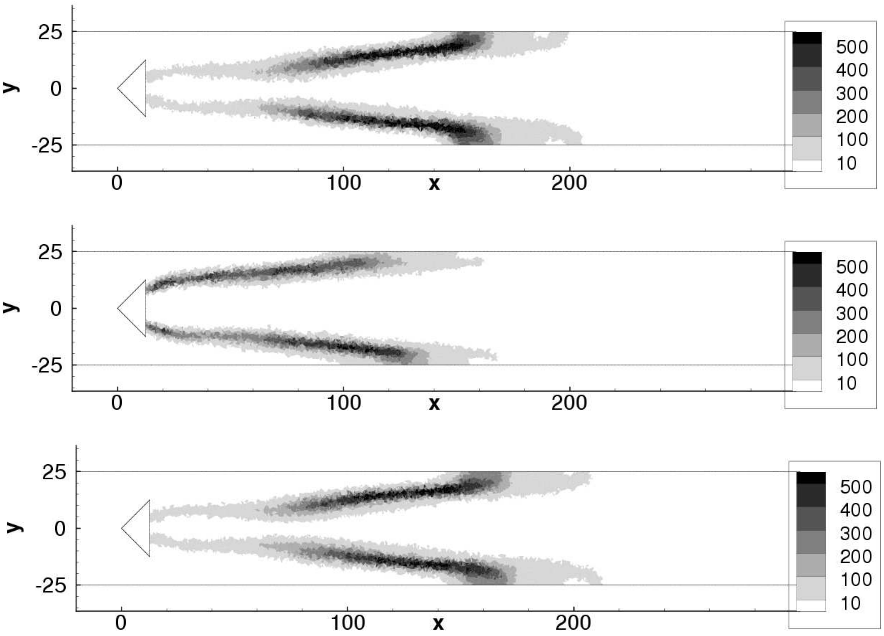

Figure 5.13 : *Time averaged reaction rate (kg/$m^3 \cdot s$) of the principal reaction, $C_3H_8 + 5O_2 \Longrightarrow 3CO + 4H_2O$, on several z planes. Top to bottom, on $z = -0.035$, $z = 0$, and $z = 0.035$ (m) planes. Scales are given in mm.*

between near wall region and in the center of the chamber, then, resulted in the difference of the size of the recirculating zone found in the time averaged fields as will be discussed below.

Structure of the recirculation zone

In two-dimensional simulations presented in the previous chapter, the recirculation zone found in time averaged fields behind the flame holder consisted of two vortices. Also in the three-dimensional simulation performed here, two vortices were found in the time averaged field of flow velocity, and they contained a three-dimensional motion. Figure 5.15 is the cross-sectional fields of the time averaged velocity in the x direction, $[\widetilde{u}_x]$, at the center of the chamber ($z = 0$) and close to the lateral walls ($z = 0.035$ and $z = -0.035\,m$) with the streamlines based on the x and y components of the time averaged velocity fields. $[\cdot]$ represents the time averaging, $[Q] = \int_{t_0}^{t_f} Q(t)dt / \int_{t_0}^{t_f} dt$, where t_f and t_0 are the final and start times of the averaging period respectively. The existence of the stagnation points in the figures of $z = 0.035$ and $z = -0.035$ planes were caused by sources due to the convection in the z direction. The size of the recirculation zone, where the x component of the time averaged velocity $[\widetilde{u}_x]$

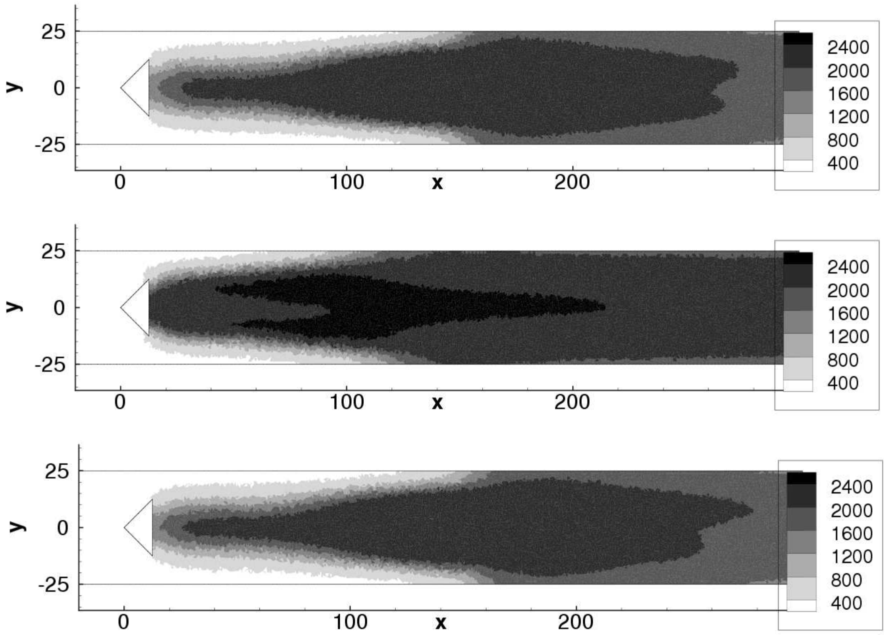

Figure 5.14 : *Time averaged temperature (K) on several z planes. Top to bottom, on $z = -0.035$, $z = 0$, and $z = 0.035$ (m) planes. Scales are given in mm.*

was negative, was considerably larger close to the walls than in the middle of the combustion chamber.

Figure 5.16 displays the streamlines of the time averaged flow field in the recirculation zone based on the velocity components of y and z directions in $x = 0.015$, $x = 0.0325$, and $x = 0.05$ (m) planes with the amplitudes of the time averaged velocity in z direction $[\widetilde{u}_z]$. Directly downstream of the flame holder ($x = 0.015$), the streamlines pointed towards the center of the chamber, while they pointed opposite directions in the other planes at $x = 0.0325$ and $x = 0.05$ (m).

Figure 5.17 presents the streamlines of the time averaged flow field that started from vertical lines at $(x, z) = (0.02, 0.035)$(m) and $(x, z) = (0.02, -0.035)$, with the time averaged field of the z component of the flow velocity $[\widetilde{u}_z]$ on the $y = 0$ plane. All the streamlines, started in the recirculation zone close to the wall, came to the center of the combustion chamber, being involved into the recirculation motion, and exited from the recirculation near the centerline of the chamber.

These results show that there existed a recirculation motion, that advected heat and mass from the wall-sides to the center of the chamber directly downstream of the flame holder.

5.4.2 Temporal evolution and time average of the flame surface

Temporal evolution of β and the efficiency fields

In Figures 5.18 and 5.19, temporal evolutions of dynamically calculated Charlette's constant β and the value of the efficiency function E on the $\widetilde{c} = 0.5$ surface are shown. The progress variable was defined using the mass fraction of C_3H_8. To present the profile of the flame surface, contour lines of the y coordinate are shown on the surface.

As the first (left top) figures of Figures 5.18 and 5.19 indicate, a hill was observed behind the flame holder at $t - t_0 = 70.2$ (ms). The hill was convected downstream changing its height, and at $t - t_0 = 73.3$, it reached the upper wall of the combustion chamber. The zone where the flame surface interacted with the wall became larger at $t - t_0 = 74.1$, and the profiles of the flame surface turned to be similar to that of at $t - t_0 = 70.2$. Thus, these six figures correspond to a cycle of the periodic motion of the flame surface. The period is approximately 4 ms.

Throughout the period, the y coordinates of the flame surface were always higher close to the centerline of the chamber than close to the lateral walls. This was related to the heat loss boundary conditions applied to the walls. The chemical reaction beside the lateral walls was limited by low temperature compared with that in the middle of the chamber as already shown in Figures 5.13 and 5.14.

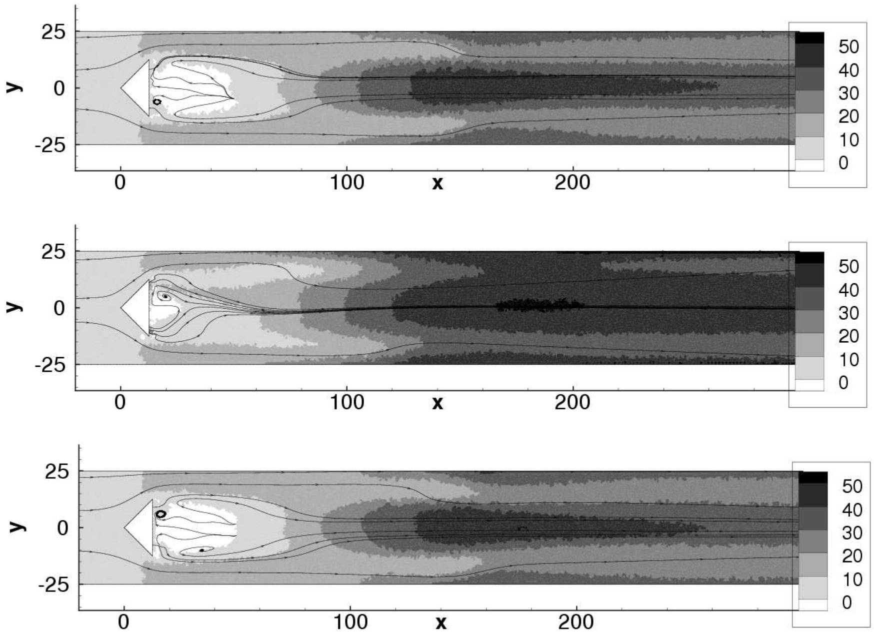

Figure 5.15 : *Amplitude of the time averaged* x *component of the flow velocity* $[\widetilde{u}_x]$ *(m/s) and the streamlines of the time averaged field based on the velocity components of the* x *and* y *directions. Top to bottom, on* $z = -0.035$, $z = 0$, *and* $z = 0.035$ *(m) planes*

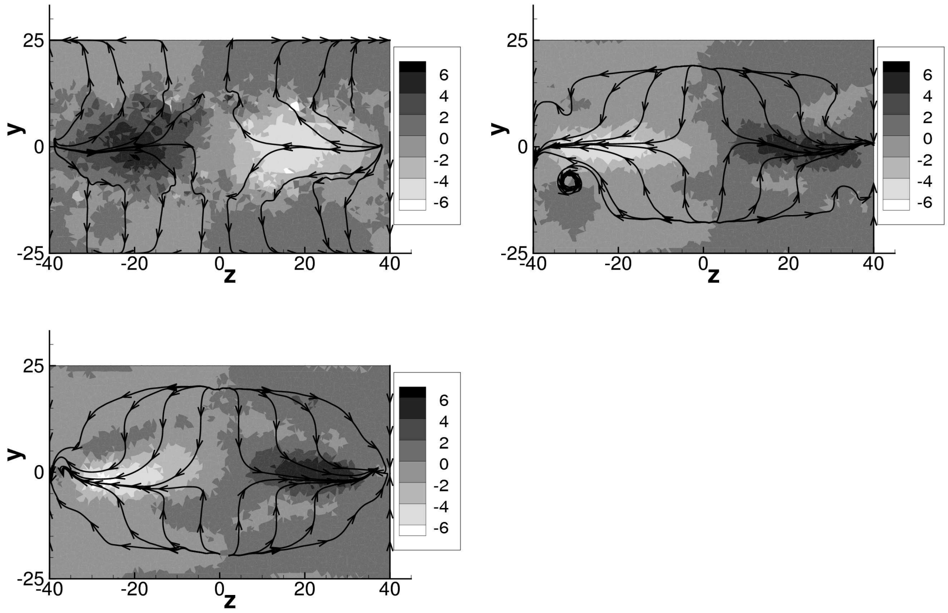

Figure 5.16 : *Amplitude of the time averaged z component of the flow velocity* $[\widetilde{u}_z]$ *(m/s) and the streamlines of the time averaged field based on the velocity components of the z and y directions. On* $x = 0.015$ *(m) (top left),* $x = 0.0325$ *(m) (top right), and* $x = 0.05$ *(m) (bottom) planes.*

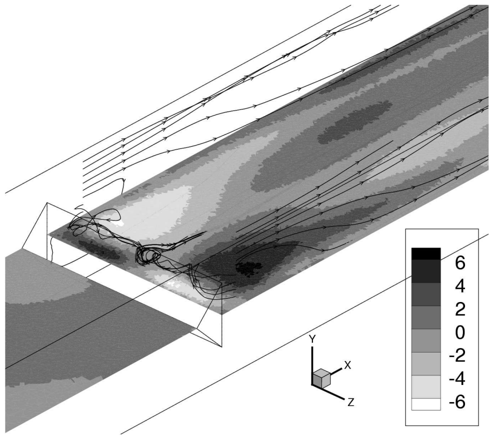

Figure 5.17 : *Streamlines of the time averaged flow field that start from vertical lines at* $(x, z) = (0.02, 0.035)$ *and* $(0.02, -0.035)$*(m), with the time averaged field of the z component of the flow velocity* $[\widetilde{u}_z]$ *(m/s) on the* $y = 0$ *plane. Scales are given in mm.*

The occurrences of local peaks in terms of the height of the flame surface along the x direction firstly found in the middle of the chamber, and then, close to the walls. Consequently the flame surface had three-dimensional profile, and the values of β varied in the z direction.

The magnitude of β is determined by the relation of the flame surface wrinkling at the flame thickness scale $F\delta_l^0$ and that at the test-filter scale $\widehat{\Delta}$. When the wrinkling of the flame surface at the scale of $F\delta_l^0$ is strong compared to that at the scale of $\widehat{\Delta}$, the term $\gamma \overbrace{W_{\Delta}(\widetilde{\mathbf{q}})} / W_{\widehat{\Delta}}(\widehat{\widetilde{\mathbf{q}}})$ becomes large, then β also becomes large. In fact, the value of the term $\gamma \overbrace{W_{\Delta}(\widetilde{\mathbf{q}})} / W_{\widehat{\Delta}}(\widehat{\widetilde{\mathbf{q}}})$ strongly depends on the wrinkling of the resolved flame surface. Thus, Figure 5.18 indicates that the resolved wrinkling of the flame surface was high close to the flame holder and it reduced with the x coordinate. Immediately downstream of the flame holder, the values of the constant β tended to be larger close to the lateral walls than in the middle of the combustion chamber. This was due to the high curvature close to the walls. Though the resolved flame surface contained a large structure in the middle of the chamber, the curvature was small and the value of β remained small. On the contrary, small wrinkling structures found close to the lateral walls resulted in the larger values of β than in the center.

However, the trend reversed after the flame surface reached the upper wall in the middle of the chamber. When it interacted with the upper wall, a bowl-shaped structure was formed around and induced high curvature. This resulted in the higher β values in the middle of the chamber than close to the wall regions.

The trend of the efficiency function E was different from that of β. Directly downstream of the flame holder, there was a zone where the efficiency function was larger than 5.0. The efficiency function had the same trend of the constant β in this zone, i.e., higher values close to the lateral walls than close to the centerline of the chamber. However, this trend was limited here, and the values of the efficiency function close to the centerline of the chamber quickly became larger than close to the lateral walls. This trend was especially remarkable in the second figure in the left column of Figure 5.19. This was caused by the different magnitude of the flcutuating velcity u'_{Δ} at the flame thickness scale.

In the results presented in Figures 5.18 and 5.19, the fluctuating velocity was higher in the middle of the chamber than beside the lateral walls. Then turbulence was stronger in the middle, but the flame surface was wrinkled in a manner that it had a larger structure here. Most part of the wrinkling was resolved on the mesh, and the value of the constant β became lower here than beside the lateral walls. However, the high fluctuating velocity kept the efficiency function larger than that in the zones close to the walls.

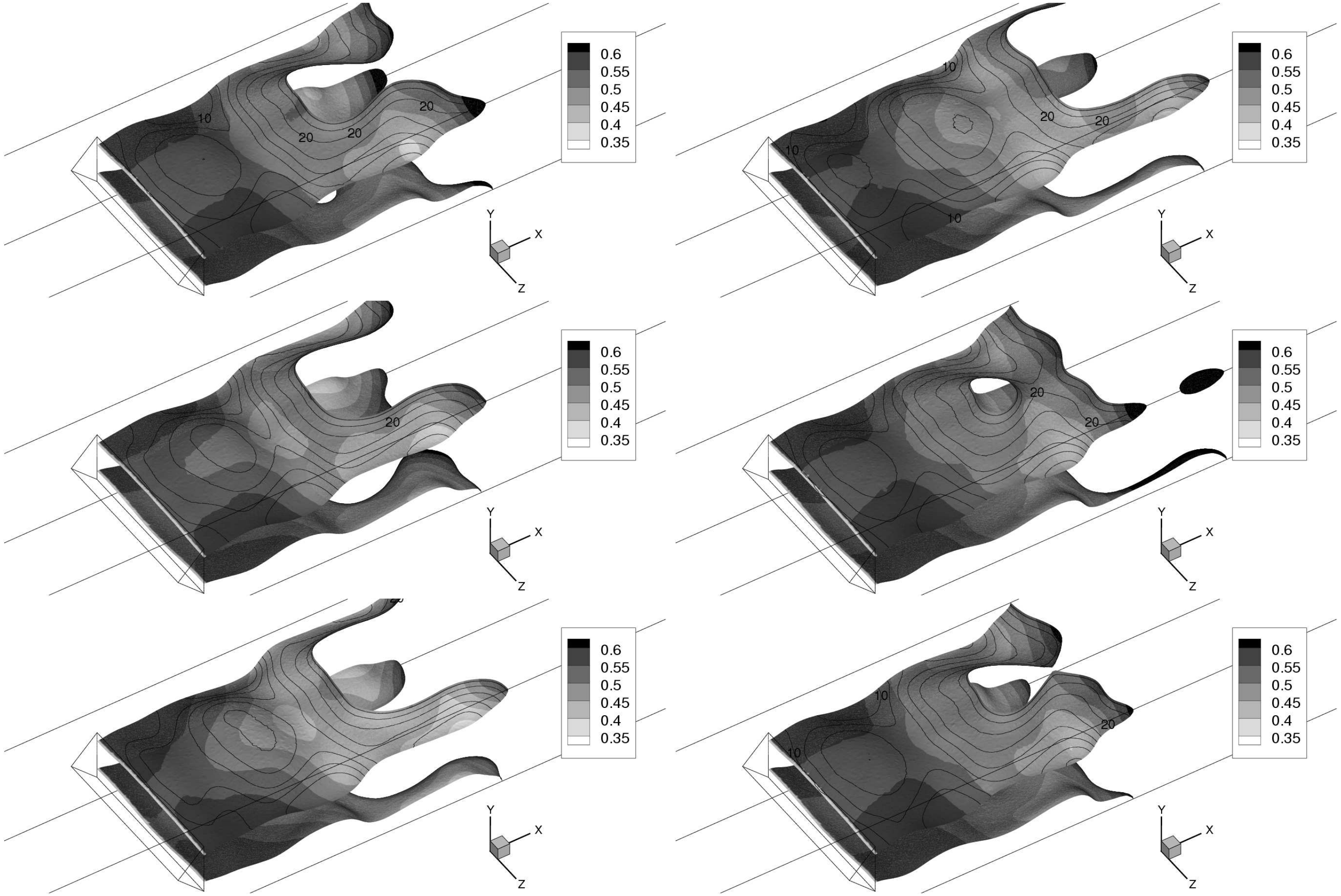

Figure 5.18 : *Temporal evolution of dynamically calculated Charlette's constant* β *on the* $\widetilde{c} = 0.5$ *surface at* $t - t_0 =$ 70.2, 71.0, 71.8, 72.5, 73.3, *and* 74.1 *(ms) (top to bottom, left to right). The contour line indicates the* y *coordinate (mm).*

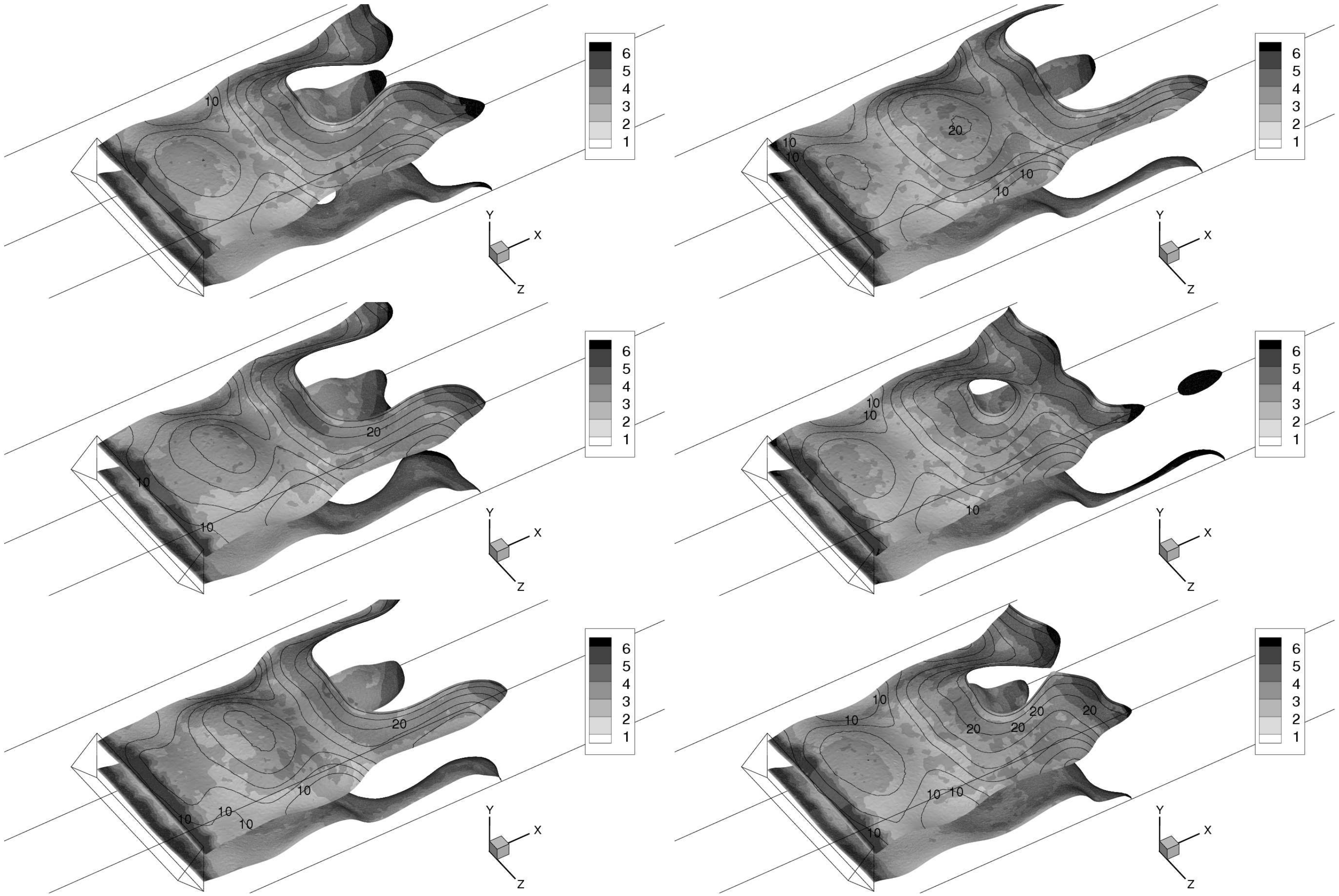

Figure 5.19 : *Temporal evolution of the value of the efficiency function on the* $\widetilde{c} = 0.5$ *surface at* $t - t_0 = 70.2$, 71.0, 71.8, 72.5, 73.3, *and* 74.1 *(ms) (top to bottom, left to right). The contour line indicates the* y *coordinate (mm).*

Analysis of the time averaged properties

The time averaged fields of Charlette’s constant β and the value of the efficiency function E in the planes of $z = 0$, $z = -0.035$, and $z = 0.035$ (m) are presented in Figures 5.20 and 5.21. Since the values of the constant β were calculated only in the reaction zone, they were set to zero outside of the flame. The time averaged values of β were then obtained by summing up the values calculated in the presence of the flame multiplied by the time step, and dividing it by the sum of the time steps, during which the flame had been present. Zero values were also taken into account, only when the values are calculated in the presence of the reaction zone. The time averaged values of the efficiency function E were also calculated in the same manner. In Figure 5.20, though the time averaged fields of β on $x = -0.035$ and $z = 0.035$ (m) planes show small differences at $x \approx 0.04$ and $x \approx 0.12$ (m), the β values at these positions are approximately 0.6 and 0.4 respectively, and the results of these two planes are quite similar and symmetrical along the $z = 0$ plane.

Unlike to the two-dimensional case, the two flame surfaces were completely separated and the value of the constant β was always zero between these flame surfaces. The values of both β and the efficiency function in the reaction zone were higher than the values observed in the two-dimensional simulations (see Figures 4.9, 4.20, and 4.21 of Chapter 4). This is due to the fact that the reaction rate ratio $\overbrace{W_{\Delta}(\widetilde{\mathbf{q}})}/W_{\gamma\Delta}\left(\widehat{\widetilde{\mathbf{q}}}\right)$ that appears in the formulation, was larger than in the two-dimensional simulations, meaning that the wrinkling of the resolved flame surface was stronger. It was especially strong immediately behind the flame holder and in the zone, where the flame reached the walls. However, the values of β are between 0.4 and 0.6 except at the tail of the flame, and close to the recommended value 0.5 by Charlette et al. (2002a).

The values of these time averaged fields are in good accordance with the values observed in the temporal evolution of the flame surface. This indicates that periodic motions of the flame surface are similar to the one discussed above, and the presented period represented well the others.

5.4.3 Output of the dynamic Smagorinsky model

Figures 5.22 and 5.23 respectively display the time averaged fields of the Smagorinsky constant C_S calculated with Moin’s procedure in the $z = 0$ plane and the turbulent viscosity μ_t in $z = 0$, $z = 0.035$, and $z = -0.035$ planes. As the intermediate terms for the calculation of C_S were averaged in the z direction, the fields of C_S were identical in any z planes. Thus, only the field in the $z = 0$ plane is displayed.

Same as the two-dimensional simulations performed in the previous chapter, time averaged value of C_S took high values immediately downstream of the flame holder and in the reaction zone. The values of C_S were of the same order

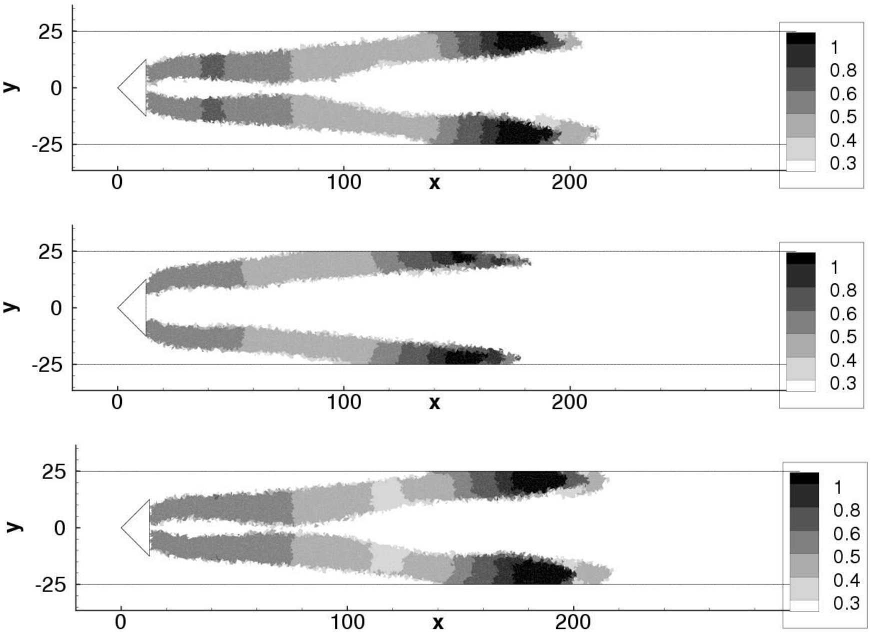

Figure 5.20 : *Time averaged field of Charlette’s constant β. The time averaged values were calculated using the values at the presence of the reaction zone and the total present time of the reaction zone at the target position. Top to bottom, $z = -0.035$, $z = 0$, and $z = 0.035$ (m) planes. Scales are given in mm.*

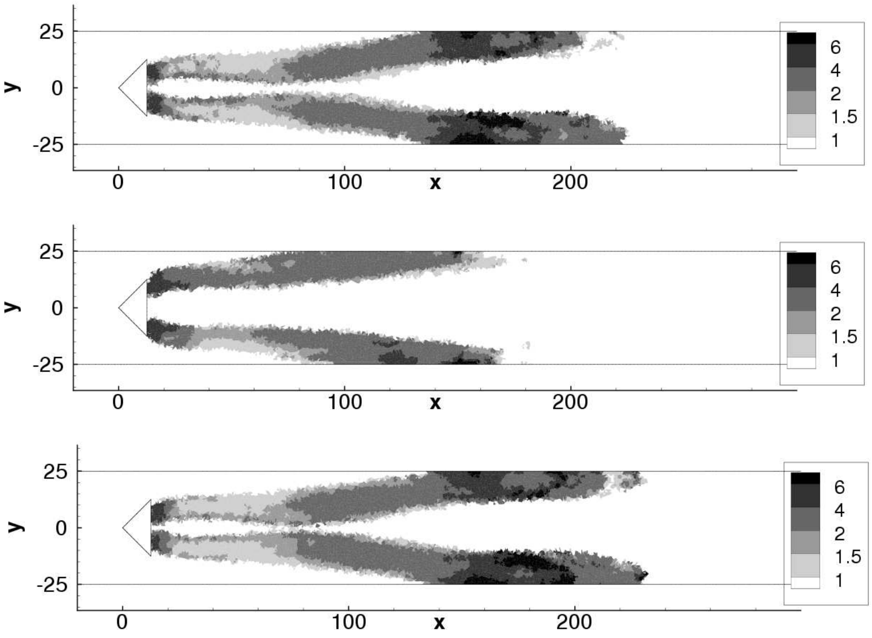

Figure 5.21 : *Time averaged field of the efficiency function. The time averaged values were calculated using the values at the presence of the reaction zone and the total present time of the reaction zone at the target position. Top to bottom,* $z = -0.035$*,* $z = 0$*, and* $z = 0.035$ *(m) planes. Scales are given in mm.*

of the magnitude as the two-dimensional case presented in the second figure of Figure 4.15 in Chapter 4, but the turbulent viscosity was considerably larger than in the two-dimensional case (see Figure 4.16 of Chapter 4). Consequently the turbulence in the burnt gas became weaker than in the two-dimensional case, and C_S was also lower. This represents the higher dissipation of three-dimensional turbulence than that of the two-dimensional one.

5.5 Comparison with experimental results

In this section, the simulation results are compared with the experimental results obtained by Knikker et al. (2002) and Knikker et al. (2004) by appliying the Planar laser induced fluorescence (PLIF) on the OH radical in the center-plane of the combustion chamber.

The field of the instantaneous progress variable c was reproduced assuming an infinitely thin flame front. Then Favre averaged field of the progress variable $\widetilde{c}$ was obtained by a Gaussian filter of size $\mathit{\Delta} = F\delta_l^0 = 9.69$ (mm), and the ensemble average of the progress variable $[\widetilde{c}]$ was obtained by processing 200 images.

Figure 5.24 compares the time averaged Favre filtered progress variables $[\widetilde{c}]$ and its resolved variance $\left[\widetilde{c}^2\right] - [\widetilde{c}]^2$, obtained from the simulation performed in this chapter, and in the experiments of Knikker et al. (2002) and Knikker et al. (2004). $[\cdot]$ represents time averaging, $[Q] = \int_{t_0}^{t_f} Q(t)dt / \int_{t_0}^{t_f} dt$, where t_f and t_0 are the final and start times of the averaging period respectively.

The results indicate qualitatively similar trends, that the flame surface approached to the walls and the variance increased with the x coordinate, but all the plots also indicate that the simulated flame surface was closer to the walls than that of the experiment at every x position. This infers that the reaction rate was overestimated in the simulation.

Several factors can be mentioned as possible sources of this overestimation, for example, lower heat losses at the walls than in reality, the use of the two-step reaction model, the effect of the assumption applied to post-process the experimental results that the flame is infinitely thin, and the possibility that the stabilization of flame at the flame holder was not reproduced well through the thickened flamelet approach, i.e. the interaction between the thickened flame and turbulence was modified by flame thickening. The last one is the same problem as that Gonçalves dos Santos (2007) encountered. Here, however, the discussion is focused on the values of the efficiency function calculated with the dynamic thickened flamelet model, assuming that the overestimation of the reaction rate was due to the higher values of the efficiency function than required. This assumption is plausible especially immediately downstream of the flame holder, where the dynamic thickened flamelet model predicted values of the efficiency function larger than 4.0 as shown in Figures 5.19 and 5.21.

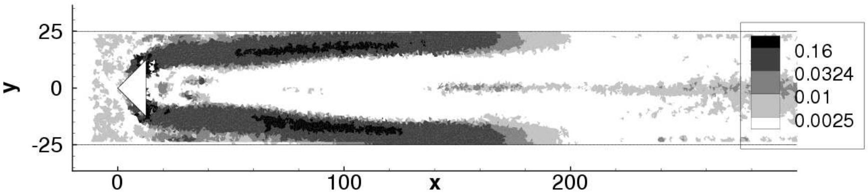

Figure 5.22 : *Time averaged field of the dynamically calculated Smagorinsky constant* C_S. *Scales are given in mm.*

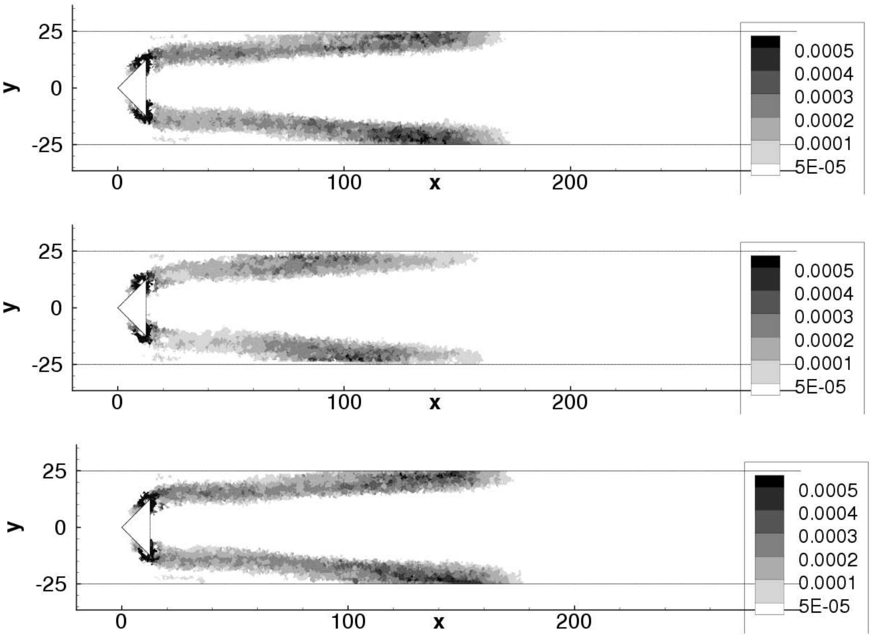

Figure 5.23 : *Time averaged fields of the turbulent viscosity* μ_t. *Top to bottom,* $z = -0.035$, $z = 0$, *and* $z = 0.035$ *(m) planes. Scales are given in mm.*

The whole flame surface would retreat to the downstream, if the values of the efficiency function were smaller in this zone, and may become closer to that obtained through the experiment.
In this study, the formulation of the dynamic procedure was modified to avoid unphysically high values of β. The motivation of this modification was that the value of $u'_{\gamma\Delta}$ calculated by the relations,

$$\epsilon = \frac{u'^3}{\Delta_x} = \frac{{u'_\Delta}^3}{\Delta} = \frac{{u'_{\gamma\Delta}}^3}{\gamma\Delta} \tag{5.4}$$

and

$$u'^3 = c_2 \Delta_x^3 \nabla^2 (\nabla \times \widetilde{\mathbf{u}}) \tag{5.5}$$

did not yield reasonable values of β. Both u'_Δ and $u'_{\gamma\Delta}$ were so small that the term $\left(1 + \min\left[\frac{\gamma\Delta}{\delta_l^0}, \mathbf{\Gamma}\frac{\langle u'_{\gamma\Delta}\rangle}{s_l^0}\right]\right) / \left(1 + \min\left[\frac{\Delta}{\delta_l^0}, \mathbf{\Gamma}\frac{\langle u'_\Delta\rangle}{s_l^0}\right]\right)$ in the formulation of the dynamic procedure, Equation 1.89, became approximately unity, and consequently β diverged. The modification was done by approximating that the ratio of the terms related to the turbulence strength at the scale of the thickness of the thickened flame $F\delta_l^0$ and that at the test filter scale $\widehat{\Delta}$ is equal to the effective filter size ratio γ,

$$\frac{1 + \min\left[\frac{\gamma\Delta}{\delta_l^0}, \mathbf{\Gamma}\frac{\langle u'_{\gamma\Delta}\rangle}{s_l^0}\right]}{1 + \min\left[\frac{\Delta}{\delta_l^0}, \mathbf{\Gamma}\frac{\langle u'_\Delta\rangle}{s_l^0}\right]} \approx \gamma\,. \tag{5.6}$$

This approximation avoided the apparition of unphysically high values of β as observed in Chapter 3 and kept it between 0 and 1.
However the comparison of the results of the simulation performed with this modified model and the experiment indicates that the values of the efficiency function calculated with this approximation were higher than those expected from the experimental result, showing that the values of β was higher than those in reality. This means that the left-hand-side term of Equation 5.6 should have been larger than γ, and the modified version of the dynamic procedure requires further development.
The other possibility to obtain the value of the left-hand-side term of Equation 5.6 is to solve the balance equations for the subgrid-scale turbulent kinetic energy k_Δ and $k_{\gamma\Delta}$, at the flame thickness scale $\Delta = F\delta_l^0$ and the test filter scale $\gamma\Delta$ and to calculated u'_Δ and $u'_{\gamma\Delta}$. This method was not tested in this study, as it requires to close and solve two additional transport equations and increase the numerical costs. However, this is worth testing in the future.
From the comparison of the results of the simulation and the experiment, the dynamic thickened flamelet model was observed to predict the reaction rate

higher than in the experiment. It may be related to the problem that Gonçalves dos Santos (2007) also encountered. The stabilization of flame at the flame holder was not reproduced well through the thickened flamelet approach, i.e. the interaction between the thickened flame and turbulence was modified by flame thickening. However, these two flames are qualitatively quite similar, and this fact shows the capability of the dynamic thickened flamelet model of calculating the turbulent combustion without any input for the efficiency function.

5.6 Computational costs of the dynamic procedures

Table 5.1 gives the numerical parameters of the simulation performed in this chapter and tables 5.2 and 5.3 compare its computational costs for different CPU numbers with optimized combinations of the CPU numbers for the AVBP code, which conducted the simulation, and the DTF-DS code, which calculated the values of the model constants. These values were obtained through simulations on an IBM Power 6 cluster of IDRIS (Institute for Development and Resources in Intensive Scientific computing) in France. As explained in Appendix B, the model constants such as Charlette's constant β and the Smagorinsky constant C_S were calculated separately from the simulation of the turbulent combustion which was performed in the AVBP code. The two codes were coupled every 100 iterations (see Figure B.2).
From the balance of the number of processors for the AVBP and DTF-DS codes shown in Table 5.2 the simulations with the dynamic procedures cost more than twice as much as those with constant model constants, but as Table 5.3 shows, the percentage of the CPU time of the dynamic procedures in the total CPU time decreased as the number of processors increased. The increase of the computational costs with the increase of the number of processors occurred at the AVBP side rather than at the DTF-DS side. This resulted from the different frequencies of data exchanges among the CPUs in each code, i.e., the increase of data exchange due to the increase of CPU number was more dramatic in the AVBP code than in the DTF-DS code, where the AVBP code computed 100 iterations while the DTF-DS code calculated Charlette's constant β just once. When a larger number of processors are available, the percentage is expected to further decrease, and the additional cost due to the implementation of the dynamic procedures becomes less important. At least in the present study, the total computational costs remained at an accessible level. Furthermore, the present study did not focus on the optimization of the computational performance of the dynamic thickened flamelet model. The computational costs can probably be decreased by introducing sophisticated algorithms.

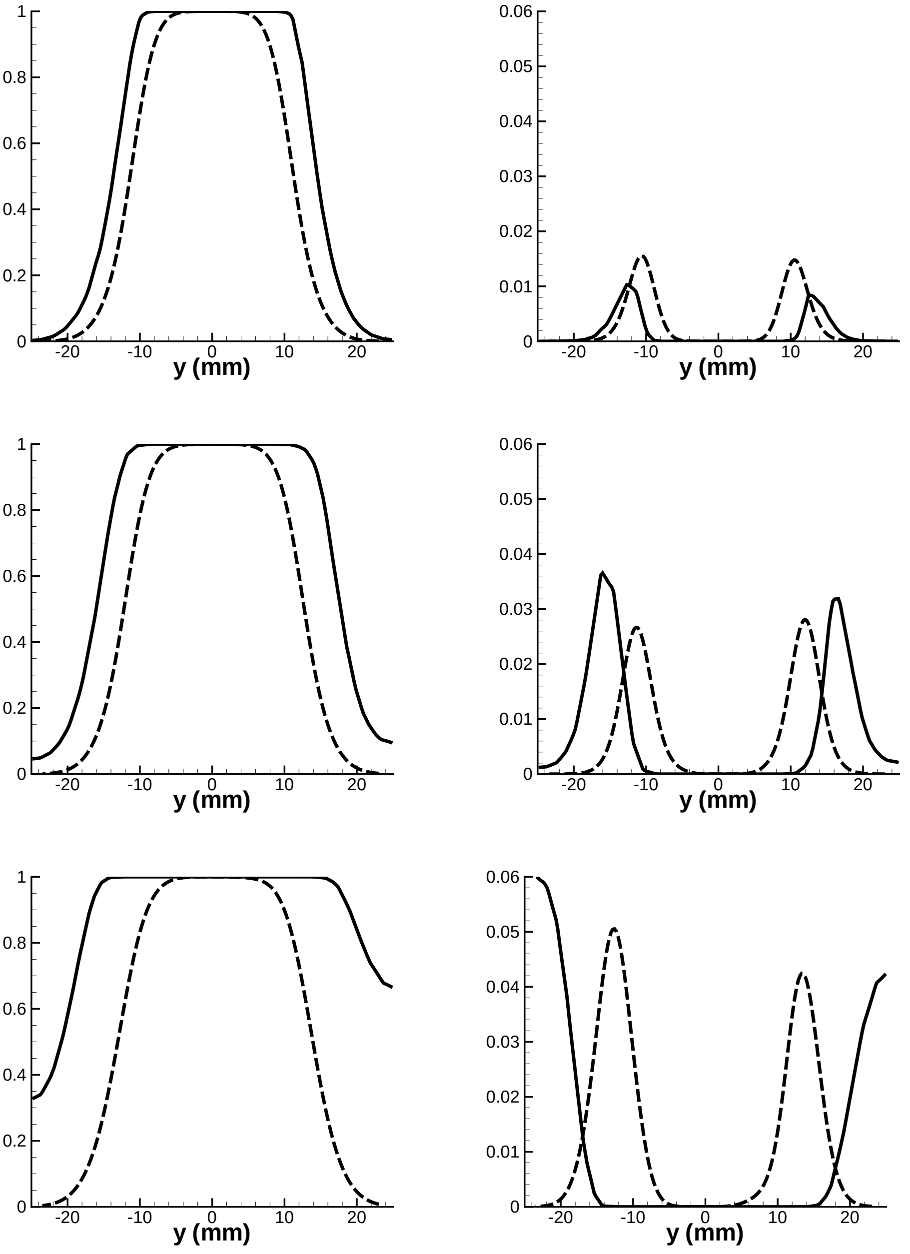

Figure 5.24 : *Comparison of the time averaged filtered progress variable* $[\widetilde{c}]$ *(left) and its resolved variance* $\left[\widetilde{c}^2\right] - [\widetilde{c}]^2$ *(right) obtained through the simulation (solid line) and the experimental data (dashed line), where* $[\cdot]$ *represents the time averaging. Top to bottom, at* $x = 0.0325$*,* 0.0725*, and* 0.1125 *(m). These distances respectively correspond to* 0.02*,* 0.06*, and* 0.10 *(m) downstream of the flame holder. Scales are given in mm in the plots.*

Number of grid points	Number of iterations	Coupling frequency
460434	300000	100

Table 5.1 : *Numerical parameters of the simulation.*

Number of processors			Computational	Physical	CPU	Restitution
Total	AVBP	DTF-DS	efficiency (μs)	time (s)	time (h)	time ($days$)
64	23	41	201.7	0.08	7740	5.0
128	50	78	211.4	0.08	8110	2.6
192	81	111	233.5	0.08	8960	1.9

Table 5.2 : *Comparison of the computational costs of the simulation performed with the dynamic thickened flamelet (DTF) and the dynamic Smagorinsky (DS) models. These values were obtained through simulations on an IBM Power 6 cluster of IDRIS (Institute for Development and Resources in Intensive Scientific computing) in France. The calculation of DTF and DS models were performed successively on the same processors. Computational efficiencies were calculated through* $[\,CPU\ time\,]\,/\,([\,number\ of\ iterations\,] \times [\,number\ of\ grid\,points\,])$.

Number of processors	CPU time (h)		
	Total	AVBP	DTF-DS
64	7740	2780	4960
128	8110	3150	4960
192	8960	3780	5180

Table 5.3 : *Comparison of the CPU time of the simulation part (AVBP) and the part of the dynamic procedures (DTF-DS).*

5.7 Conclusion

In this chapter, a three-dimensional full dynamic simulation of a V-shape flame was performed. The time averaged field of the Favre filtered progress variable $[\widetilde{c}]$ was then compared to the experimental result. The study in this chapter is concluded as follows:

- The analysis of vorticity and helicity revealed the existence of three-dimensional turbulent structure. This fact shows the importance of the three-dimensional simulation.
- In addition to a recirculation motion of two vortices that lie along the spanwise direction behind the flame holder, a convection motion from the wallside to the center of the chamber was observed in the recirculation zone.
- The heat loss boundary condition yielded the difference of the temperature between close to the centerline of the combustion chamber and beside the lateral walls. It resulted in the remarkable difference of the reaction rate between these zones.
- The comparison of the result with that of the experiment infers that the values of the dynamically calculated Charlette's constant were larger than the values required to reproduce the experimental result. It could be caused by poor prediction of the turbulence strength at the flame thickness scale and at the test-filter scale or poor descriptions of the flame stabilization immediately downstream of the flame holder by the thickened flamelet model.
- The simulation result may be developed by solving transport equations of kinetic energy for the calculation of fluctuating velocity.
- The numerical cost of the simulation performed with the dynamic procedures was more than twice as much as that of simulations with constant model constants, but it remains at an accessible level.

Conclusions and perspectives

Conclusions

In this study, the dynamic thickened flamelet model, which had been originally proposed by Charlette et al. (2002b), was implemented into the AVBP code, which was developed by CERFACS and IFP for simulations of turbulent combustion, and a series of simulations of a V-shape flame stabilized downstream of a triangle flame holder were performed in combination with the dynamic Smagorinsky model.

For the implementation, the thickened flamelet model was first tested with a one-dimensional laminar flame resolved on a sufficiently fine computational grid, where the value of the flame front wrinkling factor should be unity. The ability of the dynamic thickened flamelet model in a weak form was well verified, while that in a strong form induced divergence of the efficiency function, and did not represented laminar conditions.

The thickened flamelet model in a weak form was then tested using a laminar one-dimensional flame resolved on an LES mesh by the use of the thickened flamelet approach. It succeeded in reproducing laminar conditions, despite that the mesh was relatively coarse and the flame was artificially thickened.

After the tests under laminar conditions, the model was applied to an instantaneous solution of a two-dimensional turbulent flame, obtained through a simulation with a fixed constant model and thickened flamelet approach. The output of the original model was, however, not reasonable. This was due to poor predictions of the turbulence strength at the test-filter scale. A modified formulation of the model that does not require the prediction of the turbulence strength was, therefore, proposed.

Using this modified formulation of the dynamic thickened flamelet model, the effects of numerical parameters, such as the test-filter size, the width of the averaging interval, and the choice of the reaction model in the calculation of the Charlette's constant β, were investigated, and the parameters were determined for multi-dimensional simulations. Boger's algebraic model and the reduced Arrhenius law based on the progress variable were verified to be efficient in the calculation of the constant β, while the standard Arrhenius law was observed to be strongly influenced by the use of different Schmidt numbers Sc for each chemical species, and caused numerical problems. Thus, only the two formers were chosen for multi-dimensional simulations.

Two-dimensional simulations were conducted with the previously determined parameters, and the result was compared with those obtained with the thickened flamelet model with constant values of β. The result obtained using Boger's algebraic model in the calculation of the constant β was close to the results calculated with $\beta = 0.3$ and $\beta = 0.5$. The dynamic thickened flamelet model succeeded in reproducing a realistic turbulent combustion without any empirical input for the constant β. Boger's algebraic model was, thus, chosen to be used in the three-dimensional simulation for the calculation of the constant β.

Following the same manner, the dynamic Smagorinsky model was also tested. Because the density of the flow media significantly changes across a flame front, the output of the dynamic Smagorinsky model with density change (Moin's procedure) was also investigated in comparison with the standard dynamic Smagorinsky model.

Applying a LES filter to a laminar one-dimensional flame, analytical values of the subgrid-scale flux of momentum was obtained as the difference of filtered and non-filtered fields. The obtained values revealed the existence of the subgrid-scale flux of momentum in the direction opposite to the prediction of the usual gradient assumption in a laminar one-dimensional flame. However the magnitude was small compared to the resolved momentum flux and it was negligible.

Then the dynamic Smagorinsky models, both with and without the density change, were applied to the LES filtered laminar one-dimensional flame. Both models reproduced well the subgrid-scale flux of momentum and yielded similar values to the analytical values.

The models were then applied to a laminar one-dimensional flame resolved on a LES mesh using the thickened flamelet approach. Both of them predicted a subgrid-scale flux of momentum opposite to the direction of the usual gradient assumption, but the magnitude of the subgrid-scale flux was smaller than that obtained in the previous test, i. e., the flux would also be negligible in multi-dimensional simulations performed in this study. The values of the Smagorinsky constant C_S were, thus, set to zero in the multi-dimensional simulations of this study, when the dynamic Smagorinsky model returned negative C_S values.

The test with an instantaneous solution of a two-dimensional turbulent flame was also performed with both models. Both of them predicted negative C_S in the flame and their predictions were quite similar.

These two dynamic Smagorinsky models were coupled with the dynamic thickened flamelet model for performing two-dimensional simulations. The time averaged fields of the dynamically determined Smagorinsky constant C_S and turbulent viscosity μ_t were, then, compared. Contrary to the test performed with an instantaneous solution of a two-dimensional turbulent flame, the time averaged fields were considerably different, and the difference demonstrated the importance of considering the density change across the flame front.

Lastly, a three-dimensional simulation of a V-shape flame was performed using the dynamic thickened flamelet model and the dynamic Smagorinsky model with the density change, and the result was compared with the experimental data of Knikker et al. (2002) and Knikker et al. (2004). The comparison inferred that the magnitude of the efficiency function calculated with the dynamic thickened flamelet model was larger than the values required to reproduce the experimental data. However, the results were qualitatively quite similar, and this fact proved the feasibility of the dynamic thickened flamelet model to compute the turbulent combustion without any empirical input for the efficiency function.

From the investigations of the present study of the dynamic thickened flamelet model, several conclusions can be drawn:

- The original dynamic thickened flamelet model proposed by Charlette et al. (2002b) causes a divergence of the constant β when the turbulence strength is weak. This is due to the close values of fluctuating velocities ${u'}_{\Delta}$ and ${u'}_{\gamma\Delta}$ at the flame thickness scale and test-filter scale. To overcome this problem, a modification was added in this study.

- The three-dimensional simulation of a V-shape flame stabilized downstream of a triangular flame holder was performed with the modified dynamic thickened flamelet model, and the result was compared with the experimental data. The comparison showed the feasibility of the dynamic thickened flamelet model to compute a turbulent combustion without any empirical input. However, some discrepancies were found between the numerical results and experimental data.

- These discrepancies could be caused by poor prediction of the turbulence strengths at the flame thickness scale and at the test-filter scale. For the development of the precision of the dynamic thickened flamelet model, a more appropriate procedure to calculate the turbulence strength is required. Another possible cause of the errors lies in the poor description of the flame stabilization immediately downstream of the flame holder by the thickened flamelet model.

- The numerical cost of the simulation performed with the dynamic procedures was more than twice as much as that of simulations with fixed model constants, but it remains at an accessible level. It will be further efficient by using a greater number of processors than in the present study and by developing the computational algorithm for the dynamic procedures.

Future works

From the first proposition of the dynamic thickened flamelet model by Charlette et al. (2002b), there have been little attempt for its development. The model, therefore, still remains in a primitive stage. Further investigations are required for the development. The major topics for this are summarized as follows:

- Development for the calculation of turbulent intensity at the thickness scale of the thickened flame and at the test filter scale: The discrepancies found between the result of the three-dimensional simulation and the experimental data was probably caused by the poor approximation of the terms related to the turbulence intensity. Solving transport equations of kinetic energy is one of the powerful candidates to development the precision of the dynamic thickened flamelet model.

- Further investigation of the impact of the reaction model used in the calculation of Charlette's constant β: In the present study, three reaction model were tested for the calculation of the model constant β, but only Boger's algebraic model was applicable to the three-dimensional simulation. However, It is not obvious to say that this model is the best one to be used in the dynamic thickened flamelet model. For example, the Arrhenius law can also be used, when the Schmidt numbers Sc are identical for all chemical species. The dependence of the choice of the reaction model on the numerical configuration should be further investigated.

- Simulations of turbulent combustion under variable conditions of turbulent intensity, equivalence ratio of the fuel-air mixture, and geometries of the combustion chamber: In this study, only one combination of the inlet speed, the equivalence ratio, and the geometry of combustion chamber was considered. Simulations and experiments of different numerical configurations and geometries of combustion chamber are required for the development and inspections of the dynamic thickened flamelet model.

- Improvement of the algorithms and numerical setup: Because the present study focused on the feasibility of the dynamic thickened flamelet model to compute turbulent combustion, the algorithms in the computational code were not highly developed. As the dynamic procedure mainly consists of filtering and integrating processes, the development of these subroutines may dramatically decrease the numerical costs. The coupling frequency of the AVBP code and the DTF-DS code, which was set to 100 in the present study, can also be further optimized depending on numerical configurations.

References

Abdel-Gayed, R. G., D. Bradley, and M. Lawes (1987). Turbulent burning velocities: A general correlation in terms of straining rates. *Proceedings of the Royal Society of London A 414*, 389–413.

Bardina, J., J. H. Ferziger, and W. C. Reynolds (1980). Improved subgrid-scale models for large-eddy simulation. *AIAA paper* (80), 1357.

Bardina, J., J. H. Ferziger, and W. C. Reynolds (1983). Improved turbulence models based on large eddy simulations of homogeneous, incompressible, turbulent flows. Department of mechanical engineering report tf-19, Stanford University.

Baum, M., T. Poinsot, and D. Thévenin (1995, February). Accurate boundary conditions for multicomponent reactive flows. *Journal of Computational Physics 116*(2), 247–261.

Blint, R. J. (1986, September). The relationship of the laminar flame width to flame speed. *Combustion Science and Technology 49*(1-2), 79–92.

Boger, M. and D. Veynante (2000). Large eddy simulations of a turbulent premixed v-shape fllame. In *Advances in Turbulence VIII*, pp. 449–452. CIMNE.

Boger, M., D. Veynante, H. Boughanem, and A. Trouvé (1998). DNS analysis of flame surface density models for LES of turbulent premixed combustion. *27th Symposium (international) on Combustion*, 917–925.

Boger, M. M. (2000). *Modélisation de sous-maille pour la simulation aux grandes échelles de la combustion turbulente prémélangée.* Ph. D. thesis, Ecole Centrale de Paris.

Bou-Zeid, E., N. Vercauteren, M. B. Parlange, and C. Meneveau (2008, November). Scale dependence of subgrid-scale model coefficients: An a priori study. *Physics of Fluids 20*(11), 115106.

Bourlioux, A. (2000, May). Semi-analytical validation of a dynamic large-eddy simulation procedure for turbulent premixed flames via the g-equation. *Combustion Theory and Modelling 4*, 363–389.

Boussinesq, J. (1877). Essai sur la théorie des eaux courantes. *mémoires présentée par divers savants à l'Academie des sciences 23*, 1–680.

Bradley, D. (1992). How fast can we burn? *24th Symposium (International) on Combustion*, 247–262.

Bray, K. N. C. (1996). The challenge of turbulent combustion. *26th Symposium (international) on Combustion*, 1–26.

Bray, K. N. C., M. Champion, and P. A. Libby (1989). In R. Borghi and S. N. Murphy (Eds.), *Turbulent Reacting Flows*, pp. 541–563. Springer.

Bray, K. N. C., P. A. Libby, G. Masuya, and J. B. Moss (1981). Turbulence production in premixed turbulent flames. *Combustion Science and Technology 25*, 127–140.

Butler, T. D. and P. J. O'Rourke (1977). A numerical method for two dimensional unsteady reacting flows. *16th Symposium (international) on Combustion*, 1503–1515.

Candel, S. and T. Poinsot (1990). Flame stretch and the balance equation for the flame area. *Combustion Science and Technology 70*(1-3), 1–15.

Catrakis, H. J. and P. E. Dimotakis (1996, October). Scale distributions and fractal dimensions in turbulence. *Physical Review Letters 77*(18), 3795–3798.

Chakraborty, N. and R. Cant (2009). Direct numerical simulation analysis of the flame surface density transport equation in the context of large eddy simulation. *Proceedings of the combustion institute 32*, 1445–1453.

Charlette, F., C. Meneveau, and D. Veynante (2002a, Octorber). A power-law flame wrinkling model for les of premixed turbulent combustion part I: non-dynamic formulation and initial tests. *Combustion and Flame 131*(1-2), 159–180.

Charlette, F., C. Meneveau, and D. Veynante (2002b, Octorber). A power-law flame wrinkling model for les of premixed turbulent combustion. part II: Dynamic formulation. *Combustion and Flame 131*(1-2), 181–197.

Cheng, Y., F. S. Lien, E. Yee, and R. Sinclair (2003). A comparison of large eddy simulations with a standard k-Reynolds-averaged navier-Stokes model for the prediction of a fully developed turbulent flow over a matrix of cubes. *Journal of Wind Engineering and Industrial Aerodynamics 91*, 1301–1328.

Chester, S., F. Charlette, and C. Meneveau (2001, December). Dynamic model for les without test filtering: Quantifying the accuracy of taylor series approximations. *Theoretical and Computational Fluid Dynamics 15*(3), 165–181.

Colin, O., F. Ducros, D. Veynante, and T. Poinsot (2000, July). A thickened flame model for large eddy simulations of turbulent premixed combustion. *Physics of Fluids 12*(7), 1843–1863.

Colin, O. and M. Rudgyard (2000, August). Development of high-order taylor-galerkin schemes for LES. *Journal of Computational Physics 162*(2), 338–371.

Damköhler, G. (1940). Der einfluss der turbulenz auf die flammengeschwindigkeit in gasgemischen. *Z. Elektrochem. (English translation NACA TM 1112, 1947) 46*, 601–652.

Deardorff, J. W. (1970). A numerical study of three-dimensional turbulent channel flow at large reynolds. *Journal of Fluid Mechanics 41*, 453–480.

Donea, J. (1984). A taylor-galerkin method for convective transport problems. *International Journal for Numerical Methods in Engineering 20*, 101–119.

Erlebacher, G., M. Y. Hussaini, C. G. Speziale, and T. A. Zang (1990). ICASE Report 90-76, ICASE/NASA Langley Research Center.

Ferziger, J. (1997). Large eddy simulation: an introduction and perspective. In O. Métais and J. Ferziger (Eds.), *New tools for turbulence modeling*, Les editions de physique, pp. 29–47. Springer-Verlag.

Ferziger, J. and T. Echekki (1993, March). A simplified reaction rate model and its application to the analysis of premixed flames. *Combustion Science and Technology 89*(5-6), 293–315.

Ferziger, J. and M. Perić (2002). *Computational methods for fluid dynamics.* Springer.

Germano, M., U. Pimelli, P. Moin, and W. Cabot (1991, July). A dynamic subgrid-scale eddy viscosity model. *Physics of Fluids A 3*(7), 1760–1765.

Ghosal, S., T. S. Lund, P. Moin, and K. Akselvoll (1995). A dynamic localization model for large eddy simulation of turbulent flows. *Journal of Fluid Mechanics 286*, 229–255.

Giacomazzi, E., V. Battaglia, and C. Bruno (2004). The coupling of turbulence and chemistry in a premixed bluff-body flame as studied by les. *Combustion and Flame 138*(4), 320 – 335.

Giles, M. (1990). Non-reflecting boundary conditions for euler equation calculation. *AIAA journal 28*(12), 2050–2058.

Gonçalves dos Santos, R. (2007). *Large eddy simulations of turbulent combustion including radiative heat transfer*. Ph. D. thesis, Ecole Centrale de Paris.

Gouldin, F. C. (1987, June). An application of fractals to modeling premixed turbulent flames. *Combustion and Flame 68*, 249–266.

Gouldin, F. C., K. N. C. Bray, and J. Y. Chen (1989, September). Chemical closure model for fractal flamelets. *Combustion and Flame 77*(3-4), 241–259.

Gulder, O. L. (1991). Turbulent premixed combustion modelling using fractal geometry. *23th Symposium (International) on Combustion 23*, 835–842.

Hirsch, C. (1989). *Recent advances in the aerospace sciences*. John Wiley & Sons.

Im, H. G., T. S. Lund, and J. H. Ferziger (1997, December). Large eddy simulation of turbulent front propagation with dynamic subgrid models. *Physics of Fluids 9*, 3826–3833.

Kerstein, A. R., W. Ashurst, and F. A. Williams (1988). Field equation for interface propagation in an unsteady homogeneous flow field. *Physical Review A 37*(7), 2728–2731.

Knikker, R., D. Veynante, and C. Meneveau (2002). *A PRIORI* testing of a similarity model for Large Eddy Simulations of turbulent premixed combustion. *Proceedings of the combustion institute 29*, 2105–2111.

Knikker, R., D. Veynante, and C. Meneveau (2004, November). A dynamic flame surface density model for large eddy simulation of turbulent premixed combustion. *Physics of Fluids 16*(11), L91–L94.

Knikker, R., D. Veynante, J. Rolon, and C. Meneveau (2000). Planar laser-induced fluorescence in a turbulent premixed flame to analyze large eddy simulation models. In *10th International Symposium on Applications of Laser techniques to Fluid mechanics*. Lisbon, Portugal.

Knundsen, E. and H. Pitsch (2008, July). A dynamic model for the turbulent burning velocity for large eddy simulation of premixed combustion. *Combustion and Flame 154*, 740–760.

Kolmogorov, A. (1941). The local structure of turbulence in incompressible viscous fluid for very large reynolds numbers. *Proceedings of the USSR Academy of Sciences 30*, 299–303.

Légier, J. P., T. Poinsot, and D. Veynante (2000). Dynamically thickened flame Large Eddy Simulation model for premixed and non-premiced turbulent combustion. In *Proceeding of the Summer Program*, pp. 157–168. Center for Turbulence Research, NASA Ames/Standord University, USA.

Lesieur, M. (1997). Recent approaches in large-eddy simulations of turbulence. In O. Métais and J. Ferziger (Eds.), *New tools for turbulence modeling*, Les editions de physique, pp. 1–28. Springer-Verlag.

Lesieur, M. and O. Métais (1996, January). New trands in large-eddy simulations of turbulence. *Annual Review of Fluid Mechanics 28*, 45–82.

Libby, P. A. and K. N. C. Bray (1981). Countergradient diffusion in premixed turbulent flames. *AIAA journal 19*(2), 205–213.

Lilly, D. K. (1992, March). A proposed modification of the germano subgrid-scale closure method. *Physics of Fluids A 4*(3), 633–635.

Marble, F. E. and J. E. Broadwell (1977). The coherent flame model for turbulent chemical treactions. Project Squid TRW-9-PU, Project Squid Headquaters, Chaffee Hall, Purdue University.

McMillan, O. J., J. H. Ferziger, and R. S. Rogallo (1980). Tests of subgrid-scale models in strained turbulence. *AIAA paper* (80), 1339.

Meneveau, C. and J. Katz (2000, January). Scale-invariance and turbulence models for large eddy simulation. *Annual Review of Fluid Mechanics 32*, 1–32.

Meneveau, C. and T. S. Lund (1997, December). The dynamic smagorinsky model and scale-dependent coefficients in the viscous range of turbulence. *Physics of Fluids 9*(12), 3932–3934.

Meneveau, C., T. S. Lund, and W. H. Cabot (1996). A labrangian dynamic subgrid-scale model of turbulence. *Journal of Fluid Mechanics 319*, 353–385.

Menter, F. R. (1993). Zonal two-equations k-ω turbulence models for aerodynamic flows. *AIAA paper* (93), 2906.

Moin, P. (1991). *A new approach for large eddy simulation of turbulence and scalar transport*. Birkhauser.

Moin, P., K. Squires, W. Cabot, and S. Lee (1991, November). A dynamic subgrid-scale model for compressible turbulence and scalar transport. *Physics of Fluids A 3*(11), 2746–2757.

Moureau, V., G. Lartigue, Y. Sommerer, C. Angelberger, O. Colin, and T. Poinsot (2005, January). Numerical methods for unsteady compressible multi-component reacting flows on fixed and moving grids. *Journal of Computational Physics 202*(2), 710–736.

Nicoud, F. (1999, March). Defineing wave amplitude in characteristic boundary conditions. *Journal of Computational Physics 149*(2), 418–422.

O’Rourke, P. J. and F. V. Bracco (1979, November). Two scaling transformations for the numerical computation of multidimensional unsteady laminar flames. *Journal of Computational Physics 33*(2), 185–203.

Peters, N. (1999). The turbulent burning velocity for large-scale and small-scale turbulence. *Journal of Fluid Mechanics 384*, 107–132.

Peters, N. (2000). *Turbulent combustion*. Cambridge university press.

Peters, N., P. Terhoeven, J. H. Chen, and T. Ehekki (1997). Statistics of flame displacement speeds from computations of 2-D unsteady methane-air flames. *27th Symposium (international) on Combustion*, 833–839.

Piomelli, U. (1999). Large eddy simulations: achievements and challenges. *Progress in aerospace sciences 35*, 335–362.

Piomelli, U., W. H. Cabot, P. Moin, and S. Lee (1991, July). Subgrid-scale backscatter in turbulent and transitional flows. *Physics of Fluids A 3*(7), 1766–1771.

Piomelli, U. and J. R. Chasnov (1996). Large eddy simulations: theory and applications. In H. Hallb́ack, D. S. Henningson, A. V. Johansson, and P. H. Alfredsson (Eds.), *Turbulence and transition modelling*, pp. 269–336. Kluwer Academic Publishers, Dordrecht.

Piomelli, U. and J. Liu (1995). Large-eddy simulation of rotating channel flows using a localized dynamic model. *Physics of Fluids 7*(4), 839–848.

Pitsch, H. (2006, January). Large-eddy simulation of turbulent combustion. *Annual Review of Fluid Mechanics 38*, 453–482.

Pocheau, A. (1994). Scale invariance in turbulent front propagation. *Physical Review E 49*, 1109–1122.

Poinsot, T. and S. Lele (1992, July). Boundary conditions for direct simulations of compressible viscous flows. *Journal of Computational Physics 101*(1), 104–129.

Poinsot, T. and D. Veynante (2005). *Theoretical and numerical combustion* (second ed.). Edwards.

Pope, S. B. (2004, March). Ten questions concerning the large-eddy simulation of turbulent flows. *New Journal of Physics 6*, 35.

Quartapelle, L. and V. Selmin (1993). High-order taylor-galerkin methods for non-linear multidimensional problems. *Finite elements fluids*, 1375.

Richard, S., O. Colin, O. Vermorel, A. Benkenida, C. Angelberger, and D. Veynante (2007). Towards large eddy simulation of combustion in spark ignition engines. *Proceedings of the Combustion Institute 31*(2), 3059 – 3066.

Sagaut, P. (2000). *Large Eddy Simulation for incompressible flows.* Springer-Verlag.

Salvetti, M. V. and S. Banerjee (1995, November). A priori tests of a new dynamic subgrid-scale model for finite-difference large-eddy simulation. *Physics of Fluids 7*(11), 2831–2847.

Schmitt, P. (2005). *Simulation aux grandes échelles de la combustion étagée dans les turbines à gaz et son interaction stabilité - polluants - thermique.* Ph. D. thesis, Institut National Polytechnique de Toulouse.

Schmitt, P., T. Poinsot, B. Schuermans, and K. P. Geigle (2007). Large-eddy simulation and experimental study of heat transfer, nitric ocide emissions and combustion instability in a swirled turbulent high-pressure burner. *Journal of Fluid Mechanics 570*, 17–46.

Selle, L., G. Lartigue, T. Poinsot, R. Koch, K. Schildmacher, W. Krebs, B. Prade, P.Kaufmann, and D. Veynante (2004, June). Compressible large eddy simulation of turbulent combustion in complex geometry on unstructured meshes. *Combustion and Flame 137*(4), 489–505.

Shepherd, I., J. Moss, and K. Bray (1982). Turbulent transport in a confined premixed flame. *19th Symposium (International) on Combustion 19*, 423–431.

Smagorinsky, J. (1963). General circulation experiments with the primitive equations. *Monthly Weather Review*, 99–164.

Sutherland, J. C. and C. A. Kennedy (2003, November). Improved boundary conditions for viscous, reacting, compressible flows. *Journal of Computational Physics 191*(2), 502–524.

Tennekes, H. and J. Lumley (1976). *A frist course in turbulence.* MIT Press.

Thompson, K. W. (1987, January). Time dependent boundary conditions for hyperbolic systems. *Journal of Computational Physics 68*(1), 1–24.

Trouvé, A. and T. Poinsot (1994). The evolution equation for the flame surface density. *Journal of Fluid Mechanics 278*, 1–31.

Truffin, K. (2005). *Simulation aux grandes échelles et identification acoustique des turbines á gaz en régime partiellement premelangé.* Ph. D. thesis, Institut National Polytechnique de Toulouse.

Varoquié, B. (2004). *Analyse expérimentale de la simulation aux grandes échelles en combustion non-prémélangée.* Ph. D. thesis, Ecole Centrale de Paris.

Vervisch, L., E. Bidaux, K. N. C. Bray, and W. Kollmann (1995, October). Surface density function in premixed turbulent combustion modeling, similarities between probability density function and flame surface approaches. *Physics of Fluids 7*, 2496–2503.

Veynante, D., A. Trouvé, K. N. C. Bray, and T. Mantel (1997, February). Gradient and counter-gradient scalar transport in turbulent premixed flames. *Journal of Fluid Mechanics 332*, 263–293.

Veynante, D. and L. Vervisch (2002). Turbulent combustion modeling. *Progress in energy and combustion science 28*, 193–266.

Wilcox, D. C. (1998). *Turbulence modeling for CFD.* Dcw Industries, Incorporated.

Williams, F. A. (1985). The Mathematics of Combustion. pp. 97–131. SIAM.

Yakhot, V. (1988). Propagation velocity of premixed turbulent flames. *Combustion science and technology 60*, 191–214.

Yeung, P., S. Girimaji, and S. Pope (1990, March). Straining and scalar dissipation on material surfaces in turbulence: Implications for flamelets. *Combustion and Flame 79*(3-4), 340–365.

Yoshizawa, A. (1986). Statistical theory for compressible turbulent shear flows, with the application to subgrid modeling. *Journal of Fluid Mechanics 29*, 2152–2164.

Appendix A

Characteristic boundary condition

The idea of the characteristic boundary condition is to correct the temporal evolution of the variables calculated by the numerical scheme by using the so-called characteristic variables.

The characteristic variables are defined through transformation of the original transport equations of conservative variables. This transformation starts, in general, from the transformation of the original system into the system defined by one normal to the boundary and two tangential bases, then into the characteristic form by diagonalizing the normal Jacobian due to the first transformation. There are several ways of this. The details of this process can be found for example in Thompson (1987), Baum et al. (1995), Poinsot and Veynante (2005) and Moureau et al. (2005).

After the transformation of the original transport equations into the normal and tangential system, they write:

$$\frac{\partial V_n}{\partial t} + N + \frac{\partial V_n}{\partial \vec{n}} + T_1 \frac{\partial V_n}{\partial \vec{t_1}} + T_2 \frac{\partial V_n}{\partial \vec{t_2}} + S = 0\,. \tag{A.1}$$

$\vec{n}$ is the normal vector to the boundary pointing to outside of the computational domain. $\vec{t_1}$ and $\vec{t_2}$ are the tangential unit vectors on the boundary surface.

By diagonalizing N, the equation above becomes:

$$\frac{\partial W}{\partial t} + D \frac{\partial W}{\partial \vec{n}} = S_W - T_W \tag{A.2}$$

where

$$D = \begin{pmatrix} \vec{u}\cdot\vec{n}+c & & & & & & \\ & \vec{u}\cdot\vec{n}-c & & & 0 & & \\ & & \vec{u}\cdot\vec{n} & & & & \\ & & & \vec{u}\cdot\vec{n} & & & \\ & 0 & & & \vec{u}\cdot\vec{n} & & \\ & & & & & \ddots & \\ & & & & & & \vec{u}\cdot\vec{n} \end{pmatrix} \tag{A.3}$$

and

$$W = \begin{pmatrix} u_n + \frac{1}{\rho c}P \\ -u_n + \frac{1}{\rho c}P \\ u_{t1} \\ u_{t2} \\ -\frac{Y_1}{c^2}P + \rho_1 \\ \vdots \\ -\frac{Y_N}{c^2}P + \rho_N \end{pmatrix} \tag{A.4}$$

S_W is the sum of the terms due to diffusion and chemical reactions. T_W is related to the tangential terms. W is the vector of the characteristic variables. The waves of each characteristic variable propagate at the speeds of corresponding terms in D. There exist, thus, at least one incoming wave at any boundary in a subsonic condition.

The time evolution of the conservative variables are calculated by the numerical scheme using the original transport equations. Let us represent the vector of conservative variables by U. Then the evolution of conservative variables is:

$$\partial U_p = U^{n+1} - U^n \,, \tag{A.5}$$

where the subscript p indicates the "*prediction*" as this value should be corrected by the boundary condition. The evolution of the characteristic variables is then obtained from that of the conservative variables. By representing the transformation matrices between the two systems by L_U and R_U, it writes

$$\partial W = L_U \partial U \qquad \partial U = R_U \partial W \tag{A.6}$$

Then we get

$$\partial W_p = L_U \partial U_p \tag{A.7}$$

However, the evolution of the characteristic variables related to the incoming waves should be defined by boundary conditions.

For the clarity, the following discussion focuses on the case where the wave of the second characteristic variable goes out through the boundary. This is a typical outlet condition of subsonic simulations. Other evolutions of the characteristic variables do not need to be modified. One of the simplest ways is to calculate the evolution of incoming wave from the spatial derivative of related characteristic variable at the boundary.

$$\partial W_2 = D_{22} \frac{\partial W_2}{\partial n} \Delta t \tag{A.8}$$

The evolution of the conservative variable related to the incoming wave is then subtracted from the evolution by setting the evolution of corresponding characteristic variables to zero and the value above is substituted.

$$\partial W_c = \partial W_p - \begin{pmatrix} 0 \\ \partial W_{p2} \\ 0 \\ 0 \\ 0 \\ \vdots \\ 0 \end{pmatrix} + \begin{pmatrix} 0 \\ \partial W_2 \\ 0 \\ 0 \\ 0 \\ \vdots \\ 0 \end{pmatrix} \tag{A.9}$$

Here the subscript c indicates "*corrected*" value. This corrected evolution is then cast to the evolution of conservative variables.

$$\partial U_c = R_U \partial W_c \tag{A.10}$$

There are several candidates for the application of the characteristic boundary condition. In Hirsch (1989), a treatment of the characteristic boundary condition of advection terms in the bi-characteristic equations was presented. Utilization of Fourier decomposition at the boundary was tested in Giles (1990). Viscous and reaction terms were implemented by Sutherland and Kennedy (2003). Nicoud (1999) tested the non-reflecting boundary condition defined by different formulations and showed the dependence of the solution and its convergence speed on the formulation.

Appendix B

Implementation of the filtering process and the dynamic procedure

Implementation of the filtering process in multi-dimensional simulations

As presented in Chapter 1, the filtering process is essential in the context of the Large Eddy Simulation. It writes,

$$\overline{Q}(\mathbf{x}) = \int Q(\mathbf{x})F(\mathbf{x}-\mathbf{x}')d\mathbf{x}' \tag{B.1}$$

where $Q(\mathbf{x})$ and $\overline{Q}(\mathbf{x})$ are a physical quantity and its filtered value at a position $\mathbf{x} = (x_1, x_2, x_3)$ respectively. In the present study, Gaussian filters are used. Then,

$$F(\mathbf{x}) = f(x_1, x_2, x_3) = \left(\frac{6}{\pi \mathit{\Delta}^2}\right)^{3/2} \exp\left[-\frac{6}{\mathit{\Delta}^2}\left(x_1^2 + x_2^2 + x_3^2\right)\right] , \tag{B.2}$$

where $\mathit{\Delta}$ is the filter size. The shape of the filter is presented in Figure B.1.
In theory, the filtering should be done integrating the value of Q in the whole computational domain. However, this procedure is numerically too expensive and not efficient.
Considering the shape of a Gaussian filter, only the values of the variables of points that are within a range of $\mathit{\Delta}$ from the target point are used for the calculation of the filtered variables.

$$\begin{aligned} \overline{Q}(\mathbf{x}) &= \int Q(\mathbf{x}')F(\mathbf{x}-\mathbf{x}')d\mathbf{x}' \\ &\approx \int_{(\mathbf{x}-\mathbf{x}')^2<\mathit{\Delta}^2} Q(\mathbf{x}')F(\mathbf{x}-\mathbf{x}')d\mathbf{x}' \ . \end{aligned} \tag{B.3}$$

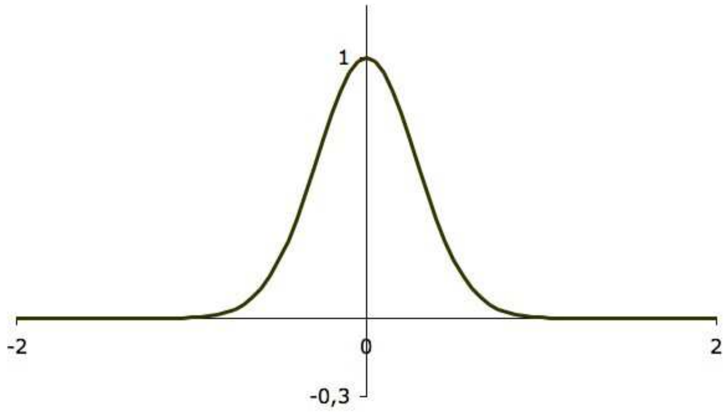

Figure B.1 : *Shape of the Gaussian filter. Horizontal axis was non-dimensioned by the filter size Δ.*

In a practical implementation, every grid point is named by a number. At the beginning of the simulation, using these numbers, the filtering code creates a list of points to be considered in the calculation of filtered variables for each grid point. Because unstructured meshes are used in the present study, the volume, dV, covered by one grid point is not constant. Then as a first step, the sums of the original values on the listed points multiplied by the values of $F(\mathbf{x}-\mathbf{x}')dV'$ are calculated at each grid, where dV' is the volume covered by a grid point at $\mathbf{x}'$. The sums are then divided by the sum of the volume. This procedure writes,

$$\overline{Q}(\mathbf{x}) \approx \frac{\displaystyle\sum_{(\mathbf{x}-\mathbf{x}')^2<\Delta^2} Q(\mathbf{x}')F(\mathbf{x}-\mathbf{x}')dV'}{\displaystyle\sum_{(\mathbf{x}-\mathbf{x}')^2<\Delta^2} dV'} \,. \tag{B.4}$$

Dynamic calculation of the model coefficients

The calculation of the model coefficients such as Charlette's coefficient β and the Smagorinsky coefficient C_S is performed separately from the computation of the turbulent combustion which is performed in the AVBP code. As Figure B.2 presents, the AVBP code sends the values of variables which are required in the calculation of the model coefficients to the code that conducts the calculation. This code is mentioned as DTF-DS code in the following. After receiving the variables, the DTF-DS code starts calculating the model coefficients β and C_S, and returns their values back to the AVBP code. Because the time step is quite small due to the use of the explicit time evolution procedure, the values of the model coefficients need not to be calculated at each iteration. Retaining the value of Gonçalves dos Santos (2007), the two codes are coupled every 100 iterations. This frequency of the update of model coefficients corresponds to each 27 μs in physical time. The AVBP code continues the simulation using the values of the coefficients returned previously, while the new values of the model coefficients are being calculated by the DTF-DS code.

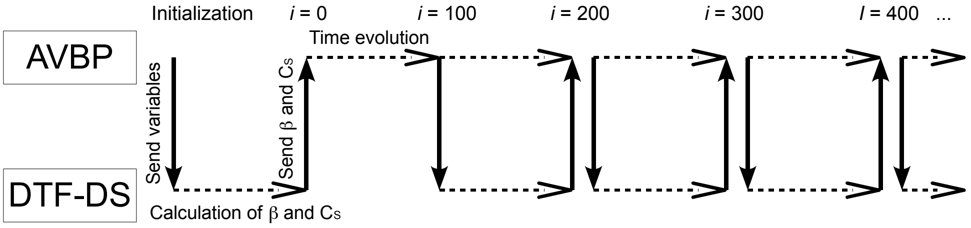

Figure B.2 : *Coupling of the AVBP code and the DTF-DS code. i in the figure represents the iteration step.*